Università degli Studi di Ferrara

DOCTORAL COURSE IN

“ENGINEERING SCIENCE”

CYCLE XXXVIII

COORDINATOR Prof. Spina Pier Ruggero

Sustainability in 3D printing: recycling and continuous fiber biocomposites

Scientific/Disciplinary Sector (SDS) IMAT-01/A

Candidate

Ing. Zanelli Marco

Supervisor

Prof. Mollica Francesco

Prof. Mazzanti Valentina

Year 2022/2025

Table of contents

Abstract 1
1. Fused Deposition Modeling technology 3
1.1 Introduction 3
1.2 Technological overview 4
1.2.1Workflow and architecture 4
1.2.2 Process parameters 5
1.2.3 Filament preparation 8
Filament production line 10
1.2.4 Continuous fiber technique 12
1.2.5 Multi-scale structure 16
1.3 Materials 18
1.3.1 Thermoplastic matrices 18
1.3.2 Reinforcing fibers 20
Fossil-based fibers 21
Natural fibers 22
2. Thermoplastic materials: Polyamides and Polyesters 25
2.1 Introduction 25
2.2 Polyamides 25
2.2.1 Preparation methods 26
Polycondensation with different molecules ($Nylon\ a, b$) 26
Ring opening and self-polycondensation ($Nylon\ a$) 27
2.2.2 Structure and properties 28
2.2.3 Eco-sustainability 31
2.3 Polyesters 33
2.3.1 Polylactic acid (PLA) 35
Preparation methods 35
Structure and properties 36
2.3.2 Polybutylene succinate (PBS) 38
Preparation methods 38

Structure and properties 39
3. Characterization of 3D-printed fiber-reinforced composites and their constituents 41
3.1 Introduction 41
3.2 Mechanical behavior 41
3.2.1 Mathematical modeling 41
Quantification of stiffness anisotropic behavior 43
Strength of a fiber-reinforced lamina 46
3.2.2 Tensile characterization 48
3.3 Density and porosity evaluation 50
3.4 Thermal characterization 50
3.5 Rheological characterization 51
3.5.1 Steady-shear mode 53
3.5.2 Dynamic oscillation mode 54
3.6 Morphological analysis 56
3.7 Methods and instruments 57
3.7.1 Tensile tests 57
3.7.2 Mass and dimensional measurements 58
3.7.3 Thermal analysis 58
3.7.4 Rheological tests 58
3.7.5 Optical analysis and preparative methods 59
4. 3D printing of polyamide 6 reinforced with short carbon fiber: characterization of virgin and recycled material 61
4.1 Introduction 61
4.2 Materials and methods 63
4.2.1 Materials 63
4.2.2 Recycling process 64
4.2.3 3D printing parameters 65
4.2.4 Material characterization 66
Voids measurements 66
Tensile characterization 66
Microscopy analysis 67
Rheological tests 67

Thermal analysis 67
4.3 Results and discussion 68
4.3.1 Thermal characterization results 68
4.3.2 Rheological results 71
4.3.3 Voids and stereomicroscope analysis 74
4.3.4 Mechanical characterization 76
Stiffness anisotropy 82
4.4 Conclusions and future developments 83
5. Mechanical characterization and anisotropy evaluation of 3D printed continuous basalt fiber composites 86
5.1 Introduction 86
5.2 Materials and methods 88
5.2.1 Materials 88
5.2.2 3D printer 88
5.2.3 Specimen preparation 91
5.2.4 Material characterization 93
Tensile characterization 93
Voids measurements 93
Rheological tests 94
Thermal analysis 94
5.3 Results and discussion 94
5.3.1 Thermal characterization results 94
5.3.2 Rheological results 97
5.3.3 Density and voids measurements 98
5.3.4 Mechanical characterization 100
Stiffness anisotropy 102
5.4 Conclusions and future developments 104
6. Continuous vegetable fiber as reinforcement in 3D printing 106
6.1 Introduction 106
6.2 Vegetable fibers 107
6.2 3D printed biocomposites: state of the art in literature 108
6.2.1 Flax fibers as continuous reinforcement 110

3D Printing techniques employed 112
Tensile properties 112
Other types of characterization and testing 114
6.2.2 Ramie fibers as continuous reinforcement 114
6.2.3 Other fibers of different nature as continuous reinforcement 115
Tensile properties 117
6.2.4 Key common features among the works analyzed 118
3D Printing techniques employed 118
Tensile characterization 119
Pre-printing fiber treatment 120
6.3 Conclusions and future developments 120
7. Continuous vegetable fiber preparation phase: workflow and fiber analysis 122
7.1 Introduction 122
7.2 Materials and methods 125
7.2.1 Materials 125
Fibers 125
Resins 126
7.2.2 Two-stage curing process 129
First-stage 130
Resin bath 131
UV curing and cleaning 134
Winding 137
Second-stage: post-processing and dimensional control 138
7.2.3 Morphological analysis 140
7.2.4 Density and fiber volume fraction evaluation 140
7.2.5 Statistical analysis 140
Data distribution 141
Data comparison 141
7.2.6 Thermal and rheological analysis 142
7.3 Results and discussions 143
7.3.1 Rheological results 143
7.3.2 Fiber morphology and diameter evaluation 144

7.3.3 Thermal results 150
..... 152
7.4 Conclusions and future developments 152
8. 3D printing of biocomposites reinforced with continuous flax fiber: mechanical characterization and comparison 154
8.1 Introduction 154
8.2 Materials and methods 155
8.2.1 Materials 155
8.2.2 3D printer and specimen prepraration 156
8.2.3 Material characterization 157
Tensile characterization 157
Voids measurements 158
Optical analysis 159
Rheological tests 159
Thermal analysis 159
8.3 Results and discussion 160
8.3.1 Thermal and rheological 160
8.3.2 Density and voids measurements 161
8.3.3 Mechanical characterization 162
Stiffness anisotropy 168
8.3.4 Morphological observations 171
Untested specimens – cross sections 171
Fracture surface – optical analysis 171
Fracture surface – SEM 173
8.4 Conclusions and future developments 176
Conclusions and future developments 177
List of acronyms and symbols 180
References 183

Abstract

This thesis investigates the relationship between additive manufacturing (AM) and sustainability through two main research paths: the recycling of fiber-reinforced thermoplastics and the development of bio-based continuous fiber composites for 3D printing. Starting from conventional polymer systems and recycling strategies, the work progresses toward fully bio-derived materials, showing that AM can combine high mechanical performance with reduced environmental impact.

The first section outlines Fused Deposition Modeling (FDM), describing key process parameters, common polymers, and reinforcement approaches with short and continuous fibers. Polyamide and polyester matrices are then examined in terms of mechanical, thermal, and rheological properties relevant to their use in composite filaments for AM.

The characterization methods adopted in the thesis are presented next, including mechanical, thermal, rheological, and morphological analyses, together with the modeling tools and instruments used.

The first experimental investigation addresses mechanical recycling of short carbon fiber-reinforced PA6. Industrial printing scraps were re-extruded into new filaments and compared with virgin material. Although grinding and reprocessing reduced molecular weight and viscosity, this did not impair mechanical behavior; transverse and shear properties even improved, likely due to enhanced interlayer adhesion. These results support the feasibility of closed-loop recycling in FDM.

The second study explores a more sustainable composite with higher performance: a continuous basalt fiber-reinforced PA12 printed using a commercial co-extrusion system. The composite achieved a tenfold increase in stiffness and strength in the fiber direction, but exhibited strong anisotropy with poor transverse properties, highlighting the need for improved fiber orientation and post-processing. Despite being more sustainable than carbon and glass fibers, basalt still has environmental limitations, motivating the search for bio-based reinforcements.

The next research phase focuses on continuous vegetable fibers. A review identifies flax and ramie as the most promising for 3D-printed biocomposites, though their variability and compatibility with existing printers remain challenges.

To address this, a two-stage process was developed to produce coated filaments made of continuous flax fibers impregnated with UV-curable thermoset resin. Boiled and bleached flax were tested to assess the influence of surface treatments. Bleached fibers yielded more uniform, dimensionally consistent filaments meeting the tolerances of commercial composite printers. The use of a thermoset resin represents a compromise between printability, mechanical performance, and sustainability.

In the final stage, both flax-based filaments were 3D-printed and mechanically tested. The biocomposites achieved about 20% fiber volume fraction and 10% void content. Continuous flax significantly increased stiffness and strength compared to neat PLA, with bleached fibers providing more regular behavior. Fractographic observations confirmed that the thermoset matrix preserved fiber integrity during printing, enabling efficient load transfer.

Overall, the thesis demonstrates that sustainable materials and high performance can be combined in AM through proper material selection and process optimization. The findings advance understanding of thermoplastic recyclability and confirm the potential of continuous natural fibers in 3D printing, encouraging future work on more eco-friendly resin systems.

1. Fused Deposition Modeling technology

1.1 Introduction

Additive Manufacturing (AM), also referred to as 3D printing, is an advanced manufacturing process that creates three-dimensional physical objects directly from computer-aided design (CAD) data. Unlike traditional subtractive manufacturing methods, which remove material from a solid block, additive manufacturing builds objects layer by layer, adding material only where needed. This layer-wise construction enables the creation of highly complex geometries that would be difficult or impossible to achieve through conventional methods.

AM can be divided into many different categories, each suited to specific materials and applications, and the most common include: Fused Deposition Modeling (FDM), Selective Laser Sintering (SLS), and Stereolithography (SLA) [1], [2]. This thesis will focus on FDM and the various subfamilies derived from it.

FDM is the most widely used AM technology due to its ease of use, low cost, and wide availability of materials. Printers are generally more affordable than other systems such as SLA or SLS, making them more accessible for home use, rapid prototyping and production of ready-to-use parts in industry. In addition, it offers greater operational security, requires less maintenance, and file modeling and modification is less complex than with other technologies. Despite having lower resolution compared to other techniques, FDM remains a practical and the most widely adopted AM technology.

1.2 Technological overview

FDM technology will initially be described from a technological point of view. Among all the aspects that characterize this technology, those of greatest interest for the purposes of this thesis will be touched upon and introduced.

1.2.1Workflow and architecture

The 3D printing process typically begins with a 3D model designed using CAD software. Once the design is complete, it is exported as an STL (Standard Tessellation Language) file, a format that approximates the shape of the object using a mesh of triangles. This file is then processed by a Slicer software, which converts the 3D model into a series of discrete 2D cross-sectional layers. The slicer also generates machine-readable instructions, commonly referred to as G-code, which guide the movements and operations of the 3D printer during fabrication (Fig. 1.1). In addition, post-printing treatments can be carried out to remove visible layers and make the surface smooth and shiny (sanding, chemical treatments with solvents), or to improve its thermal and mechanical resistance (annealing) by heating the piece to a controlled temperature to relax internal stresses.

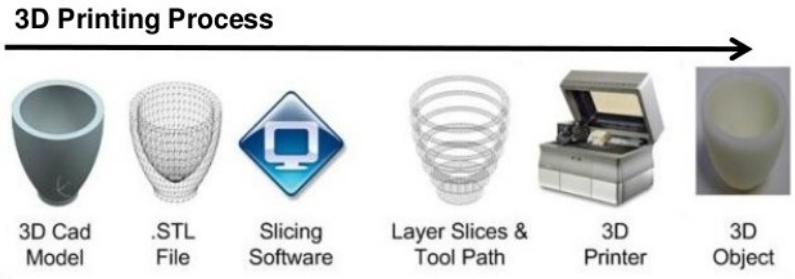

Figure 1.1: Workflow for creating 3D printed objects using FDM technology

Structurally, an FDM 3D printer consists of a frame, a printing plate, a printing head, and three motors that enable movement along three axes (X, Y, Z) (Fig. 1.2a). The thermoplastic filament is fed into the printing head, where it is melted and exits through the nozzle (Fig. 1.2b). This material is then deposited layer by layer onto the printing plate. Typically, the nozzle moves along the X and Y axes, while the platform itself moves along the Z-axis, and this allows for the creation of successive layers [3]. In addition to standard architecture, some printers have a closed printing chamber, which allows them to achieve a more uniform temperature and print

technical materials. Furthermore, a configuration with a double print head is possible, enabling the use of multiple materials in the production of the same component.

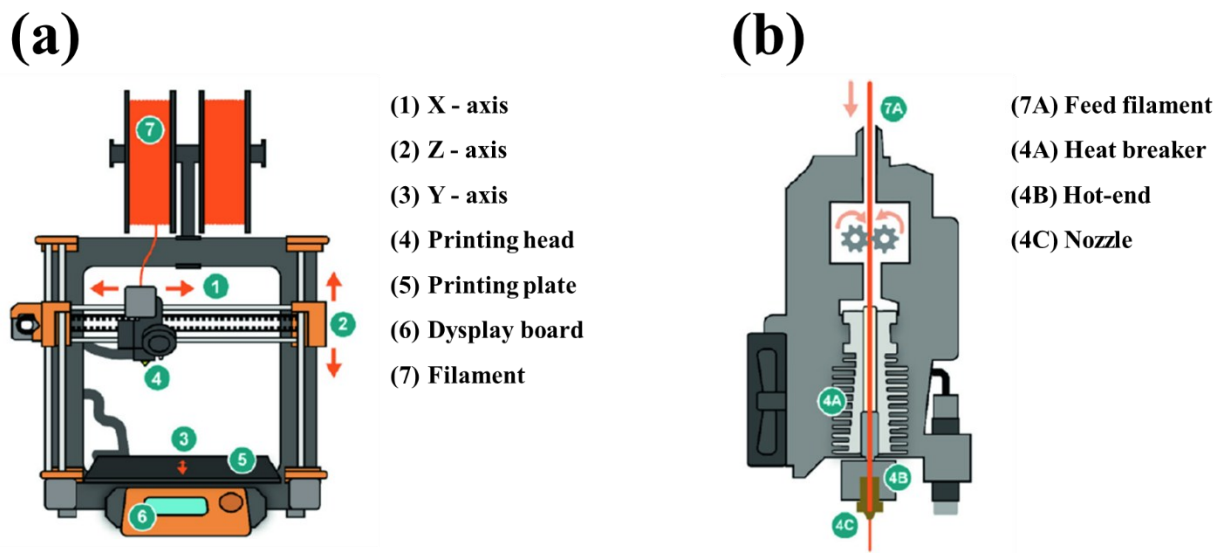

Figure 1.2: Schematic representation of (a) the architecture of an FDM printer and (b) its printing head

1.2.2 Process parameters

The slicer software is used to define the printing parameters, which are essential for ensuring good quality, adhesion, dimensional accuracy, and mechanical strength of the final printed part. In literature [4], [5], it has been extensively studied how printing parameters strongly influence the final mechanical properties and quality. Table 1.1 shows the main parameters divided into categories, alongside a brief description of each one.

Table 1.1: Main FDM process parameters

Parameter category	Parameters and description
Thermal	• *Nozzle temperature*: it regulates the melting of the filament, and consequently its fluidity, influencing surface quality, dimensional accuracy, and mechanical properties • *Printing plate temperature*: linked to the adhesion of the first layer and prevents warping, a phenomenon whereby the component, usually the lower corners, lift up causing

	the part to detach. This occurs due to uneven thermal shrinkage, which generates internal stresses that deform the part. • *Cooling*: includes a series of parameters related to the management of fans for cooling the material after extrusion. In the first layers, cooling management is essential to ensure good adhesion to the print bed, while subsequently it influences the adhesion between layers.
Geometric	• *Layer height*: thickness of the deposited line, and therefore of the relative layer • *Line width*: width of the deposited line Both parameters are related to the resolution of the final part, dimensional accuracy, printing time and mechanical strength
Structural	• *Infill pattern*: type of filling (grid, hexagons, triangles, etc.) • *Infill quantity*: percentage of internal filling (e.g., 20%, 50%, 100%) • *Raster angle*: line orientation during the material deposition in a specific 3D-printed layer • *External shells*: thickness of the outer areas that surround the part • *Top and Bottom layers*: thickness of the lower and upper areas of the part
Printing plate adhesion	• *Brim*: ring printed around the piece to increase the contact surface • *Raft*: thick base under the piece, it is a sacrificial part so it is removed after printing • *Skirt*: contour that does not touch the piece, mainly acts as a purge line to prepare the extruder for printing

The nozzle diameter is an important hardware factor that affects dimensional accuracy and mechanical properties and typically ranges from 0.4mm to 1mm for standard FDM printers. It is important to note that it is closely related to geometric parameters. Tipically, the line width is set equal, or slightly higher, to the diameter of the nozzle and the layer height is 50% or 75% of the line width. This is done for mechanical and practical reasons related to the printing process itself.

Since the layer height is always smaller than the line width, when the molten material is deposited by the nozzle onto the printing surface or another layer, it expands sideways rather than upwards and takes on an elliptical shape (Fig. 1.3a). At the same layer level, the elliptical shape ensures adhesion by leading to partial overlap between two lines deposited close to each other. Additional bonding areas are created at different layers when new lines are deposited on top of previously printed layers. However, empty spaces that remain during deposition cause porosity and voids within the printed part (Fig. 1.3b).

When new molten polymer is extruded near previously solidified material, the existing material heats up and partially re-melts. Molecular diffusion occurs in the adhesion zone with the diffusion of polymer chains, resulting in a weld between the new material and the previous one. In terms of weld strength, the quality of the adhesion zone depends on the viscosity of the polymer, which must be low enough to ensure good diffusion of the molten polymer, and on the temperature profile. The latter depends on various printing parameters, such as nozzle temperature, ambient temperature, cooling rate and printing speed.

This topic will be explored in greater depth later in the thesis.

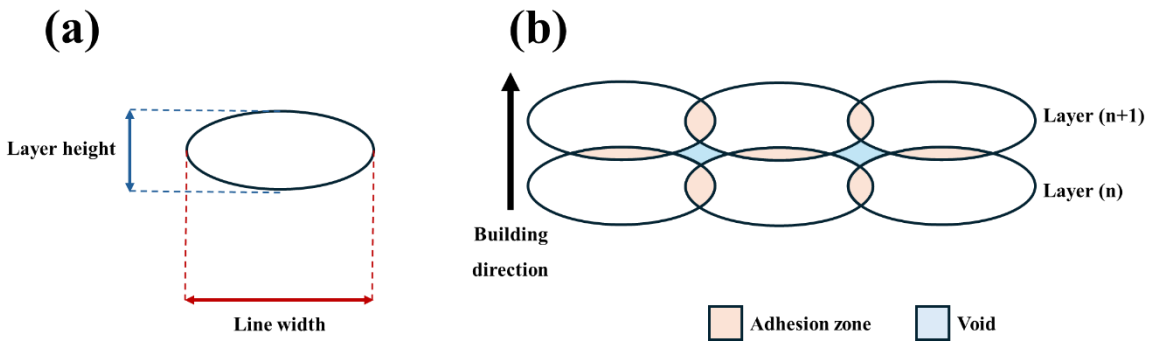

Figure 1.3: Representation of (a) the geometric parameters and (b) structure of a sequence of layers and lines

Figure 1.4a provides a better understanding of the spatial arrangement of the structural zones, relating to the structural parameters described in Table 1.1. The representative cross-section shows that the main role is played by the fully filled external areas (Top, Bottom, External Shell), while the infill's main function is to transmit load between parts.

A very important structural parameter is the raster angle (Fig. 1.4b), which represents the line orientation during the material deposition in a specific 3D printed layer, and clearly influences the mechanical properties [6]. Indeed, it is expected that due to molecular orientation induced by the line deposition, the 3D-printed part is stiffer and stronger when loaded parallel to the raster angle than in any other direction.

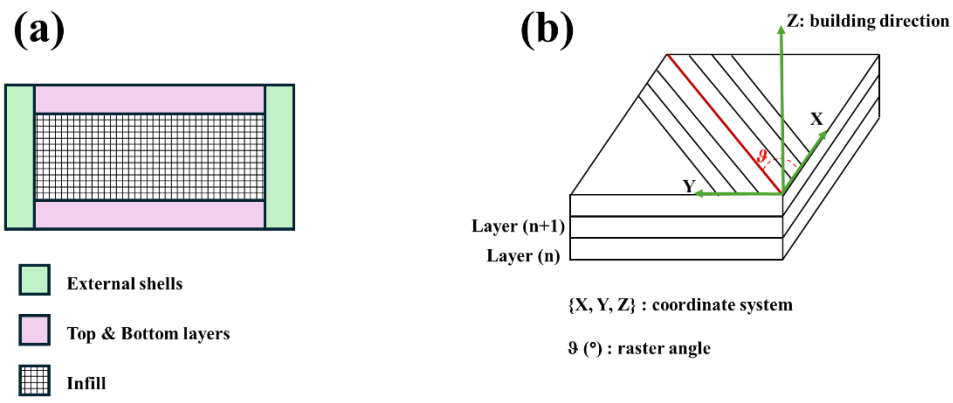

Figure 1.4: (a) cross-section of areas related to structural parameters and (b) graphical description of the raster angle

1.2.3 Filament preparation

The thermoplastics used are usually either unreinforced or reinforced with short fibers, depending on the required performance and operating conditions. The first step in 3D printing is to prepare the filament, regardless of whether the polymer is short fiber-reinforced or not.

Even non-fiber-reinforced filaments contain small percentages of inorganic fillers (talc, calcium carbonate, silica, etc.). These fillers are not added to increase mechanical strength, but mainly for technical reasons. These fillers are typically used to improve dimensional stability during cooling, reduce warping and lower the polymer's viscosity to enhance its processability during extrusion.

The effectiveness of fillers and short reinforcement fibers depends on their size, distribution, and adhesion to the matrix. These requirements ensure a homogeneous distribution of fibers, or fillers, along the filament and maintain a uniform diameter. Both factors are essential for achieving consistent print quality. As these points are crucial for short fiber reinforcement, this section will henceforth refer to this type of filler, even though the manufacturing technology can also be used for inorganic fillers.

Figure 1.5 summarizes the processing steps of filament preparation [7].

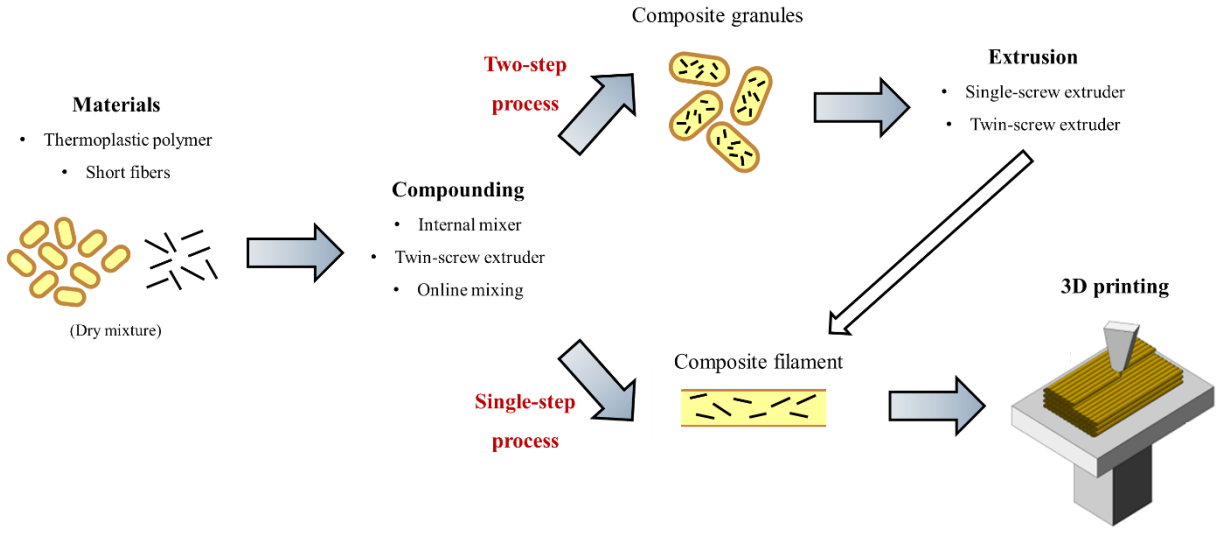

Figure 1.5: Manufacturing steps of filament production

The first step is to disperse the fibers in the thermoplastic matrix (compounding) starting from a dry mixture of raw materials. This is primarily achieved by melting the polymer; the most common methods of melt mixing are internal mixing and twin-screw extrusion.

In single-step processes, the filament and matrix are compounded to form a filament that can be used directly for 3D printing [8], [9], [10] . Overall, single-step methods are not widespread for filament production. It is difficult to optimize the manufacturing parameters to ensure both uniform fiber dispersion and good quality of the filament produced. In two-step processes, the first step is compounding (first melt mixing), which is followed by cutting. Then, the second step is filament preparation via extrusion (second melt mixing), during which the material is remelted. The purpose of the first melt mixing is to ensure a homogeneous distribution of fibers, and the second is to ensure a constant filament diameter. Therefore, in the first step, high-shear methods are preferred, which inevitably cause fragmentation of the fibers. Cutting may also

slightly decrease the average fiber dimensions. In the case of two-step methods, internal mixers [11], [12], [13], [14] and twin-screw extruders [15], [16], [17], [18] are similarly common solutions for making composite compounds. After cutting the compounds, the filaments are almost always produced with a single-screw filament extruder and before printing, it is wound onto a collection spool.

The reduction in fiber size in the two-step process is not always a negative factor. Before deposition, the composite melt is in the nozzle and the main requirement is printability, which means that the system pressure is equal to or greater than the pressure needed to overcome clogging. The mechanism of nozzle clogging is the packing and bridging of fibers in the internal cross-section of the nozzle. Therefore, if the fiber percentage and fiber size are too high, printing problems will arise, potentially leading to process failure.

Filament production line

As mentioned above, the two-step method is the most widely used technique for producing filaments for 3D printing. Once the starting granule has already been produced, it is then processed by a single-screw extruder (Fig. 1.6).

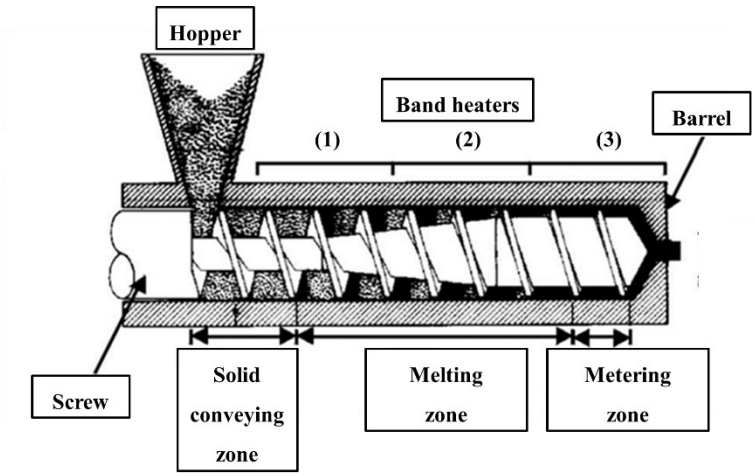

Figure 1.6: Main parts and zones of a single-screw extruder

The starting material is fed into the feed hopper volumetrically. The main body of the extruder consists of an outer cylinder (barrel) and a screw that rotates inside it, pulling the material towards the outlet die. The screw is usually *square* because the screw pitch is equal to the internal diameter of the barrel, while the profile of the core can vary depending on the type of material being processed. The standard screw typically used consists of three zones: solid conveying, compression and metering zone. In the first one, the diameter of the screw remains

constant, and the polymer is dragged towards the next zone in a solid state. In the melting zone, the material gradually changes from a solid to a fluid state as it melts. Here, the diameter of the screw increases linearly until it reaches its maximum value, which corresponds to the nominal value. In the last zone, the core is once again constant and the material is completely melted.

Heating elements are positioned around the barrel to heat the extruder, while to prevent the material from overheating, and thus maintaining the temperature at the set value, the extruder is cooled by a liquid or air system. Thermoregulation takes place in different areas of the extruder, which can vary in number from three to more than seven, depending on the length of the extruder. Approximately halfway along the length of the screw, there may also be a degassing zone, which is necessary to remove air and volatile products. These can cause defects in the extrudate if they remain trapped inside the material. The material is pushed by the screw to exit through a die mounted at the head of the extruder, which gives the melt the shape of the final product. The pressure generated at the head must be adequate to compact the outgoing material, but not too high for safety reasons, so pressure sensors are often installed.

At the extruder outlet, the molten material continues to the other stations of the filament production line (Figure 1.7).

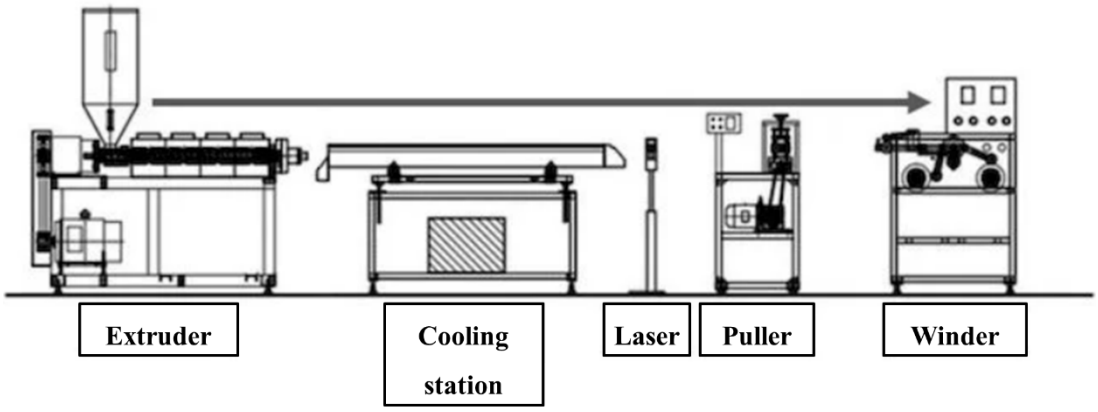

Figure 1.7: Production line for 3D printing filament

The polymer is directed through a cooling station, which may employ either forced air or a water bath depending on the required cooling rate and the thermal properties of the material. The cooling process is critical to stabilize the polymer structure and prevent internal stresses that

could compromise the filament's mechanical performance during subsequent 3D printing operations. Once sufficiently solidified, the filament is conveyed by a puller unit, which ensures a constant transport speed and mitigates variations in cross-sectional geometry. The filament is then guided to a winding system, where it is uniformly spooled under controlled tension to avoid residual stress, kinking, or deformation.

Between the cooling section and the winding unit, an inline dimensional control system, typically based on laser micrometers or optical sensors, monitors the filament diameter in real time. This step is fundamental for guaranteeing dimensional precision, since the filament must conform to standardized diameters of 1.75 mm or 2.85 mm, with tolerances generally within ±0.05 mm. Deviations beyond these tolerances can lead to extrusion inconsistencies, print defects, or even nozzle clogging during the additive manufacturing process.

Once the extrusion parameters have been optimized, the winding and pulling systems automatically adjust the tension in response to feedback from the diameter measurement system. This closed-loop control strategy ensures that any fluctuation in filament diameter is compensated for in real time, thereby maintaining product uniformity and minimizing waste.

1.2.4 Continuous fiber technique

Short fiber-reinforced polymer composites are commonly employed in additive manufacturing to enhance thermo-mechanical properties compared to neat polymers, enabling the production of semi-structural components. However, the random orientation and limited aspect ratio of short fibers inherently restrict the achievable stiffness, strength, and load-bearing capability of the printed parts. To overcome these limitations, in recent years several advanced additive manufacturing techniques have been developed to enable the deposition of continuous fiber reinforcement directly within the thermoplastic matrix during the printing process.

The integration of continuous fibers into thermoplastic matrices has led to the emergence of Continuous Fiber-Reinforced Thermoplastic Composites (CFRTPCs), a class of materials that synergistically combine the geometrical freedom of 3D printing with the superior mechanical performance traditionally associated with laminated composite manufacturing. Unlike short-

fiber systems, continuous fibers provide long-range reinforcement, allowing for a significant improvement of the mechanical performance, and fatigue resistance, while also enabling a more efficient load transfer along the fiber direction. When properly optimized, these materials offer specific strength and stiffness values that rival those of conventionally manufactured composites, thus opening the way to lightweight, high-performance structural applications in sectors such as aerospace, automotive, and sporting equipment.

The technological approaches to CFRTPC fabrication vary depending on the printing system [19], [20], [21].

In the in-situ impregnation method, fiber is directly compounded into the polymer matrix during 3D printing (Fig. 1.8). This integration occurs within the printhead, where the fiber is drawn by friction through an inlet hole or an auxiliary entrance, leading into the deposition nozzle. This approach allows for adjusting the fiber volume ratio and enables 3D printing of fibers of different nature. However, it requires modifications to the print head, is more prone to clogging, and there may be limited fiber impregnation due to brief contact time in the printhead.

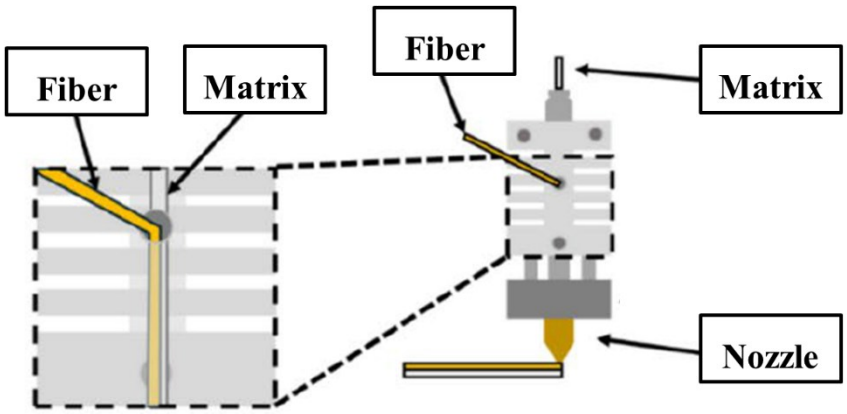

Figure 1.8: In-situ impregnation process

Another possibility is the prepreg method, which allows us to realize a prepreg filament combining fibers and a matrix, where the fiber is pre-embedded in the matrix (Fig. 1.9). Before 3D printing, the polymer matrix is melted through a single- or twin-screw extruder and subsequently pushed through a specially designed nozzle incorporating a continuous fiber feed. The result is a ready-to-use prepreg composite filament compatible with conventional printers, hence no modifications are required. However, this method has limitations in terms

of the variety of materials and the volume of fiber content, as the diameter of the fiber is limited by the capacity of the printer's filament. Moreover, adding fiber to the filament increases its stiffness, making storage challenging, especially when stiff fibers are used.

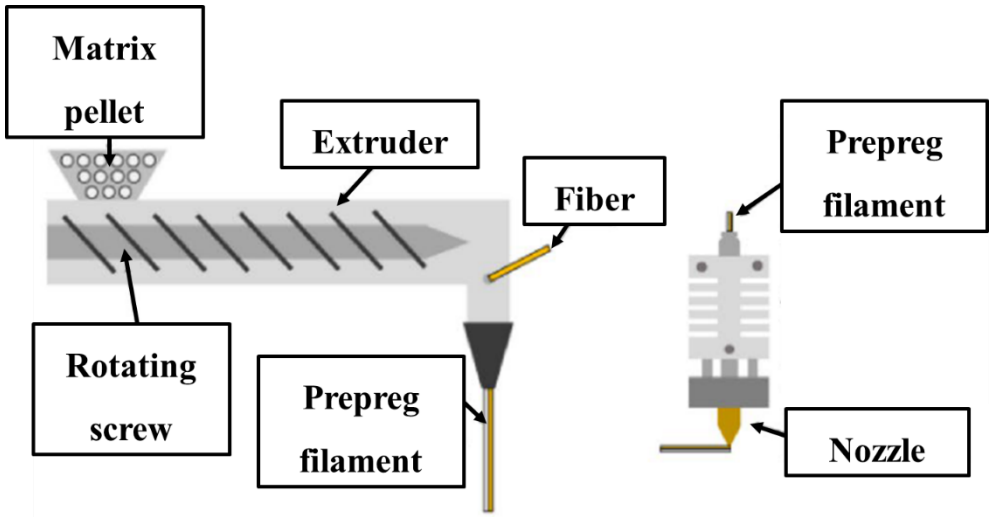

Figure 1.9: Prepreg filament preparation and printing

It is important to underline that in the field of traditional composite manufacturing, the term "prepreg" (pre-impregnated) strictly defines a semi-finished product consisting of reinforcement fibers impregnated with a polymeric matrix, typically a partially cured thermoset resin. By definition, this material requires a subsequent consolidation cycle involving heat and pressure (e.g., autoclave curing) to achieve full polymerization and final structural properties. However, within the context of Continuous Fiber 3D Printing, the terminology undergoes a significant functional shift. Here, the term "prepreg filament" refers to continuous fiber reinforcement that has been pre-processed with a thermoplastic matrix to form a filament feedstock. Crucially, unlike its traditional counterpart, the consolidation phase of this filament is already concluded during its manufacturing. The filament enters the 3D printer as a fully consolidated solid composite filament. Consequently, the subsequent 3D printing process does not serve as a curing stage for the filament itself, but rather as a deposition and melting step to integrate the reinforcement into the final component geometry.

The last option for printing CFRTPC is out-of-nozzle method, which uses two nozzles: one to extrude the main polymer, as a standard FDM printer, and the other to deposit the reinforcement fiber. This approach is highly versatile, allowing various fiber types and matrix

materials to be used. Depending on the number of input materials available for the reinforcement extruder, the method is divided into two categories. The first option is to use only the reinforcing fiber as input (Fig. 1.10a), and during the printing the fiber is pressed into the previously printed polymeric matrix. The second option is to use two inputs: the reinforcing fiber and an additional thermoplastic matrix (Fig. 1.10b), and the result is a fiber coextruded directly onto the printing plate. This solution is like the in-situ impregnation method but supported by an additional extruder usually used for external parts of the component (top, bottom, external shells), thus ensuring higher dimensional quality and lower porosity. However, due to coextrusion, the percentage of fiber that can be deposited is certainly more limited.

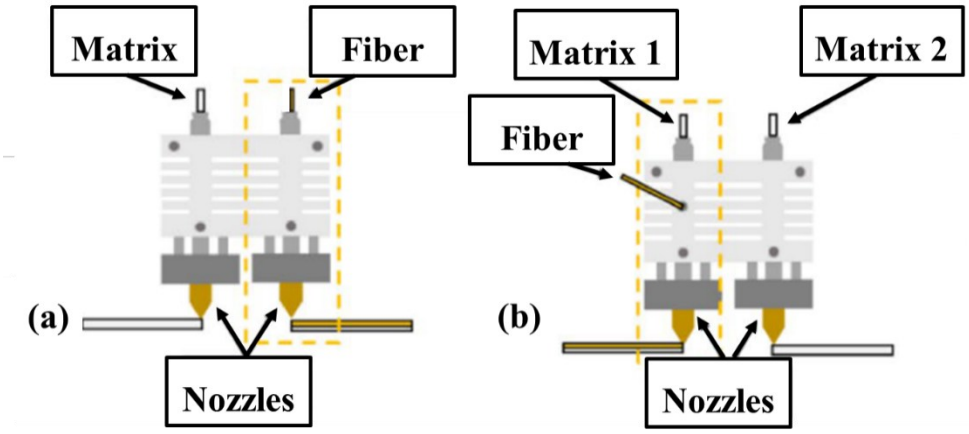

Figure 1.10: Out-of-nozzle process with (a) two input and (b) three input

Until now, in-situ impregnation techniques and the prepreg method have been mainly limited to scientific and research fields, while the latter has already been widely commercialized. The out-of-nozzle method with a single input has been developed and marketed for years by industry leader Markforged, making it the first commercial CFRTPC solution for industrial applications and ready-to-use parts. While Anisoprint implemented and brought to the market the other technique as an alternative to the previous solution. This last possibility of out-of-nozzle will be described in more detail and discussed later in the thesis.

1.2.5 Multi-scale structure

3D-printed parts reinforced with short or continuous fibers exhibit a multi-scale structure (Fig. 1.11), comprising three distinct levels: bead, lamina, and laminate. Each level is linked to specific key requirements, whose satisfaction ensures the quality of the final printed product.

When the composite is deposited on the print bed through the nozzle, it forms the first level of the 3D-printed structures, a single bead. At the bead level, the microstructural properties that influence macroscale behavior are fiber orientation, fiber-matrix adhesion, and the micro-voids.

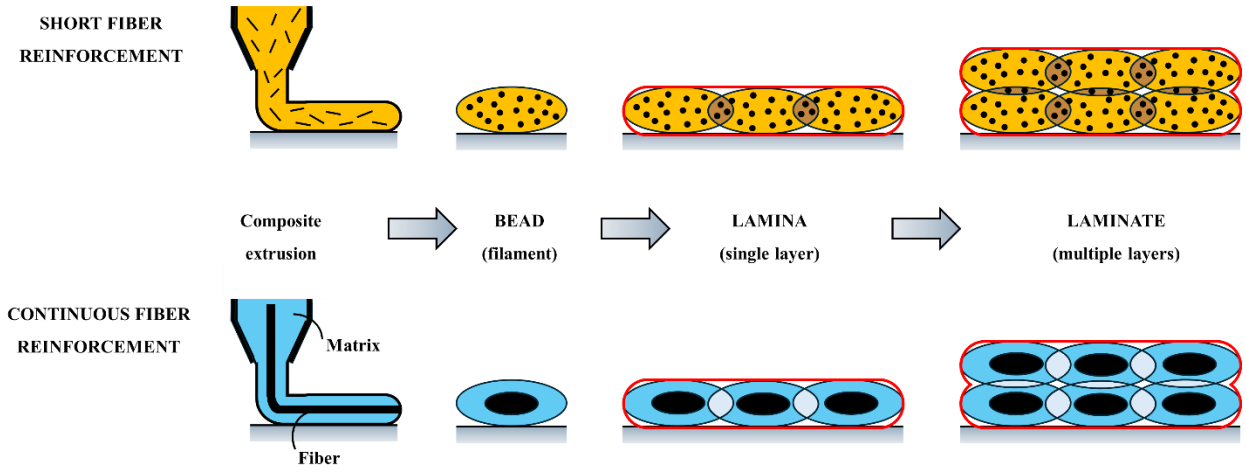

Figure 1.11: Multiscale structure of 3D printed fiber–reinforced composites

Fiber orientation is reported to be generally parallel to the printing direction [22], [23], [24], which is governed by the *raster angle* printing parameter, as described before in Section 1.2.2. The nozzle diameter has the most significant influence: narrower diameters lead to a higher degree of fiber alignment. This is expected because, as the same material flow is forced through a smaller space, the shear stresses and the radial velocity gradient increase, causing the fibers to align more effectively in the direction of flow. The same effect is achieved with a lower layer height. Hence, the smaller it is, the better the fibers align with the print direction [25].

Fiber–matrix adhesion refers to the strength of the adhesive bond between the fibers and the surrounding matrix. Strong adhesion ensures that loads are transferred effectively from the matrix to the fibers [26], [27]. Better bonding reduces the number of micro-voids at the fiber interface. Therefore, if the matrix does not fully impregnate the fibers, micro-voids can form

near the fibers due to a lack of contact between the fiber and the matrix. This typically occurs in cases of high fiber content and poor dispersion, especially in the case of short fibers. Due to their chemical nature, this problem is much more pronounced for natural fibers, as described in Section 1.3.2.2. Air entrapment voids can also form during compounding, and the presence of short fibers can increase the likelihood of air entrapment, especially in high viscosity thermoplastic melts [28], [29], [30].

The second level is when the beads are extruded next to each other to form a lamina. At the same layer level, the pattern and the number of beads in a lamina are highly customizable. It is possible to print a completely filled layer at a specific raster angle and if external shells are not used, the single layer represents the unidirectional lamina typical of classic composites (Fig. 1.12a). Alternatively, a partially filled layer can be printed by adjusting the infill and external shell printing parameters (Fig. 1.12b). With continuous fiber reinforcement, you can choose to place it in the infill only, in the outer shells only, or in the top and bottom only, in order to create more complex sandwich-type structures.

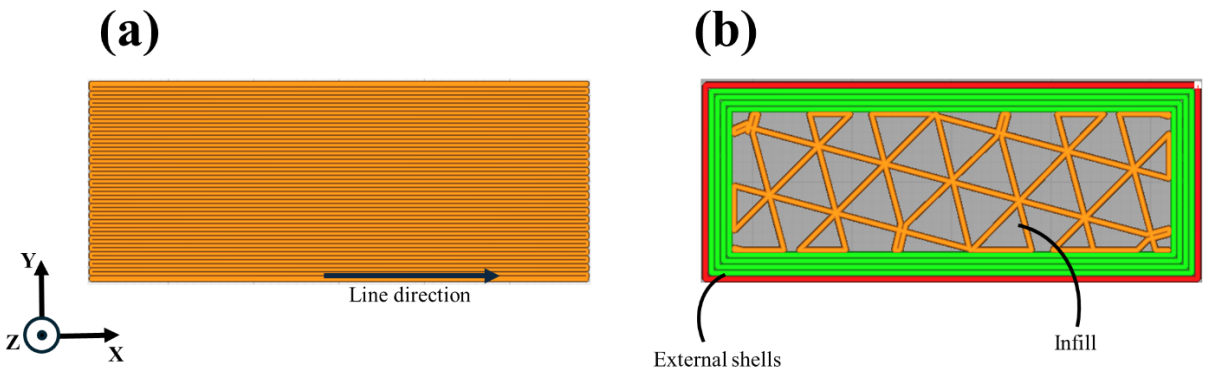

Figure 1.12: second level of the multi-scale structure for (a) completely filled unidirectional lamina and (b) partially filled lamina

At the third level, laminas are stacked on each other and new interfaces are created between the laminas (layers). If all layers are completely filled and printed with a specific raster angle, the result is a laminate (Fig.1.12a), whereas if partial filling is used for lightening purposes, the result is a structure (Fig.1.12b).

As previously described in Section 1.2.2, adhesion zones occur at the lamina and laminate (or structural) levels, where new molten polymer is deposited in proximity to existing material.

The quality of welding in the adhesion zones has a significant impact on macroscale characteristics, and it is influenced by the viscosity of the polymer and thermal phenomena. It can be expected that the fiber content influences the welding process, both in terms of quantity and the nature of the fiber. Excessive amounts of fiber can hinder diffusion phenomena at the interface, and different types of fiber have different thermal properties. Consequently, heat transfer between the fiber and matrix varies.

1.3 Materials

The materials used for 3D printing using FDM technology are mainly amorphous thermoplastic polymers, chosen for their ability to cool without significant shrinkage or dimensional distortion. Unlike semi-crystalline materials, which tend to form ordered structures during cooling and can cause warping, amorphous materials allow for greater dimensional accuracy and adhesion between layers. This stability is essential to ensure that printed parts maintain the shape designed in the CAD file.

Thermoplastics are generally utilized either in their unreinforced form or with short-fiber reinforcement, depending on the performance requirements and service conditions. As mentioned above, continuous reinforcement fibers can be used to achieve a similar level of mechanical performance to that of classic composites.

The following paragraphs provide an overview of the main characteristics of thermoplastic matrices and reinforcing fibers used in FDM technology.

1.3.1 Thermoplastic matrices

The main unreinforced thermoplastics used in FDM technology are the following ones: PLA (Polylactic Acid), ABS (Acrylonitrile Butadiene Styrene), PETG (Polyethylene Terephthalate Glycol), TPU (Thermoplastic Polyurethane) and the Nylons (Polyamides - PA) [31], [32], [33].

PLA is a biodegradable thermoplastic derived from renewable sources such as corn, sugar cane, or sugar beets. It is the most common material used in desktop 3D printing due to its ease of use, good aesthetic quality, and low cost. The advantages of PLA printing are its ease of printing, as it does not require a hot chamber or heated plate, and low warping, thanks to

excellent adhesion to the plate. On the other hand, its heat resistance is poor (60 °C), it is brittle and susceptible to ageing, particularly when left outdoors, and it is hygroscopic, meaning it absorbs a lot of moisture. Thanks to its moderate mechanical properties, it is mainly used in the fields of aesthetic prototypes and demonstration models, components for electronics or non-structural parts. An important point for PLA is its environmental compatibility, as it is one of the few industrially compostable polymers. Biodegradation requires controlled conditions (high humidity, temperature > 60°C), and it does not decompose quickly in natural environments such as the sea or soil.

ABS is an engineering thermoplastic widely used in industry. It is known for its mechanical strength, thermal stability, and good workability. Compared to PLA, it is more robust and heat resistant, but more difficult to print. Its high resistance to impact, fatigue, and heat (100 °C) makes ABS suitable for functional and mechanical parts, with high durability and good long-term performance. It also has good post-printing workability, so it can be smoothed with acetone or sanded. On the downside, ABS is difficult to print because it tends to warp, requiring a heated bed and preferably a closed chamber. Furthermore, toxic and irritating fumes (styrene) are emitted during printing, so the work environment must be adequately ventilated. ABS is not biodegradable, but it can be mechanically recycled and reused in 3D printing processes.

PETG is a modified version of PET (Polyethylene Terephthalate), containing not only ethylene glycol but also cyclohexandimethanol (CHDM), another glycol that is used to prevent crystallization and thus it improves its printability. It combines many of the advantages of PLA (ease of printing) with characteristics more similar to ABS (mechanical and thermal resistance), making it ideal for functional applications. In addition to low warping during printing, PETG has good impact and flexural strength. It also has good heat resistance, up to approximately 80 °C, and it has good chemical resistance. Unfortunately, it absorbs a lot of moisture, so if the material is not dried properly, there are obvious printing problems (stringing) and mechanically it is less resistant to abrasion than other materials. Some of the applications are functional components and structural prototypes, as well as technical objects (guides, supports, clips, etc.).

PAs (or Nylons) are a family of semi-crystalline thermoplastic polymers known for their high mechanical strength, flexibility, toughness, and wear resistance. They are widely used in industry for functional components and parts subject to mechanical stress. There are several

formulations (PA6, PA12, PA66, etc.), each with specific properties, but PA6 and PA12 are mainly used in 3D printing. PA6 has higher mechanical performance than PA12, but it is prone to warping and the printing conditions are more restrictive. On the other hand, PA12 is easier to print, but its mechanical performance is lower. The PA family is best suited to structural parts, such as brackets and mechanical supports, as well as components that are subject to wear, such as guides and sliders, or that are subject to repeated vibrations or impacts. These applications are possible thanks to the superior mechanical strength, impact and wear resistance compared to the other thermoplastics mentioned above. In addition, polyamides have good chemical resistance to oils, greases, and fuels. Unfortunately, PAs are difficult to print for two reasons mainly: the adhesion to the printing bed, which requires a specific surface, and the warpage, so it is preferable to use a closed chamber to ensure the most controlled environment possible. It is also a highly hygroscopic material, so if it is not dried properly, moisture compromises the print quality and strength of the printed part.

Table 1.2 compares the main thermoplastic materials used with FDM technology, setting out their key characteristics in terms of printing conditions and thermo-mechanical performance[31], [32], [33].

Table 1.2: Comparison between the main thermoplastic materials used with FDM technology

Material	Ease of printing	Nozzle Temperature [°C]	Plate Temperature [°C]	Mechanical performance	Thermal performance
PLA	↑↑	180 - 220	0 - 60	↑	↓ (60 °C)
ABS	↑	230 - 260	90 – 110	↑↑	↑↑ (100 °C)
PETG	↑↑	220 - 250	70 - 90	↑↑	↑ (80 °C)
PA	↑	240 - 270	70 - 100	↑↑	↑↑ (100 °C)

1.3.2 Reinforcing fibers

In recent years, the use of thermoplastic polymers reinforced with short reinforcement fibers, has become increasingly widespread in FDM 3D printing. Fibers reduce thermal shrinkage and the risk of deformation during cooling, thereby improving processability and print accuracy,

particularly with materials that are prone to warping, such as ABS and PA. Additionally, the mechanical properties improve in terms of both stiffness, strength and impact resistance compared to the base thermoplastic polymer. To further enhance mechanical properties, continuous fiber-reinforced 3D printed composites have become increasingly popular in recent years.

Both short and continuous reinforcing fibers can be of fossil origin (e.g. carbon, glass or Kevlar) [10], [11], [35], [36] or natural origin (e.g. basalt or vegetable fibers) [37], [38] to achieve a more sustainable solution. It is important to note that ceramic or metallic materials may also be present as reinforcement [39], [40], but in particulate form rather than as fibers. In both cases, the result is a fiber reinforced smart composite that can be used in a variety of applications depending on the specific fiber-matrix combination.

This chapter focuses on the characteristics and properties of fiber-based reinforcements. The general considerations apply to both continuous and short fibers.

Fossil-based fibers

The fossil-based fibers used as reinforcement in 3D printing are carbon, glass, and Kevlar. Carbon fiber is the most widespread, both in commercial products and in scientific literature. This strong interest is due to its high specific mechanical properties, combining high performance with the lowest density among the fossil fibers under analysis. It also has high thermal resistance and integrates very well with the main polymers used in FDM technology. On the other hand, it is the most expensive type of reinforcement, and parts printed with carbon fiber tend to be the most brittle. For these reasons, 3D printed parts reinforced with carbon fibers are becoming increasingly popular in sectors such as automotive and aerospace. This is particularly the case where lightweight structural and mechanical components are required, such as brackets, jigs and mechanical supports.

Glass fibers are used instead of carbon ones for printing parts because they are significantly cheaper. They offer good chemical resistance and electrical insulation, and although they have slightly lower mechanical properties than carbon fibers, they are less brittle. Unfortunately, these are the heaviest fibers among those being analyzed. Applications include less critical industrial applications (enclosures, light brackets), as well as low-cost functional prototypes

where cost is a priority and extreme performance is not required. It is also used for electrical components and insulation

Kevlar fibers are chosen for their excellent impact resistance and high tenacity, which allows them to withstand shocks and fatigue well. Generally, they are very light, but they are less stiff than glass and carbon. On the other hand, it is the most expensive fiber and is more complex to process, because Kevlar tends to degrade thermally when exposed to excessively high temperatures. This type of fiber is chosen for special applications where energy absorption and impact resistance are important, such as in the ballistic or military fields (helmets, reinforcements).

In terms of processability during 3D printing, glass fiber is the most abrasive material for printer components, especially for the nozzle and filament handling parts.

Table 1.3 compares the key characteristics of the main fossil-based short fibers used as reinforcement with FDM technology [35, 36].

Table 1.3: Characteristics of short fibers of fossil origin, used as reinforcement in 3D printing with FDM technology

Fiber	Stiffness [GPa]	Strength [MPa]	Density [g/cm^3]	Cost
Carbon	≈ 230	≈ 4500	1.75 – 1.9	↑
Glass	74 - 86	3000 – 4600	≈ 2.5	↓
Kevlar	62 - 124	2700 – 3600	≈ 1.4	↑↑

Natural fibers

The usage of fibers of natural origin as reinforcement in 3D printing with FDM technology is gaining increasing interest as an alternative to fibers of fossil origin thanks to a combination of environmental, economic, and technical advantages.

Natural fibers can be of plant or mineral origin. Among the latter, basalt is the most widespread. It can be classified as a sustainable material, because it does not require additives for its production and during the technological process, there are no emissions of toxic substances. Through melt drawing and solution spinning, this material can be used in the form of powder and reinforcement fibers, in a wide range of application areas [41], [42]. Although they do not reach the same mechanical properties as carbon fibers, basalt fibers possess strength and stiffness that are similar to glass fibers, but with an even higher density; therefore, they can be

used as an environmentally friendly substitute. Moreover, they are superior to glass in terms of heat and acoustic damping and outstanding vibration isolation, corrosion resistance, price and can operate in a sufficiently wide thermal range, so that they can even be used as a thermal shield [43], [44].

From a more sustainability perspective, vegetable fibers are derived from renewable resources, and their production requires on average 40–60% less energy than the production of fossil-based fibers, thus reducing the carbon footprint even more. Furthermore, when combined with biodegradable matrices such as PLA, they give rise to composites that can degrade more easily at the end of their life, promoting circular economy strategies and reducing the accumulation of persistent plastic waste. Economically, fibers such as hemp, flax, or jute have production costs that are 20–50% lower than fossil fibers and can be sourced locally, reducing transportation costs and logistics impacts.

Table 1.4 shows the physical and mechanical properties of the main natural fibers [45], [46]. From a mechanical properties standpoint, vegetable fibers have a typical density of 1.2–1.5 g/cm^3, significantly lower than that of glass fibers (≈ 2.5 g/cm^3) and even lower than carbon fibers (1.75–1.9 g/cm^3), allowing for the creation of lightweight components. The elastic modulus of plant fibers generally varies between 10 and 80 GPa, with tensile strengths between 200 and 1,000 MPa, values lower than those of fossil fibers but sufficient for many non-structural applications. Therefore, carbon and glass fibers maintain technical superiority in high-performance structural applications (elastic moduli >70 GPa and tensile strengths >2 GPa). Fibers of vegetable origin are a competitive choice for prototyping, lightweight components, and products with low environmental impact, combining sustainability, affordability, and adequate mechanical properties. A further advantage is their lower abrasiveness: vegetable fibers do not significantly damage brass nozzles, unlike carbon and glass, thus reducing maintenance costs.

Table 1.4: The mechanical and physical properties of natural fibers

Fiber	Stiffness [GPa]	Strength [MPa]	Elongation at Break [%]	Density [g/cm^3]
Basalt	80 - 115	2600 - 4840	2.85 – 3.90	3.00
Sugar palm	0.5 – 3.4	15.5 - 290	5.7 – 28	1.30
Sisal	9.0 – 38.0	400 – 700	2.0 – 14.0	1.50

Oil pal	9.0	400	18.0	1.55
Jute	10.0 – 30.0	393 - 800	1.2 – 1.8	1.60
Kenaf	53.0	930	1.6	1.45
Hemp	70.0	550 - 900	1.6 – 4.0	1.48
Cotton	5.5 – 12.6	287 - 900	2.0 – 10.0	1.60
Bamboo	17.0	290	/	1.25
Flax	27.6	345 - 1500	1.2 – 3.2	1.50
Pineapple	60.0 – 82.0	413 – 1627	14.5	1.44
Banana	27.0 – 32.0	529 - 914	5.9	1.35

While the use of vegetable fibers as reinforcement in FDM 3D printing offers advantages in terms of sustainability and lightness, it presents technical challenges that limit its applicability in high-performance contexts. One of the main issues is the high hygroscopicity of vegetable fibers, which easily absorb moisture from the environment. This can compromise fiber-matrix adhesion and generate porosity during extrusion, thereby reducing the mechanical properties of the printed piece. Furthermore, the biological nature of these fibers results in variability in their physical and mechanical properties, which are influenced by plant species, cultivation conditions and processing methods. This makes it more difficult to guarantee uniform performance[38], [47]. Chemically, the polarity of the cellulose, which nis the main constituent of vegetable fibers, is incompatible with many non-polar polymers used in FDM printing (e.g ABS). This requires chemical treatments or the use of coupling agents to improve adhesion, such as the usage of silanes and maleic anhydrides [48], [49]. In addition, vegetable fibers have low thermal stability, as they begin to thermally degrade at around 200–220 °C. This reduces their compatibility with technical polymers that can be processed at higher temperatures.

The thesis will explore 3D printing with plant fibre reinforcement in greater detail soon, covering both the technology and the materials.

2. Thermoplastic materials: Polyamides and Polyesters

2.1 Introduction

Chapter 1 introduced the most common thermoplastic materials used in FDM 3D printing technology, either on their own or as a matrix for producing short or continuous fiber-reinforced composites. In this thesis, the thermoplastic materials used belong to two families: polyamides and polyesters. This chapter will therefore examine their characteristics, and performance in greater depth. Further details and additional information can be found in traditional polymer engineering textbooks [50] [51], [52], [53], [54].

2.2 Polyamides

Polyamides, also known as Nylons, are widely commercially available semicrystalline plastics that can be used in various forms such as fibers, adhesives and rubbers. They have the common feature that the amidic group ($-CONH-$) occurs repeatedly in the main polymer chain (Fig. 2.1). Depending on the polyamide, monomeric units (R) of different types may also be repeated in the main chain.

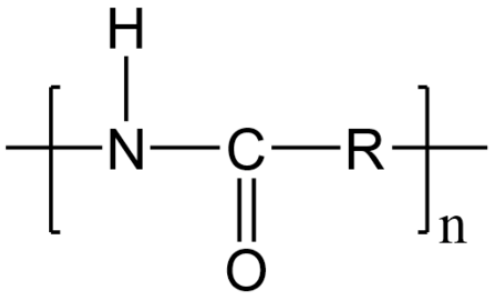

Figure 2.1: Amide group in polymer chain

This work will focus only on aliphatic polyamides, i.e. those whose main chains consist of methylene groups ($-CH_2-$) between the amidic groups ($-CONH-$). Consequently, there are no benzene rings in the main chain, a characteristic of aromatic polyamides (e.g. Kevlar and Nomex).

2.2.1 Preparation methods

A first classification can be made based on the method of preparing polyamides. One of these is polycondensation, which is a polymerization reaction involving different molecules, also of different nature, which are joined together to form a longer chain. Its main characteristic is that at every chain propagation step, a small molecule is released as a byproduct of the chain growth reaction. Another possibility is ring opening polymerization, to create long-open chains. This reaction is quite interesting, since no small molecules need to be released, thus allowing the possibility of higher molecular weights. This chapter will briefly describe these two main processes.

Polycondensation with different molecules ($Nylon\ a,b$)

One possibility for the formation of polyamides is the reaction between a dicarboxylic acid (adipic acid) and diamine (hexamethylenediamine). The reaction between an amino group ($-NH_2$), belonging to diamine, and a carboxyl group ($-COOH$), from the acid part, generates an amidic bond ($-CONH\ -$)(Fig. 2.2). One water molecule is created for every bond formed. It is important to remove water during the polyamide formation process; otherwise, equilibrium is promoted rather than polymerization, and this would limit chain.

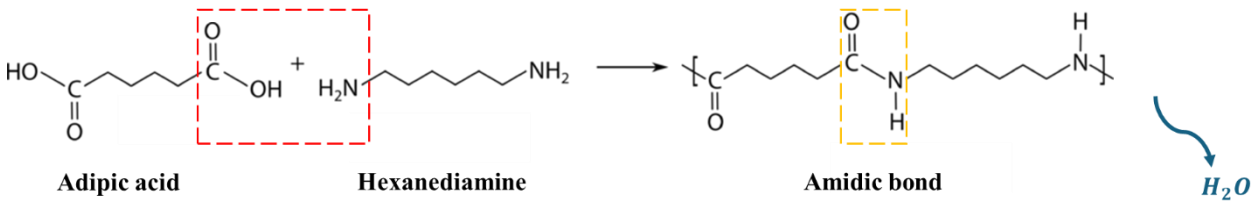

Figure 2.2: Simplified scheme of the polycondensation reaction

In the polyamide chain, two distinct parts can be observed: an acidic part and an amine part. For this reason, their nomenclature ($Nylon\ a,b$) includes two numerical indices relating to the number of carbon atoms (C) in each respective part. The first index (a) refers to the amine part and the second (b) to the acid part. For example, both $Nylon\ 6{,}10$ and $Nylon\ 6{,}6$ have six carbon atoms in the amine part; it is the increase in C in the acid part that is the difference (Fig. 2.3).

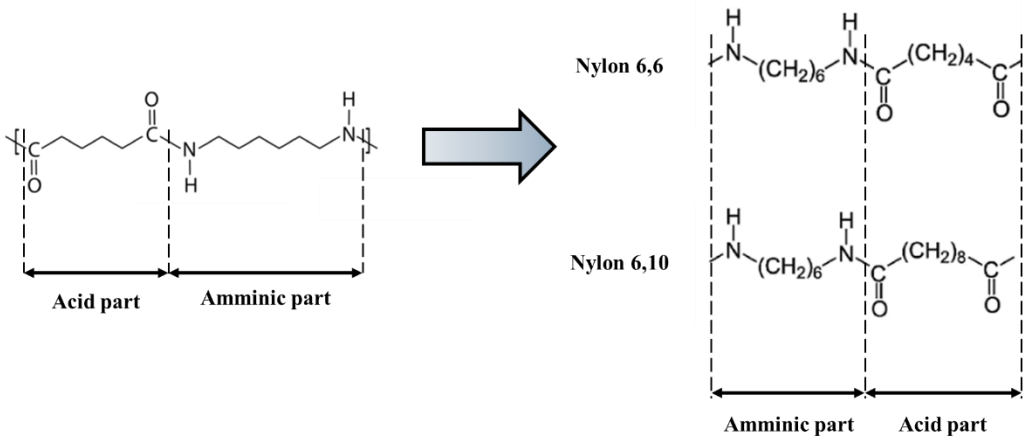

Figure 2.3: Comparison between the structure of a Nylon 6,6 and Nylon 6,10

Ring opening and self-polycondensation ($Nylon\ a$)

Another method of producing polyamides involves opening cyclic monomers (lactams) and then carrying out a polycondensation reaction between the resulting open chains. This process is referred to as self-polycondensation because the polyamide is obtained from the same monomer rather than a pair of different ones.

Among the various possible cyclic starting monomers, for the purposes of this thesis we will focus mainly on ε-caprolactam and ω-laurolactam. Two different polyamides are obtained from their processing, respectively $Nylon\ 6$ and $Nylon\ 12$, but the work steps are the same.

First, the lactam ring is opened under high temperature (~250 °C) and pressure-controlled conditions, and in the presence of water as an initiator. The amino group ($-NH_2$) of one molecule reacts with the carboxyl group ($-COOH$) group of another, thus generating the amidic bond ($-CONH-$) (Fig. 2.4). The reaction continues until very long chains are obtained and similar to the other process, water removal is essential.

The nomenclature for Nylons ($Nylon\ a$) produced using this process has a single numerical index, which always refers to the number of carbon atoms present. $Nylon\ 12$ is obtained from laurolactam and it has a total of 12 carbon atoms: 11 of these derive from the corresponding methylene groups (CH_2) the other from the carbonyl group (CO). $Nylon\ 6$ is obtained from caprolactam and overall presents 6 carbon atoms. Similar to $Nylon\ 12$, one carbon atom is always provided by CO and the remaining five by CH_2. Therefore, the difference in the number of C atoms lies in the starting cyclic monomer because one C atom is always associated with the carbonyl group.

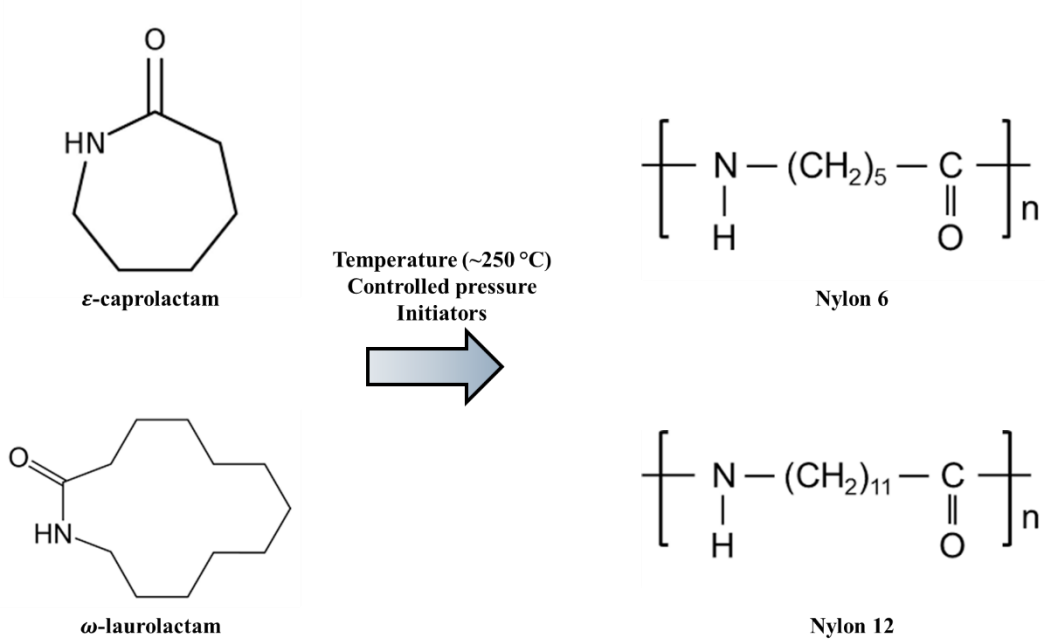

Figure 2.4: Ring-opening and self- polycondensation processes

2.2.2 Structure and properties

The structure of polyamide will differ depending on how it is produced, resulting in changes to its mechanical, thermal and physical properties.

Aliphatic polyamides such as $Nylon\ 6$, $Nylon\ 12$ or $Nylon\ 6{,}6$ are linear polymers and thus thermoplastic. They contain polar ($-CONH\ -$) groups that are spaced out at regular intervals. These groups cause hydrogen bonds to form between neighboring molecules, inducing high intermolecular attraction, and their regularity allows and promotes crystallization. These polymer chains also have aliphatic chain segments ($-CH_2\ -$) which give a measure of flexibility in the amorphous region.

There are several structural variables which can considerably affect the properties of the aliphatic polyamides, among which the most significant are: concentration of amidic groups, the number of methylene groups in the intermediates, lateral substitutes and crystallinity.

As the concentration of amidic groups increases, the distance between the polar groups ($-CONH\ -$) decreases accordingly, resulting in greater intermolecular forces of attraction. This

affects several properties. The density increases because the amidic group is much heavier than the methyl group, and because the chains are closer together due to their ability to form more hydrogen bonds. The polymer mechanical properties (strength, stiffness, hardness and resistance to creep) increase as the force required to separate its molecules increases. For the same reason, the melting temperature (Tm) and the heat deflection temperature (HDT) also increase (Tab. 2.1) [50, 51].

Table 2.1: Mechanical and thermal properties of typical polyamides

Property	$Nylon\ 6{,}6$	$Nylon\ 6$	$Nylon\ 6{,}10$	$Nylon\ 12$
Yield stress [MPa]	80	76	55	45
Stress at break [MPa]	/	/	/	54
Elongation at break [%]	80-100	100-200	100-150	200
Young's modulus [GPa]	3.0	2.8	2.1	1.4
Rockwell hardness	R118	R112	R111	R107
Tm [°C]	264	215	215	175
HDT [°C]	200	155	160	140

The amide group is polar, thus it attracts water from ambient humidity, giving polyamides their typical hygroscopic behaviour. The higher the concentration of amidic groups, the greater the hygroscopicity (Fig. 2.5). For example, the amide groups in $Nylon\ 6$ are much closer together than in $Nylon\ 12$. This means that the latter has lower thermo-mechanical properties but is less hygroscopic. The presence of water has a dual effect on polyamides. At elevated temperatures it promotes hot hydrolysis of the amide bonds, causing chain scission and loss of molecular weight, which deteriorates the mechanical properties. At the same time, absorbed water acts as a plasticizer at ambient conditions: it disrupts interchain hydrogen bonding, lowers the glass transition temperature and stiffness, and increases flexibility and impact strength. To avoid the problem of hydrolysis, it is necessary to ensure that the Nylons are completely dry before processing. Another important factor is crystallinity. The higher the crystallinity, the less water is absorbed, and therefore the less effect humidity has on the polymer's properties.

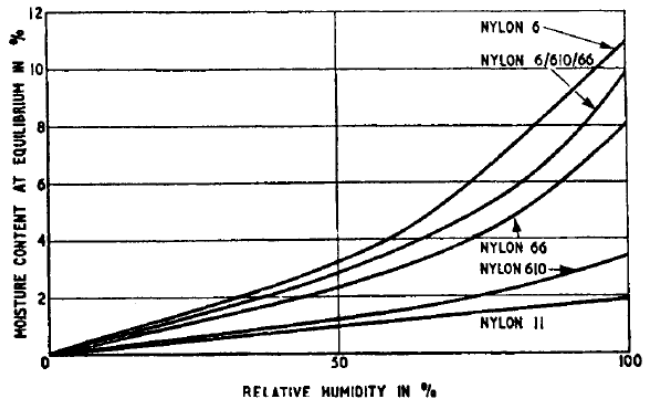

Figure 2.5: Trends in water absorption as the number of amide groups increases at different relative humidity values in the environment.

There is also considerable uncertainty regarding the numerical values of the glass transition temperature (Tg). Rigorously dried polymers appear to have Tg of about 50°C, these figures dropping towards 0°C as water is absorbed.

It has been observed that polymers from intermediates with an even number of methylene groups have higher melting points than similar polymers with an odd number of methylene groups: $Nylon\,6{,}6$ has a higher melting point than either $Nylon\,5{,}6$ or $Nylon\,7{,}6$. These differences are due to the differences in the crystal structure of polymers with odd and even methylene groups which develop in order that oxygen atoms in one molecule are adjacent to amino groups of a second molecule.

Another factor is the replacement of the hydrogen atom in the $(-CONH-)$ group by such groups as $(-CH_3)$ and $(-CH_2OCH_3)$, which will cause a reduction in the interchain attraction.

The properties of the nylons are considerably affected by the amount of crystallization: for example, $Nylon\ 6$ slowly cooled and subsequently annealed, may be 50-60% crystalline, while rapidly cooled may be only 10% crystalline. The degree of crystallinity affects water absorption, as mentioned above, electrical and mechanical properties. In particular, high crystallinity leads to high abrasion resistance. As with other crystalline polymers, properties are dependent not only on total percentage crystallinity but also on the size of morphological structures. According to the method of processing, different morphological structures will be produced: slowly cooled melts may form spherulites, while rapidly cooled polymers may form only fine aggregates.

With regard to environmental stress cracking, nylons are susceptible to attack by mineral acids. The rate of attack depends on the specific type of nylon as well as on the nature and

concentration of the acid, with nitric acid being generally aggressive at all concentrations. In contrast, nylons exhibit very good resistance to alkalis at room temperature. However, their overall chemical resistance decreases significantly at elevated temperatures.

Because of the high cohesive energy density in their crystalline state the polymers are soluble only in a few liquids of similar high solubility parameters and which are capable of specific interaction with the polymers. The electrical insulation properties are quite good at room temperature in dry conditions and at low frequencies. Because of the polar structure they are not good insulators for high-frequency work and since they absorb water they are also generally unsuitable under humid conditions.

2.2.3 Eco-sustainability

Polyamides exhibit substantial differences in terms of eco-sustainability, depending on the origin of their raw materials, the synthesis routes employed, and consequently their overall environmental impact. Among the most common grades, $Nylon\ 6$, and $Nylon\ 6{,}6$ are generally regarded as the least sustainable options [55], [56]. Both are derived exclusively from fossil-based feedstocks, and their production processes are energy-intensive. In particular, the synthesis of $Nylon\ 6{,}6$ requires a higher energy input compared to $Nylon\ 6$, which results in an even greater carbon footprint and overall environmental burden. At present, no commercially available bio-based alternatives exist for these two polyamides, which limits the possibility of reducing their dependence on non-renewable resources. Nevertheless, both materials benefit from well-established recycling routes. In addition to mechanical recycling, which enables the reprocessing of production scrap and end-of-life parts into secondary raw material, chemical recycling technologies have also been developed. These allow the depolymerization of $Nylon\ 6$, and $Nylon\ 6{,}6$ into their original monomers, which can subsequently be purified and repolymerized to yield virgin-quality polyamides. Such recycling strategies significantly reduce the environmental impact of these materials, offering a partial mitigation of their otherwise high fossil and energy dependency.

$Nylon\ 12$ is predominantly produced from petroleum-derived feedstocks. However, partially bio-based grades are available, in which it can be copolymerized with materials derived from castor oil [57]. From an environmental standpoint, $Nylon\ 12$ generally exhibits a lower impact

compared to $Nylon\ 6$, and $Nylon\ 6{,}6$, primarily due to its comparatively less energy-intensive synthesis process. Nonetheless, its overall sustainability remains constrained by a strong reliance on fossil resources, which continue to represent the bulk of its raw material supply.

Among the various polyamides, $Nylon\ 11$ stands out as the most sustainable option. This polymer is almost entirely derived from renewable feedstocks, particularly castor oil, which makes it less dependent on fossil sources [58]. The production of $Nylon\ 11$ is associated with a reduced carbon footprint and favorable life cycle performance, making it attractive in applications where environmental considerations are critical. However, the large-scale adoption of $Nylon\ 11$ is limited by several factors. These include its significantly higher cost, the concentration of production among a few industrial players, its lower thermal resistance and stiffness compared with $Nylon\ 6$ and $Nylon\ 6{,}6$, its dependency on castor oil-based feedstock with associated supply fluctuations, and its more restricted availability of grades and processing know-how. These factors further reduce its competitiveness for widespread industrial use.

Table 2.2 summarizes origin of raw materials, environmental impact and recyclability of the polyamides just analyzed.

Table 2.2: Comparison of the main polyamides in terms of sustainability factors

Polyamide	Raw material origin	Environmental impact (CO_2 footprint)	Recycling Options
$Nylon\ 6{,}6$	Fossil-based	↑↑↑ No bio-based alternative	Mechanical and chemical (monomer recovery)
$Nylon\ 6$	Fossil-based	↑↑ No bio-based alternative	Mechanical and chemical (depolymerization to caprolactam)
$Nylon\ 12$	Mainly fossil-based, partially bio-based	↑ Still strongly fossil-dependent	Mostly mechanical
$Nylon\ 11$	Bio-based	↓↓ Entirely bio-based derived	Mechanical, less established

2.3 Polyesters

Polyesters are encountered in many forms such as fibers, films, surface coating resins, rubbers and plasticizers. The common factor in these widely different materials is that they all contain ester groups ($-COO-$) in the main chain (Fig. 2.6). The diversity in polyester properties arises from the nature of the monomeric units (R, R') and the degree of crystallinity in the structure.

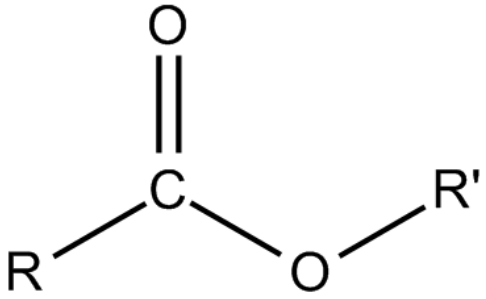

Figure 2.6: Ester group in polymer chain

Polyesters can be broadly divided into aromatic polyesters, such as polyethylene terephthalate (PET) and polybutylene terephthalate (PBT), and aliphatic polyesters, such as polylactic acid (PLA) and polybutylene succinate (PBS). As with Nylons, the difference lies in the fact that the former family has a benzene ring in its main chain, while the latter does not (Fig. 2.7). Its presence in the main chain significantly enhances rigidity, thermal stability, and barrier properties. For this reason, aromatic polyesters are known for their high strength and thermal resistance.

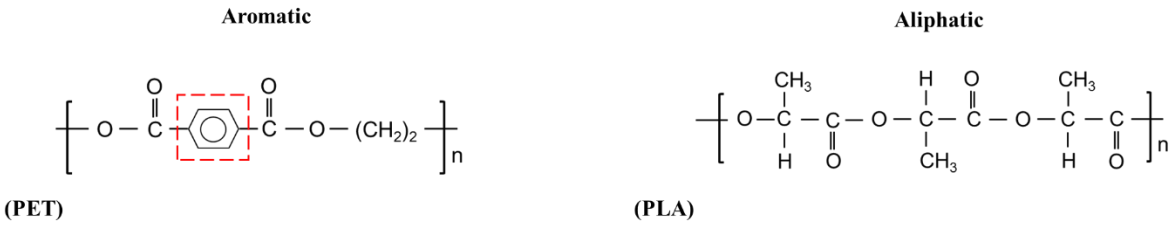

Figure 2.7: Comparison between representative aromatic and aliphatic polyesters, the benzene ring is highlighted in red

The distinction between aromatic and aliphatic polyesters is not only structural but also crucial in determining environmental impact and sustainability.

Traditional aromatic polyesters like PET and PBT are synthesized from petroleum-derived monomers (terephthalic acid and glycols). Recently, efforts have been made to replace fossil-based monomers with bio-based alternatives. For instance, bio-PET can be produced using bio-ethylene glycol (from bio-ethanol fermentation), although terephthalic acid is still

predominantly petroleum-derived. The aromatic rings introduce steric hindrance and high crystallinity, which make the ester bonds far less accessible to hydrolytic and enzymatic attack. Consequently, PET and PBT are considered non-biodegradable under environmental conditions. Their persistence in ecosystems is a major issue, as illustrated by the accumulation of PET bottles and microplastics. Recycling technologies (mechanical and chemical recycling) are currently the main strategies for reducing their environmental footprint, rather than biodegradation [59], [60], [61]. On the other hand, many aliphatic polyesters are inherently more compatible with renewable feedstocks. PLA is the prime example, synthesized from lactic acid obtained via fermentation of agricultural resources (corn, sugarcane). PBS can also be produced from succinic acid derived from biomass fermentation. It is also possible to obtain butanediol from renewable sources, meaning that PBS can ultimately be fully green.

As with nylons, polyesters are susceptible to hydrolysis and plasticization caused by water absorption. The ester group in polyesters is polar, thus it attracts water from ambient humidity, giving polyesters moderate hygroscopic behavior. The higher the concentration of ester groups along the chain, the more pronounced the water uptake. Aliphatic polyesters feature flexible methylene segments between ester groups, which expose the bonds to hydrolysis. The absence of aromatic rings reduces steric hindrance, and the irregular synthesis results in less crystallinity, allowing water molecules and enzymes to access the ester groups more easily. Hence, aliphatic polyesters can be biodegradable, with degradation occurring through hydrolysis of ester bonds followed by microbial assimilation of the resulting oligomers. The effect of water may be desired and sought after in certain environments to promote degradation at the end of life, but on the other hand, it is important to dry the polyesters thoroughly before processing.

Biodegradability depends strongly on polymer type and environmental conditions: PLA degrades efficiently under industrial composting (58 °C, high humidity), but much more slowly in soil or marine environments. PBS degrades at lower temperatures and in a wider range of environments. Thus, aliphatic polyesters are at the forefront of the bio-based plastics market, combining both renewable origin and biodegradability. Among the biodegradable polyesters currently available for 3D printing, PLA and PBS will be examined in greater detail below. The study and development of these materials have increased significantly in recent decades, compared to traditional polymers. In addition to the standard scientific literature, the section

on biodegradable polyesters draws on more recent publications on both PLA [62], [63], [64], [65], [66]and PBS [67], [68], [69], [70].

2.3.1 Polylactic acid (PLA)

PLA is probably the most commercially relevant bio-based polyester. The most common feedstocks for PLA production are starch or agricultural crops, which provide fermentable sugars (corn, sugarcane, wheat, potato). Lactic acid can be obtained by two routes: fermentation or chemical synthesis. The latter is based on petroleum-based components, like acetaldehyde or acrylonitrile. Although possible, this method is less common for PLA production because it does not align with the renewable and biodegradable profile of the polymer. On the other hand, fermentation involves microorganisms converting sugars into lactic acid under controlled pH and temperature conditions. This is the most sustainable approach, as it uses renewable raw materials.

Preparation methods

The synthesis of polylactic acid (PLA) can be achieved through two main routes: direct polycondensation of lactic acid or ring-opening polymerization of lactide (Fig. 2.8).

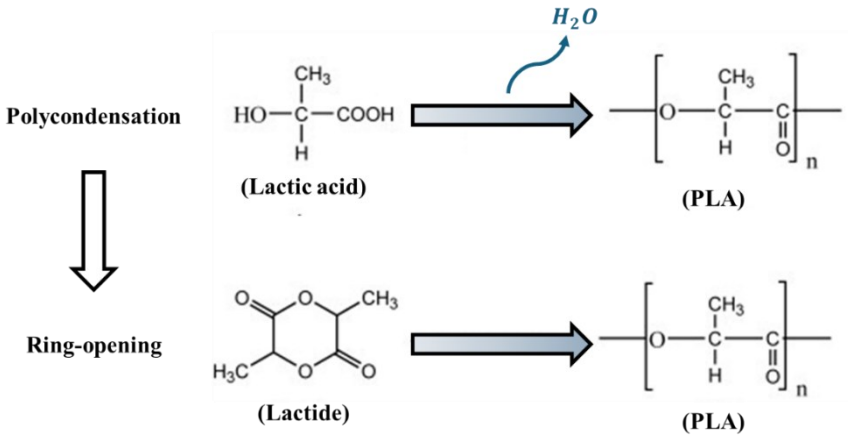

Figure 2.8: Methods for the synthesis of PLA

The direct polycondensation of lactic acid monomers is the simplest approach. During this process, the hydroxyl group ($-OH$) of one lactic acid molecule reacts with the carboxyl group ($-COOH$) of another, forming an ester bond and releasing water.

However, direct polycondensation has several limitations related to water production. Strong vacuum and high temperatures are required to continuously remove water and drive the

polymerization forward. The reaction equilibrium disfavors high molecular weight polymers due to the accumulation of water. Hence, the molecular weights typically achieved are low, which restricts the mechanical performance of the resulting PLA. For these reasons, direct polycondensation is mainly used for oligomers, which can later be converted into high-molecular-weight PLA by other methods.

The most industrially relevant route to PLA production is ring-opening polymerization of lactide, the cyclic dimer of lactic acid. Lactic acid is first oligomerized to form low-molecular-weight chains, which then undergo depolymerization and cyclization to yield lactide. In the presence of catalysts, the lactide undergoes ring-opening polymerization, producing high-molecular-weight PLA. The choice of catalyst and reaction conditions influences not only molecular weight but also color, purity, and thermal stability of PLA. This method enables excellent control over molecular weight, polymer architecture (e.g. linear or branched) and stereoregularity. It is suitable for use in packaging, fibers and biomedical applications.

Structure and properties

The properties of PLA are strongly determined by its chemical structure, in particular the presence of the ester group ($-COO-$) and the stereochemistry of the lactic acid units. These structural features govern the degree of crystallinity, the mechanical performance, and the interaction with water molecules.

As previously mentioned, lactide is the cyclic dimer of lactic acid, obtained through the dehydration and cyclization of two lactic acid molecules. Lactide exists in three stereoisomeric forms, depending on the configuration of the lactic acid units (Fig. 2.9): L-lactide (from L-lactic acid), D-lactide (from D-lactic acid) and meso-lactide (from both enantiomers).

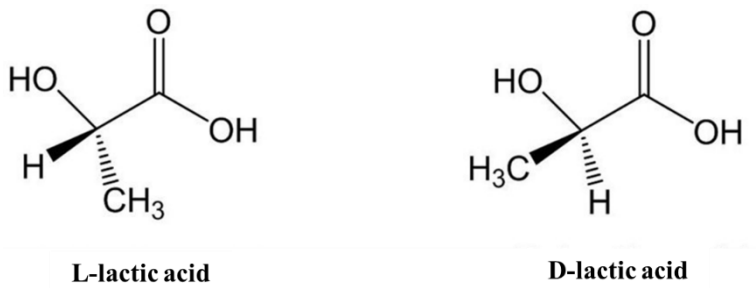

Figure 2.9: Stereoisomers of lactic acid

L-lactic acid is biologically compatible, and it is found naturally in living organisms as it is the product of most biological fermentation pathways (e.g., from glucose via lactic acid bacteria). L-lactide is formed by two molecules of L-lactic acid, and poly-L-lactic acid (PLLA) is produced through its ring-opening. PLLA is a highly stereoregular polymer with a high degree of crystallinity (up to ~40%), a melting point around 170–180 °C, and superior mechanical strength. This type of PLA degrades more slowly due to the ordered crystalline domains, making it suitable for long-term biomedical applications (e.g., resorbable implants, sutures).

The other stereoisomer is D-lactic acid. Although it is rare in nature and in biological systems, it can be produced by specific microorganisms during fermentation. Two molecules of D-lactic acid produce D-lactide, which is the basis of poly-D-lactic acid (PDLA), obtained through the ring-opening process again. PDLA has lower crystalline properties than PLLA but opposite chirality.

When blended with PLLA, PDLA can form a stereocomplex PLA, where chains of opposite chirality crystallize together. This solution exhibits significantly higher melting temperature (~220 °C) and improved thermal stability compared to PLLA or PDLA alone.The last one is the meso-lactide, formed by one L- and one D-lactic acid unit. Its polymerization leads to atactic, amorphous PLA, with low crystallinity and faster degradation rates.

In terms of crystallinity, PDLA tends to be more amorphous than PLLA. As with other polymers, slow cooling or annealing favors crystallization, leading to higher stiffness and thermal resistance. Rapid cooling tends to trap the chains in an amorphous state, improving transparency but lowering dimensional stability.

The mechanical performance of PLA is strongly influenced by crystallinity: a higher crystallinity induces higher strength and modulus, but increased brittleness. On the other hand, amorphous PLA has lower strength but improved toughness and transparency.

PLA is often described as a rigid and brittle thermoplastic, with properties comparable to PET and polystyrene, but lower ductility. It presents a tensile strength around 50–70 MPa, a Young's modulus about 2–3 GPa typically and elongation at break lower than 10% [63], [71].

Due to the presence of polar ester groups, PLA exhibits a certain degree of hygroscopicity, although significantly lower than polyamides. Absorbed moisture can plasticize the polymer, lowering the glass transition temperature (Tg) and reducing stiffness. Over time, water also

promotes hydrolysis of ester bonds, leading to chain scission and loss of mechanical integrity. Water diffusion occurs mainly through amorphous domains; hence, highly crystalline PLA is more resistant to hydrolysis, while amorphous PLA degrades more rapidly.

This water sensitivity is a double-edged sword: while it is beneficial for biodegradability, it limits the long-term performance of PLA in humid environments. It must also be properly dried before processing.

2.3.2 Polybutylene succinate (PBS)

Polybutylene succinate (PBS) is a type of aliphatic polyester that is widely regarded as one of the most promising biodegradable thermoplastics, thanks to its balanced combination of mechanical performance, processability and compostability. Although PBS belongs to the same family as PLA, it has distinct structural and functional features that make it a complementary material for different applications.

Preparation methods

PBS can be synthesized through direct polycondensation or esterification followed by transesterification (Fig. 2.10). Through the first approach, succinic acid reacts with 1,4-butanediol in a condensation reaction, producing ester bonds and releasing water as a by-product. The reaction requires high temperature and efficient removal of water to reach high molecular weights. The other method also uses 1,4-butanediol, but instead of succinic acid, dimethyl succinate can be used. The two components are processed via transesterification process, releasing methanol. This method can offer better control over molecular weight and product purity. In both cases, metal catalysts (typically titanium-based compounds) are used to accelerate the polycondensation and achieve high-molecular-weight PBS suitable for industrial processing.

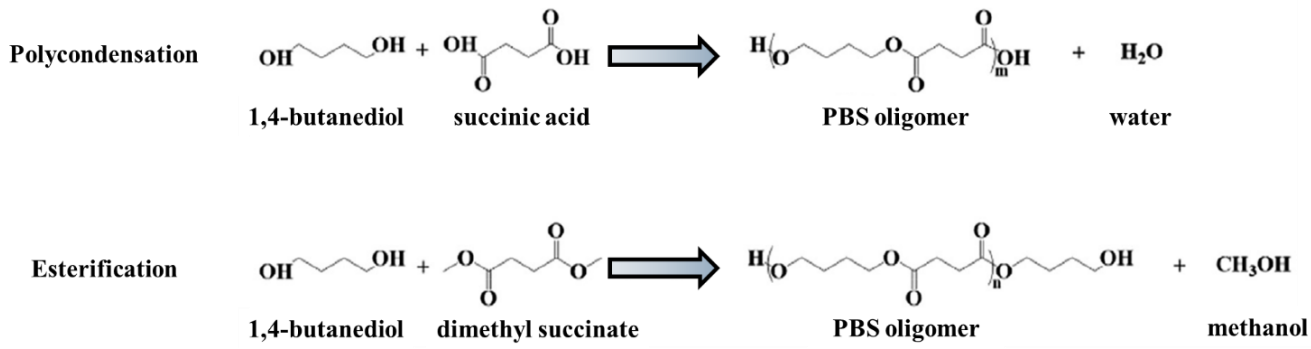

Figure 2.10: Synthesis of PBS

Traditionally, PBS has been synthesized from petrochemical succinic acid and 1,4-butanediol. However, in recent years, significant advances have been made to obtain both monomers from renewable resources, opening the way to 100% bio-based PBS. Succinic acid can be produced via fermentation of carbohydrates (glucose, sucrose, starch, lignocellulosic biomass) by microorganisms. Bio-based succinic acid production is attractive because it uses low-cost raw materials and sequesters CO_2 during fermentation. 1,4-Butanediol is traditionally fossil-derived but can also be obtained from biomass sugars through microbial fermentation, or via catalytic hydrogenation of bio-succinic acid.

Thanks to these biotechnological routes, PBS can be produced as a fully bio-based polymer, positioning it as a promising alternative in the family of biodegradable plastics, with a lower environmental footprint compared to PLA (which relies mainly on starch/sugar feedstocks).

Structure and properties

PBS is a linear aliphatic polyester with ester groups regularly spaced along the chain. This structure leads to a semicrystalline structure, with a crystallinity degree typically around 30–40%. The crystalline regions, related to the ester groups, contribute to relatively high thermal resistance, while the amorphous domains impart some ductility. It has a melting point of 115 °C and a glass transition temperature around 32 °C, which explains its good flexibility at low temperatures.

PBS is less rigid but far more ductile than PLA, allowing better toughness and impact resistance. It presents a strength of (30 – 50) MPa, a Young's modulus around (0.4–0.6) GPa and

an elongation at break up to 200–300%. PBS, like PLA, contains hydrolysable ester bonds, but its hydrophobic aliphatic chains limit water uptake. Water absorption is generally lower than PLA, which enhances dimensional stability in humid environments. Hydrolytic degradation occurs more slowly compared to PLA, although still significantly faster than aromatic polyesters like PET.

The biodegradability of PBS is superior to that of PLA in many environments (composts, soil and aquatic environments) due to its chemical structure and thermal/mechanical profile. Given its low Tg, PBS chains are flexible under ambient and natural environmental conditions. This enhances molecular mobility and facilitates the enzymatic attack and hydrolysis of ester bonds, even at low temperatures. By contrast, PLA (Tg ~ 60 °C) remains rigid and glassy under the same conditions, limiting water diffusion and enzymatic activity. PBS has a linear aliphatic structure with evenly spaced ester groups, making them more accessible to water and enzymes compared to the PLA configuration. In addition, it is semicrystalline, and its crystalline regions are less densely packed than those of PLA. This means hydrolysis and enzymatic degradation can proceed more efficiently, especially in the amorphous domains.

PBS degrades not only under industrial composting conditions, but also in soil and aquatic environments, where PLA degradation is very slow. This makes PBS more promising for applications in agriculture (e.g., mulch films) and marine packaging, where post-use collection is challenging. Table 2.3 summarizes and compares the main characteristics of PLA and PBS [50,54].

Table 2.3: Mechanical, thermal and sustainable properties of typical biodegradable polyesters

Property	PLA	PBS
Tg [°C]	55-65	-32
Tm [°C]	150-180	115
Tensile strength [MPa]	50-70	30-50
Young's modulus [GPa]	2.0-3.0	0.4-0.6
Elongation at break (%)	<10	200-300
Biodegradability	Industrial composting	Broader (soil, composting)
Feedstock	Renewable (fermentation)	Potentially 100% renewable

3. Characterization of 3D-printed fiber-reinforced composites and their constituents

3.1 Introduction

In this thesis, various fiber-reinforced composites were 3D printed and analyzed, with different types of matrix and reinforcing fibers. In addition to the composite's overall features, it is also important to assess the characteristics of its individual components, i.e. the matrix and reinforcement. The objective of this chapter is to describe the most common characterization methodologies used to study composites and their constituents, in order to evaluate their mechanical, thermal, and rheological properties. Depending on the objective of each chapter, analyses were performed either on the composite itself, or on the composite and its individual components for comparison purposes.

First, the mechanical tests used to evaluate the mechanical properties of the material under analysis will be described, along with the mathematical modelling methods used to interpret and compare their performance. Next, the physical, thermal and rheological analyses used to will be introduced. Finally, the morphological analysis methods used to evaluate the quality of the printed object and fracture surfaces will be explained.

This chapter is divided into a first part providing theoretical background and a description of the tests carried out, followed by a second part describing the methods used and the instruments employed.

3.2 Mechanical behavior

As well-known from literature, fiber reinforced 3D printed polymeric materials can be regarded and modeled as anisotropic materials like composites [6], [72], [73], [74] and consequently tested according to their standards.

3.2.1 Mathematical modeling

Referring to the meso-scale structure introduced in Section 1.4.2.4, a layer printed with a specific raster angle is often anisotropic in the same way as a unidirectional composite lamina, hence it can be modelled using lamina macromechanics [75], [76].

Two right-handed coordinate systems are normally considered (Fig. 3.1): the first one, indicated with x, y, z , is a convenience coordinate system that is related to the external loading, while x_1, x_2, x_3 is related to material symmetry. In particular, axes x_3 and z coincide and are normal to the deposed layer, while x_1 is rotated with respect to x by the raster angle ϑ. Since a 3D printed layer can be thought of as an orthotropic elastic material loaded in plane stress, four constants are necessary to represent its behavior, namely E_1, E_2, G_{12}, ν_{12}. E_1 and E_2 are the Young's moduli in the longitudinal and transverse directions, G_{12} is the in-plane shear modulus, while ν_{12} is the Poisson's ratio, describing the contraction in the x_2 direction when the layer is loaded in tension in the x_1 direction. Concerning tensile strength, it is assumed that only three independent material constants S_L, S_T, S_{LT}, describe the mechanical behavior and these are longitudinal, transverse and shear strength, respectively.

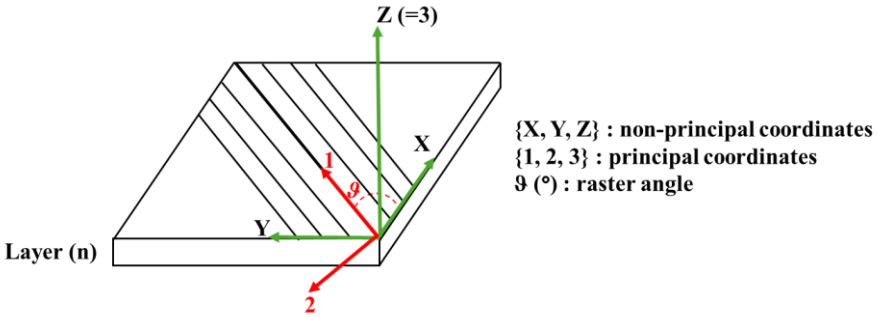

Figure 3.1: the lamina and its coordinate systems

Following the usual notation, the layer stiffness matrix $[Q]$ in the x_1, x_2, x_3 coordinate system is :

$$\{\sigma\} = [Q]\{\varepsilon\} \text{ or } \begin{Bmatrix}\sigma_1\\ \sigma_2\\ \sigma_6\end{Bmatrix} = \begin{bmatrix}Q_{11} & Q_{12} & 0\\ Q_{12} & Q_{22} & 0\\ 0 & 0 & Q_{66}\end{bmatrix}\begin{Bmatrix}\varepsilon_1\\ \varepsilon_2\\ \varepsilon_6\end{Bmatrix} \quad (1)$$

where σ_1 and σ_2 are the normal stresses and σ_6 is the in-plane shear stress. In analogy, ε_1 and ε_2 are the normal strains and ε_6 is the in-plane engineering shear strain. The stiffness matrix components are:

$$Q_{11} = \frac{E_1}{1-\nu_{12}\nu_{21}}, Q_{22} = \frac{E_2}{1-\nu_{12}\nu_{21}}, \; Q_{12} = \frac{\nu_{12}E_2}{1-\nu_{12}\nu_{21}}, Q_{66} = G_{12} \text{ with } \nu_{21} = \nu_{12}\frac{E_2}{E_1} \quad (2)$$

The stiffness matrix changes its representation in the x, y, z coordinate system as follows:

$$\begin{Bmatrix}\sigma_x\\ \sigma_y\\ \sigma_s\end{Bmatrix}=\begin{bmatrix}Q_{11}^{\vartheta} & Q_{12}^{\vartheta} & Q_{16}^{\vartheta}\\ Q_{12}^{\vartheta} & Q_{22}^{\vartheta} & Q_{26}^{\vartheta}\\ Q_{16}^{\vartheta} & Q_{26}^{\vartheta} & Q_{66}^{\vartheta}\end{bmatrix}\begin{Bmatrix}\varepsilon_x\\ \varepsilon_y\\ \varepsilon_s\end{Bmatrix} \quad (3)$$

where ε_x, ε_y and σ_x, σ_y are the normal strains and stresses, and ε_s and σ_s are the engineering shear strain and stress in the $x-y$ plane. The stiffness matrix [Q^{ϑ}] depends on ϑ and on matrix $[Q]$ through:

$$\begin{aligned}
Q_{11}^{\vartheta} &= Q_{11}\cos^4\vartheta + Q_{22}\sin^4\vartheta + 2(Q_{12}+2Q_{66})\cos^2\vartheta\sin^2\vartheta\\
Q_{22}^{\vartheta} &= Q_{11}\sin^4\vartheta + Q_{22}\cos^4\vartheta + 2(Q_{12}+2Q_{66})\cos^2\vartheta\sin^2\vartheta\\
Q_{12}^{\vartheta} &= (Q_{11}+Q_{22}-4Q_{66})\cos^2\vartheta\sin^2\vartheta + Q_{12}(\cos^4\vartheta+\sin^4\vartheta)\\
Q_{16}^{\vartheta} &= (Q_{11}-Q_{12}-2Q_{66})\cos^3\vartheta\sin\vartheta - (Q_{22}-Q_{12}-2Q_{66})\sin^3\vartheta\cos\vartheta\\
Q_{26}^{\vartheta} &= (Q_{11}-Q_{12}-2Q_{66})\cos\vartheta\sin^3\vartheta - (Q_{22}-Q_{12}-2Q_{66})\sin\vartheta\cos^3\vartheta\\
Q_{66}^{\vartheta} &= (Q_{11}+Q_{22}-2Q_{12})\cos^2\vartheta\sin^2\vartheta + Q_{66}(\cos^2\vartheta-\sin^2\vartheta)^2
\end{aligned} \quad (4)$$

Quantification of stiffness anisotropic behavior

The four stiffness lamina engineering constants (E_1, E_2, G_{12}, ν_{12}) can also be transformed from the principal material axes (x_1, x_2, x_3) to the non-principal coordinate coordinates (x, y, z). For example, the variation in Young's modulus, based on the raster angle (ϑ), is described as follows:

$$E_x = \left[\frac{\cos(\vartheta)^4}{E_1} + \left(\frac{1}{G_{12}} - \frac{2\nu_{12}}{E_1}\right)\cos(\vartheta)^2\sin(\vartheta)^2 + \frac{\sin(\vartheta)^4}{E_2}\right]^{-1} \quad (5)$$

To better appreciate its variation, it can be plotted as a function of ϑ (Fig. 3.2).

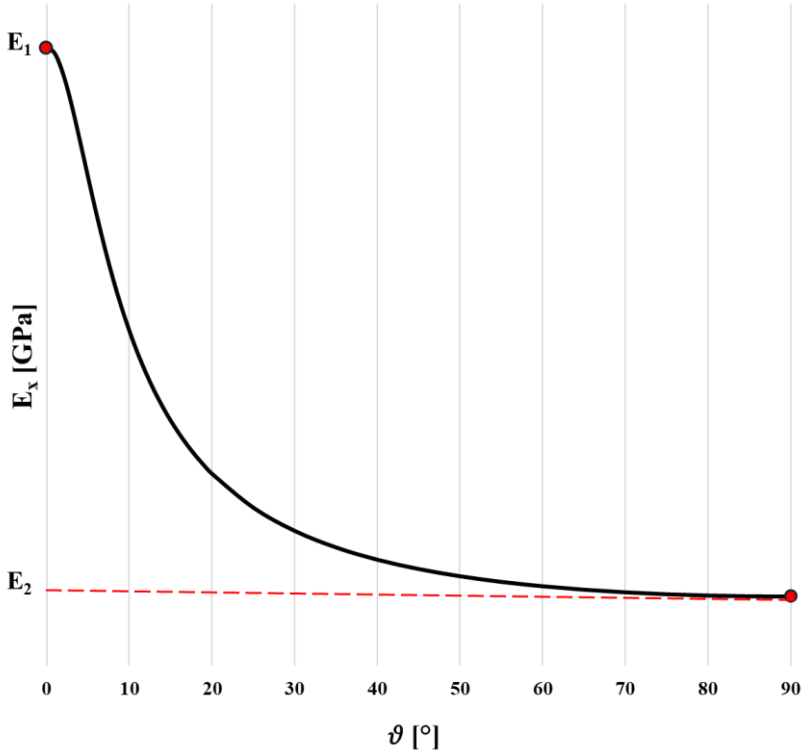

Figure 3.2: Variation of Young's modulus with lamina orientation (ϑ)

E_x generally decreases monotonically from E_1 at $\vartheta = 0°$ to E_2 at $\vartheta = 90°$. If the material is highly anisotropic ($E_1 \gg E_2$), the curve will show a sharp drop, as the angle changes slightly from 0°, while if it tends to be isotropic ($E_1 \approx E_2$) the curve will tend to be flat. Despite this, it is not necessarily true that the extremum values occur along the principal material directions [76], and it is not so easy to graphically assess the influence of the shear modulus (G_{12}) on E_x . Similar transformation equations, graphical representations and considerations may be found also for ν_{xy} and G_{xy}.

The effects of lamina orientation on stiffness are difficult to assess from inspection of stiffness transformation equations such as Eq.4 and Eq.5. For this reason, a more convenient 'invariant' form has been proposed by Tsai and Pagano [77], [78] to better interpret and evaluate the anisotropy of the lamina.

An alternative form of Eqs. 4 was introduced as follows:

$$
\begin{aligned}
Q_{11}^{\vartheta} &= U_1 + U_2\cos(2\vartheta) + U_3\cos(4\vartheta) \\
Q_{22}^{\vartheta} &= U_1 - U_2\cos(2\vartheta) + U_3\cos(4\vartheta) \\
Q_{12}^{\vartheta} &= U_4 - U_3\cos(4\vartheta) \\
Q_{16}^{\vartheta} &= \tfrac{U_2}{2}\sin(2\vartheta) + U_3\sin(4\vartheta) \\
Q_{26}^{\vartheta} &= \tfrac{U_2}{2}\sin(2\vartheta) - U_3\sin(4\vartheta) \\
Q_{66}^{\vartheta} &= \tfrac{1}{2}(U_1 - U_4) - U_3\cos(4\vartheta)
\end{aligned}
\quad \text{with} \quad
\begin{aligned}
U_1 &= \tfrac{1}{8}(3Q_{11} + 3Q_{22} + 2Q_{12} + 4Q_{66}) \\
U_2 &= \tfrac{1}{2}(Q_{11} - Q_{22}) \\
U_3 &= \tfrac{1}{8}(Q_{11} + Q_{22} - 2Q_{12} - 4Q_{66}) \\
U_4 &= \tfrac{1}{8}(Q_{11} + Q_{22} + 6Q_{12} - 4Q_{66})
\end{aligned}
\tag{6}
$$

It can be shown that U_1 and U_4 are invariant quantities under a change of reference frame, therefore they represent the isotropic contributions to material stiffness. The other two quantities, U_2 and U_3, are not invariant and hence they are the orthotropic contributions and have a direct physical meaning in terms of deviation from the isotropic behavior. In particular, U_2 is related to the difference between longitudinal and transverse properties, i.e. between the two Young's moduli E_1 and E_2, which is zero in the case of an isotropic material. U_3 is related to the dependence of G_{12} on E_1, E_2, and ν_{12} and again is zero in the case of an isotropic material, since in that case the shear modulus can be obtained as a function of Young's modulus and Poisson's ratio.

Tsai and Hahn [78] showed that it is convenient to represent the components of the stiffness matrix in the reference system x, y, z (Eq.6) through two generalized Mohr's circles (Fig.3), based on U_1, U_2, U_3, U_4. The center of the first circle is placed on the abscissa axis at a distance U_4 from the origin and its radius is U_3. The center of the second circle is located at a distance U_1 from the center of the first circle and its radius is U_2.

This representation is convenient to evaluate graphically and can be used to qualitatively describe the degree of anisotropy of the in-plane stiffness. In fact, if the material is strongly anisotropic the two circles will appear large with respect to their distance (Fig. 3.3a). On the other hand, if the material is isotropic $U_1 \neq 0$ and $U_2 = U_3 = 0$, thus the circles will collapse to single points, and their distance is the only significant quantity (Fig. 3.3b).

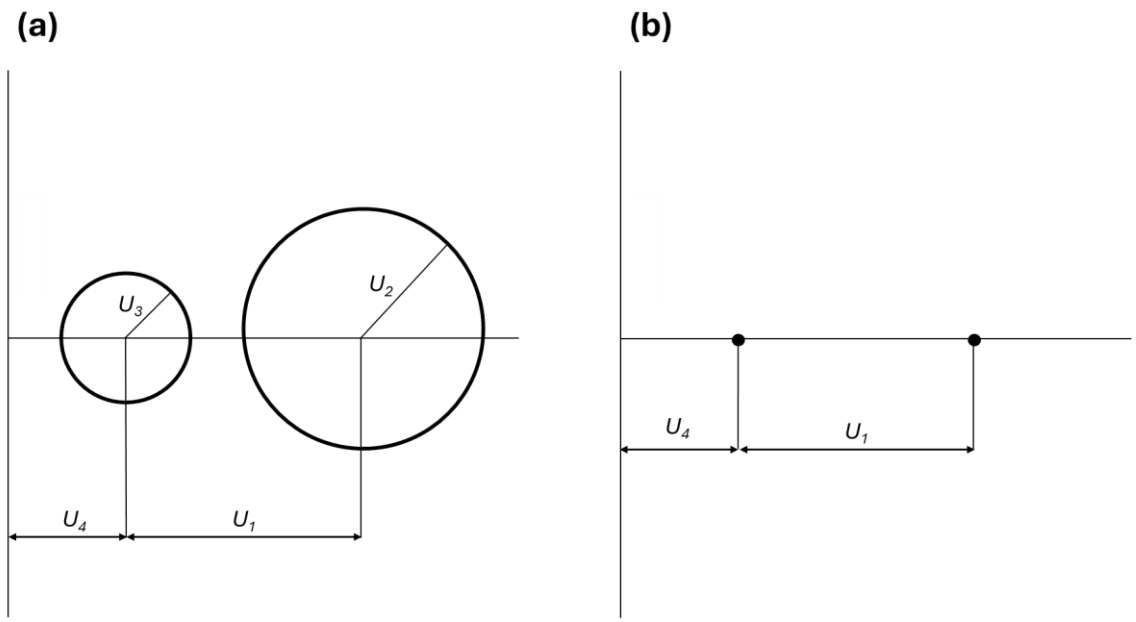

Figure 3.3: Generalized Mohr's circles for a) orthotropic lamina and for b) isotropic lamina

The novelty of this part of the thesis is the introduction of two quantitative parameters for a better interpretation of anisotropy. The graphical analysis developed by Tsai and Hahn can be also supported quantitatively through the ratios $\frac{U_2}{U_1}$, $\frac{U_3}{U_1}$, which represent the relative weight of the orthotropic components with respect to the isotropic one. In the definition of the two ratios, U_1 is preferred to U_4 because it can never be zero. When these ratios are relatively large, the material has a pronounced anisotropy, while if the material is isotropic, they will be close to zero. Moreover, if $\frac{U_2}{U_1}$ is greater than $\frac{U_3}{U_1}$, anisotropy is mainly due to the difference between the longitudinal and transverse properties. On the opposite side, the anisotropic behavior is due to the shear properties.

Strength of a fiber-reinforced lamina

Given the different behavior of the lamina under tension and compression, five independent material constants are required to fully describe its strength behavior: two for the longitudinal direction (S_L^+, S_L^-), two for the transverse direction (S_T^+, S_T^-) and one for shear resistance (S_{LT}). Very often it is reasonable to assume that tensile and compressive values are the same in absolute value. Hence, only three strength material constants (S_L, S_T, S_{LT}) are needed to obtain the basis for the analysis simplified analysis of lamina strength under simple stress states. S_L, S_T, S_{LT} are referred to the principal axes (x_1, x_2, x_3), while the known-external stress field (σ_x,

σ_y, σ_s) is referred to x, y, z coordinate system. The first step in all calculations must be the transformation of σ_x, σ_y, σ_s to the principal lamina axes, as follows:

$$\begin{Bmatrix}\sigma_1\\ \sigma_2\\ \sigma_6\end{Bmatrix} = \begin{bmatrix}\cos(\vartheta)^2 & \sin(\vartheta)^2 & 2\cos(\vartheta)\sin(\vartheta)\\ \sin(\vartheta)^2 & \cos(\vartheta)^2 & -2\cos(\vartheta)\sin(\vartheta)\\ -\cos(\vartheta)\sin(\vartheta) & \cos(\vartheta)\sin(\vartheta) & \cos(\vartheta)^2 - \sin(\vartheta)^2\end{bmatrix}\begin{Bmatrix}\sigma_x\\ \sigma_y\\ \sigma_s\end{Bmatrix} \tag{7}$$

By doing so, it is possible to obtain principal stress values (σ_1, σ_2, σ_6) and a comparison can be made with the appropriate limit strengths. It may be pointed out that uniaxial stress applied in any direction other than the principal material axes produces multiaxial stresses along the principal material axes. For example, an external tensile stress state along the x-axis involves $\sigma_x \neq 0$ and $\sigma_y = \sigma_s = 0$. Substituting this into Eq.7, the following stress state is obtained in the reference system (x_1, x_2, x_3):

$$\begin{aligned}\sigma_1 &= \sigma_x \cos(\vartheta)^2\\ \sigma_2 &= \sigma_x \sin(\vartheta)^2\\ \sigma_6 &= -\sigma_x \cos(\vartheta)\sin(\vartheta)\end{aligned} \tag{8}$$

With these assumptions, the Tsai-Hill criterion provides a single function for predicting failure by considering the interaction between strengths. In the case of in-plane-stress states the failure initiates when the following equality is true:

$$\frac{{\sigma_1}^2}{{S_L}^2} - \frac{\sigma_1\sigma_2}{{S_L}^2} + \frac{{\sigma_2}^2}{{S_T}^2} + \frac{{\sigma_6}^2}{{S_{LT}}^2} = 1 \tag{9}$$

On the other hand, if the combination of stresses is less than unity, no failure of the lamina occurs. Hence, this approach can be used either to predict the strength of the lamina once all three limits (S_L, S_T, S_{LT}) are known, or to obtain one of the strength values required for a complete mechanical characterization. Usually S_L and S_T are known and the shear strength S_{LT} is sought.

3.2.2 Tensile characterization

Tensile tests were performed on all materials involved in this thesis to obtain the seven independent material constants necessary for a complete characterization of the in-plane properties.

When considering structural applications of 3D-printed composites, the strength value of interest is the yield strength. Hence, in this thesis, it assumed that S_L, S_T and S_{LT} are related to the yield values obtained from mechanical characterization.

ASTM D3039 standard [79] was used to measure longitudinal and transverse properties, by printing specimens at 0° and 90° raster angle. In particular, Young's modulus E_1, Poisson's ratio ν_{12} and longitudinal yield strength $\sigma_Y^{0^\circ}$ (=S_L) were obtained from 0° raster angle, while Young's modulus E_2 and transverse yield strength $\sigma_Y^{90^\circ}$ (=S_T) were evaluated from 90° specimens.

Two methods were used in this thesis to characterize shear properties: ASTM D3518 standard [80], through specimens printed at ±45° raster angles, and 10° off-axis tensile test method [81], [82].

ASTM D3518 uses an ±45° laminate, which is a symmetrical and balanced composite with a lay-up composed only of +45° plies and -45° plies. If only unidirectional laminae oriented at +45° or -45° were used, there would be a significant coupling effect. The clamps constrain these deformations, and consequently parasitic stresses are generated near the gripping jaws. Thanks to the symmetrical and balanced ±45° sequence, these problems are greatly reduced, and shear stress in the plane of the individual lamina is therefore predominant. Hence, using this first method, the axial deformation generated by the tensile test is converted to an in-plane shear stress state within the individual unidirectional layers. From which it is possible to evaluate the shear modulus G_{12}, the shear yield strength τ_Y and the yield strength $\sigma_Y^{45^\circ}$ for the individual lamina. As stated in the standard, it can be assumed that $\sigma_Y^{45^\circ}$ is twice τ_Y. Although this standard enables G_{12} to be calculated accurately, it has limitations, as it is not guaranteed that failure is solely due to in-plane shear stresses. In addition to the intralaminar shear component, which lies in the plane of the single lamina and is of interest, interlaminar shear stresses are also generated between laminae due to out-of-plane coupling effects. If the fracture surface does not show delamination, it is reasonable to conclude that the failure is mainly due to intralaminar stresses present in the plane of the lamina.

Looking at the other test, the laminate is made up of laminae that are all oriented at 10°. In this case, the sample is practically unidirectional with a very small angle, close to 0°. For this reason, the dominant deformation and stress field on the specimen are predominantly axial with limited coupling effects. Consequently, there is mainly intralaminar shear stress and the Young's modulus E_{10} and the yield strength $\sigma_Y^{10^\circ}$ are obtained directly from the 10° off-axis tensile test. Unlike ASTM D3518, the shear modulus of the lamina is obtained once the longitudinal and transverse properties are known. Indicating with E_{10} (=E_x) the Young's modulus at 10° (i.e. $\pi/18$), G_{12} can be obtained through Eq.5. This measurement method is subject to error and is less accurate than the previous. Furthermore, the alignment of the sample during the tensile test is critical, as even small angular errors can significantly impact the results. Thanks to the limited effects of out-of-plane coupling effects and parasitic stresses, the 10° method is preferable for strength evaluation.

Several works in the literature have focused on comparing in-plane shear characterization techniques for composites[82], [83], [84], [85]. Regarding G_{12}, the ASTM D3518 standard is preferable because, thanks to its ±45° lay-up, it produces a deformation field dominated by shear. Since out-of-plane coupling effects mainly influence strength, the deformation measurement reflects γ_{12} well in the elastic field. In addition, the calculation of G_{12} is based on a simple linear formula. On the other hand, in the 10° test, the shear component is 'hidden' within a predominantly axial stress field. To obtain G_{12}, a more complex equation must be solved, which depends on the values obtained from the longitudinal tests at 0° and transverse tests at 90°, so this measurement is more sensitive to errors and variability (e.g. incorrect fiber alignment). For this reason, G_{12} values obtained using the 10° test are generally more dispersed and less reliable than those obtained using the ±45° method of ASTM D3518. In both methods S_{LT} is obtained through Eq.9 by setting σ_x equals to either $\sigma_Y^{10^\circ}$ or $\sigma_Y^{45^\circ}$, respectively, in Eq.8. It is important to remember that the use of ASTM D3518 implies out-of-plane coupling effects, so it is only correct to use it if the failure does not involve delamination. Concluding, both tests are valid taking the relevant limitations into account: tensile shear test from ASTM D3518 should result in higher shear modulus and a lower strength.

3.3 Density and porosity evaluation

As described in Section 1.3, voids are inevitable in 3D printing, so it is important to evaluate their quantity in relation to the printing parameters used and the mechanical performance obtained from the tests.

Density was measured for the filaments before printing ρ_x^f and for the specimens before testing ρ_x^s, where x is the considered material. The calculation of ρ_x^s was performed for each orientation of the tensile specimens, and for the rheological samples. Assuming that filament porosity is zero, voids percentage of the specimens $\%v$ was evaluated as follows:

$$\%v = \left(1 - \frac{\rho_x^s}{\rho_x^f}\right) \cdot 100 \tag{10}$$

3.4 Thermal characterization

Differential Scanning Calorimetry (DSC) is a thermal analysis technique that measures how the heat flow absorbed or released by a sample varies when it is heated or cooled at a controlled rate. When a material is heated or cooled, it can undergo physical transitions (e.g., melting, glass transition, crystallization) or chemical reactions (decomposition, cross-linking). These phenomena involve the absorption or release of heat, i.e., a change in the enthalpy of the system. During the test, a controlled thermal profile for heating and cooling is set, and heat flow is recorded. If the sample absorbs heat, it is undergoing an endothermic process (melting, evaporation, glass transition), while if it releases heat, it is undergoing an exothermic process (crystallization, chemical reactions like degradation etc.). The result is a curve (thermogram) that shows the heat flow as a function of temperature or time.

DSC is used to determine specific heat, transition enthalpies, the crystalline fraction and the characteristic temperatures, such as the glass transition temperature T_g and the melting temperature T_m. The crystalline fraction χ_c, evaluated as a percentage, was obtained as follows:

$$\chi_c = \frac{\Delta H_m}{\Delta H_{m0}(1-w_t)} * 100, \quad (11)$$

where w_t is the mass fraction of fillers or reinforcement fibers, ΔH_m is the experimentally measured melting enthalpy and ΔH_{m0} is the melting enthalpy of the fully crystalline polymeric matrix, specific for each material under analysis, which can normally be taken from the literature.

Thermogravimetric analysis, or TGA, is an additional thermal analysis technique. It measures how the mass of a sample changes as it is heated (or cooled) in a controlled atmosphere by applying controlled thermal heating. The system records the changes in mass as the temperature varies in real time. TGA is useful for obtaining information on the thermal stability of a material, decomposition temperatures, moisture content, and percentage of fillers or residues in composite materials

3.5 Rheological characterization

For thermoplastic materials, it is important to measure viscosity, which is related to fluid flow resistance. Its physical meaning can be obtained from the following equation:

$$\tau = \eta * \dot{\gamma}, \quad (12)$$

where τ is shear stress, $\dot{\gamma}$ is shear rate, which represents the speed at which the layers of fluid flow over each other, and η is the viscosity of the fluid. A fluid is considered Newtonian if η depends only on temperature and pressure. On the other hand, a fluid has a non-Newtonian behavior if η depends on other factors, such as shear rate, viscoelasticity effects, etc.

In the molten state, thermoplastic polymers generally exhibit pseudoplastic non-Newtonian behavior, whereby their shear viscosity η decreases as the shear rate $\dot{\gamma}$ increases. Figure 3.4 shows the trend on a bi-logarithmic scale.

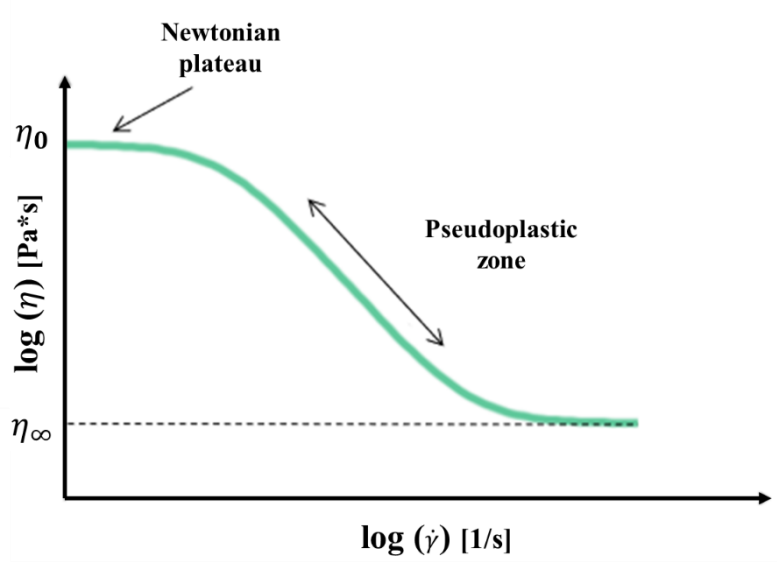

Figure 3.4: Shear viscosity behavior as a function of deformation rate for a pseudoplastic material

Three main zones can be identified: a Newtonian plateau at low strain rates, an intermediate pseudoplastic zone, and a second plateau at very high strain rates. The viscosity at strain rates close to zero is called zero shear viscosity (η_0).

At low strain rates, the processes of breaking and reforming intermolecular bonds are balanced. This keeps the number of entanglements between macromolecules, and therefore the material's viscosity, unchanged. As the strain rate increases, intermolecular bonds break faster than they form, reducing the number of entanglements. Therefore, in the pseudoplastic zone, viscosity decreases as the strain rate increases, and this trend can be modelled using the following power law:

$$log(\eta) = log(k) + (n-1)\log(\dot{\gamma}), \tag{13}$$

where n is called the pseudoplasticity index, generally ranging from 0.4 to 0.9, and k is called the consistency index, varying from 10^2 to 10^5 Pa depending on the material.

Finally, assuming that extremely high strain rates can be achieved, entanglements are completely eliminated. At this point, the macromolecules are unconstrained with respect to each other, thus they can align with each other and have greater freedom to flow. Viscosity therefore remains constant even at higher deformation rates and is called infinite shear viscosity (η_∞), which is generally several orders of magnitude lower than η_0 .

There are various ways to analyze the rheological properties of thermoplastic materials. One of them is the parallel plate rotational rheometer, which can be used in steady-shear or dynamic oscillation mode.

3.5.1 Steady-shear mode

In this mode, one of the two plates of the rheometer rotates at a constant rate while the other remains stationary. In this way, the sample, trapped between the two plates, is subjected to a continuous shearing flow ($\dot{\gamma} = cost$) (Fig. 3.5).

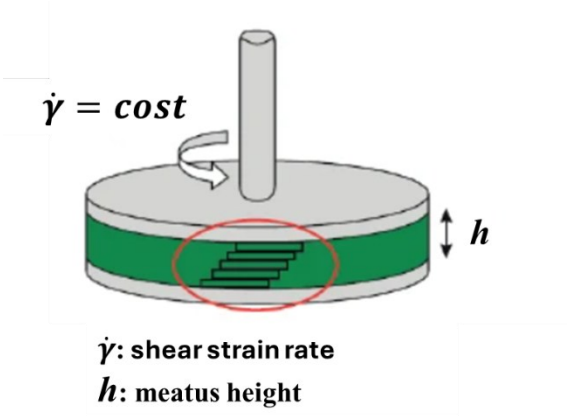

Figure 3.5: Parallel plate rotational rheometer: steady-shear mode

A transducer measures the torque M_t, thereby obtaining the shear stress τ as follows:

$$\tau = \frac{2M_t}{\pi R^3}, \tag{14}$$

where R is the radius of the sample.

This test can be performed by controlling the shear strain rate, as described above, or by controlling the shear stress. Regardless of the control mode, shear viscosity η can be determined through Eq.12.

Although this method of analysis is simple and fast, it has several limitations. For example, it does not provide information on the viscoelasticity of the material. Furthermore, excessively high shear rates induce high centrifugal force, causing the fluid to move away from the analysis area.

3.5.2 Dynamic oscillation mode

Typically, a parallel plate rheometer operating in dynamic oscillation mode at low shear strains is used to determine the viscoelastic properties of polymeric materials. In this test, the upper geometry no longer rotates in a continuous way but performs a sinusoidal oscillation. Molten material is placed between two plates, one of which oscillates with frequency ω and amplitude γ_0, imposing the following sinusoidal deformation on the material (Fig. 3.6):

$$\gamma(t) = \gamma_0 sin(\omega t), \tag{15}$$

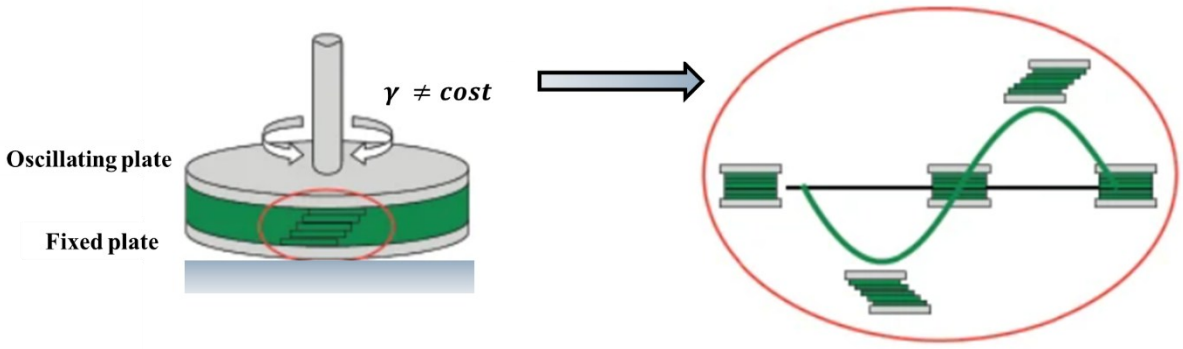

Figure 3.6: Parallel plate rotational rheometer: steady-shear mode

The shear stress τ is calculated through Eq.14, as described above for the steady-shear mode. A viscoelastic material is a material that exhibits a behavior that is intermediate between an ideal liquid (viscous) and an ideal solid (elastic). Due to the viscous component, the material's response in terms of stress will be out of phase with the imposed deformation by an amount δ. The shear stress obtained will therefore have the following trend:

$$\tau(t) = \tau_0 sin(\omega t + \delta), \tag{16}$$

which is graphically represented in Figure 3.7.

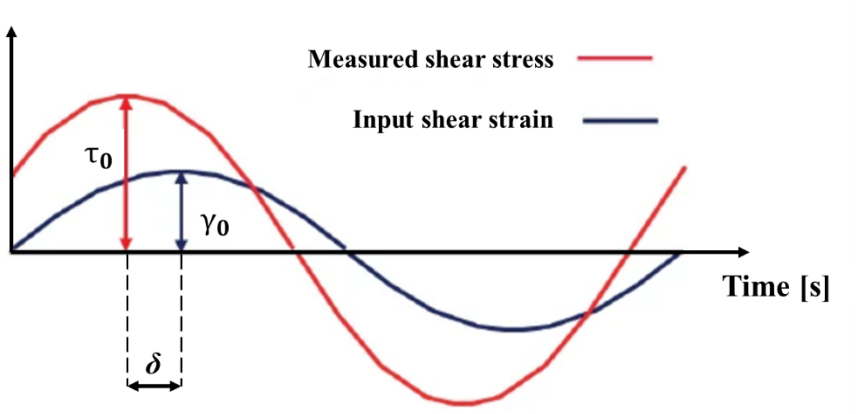

Figure 3.7: Input and output signal during a test in dynamic mode

At this point, two quantities related to viscoelastic behavior can be defined: the storage modulus G' and the loss modulus G''. The former is proportional to the elastic energy stored in the material, while G'' is proportional to the energy dissipated by viscous friction. Knowledge of G' and G'' allows one to understand whether the material's response is more elastic or viscous. If $G' > G''$, the material behaves more like an elastic solid, while if $G'' > G'$, the material behaves more like a fluid, with non-Newtonian viscous behavior. The moduli G' and G'' are defined according to the following formulae:

$$G'(\omega) = \frac{\tau_0}{\gamma_0} cos(\delta) \tag{17}$$

$$G''(\omega) = \frac{\tau_0}{\gamma_0} sin(\delta) \tag{18}$$

To determine the viscosity of the material, a complex modulus G^*must be defined:

$$G^* = \sqrt{(G')^2 + (G'')^2}\ . \tag{19}$$

From G^*, the complex viscosity η^* can therefore be defined as follows:

$$\eta^* = \frac{G^*(\omega)}{\omega} \tag{20}$$

η^* is not the shear viscosity derived from a flow subjected to shear, but it only has the same dimensions.

It is important that measurements of the viscoelastic characteristics (G' , G'') are carried out in the linear viscoelastic region (LVR) of the material. The LVR is typically determined by the *strain sweep test*, which measures the material's response to increasing strain amplitudes (γ) at a constant frequency (ω) and temperature. For example, by plotting (Fig. 3.8) the trend of the storage modulus (G') as γ varies, we can determine the LVR limit. This corresponds to the point at which G' is no longer constant but instead becomes dependent on deformation.

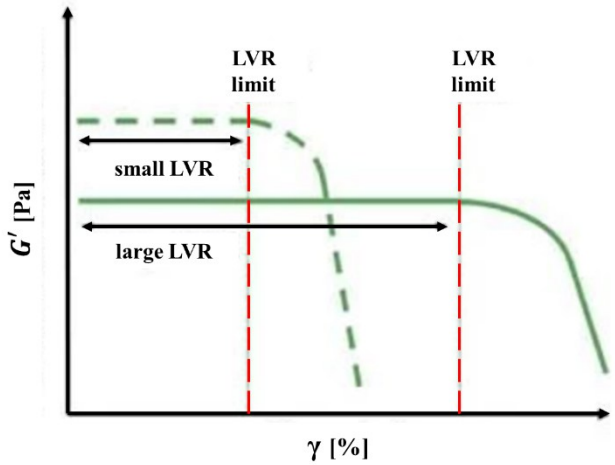

Figure 3.8: LVR region analysis from strain sweep test

If the material is in a linear viscoelastic regime, it is very common to assume the Cox-Merz rule, whereby:

$$\eta^*(\omega) = \eta(\dot{\gamma}) \, . \tag{19}$$

According to this, the relationship between η^* and ω is the same as that between η and $\dot{\gamma}$, and this is valid for most polymer fluids.

3.6 Morphological analysis

Morphological observations were carried out on the filaments, on the untested printed samples, and on their fracture surfaces.

The analysis of the latter is useful for analyzing any peculiarities of the material at failure and, in the case of 3D-printed continuous fiber-reinforced composites, it is used to evaluate the adhesion between the fiber and the matrix.

The quality and surface characteristics of the pre-print filaments are assessed by analyzing them from above, while the cross-section is analyzed to determine the actual diameter, any porosity or internal defects.

From the cross-sectional view of untested tensile specimens, the printing quality and the presence and spatial distribution of the voids can be assessed.

3.7 Methods and instruments

The following sections describe the methods used for the various analyses described above, the instruments involved, and the test conditions.

3.7.1 Tensile tests

Tensile tests were carried out at room temperature at a specific crosshead speed for each material being analyzed, using a universal testing machine (INSTRON 34TM-30, INSTRON, USA) with a 30 kN load cell. The tests were performed on rectangular samples with different raster angles, and at least three specimens were tested for each orientation. The dimensions and orientations of the samples will be specified in the individual chapters relating to each material. Digital Imaging Correlation or DIC (DANTEC DYNAMICS, Skovlunde, Denmark) was used to measure both longitudinal and transverse strain, as an average value over the analyzed area, in the samples oriented at 0° and ±45°. To ensure readability by the DIC cameras, the surface of the samples that were attached to the hot plate was painted with water-based ink. For 90° and 10° samples, a strain gage extensometer (INSTRON 2620 601, with 5 mm full scale) was used to assess the specimen deformation in the testing direction.

E_1, E_2, ν_{12} and E_{10} were estimated between 1000$\mu\varepsilon$ and 3000$\mu\varepsilon$, as described in ASTM D3039 and in the related shear method at 10°, whileG_{12} was calculated between 1500$\mu\varepsilon$ and 4000$\mu\varepsilon$, as reported in ASTM D3518. Yield strength values $\sigma_Y^{0^\circ}$, $\sigma_Y^{90^\circ}$, $\sigma_Y^{10^\circ}$ and τ_Y were evaluated as offset strengths, with the value of the offset strain being 10000$\mu\varepsilon$.

Ultimate tensile strain $\varepsilon_{ul}^{0^\circ}$, $\varepsilon_{ul}^{90^\circ}$ and $\varepsilon_{ul}^{10^\circ}$ should be evaluated at complete failure of the specimens. Similarly, the ultimate shear strain γ_{ul} was measured from the shear characterization with ASTM D3518.

3.7.2 Mass and dimensional measurements

Mass measurements were performed in all cases with a precision scale (AdventurerPro AV4102C, Pine Brook, NJ USA, with ± 0.01 g resolution). The cross-sectional area of the filaments was measured with a stereomicroscope (Leica MZ6, with Leica EC3 camera) and a caliper (± 0.01 mm resolution) was used to measure the dimensions of the samples and the precise length of the filaments (about 50 mm).

3.7.3 Thermal analysis

In this thesis DSC analyses were performed on a DSC 8000, Perkin Elmer Inc. (Waltham, Massachusetts, USA) equipped with IntraCooler II cooling device and Pyris software (Version 13.3, PerkinElmer Inc., Waltham, Massachusetts, USA) for instrument control, data acquisition and analysis. The instrument was calibrated for temperature and energy with high-purity indium and lead as standards. All tests were conducted in a nitrogen atmosphere with two thermal cycles at a heating/cooling rate of 10°C/min between 30 and 250 °C.
Measurements were carried out on 10-15 mg of material derived from filament before printing or from 3D printed samples.

Material properties from TGA analyses were obtained through TGA 4000 thermobalance Perkin Elmer Inc. (Waltham, Massachusetts, USA). Measurements were conducted on 5-10 mg of each material under nitrogen atmosphere (30 mL/min), from 30 to 900 °C at a heating rate of 10 °C/min.

3.7.4 Rheological tests

The ARES rheometer from Rheometric Scientific (New Castle, Delaware, USA) was used in this thesis for both dynamic oscillation and steady-shear mode. This rheometer has a smooth surface and a parallel plate configuration: plates with diameters of 25 mm and 50 mm were employed for dynamic oscillation and steady-shear analysis, respectively.

Tests in steady shear mode were performed at room temperature (28 °C), with approximately 1 mm thick analysis meatus and different shear rates ($\dot{\gamma}$) were explored:1, 3, 10 and 30 s^{-1}.

Three types of rheological experiments were carried out in dynamic oscillation mode: strain, frequency and time sweep, both performed at different temperatures.

In this thesis, for the *strain sweep test*, the frequency was set at 1 rad/s and the strain was evaluated between 1% and 10%, for each temperature and for all the material explored.

In the *frequency sweep test*, the response of the material in terms of complex viscosity was investigated as a function of frequency at constant strain and temperature. From this test, it is possible to evaluate the storage modulus (G'), the loss modulus (G'') and the complex viscosity through Eq. 20. In this work, frequency response was investigated between 0.1 and 100 rad/s, for all tests performed in this thesis.

The *time sweep test* is useful for evaluating the stability of the material over time and the potential for degradation by monitoring the trends of G^*, G' and G'' at a specific temperature over time. During the test, the material is held at a predefined temperature and subjected to constant strain and frequency.

Both the frequency and time sweep tests are performed with constant strain, which is taken inside the LVR as a result of the strain sweep test.

3.7.5 Optical analysis and preparative methods

Morphological observations were carried out with a stereomicroscope (Stereo WILD –DFC 420, Leica, Switzerland) and optical microscope (DMRM, Leica, Switzerland), both equipped with LAS software (Version 4.12, Leica. Switzerland) for data and image acquisition. In addition, a Scanning Electron Microscope (SEM) type Zeiss EVO MA 15 (Oberkochen, Germany) was also used. All SEM micrographs were collected at an accelerating voltage of 10 kV using secondary electrons. Energy Dispersive X-ray Spectroscopy (EDS) was also used to support the SEM analyses. The EDS system is a detector connected to the SEM. When the electron beam hits the sample, it emits characteristic X-rays, which allow us to identify which chemical elements are present and in what quantities.

The preparative procedure is the same for both the cross-section of the filaments and the untested samples. The material under consideration is first cut manually, then cold-embedded in a two-component epoxy resin (Struers S.A.S., Champigny sur Marne Cedex, France), before being lapped using a DAP-V polishing machine (Struers S.A.S., Champigny sur Marne Cedex,

France). Specimens were then prepared with wet sandpaper (240, 400, 800, 2400 and 4000 grit) and lapped until a very smooth surface was obtained. The surface was then dried in ambient air and finally observed.

4. 3D printing of polyamide 6 reinforced with short carbon fiber: characterization of virgin and recycled material

4.1 Introduction

Among the polymers commonly used in FDM 3D printing, polyamides stand out due to their relatively high mechanical and thermal properties, which make them suitable for semi-structural applications.

As described in Section 2.2, there are different types of polyamides. Among these, those used in 3D printing are PA6,6, PA6, PA11 and PA12. The latter is the most widely used in commercial filaments due to its lower hygroscopicity and greater ease of printing, despite having some of the lowest mechanical properties among all polyamides. PA11 is gaining ground mainly thanks to its biobased origin from castor oil. It is a material that offers good chemical and impact resistance, and its mechanical performance is comparable to that of PA12. PA6,6 is the polyamide with the best mechanical and thermal performance among those mentioned, but it is also the most hygroscopic. For these reasons, it is the most difficult to print. In fact, it requires a heated and closed chamber with very accurate temperature control for both the plate and the chamber. The filament must also be thoroughly dried. PA6 has slightly lower thermo-mechanical properties than PA6,6 but is easier to print. It is also highly sensitive to environmental humidity, so it must be dried before processing. In summary, PA6 offers better performance because it provides an optimal compromise between mechanical and thermal resistance, processability, and cost.

In addition, these thermoplastics generally exhibit favorable printability. Thanks to their low viscosity, they can also be readily combined with reinforcing fibers, such as glass, basalt or carbon. This further improves their mechanical performance and fields of application [86], [87].

Due to their enhanced properties, 3D printed fiber-reinforced polyamides have been widely use across multiple industrial sectors. However, with the increasing emphasis on eco-sustainability and circular economic principles, the issue of mechanical recycling has become particularly relevant. Material waste production is inherent to the FDM process, which can originate from the removal of support structures, purging operations, failed or defective prints, as well as from the disposal of end-of-life printed components. These wastes represent a potential secondary resource that could be reintegrated into the production cycle.

A promising strategy is to reuse this scrap material to create new 3D printing filaments. Since the original feedstock has already been formulated and optimized for extrusion-based additive manufacturing, reusing it can help preserve its desirable rheological and mechanical characteristics. Typically, the recycling pathway begins with a size reduction step, where the waste material is milled into smaller particles. This is followed by a thermal reprocessing stage in which the polymer is melted and extruded into filament form. The recycled filament can then be melted and deposited again during the actual printing process, thereby completing the recycling loop.

The number of studies addressing the mechanical recycling of reinforced polyamides for FDM is still limited. This can be partly attributed to the intrinsic challenges of the process, as highlighted by Mergulhao et al. [88]. In their work, a commercial carbon fiber-reinforced PA6, marketed as “Onyx” and specifically designed for 3D printing by Markforged (Waltham, MA, USA), was recycled. Although the material could be successfully milled and re-extruded into filament form, the subsequent print quality was inadequate, and the recycled filament exhibited reduced stiffness and strength compared to the virgin counterpart.

Contrasting results were obtained by Ding et al. [89] and Lohr et al. [90], who also focused on recycling Onyx. Ding et al. [89] produced recycled filament by thermally straightening a knitted 3D printed structure, thereby avoiding the milling step and improving printability. Remarkably, the tensile performance of the recycled prints surpassed that of parts produced from virgin filament, showing higher stiffness and strength. Similarly, Lohr et al. [90]reported enhanced bending properties after the first recycling step, although a decline was observed upon a second cycle. At the same time, in agreement with Mergulhao et al. [88], they found that the intrinsic filament properties deteriorated after the first recycling.

A larger number of recycling cycles was reported only for unreinforced PA12. Vidakis et al. [91] achieved six successive reprocessing steps, which is consistent with the higher thermal stability of PA12 compared to PA6 [92]. Interestingly, the mechanical performance of 3D printed specimens increased up to the fourth cycle, before undergoing a sharp decrease thereafter.

Recycling of reinforced PA12 was investigated by Bandinelli et al. [93] using a slightly different extrusion-based technology, Fused Granular Fabrication (FGF), which employs pellets instead of filament. A key aspect of this study was the assessment of anisotropy induced by the short carbon fibers composites properties [6]. While previous works [89],[90], [91] considered only

±45° raster orientations, Bandinelli et al. [93]manufactured tensile specimens with 0° raster orientation to assess longitudinal properties, and helically printed tubular specimens to measure transverse properties under axial tension. In line with other studies [89],[91], [90], the recycled material displayed superior stiffness and strength compared to virgin material, with the improvement being particularly pronounced in the transverse direction.

The aim of this chapter is to recycle a short carbon fiber reinforced PA 6 scrap, coming from industrial 3D printers, and to compare it with the virgin material. Onyx was selected for convenience as reference material, because it was specifically developed for industrial 3D printers and is common for ready-to-use parts. Tensile tests at 0°, 90° and ±45° are employed to characterize the anisotropic in-plane properties of the virgin and recycled materials. These results are supported by rheological and thermal characterization to achieve a better understanding of the effect of recycling on mechanical performance and printability. The main points of novelty of this chapter, in contrast with the studies present in literature, are the complete characterization of anisotropy in the mechanical properties for both virgin and recycled materials, and the proposed explanation for the unexpected differences in such properties between the virgin and the recycled material.

4.2 Materials and methods

4.2.1 Materials

The thermoplastic examined in this study is a commercial PA6 reinforced with 10 wt.% short carbon fibers, marketed under the name Onyx by Markforged (Waltham, MA, USA). Markforged 3D printers are designed to operate exclusively with proprietary materials and a fixed set of printing parameters. Among the few materials available, Onyx is one of the most widely utilized. Its mechanical properties are reported in the technical datasheet [94] and summarized in Table 4.1. In the following, the commercially obtained virgin Onyx will be denoted as “V,” while the recycled material will be referred to as “R.”

Table 4.1: Onyx mechanical properties from technical datasheet

Density [g/cm^3]	Young's modulus [GPa]	Yield stress [MPa]	Strain at break [mm/mm]	HDT [°C]	Impact strength [J/m]
1.2	2.4	40	0.25	145	330

4.2.2 Recycling process

Recycling process started from Onyx scraps supplied by Katakem (Catanzaro, Italy). These scraps consist of highly heterogeneous elements, such as supports and purge lines produced at the beginning of each print. They also include parts that are either unsuitable for their intended purpose or have been discarded due to printing failures. As previously mentioned, the processing parameters of Markforged printers cannot be adjusted by the user; therefore, Onyx always undergoes the same thermal history, regardless of the source. More specifically, the material is always printed with a 0.4 mm nozzle at 275 °C on an unheated Garolite build surface, with a suitable adhesive layer.

Larger scraps were first cut with a circular saw to obtain pieces of about 100 mm, suitable for grinding. The material was then shredded using a single-shaft machine equipped with three equally spaced blades. The resulting heterogeneous flakes were subsequently sieved with a 4 mm mesh to achieve a more uniform granulometry. Before re-processing, the sieved flakes were dried overnight at 85 °C.

Filament extrusion was carried out using a MicroEx 3D single-screw extruder (Eur.Ex.Ma., Varese, Italy), equipped with a 17.5 mm diameter screw and an L/D ratio of 22.5, operated at 40 RPM. The extruder included three heating zones, two along the barrel and one at the die, set at 215 °C, 240 °C and 220 °C, respectively. Cooling was provided by a forced-air system consisting of three fans. An in-line monitoring unit controlled the filament diameter before pulling and winding, keeping it at 1.75 mm with a dimensional tolerance of ±0.1 mm. Figure 4.1 schematically illustrates the recycling workflow leading to the production of the R filament from Onyx scraps. Only one recycling run is studied in this work, as already in the second recycling run the material viscosity appeared to be too low to allow extrusion within the required tolerance.

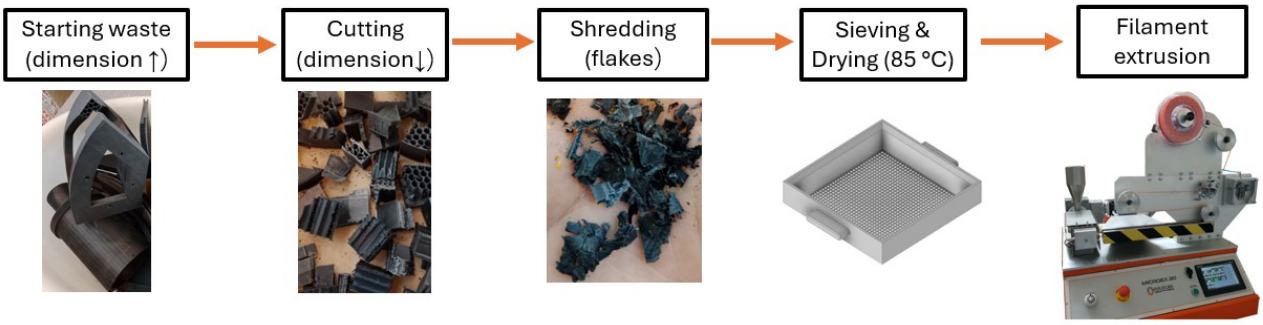

Figure 4.1: Onyx recycling workflow

4.2.3 3D printing parameters

To ensure consistent quality and printing reliability, Markforged printers restrict the use of non-proprietary materials and limit the possibility of modifying printing parameters. For this purpose, each print job begins with a material verification routine. As the R material has undergone milling and two heating cycles, it may differ sufficiently from the virgin (V) filament that either the printing quality cannot be guaranteed, or the initial control routine prevents the job from starting. In addition, Markforged printers enforce a fixed ±45° raster angle for 100% infill parts, making it impossible to characterize Onyx in both the longitudinal and transverse directions. For these reasons, a different printer had to be employed for both materials, using identical printing parameters, to allow a complete characterization without processing-related bias.

In this work, the selected printer was an Anet A8 Plus (Anet Technology Co., Shenzhen, Guangdong, China), equipped with a 0.6 mm nozzle. To ensure stable conditions and reliable specimen fabrication, the printer was housed inside a custom-built enclosure. Printing was managed using Ultimaker Cura software, version 5.6.0, and the main parameters used for the fabrication of rheological and mechanical specimens are summarized in Table 4.2. Adhesion to the glass build plate was enhanced with an adhesive supplied by Thought 3D (Qormi, Malta), while an 8-line brim was applied through the slicer settings. Prior to printing, both V and R filaments were dried at 85 °C for 24 hours, and during printing, the spools were stored in a passive dry box (Markforged, Waltham, Massachusetts, USA) containing silica salts.

Table 4.2: V and R printing parameters

Parameter [unit]	**Value**
First layer height [mm]	0.2
Layer height [mm]	0.3
Line width [mm]	0.4
External shells	0
Top and Bottom layers	0
Infill [%]	100
Infill pattern - Rheology	Concentric
Infill pattern - Tensile	Unidirectional
Infill raster angle - Tensile	0°, 90°, $[\pm 45°]_{2s}$
Printing speed [mm/s]	30
Extrusion temperature [°C]	250
Plate temperature [°C]	70

4.2.4 Material characterization

Voids measurements

Porosity is calculated according to Eq.10, as reported in Section 3.3. Before testing, the density of the rheological and tensile specimens (ρ_x^s) was measured. The material, whether virgin or recycled, is indicated by x. The reference density of the filament (ρ^f) was assumed to be the same for both materials, equal to 1.2 g/cm^3, in agreement with the material datasheet.

Tensile characterization

Tensile tests were carried out for both materials in accordance with the procedures detailed in Section 3.7.1 and in line with the ASTM D3039 and ASTM D3518 standards, in order to achieve a comprehensive characterization of the in-plane properties [79], [80]. The first one is used to measure longitudinal and transverse properties, by printing specimens at 0° and 90° raster angle. The second standard is used for measuring the shear stress-strain response and properties through specimens printed with ±45° raster angle. As reported in Section 3.2.1, S_{LT} is obtained through Eq.9 by setting σ_x equals to $\sigma_Y^{45^\circ}$, which is twice τ_Y.

For both cases, the samples are rectangular in shape, 110 mm long, 15 mm wide and 2.3 mm thick. The tests were performed on three samples per raster angle (0°, 90°, ±45°), for a total of

nine samples per material. For all specimens, Digital Imaging Correlation (DIC) was used to measure both longitudinal and transverse strain, as an average value over the analyzed area.

Finally, after characterizing the materials, the anisotropy of the in-plane stiffness properties was evaluated for both virgin and recycled materials, as proposed in Section 3.2.1.

Microscopy analysis

Fracture surfaces and morphological observations of the longitudinal and transverse cross sections of untested tensile specimens were analyzed to evaluate the printing quality and the presence and spatial distribution of the voids. The transversal polished cross section is obtained from the 0° sample, while the longitudinal cross section is taken from the 90° sample.

The samples were embedded and prepared before being analyzed under a stereomicroscope. Section 3.7.5 outlines the equipment specifications and preparation procedure.

Rheological tests

Rheological characterization was performed in dynamic oscillation and strain-controlled mode, both for V and R materials. The specimens are in the shape of a disc, 25 mm in diameter and 2 mm thick. Prior to testing, a void content of less than 10% was verified so that the accuracy of the measurements was ensured.

Three types of rheological experiments were done: strain, frequency and time sweeps, all performed at two different temperatures, i.e., 200 and 215 °C. Rheological analysis techniques and the instrumentation used are reported in detail in Section 3.7.4.

Thermal analysis

Both virgin and recycled Onyx were analyzed through DSC and TGA analysis. The latter was performed to evaluate the fiber mass fraction. DSC was used to determine the crystalline fraction (χ_c) and characteristic temperatures, such as the glass transition temperature T_g and the melting temperature T_m. Equation 11 was used to calculate the crystalline fraction, setting ΔH_{m0} equal to 230 J/g [95]. An isothermal DSC analysis was also performed on V and R materials. Both tests were carried in nitrogen atmosphere. The samples were heated up quickly (about 1 minute) to 200 °C and the temperature was subsequently maintained for 30 minutes.

Measurements were carried out on 10-15 mg of material derived from 3D printed samples, and three analyses were performed for both V and R materials. By doing so, it is possible to examine the material in its post-printing state, that is, in the same conditions at which it will be mechanically tested. The instrumentation and procedure for thermal analysis are detailed in Section 3.7.3.

4.3 Results and discussion

4.3.1 Thermal characterization results

Based on TGA analysis, the material exhibits a residual mass of 14.3 ± 2.1 % at 900 °C (Fig. 4.2), with the major weight decrease occurring between 380 and 450 °C. The remaining mass is attributed to the presence of carbon fibers, in good accordance with both the manufacturer's specifications and previously reported data in the literature[96]. A slight mass loss (<5%) is also observed in the 80–150 °C interval, which can be ascribed to the evaporation of absorbed moisture.

After the recycling process, no changes were made to the composition of the material (e.g., blend). For ease of visualization, only the curve for the virgin material is shown in Fig. 4.2, because the curves obtained from TGA for virgin and recycled Onyx are identical.

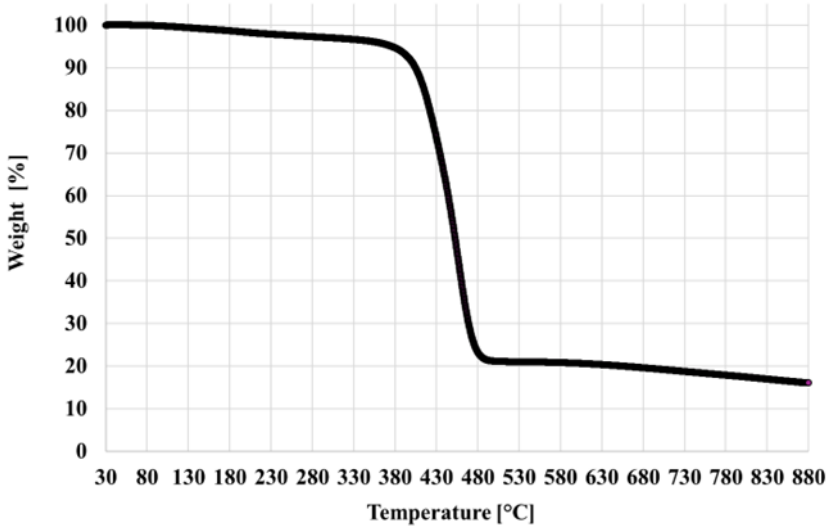

Figure 4.2: Representative TGA plot for V

Representative DSC curves for both V and R are shown in Figure 4.3. The areas under the cooling and melting peaks are consistently larger for V compared to R, suggesting a higher crystalline fraction in the former. In the first heating cycle (Fig. 4.3a), both materials exhibit two peaks: the first appears around 120 °C for R and at approximately 140 °C for V, attributable to low-order crystalline fractions generated by rapid cooling and subsequent ageing. The main melting peak occurs between 190 °C and 210 °C for both materials, although for R it is slightly shifted toward higher temperatures. This tendency is also evident in the cooling curves (Fig. 4.3b), where the crystallization peak of R is clearly displaced to higher temperatures compared to V. Moreover, the peak shapes are distinct: R is characterized by a wider and lower peak, while V exhibits a sharper and higher one. This phenomenon is most likely linked to degradation phenomena occurring during recycling, which lead to a broader molecular weight distribution. The presence of shorter polymer chains increases molecular mobility[97], [98], thus enhancing the crystallization kinetics of R. As a result, crystallization in R starts earlier and proceeds over a broader temperature interval. Similar effects of recycling-induced degradation on this material have also been documented in [99].

During the second heating cycle (Fig. 4.3c), the secondary peaks at lower temperatures are no longer observed, and the most notable difference lies in the morphology of the main melting peaks. The V sample shows two distinct cusps, associated with the α- and γ- crystalline phases of polyamides[99], [100], [101], whereas the R sample presents only a single cusp, positioned close to the second cusp of V. In addition to the disappearance of the secondary peaks, comparison of the first and second heating reveals a decrease in the intensity of the main melting peak, which is more pronounced for V. Meanwhile, the peak profile of R remains substantially unchanged.

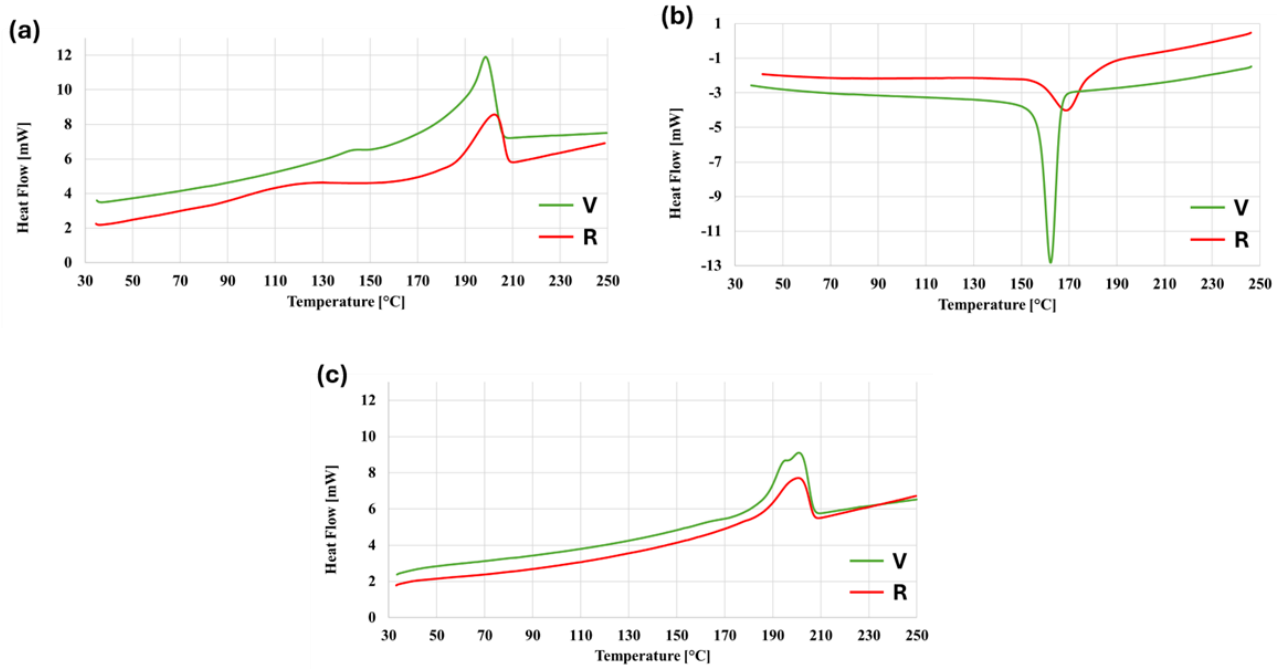

Figure 4.3: DSC thermograms of V and R, for a) first heating, b) cooling and c) second heating

The characteristic temperatures and crystalline fractions obtained from DSC analysis are reported in Tab. 4.3 for both materials, quantitatively confirming the qualitative trends shown in Fig. 4.3. The melting temperatures in the two heating cycles are identical, whereas the crystallization peaks differ by approximately 7 °C. Overall, V exhibits a slightly higher crystalline fraction compared to R. When comparing the first and second heating cycles, the crystallinity of R remains constant (around 16%), while in V a small decrease is observed (from 22% to 19%). This slight reduction can be attributed to the filament manufacturing process, where cooling and stretching occur immediately after extrusion.

Table 4.3: Thermal characterization from DSC

	V			R	
DSC phases	Peak Temp. [°C]		χ_c [%]	Peak Temp. [°C]	χ_c [%]
1° Heating	199.9 (1.5)		22.4 (1.8)	201.0 (1.0)	16.3 (0.3)
Cooling	162.6 (0.4)		21.2 (1.8)	169.5 (0.3)	15.5 (2.2)
2° Heating	194.8 (0.2)	201.0 (0.6)	19.0 (0.2)	199.6 (0.8)	16.4 (0.8)

4.3.2 Rheological results

The strain sweep tests ensured that a strain of 1% was sufficient for remaining within the LVR and this value was used for performing all the other rheological measurements. Fig. 4.4 shows the curves obtained from the frequency sweep tests, at 200 °C and 215 °C. For both materials, the trend of complex viscosity η^* is given as a function of frequency ω. At low frequencies, part of the Newtonian plateau can be seen, except for R at 215 °C. The η^* curve for R lies below that for V at both temperatures. This drop in viscosity is related to the decrease in molecular weight due to material degradation, which confirms the DSC observations [100], [102], [103].

This is consistent with the work of Ding et al. [89], who performed a quantitative analysis of matrix degradation using Gel Permeation Chromatography (GPC). In the GPC experiment, molecules are separated according to their respective molecular weight. The smaller the molecule, the longer it stays in the column, so small molecules are eluted from the column later. The authors found that the elution time of PA6 in virgin Onyx was shorter than in recycled Onyx. This suggests that the thermal processes that are involved as a consequence of the recycling process result in the pyrolysis of the PA6 matrix's molecular chain, producing shorter molecules. This is related to degradation of the PA6 matrix. At the same time, shorter molecular chains mean that the resin has better fluidity and lower melt viscosity.

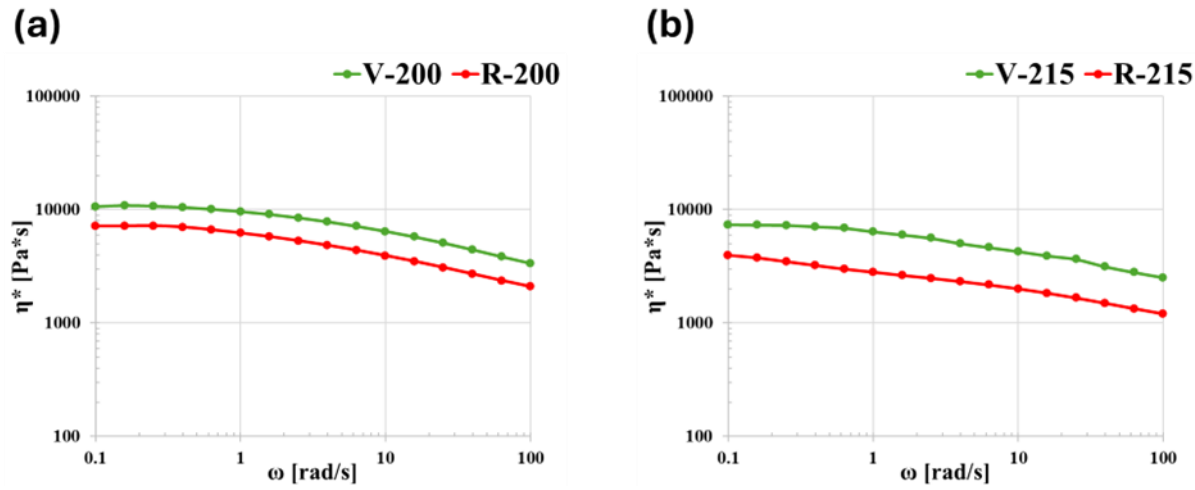

Figure 4.4: Complex viscosity as a function of frequency for V and R at a) 200 °C and b) 215 °C

The degradation of R is also evident from the plots of G' and G'' versus ω, when compared to those of V (Fig. 4.5). As the trends are similar at both temperatures, only the curves at 200 °C are shown. For R, the slopes of the curves indicate that the crossover point between G' and G'' occurs at higher frequencies, reflecting a reduction in the relaxation time of the polymer chains (i.e., the chains relax more rapidly), which further confirms the degradation of R. Across the entire analyzed frequency range, both materials exhibit fluid-like behavior ($G'' > G'$), with both moduli increasing as frequency rises.

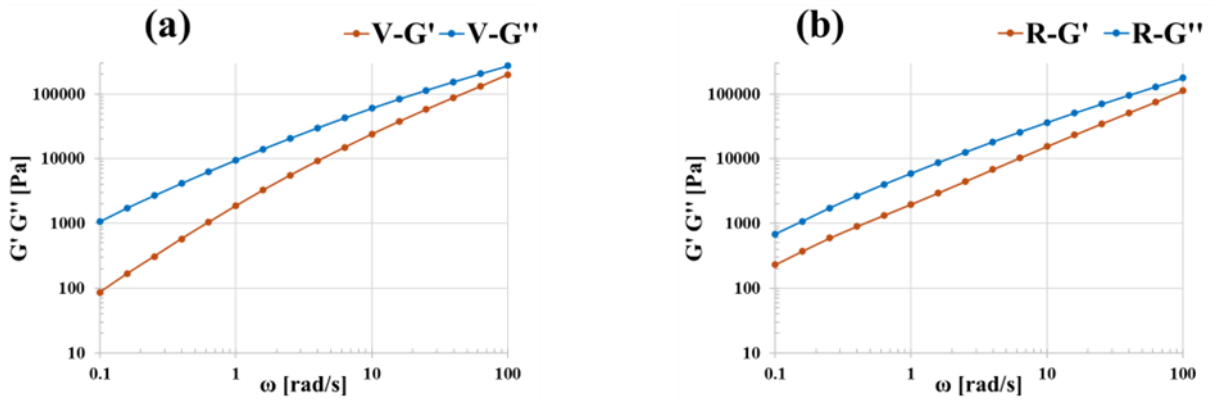

Figure 4.5: G′ and G′′ as a function of ω at 200 °C for a) V and b) for R

The thermal stability of the materials was assessed using a time sweep test at a frequency of 1 rad/s over a total duration of 900 seconds. Fig. 4.6 illustrates the evolution of G^* throughout the test. For both materials, the curves at 215 °C lie below those at 200 °C. In the case of V, the G^* curve at 200 °C shows a slight increase, whereas at 215 °C the material becomes unstable after approximately 600 seconds (Fig. 4.6a). For R, stability at 215 °C is maintained for about 400 seconds (Fig. 4.6b), while at 200 °C $G*$ rises sharply.

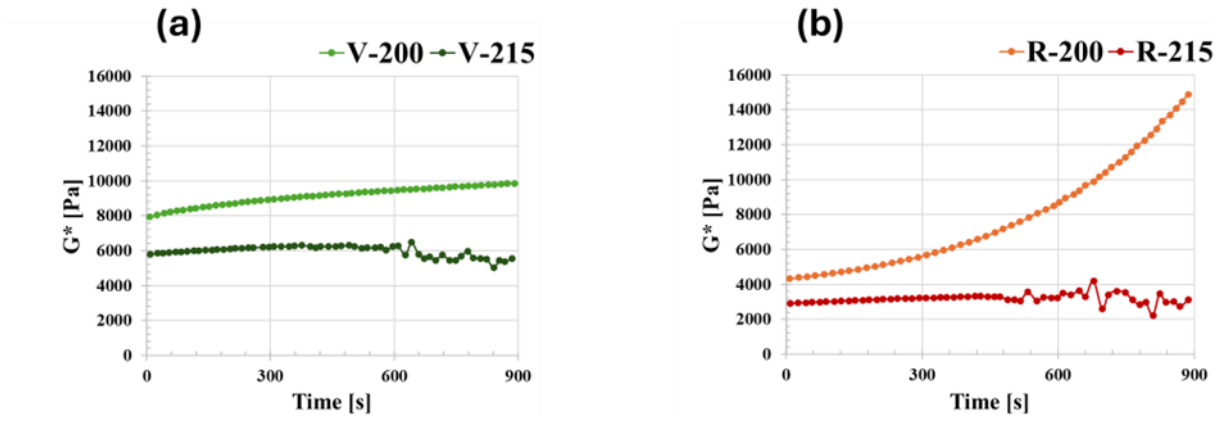

*Figure 4.6: G*as a function of time at 200 °C and 215 °C for a) V and b) R*

To further investigate this trend, the time-dependent behavior of G' and G'' at 200 °C was analyzed for both materials (Fig. 4.7). For V, the material remains stable throughout the test period (Fig. 4.7a), with G' remaining essentially constant and G'' showing only a slight increase. In contrast, both G' and G'' of R increase over time (Fig. 4.7b), with the slope of G' being considerably steeper than that of G''. This suggests that the pronounced rise in G^* observed in Figure 4.6 is primarily due to an increase in the storage modulus, consistent with an increase in solid-state behavior for R

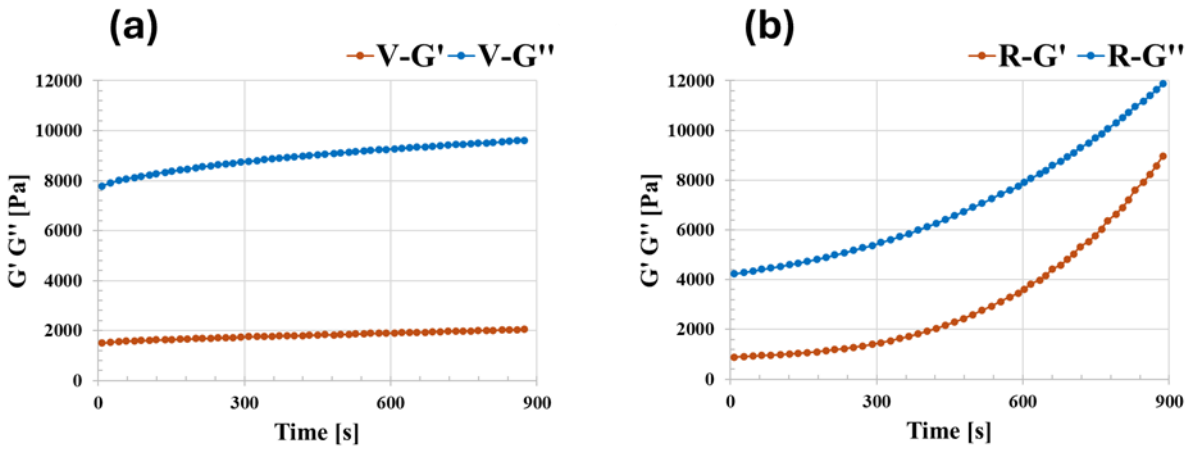

Figure 4.7: G' and G'' as a function of time at 200 °C for a) V and b) R

In order to explain this behavior, the isothermal DSC scan at 200°C was performed on both materials (Fig. 4.8). It can be seen that in the same time frame as observed in Fig. 4.6 the R material undergoes an endothermic transformation, which is not compatible with crystallization. As a consequence, the sharp increase in the G^* curve at 200°C is most probably due to a degradation process, which induces cross-linking of the material. Indeed, polyamides degradation is quite a complex phenomenon [104], [105], which may evolve either towards chain scission or towards branching and cross-linking, depending on various environmental factors [106], [107]. In particular, it has been found that at relatively lower temperatures degradation is mostly by cross-linking, while at higher temperatures chain scission seems to be the main result [107]. Notice anyway that degradation occurs mostly on the R material, rather than V, due to the higher presence of $-NH_2$ chain ends in R, consequence of its first degradation occurring during previous recycling. The presence of these chain ends is the key intermediate step that leads to branching and subsequent cross-linking of the polymer chains according to [108], [109].

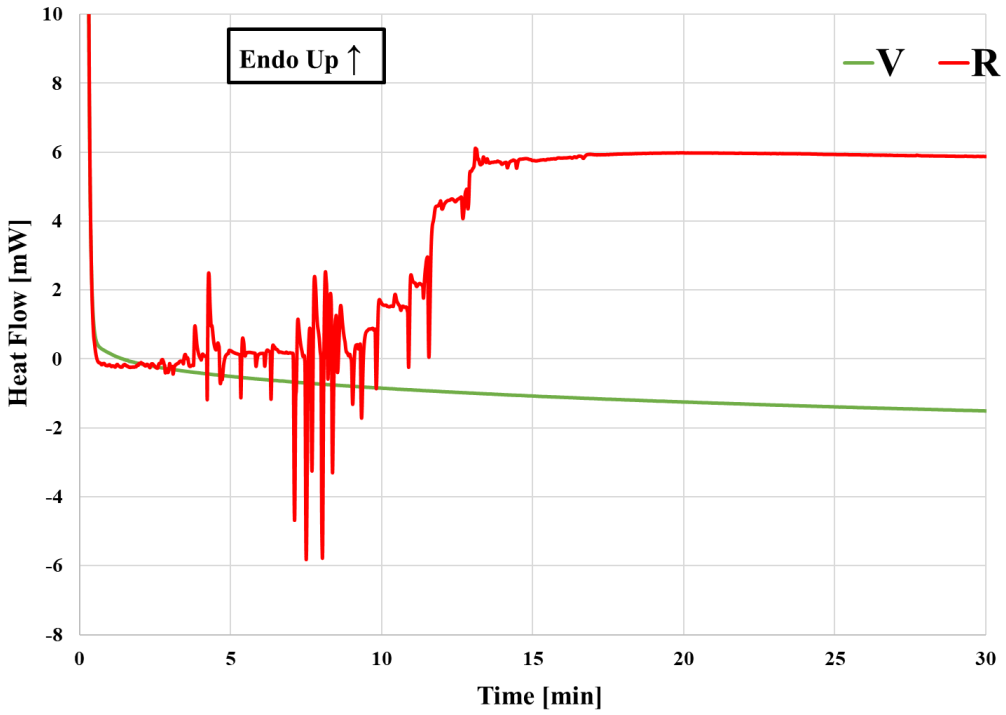

Figure 4.8: Isothermal DSC thermograms of V and R materials

4.3.3 Voids and stereomicroscope analysis

The void content was determined using Eq. 10 (Section 3.3.), with the corresponding values reported in Tab. 4.4. The results are presented as a function of the raster angle of the specimens, given that this parameter often influences void formation [72]. In the present study, however, the void content remains around 5% for all samples, except for V at 0°. All measurements show low standard deviations, reflecting good printing quality and process reproducibility. The slight reduction in void content for R is likely related to its lower viscosity, which facilitates the filling of voids during printing.

Table 4.4: Voids percentage, values in parenthesis represent standard deviation

Material	V			R		
Raster angle	0°	90°	±45°	0°	90°	±45°
v [%]	6.7 (0.9)	5.0 (0.9)	5.8 (0.8)	4.6 (0.8)	4.3 (0.4)	4.7 (0.2)

The polished transversal cross sections observed at the stereomicroscope are shown in Fig. 4.9 for the V (Fig. 4.9a) and R (Fig. 4.9b) materials. The presence and spatial distribution of porosities are visualized clearly. In both cases, a homogeneous distribution of roughly triangle shaped voids is observed in the contact areas between subsequent deposited lines, which is typical for material extrusion-based 3D printing. The voids of V (Fig.4.9a) are larger than those seen for R (Fig.4.9b). In addition, the typical elliptical shape can be observed for V (Fig. 4.9a), while R (Fig. 4.9b) shows a more compact and squared shape. As a consequence, R seems to better fill the available room, spreading more evenly.

Interestingly, each deposited line of both materials is characterized by about the same height, which is reasonable as this is one of the superimposed processing parameters. The main differences between V and R are related to the general shape and the size of the line base (B), which can be inferred from the straight line connecting two adjacent voids (Fig. 4.9). At least 20 line bases were observed at the microscope, and a base length equal to 0.47 ± 0.05 mm was measured for V while 0.59 ± 0.03 mm was obtained for R. These observations are generally consistent with the void percentages reported in Tab. 4.4.

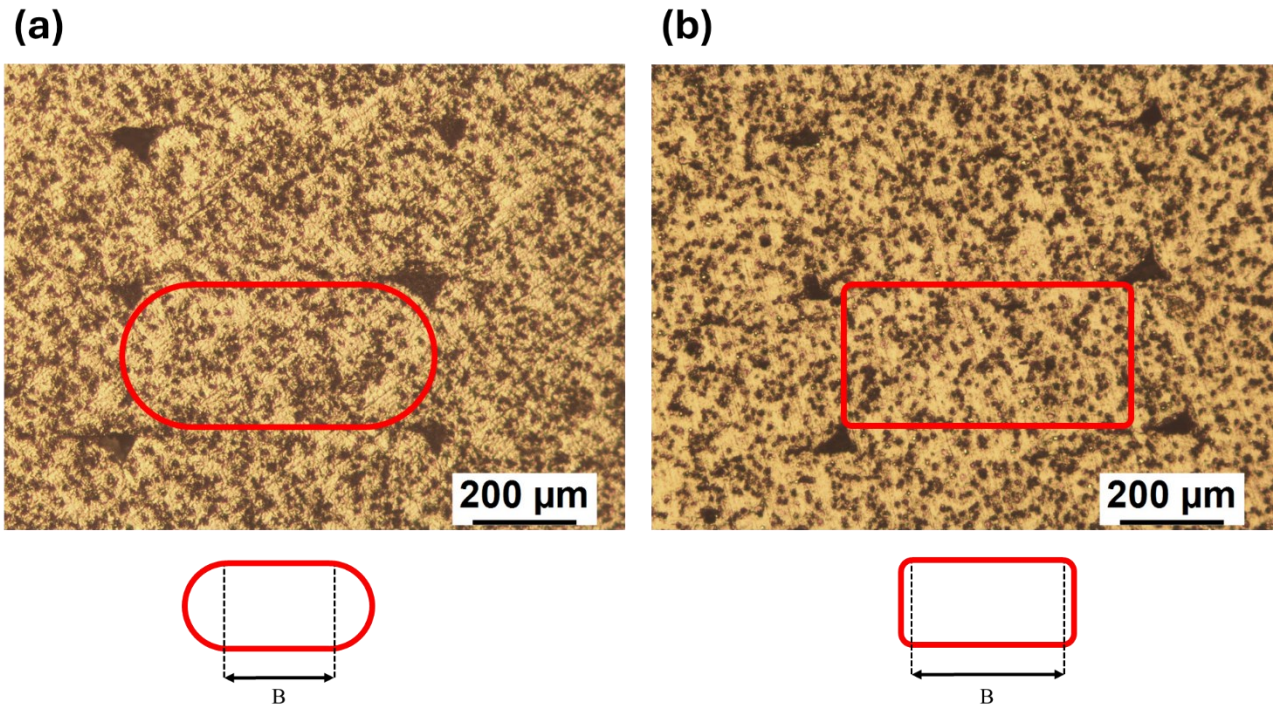

Figure 4.9: Representative transversal cross sections for a) V and b) R, where B is the base of the deposited line

Additional information can be obtained from the polished cross sections of 90° samples of both materials (Fig. 4.10), examined at the side edge. In the case of V (Fig. 4.10a) the adjacent layers are characterized by a rounded end, while the R material (Fig. 4.10b) has a squared shape. Furthermore, it can be seen that the layers of V are self-supporting (Fig. 4.10a), while those of R tend to lean downward (Fig. 4.10b). This behavior is in line with the lower viscosity of R found in the rheological analyses (Fig.4.4).

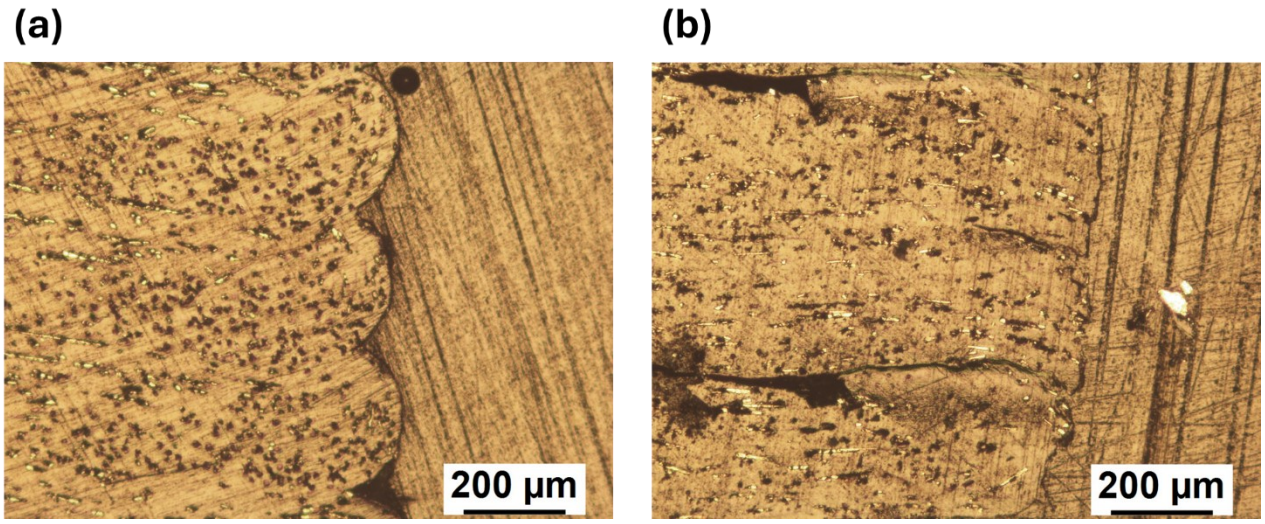

Figure 4.10: Representative cross section of 90° samples for a) V and b) R

4.3.4 Mechanical characterization

Representative stress–strain curves, for V and R, are compared in Fig. 4.11a for the longitudinal and transverse directions, and in Fig. 4.11b for shear properties. Both materials exhibit elasto-plastic behavior in all orientations. As expected, longitudinal properties are higher than transverse ones for both materials. The longitudinal curves of V and R coincide in the initial linear elastic region (Fig. 4.11a). The 90° curve of R shows a steeper initial slope compared to V, indicating greater transverse stiffness (Fig. 4.11a). A moderate increase in yield strength is also observed for R, although it is less pronounced than the stiffness enhancement. A similar trend is seen in Fig. 4.11b, where R displays superior shear properties relative to V, in terms of both stiffness and yield strength. The most notable difference is that R is significantly more brittle than V. This embrittlement is clearly associated with degradation caused by the recycling process, as discussed in Sections 4.3.1 and 4.3.2. It is particularly evident in transverse and

shear specimens, where the matrix contribution to the composite's mechanical performance is more significant.

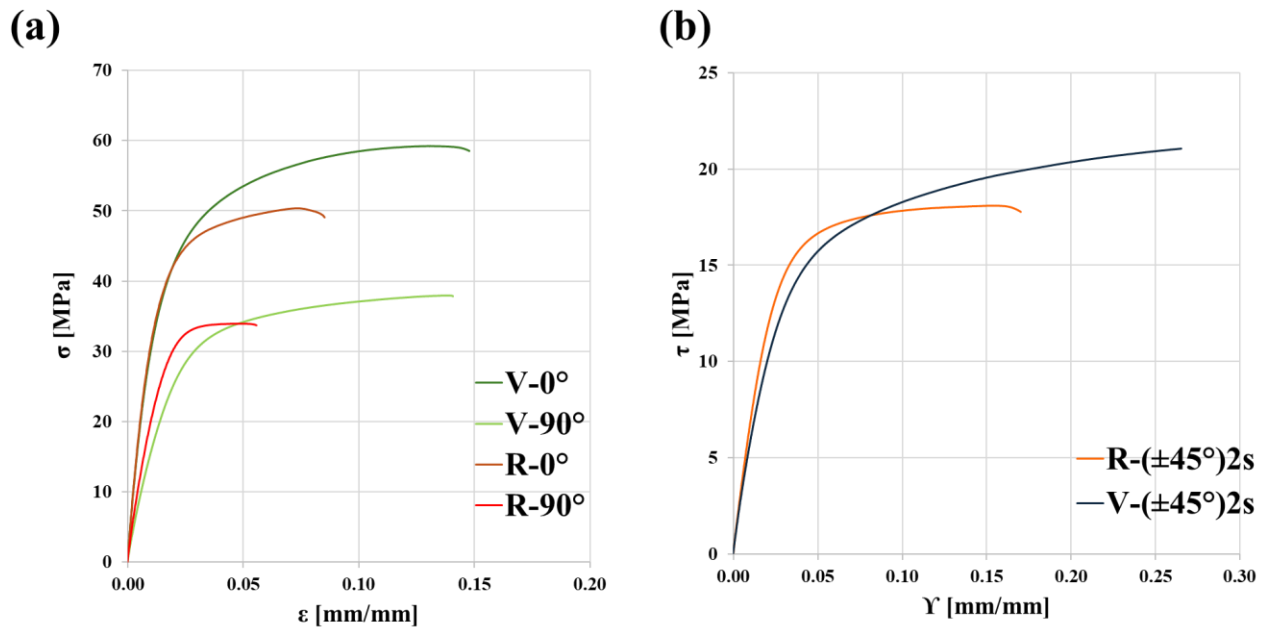

Figure 4.11: Comparison of representative curves of V and R for a) longitudinal and transverse characterization and b) shear characterization

The notable reduction in strain at break is quantitatively confirmed by the values reported in Tab. 4.5, which summarize the results from longitudinal, transverse, and shear testing.

Once S_L (=$\sigma_Y^{0^\circ}$) and S_T (=$\sigma_Y^{90^\circ}$) are known from the longitudinal and transverse samples, the Tsai-Hill criterion is used to calculate S_{LT}. Its values are 5.18(0.28) MPa and 7.11(0.69) MPa, respectively for virgin and recycled material. From examination of the fracture surface (Fig.4.12), it is clear that there was no delamination of the layers for either material. Therefore, the use of this criterion is correct, as described in Section 3.2.2.

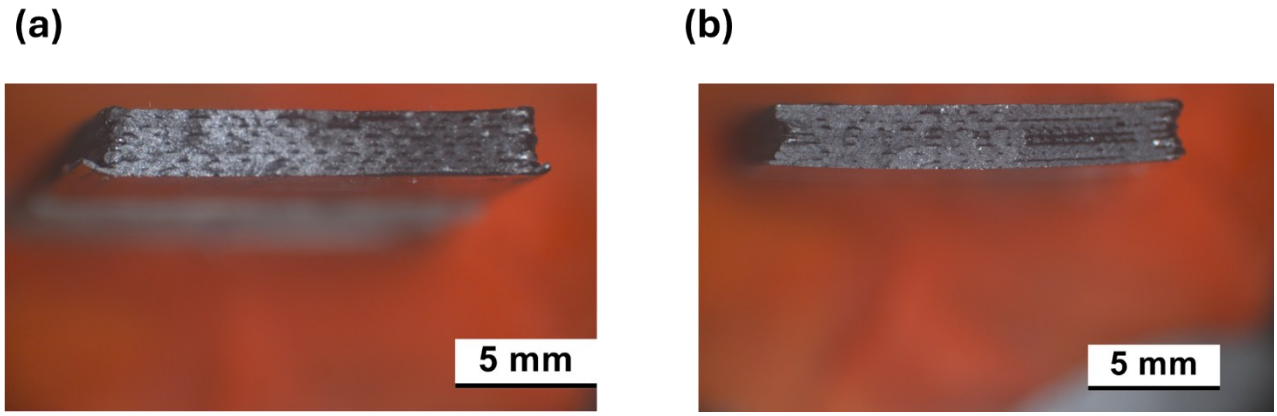

Figure 4.12:Fracture surface of ±45° samples for a) V and b) R

Regarding stiffness, E_1 remains unchanged between V and R, as the fibers predominantly govern the composite's mechanical response in the longitudinal direction. By contrast, at 90° and ±45° orientations the matrix plays a larger role: E_2 and G_{12} increase by 40% and 25% , respectively, from V to R. A similar trend is observed for yield strength. Overall, these results indicate that R generally exhibits higher mechanical properties than V.

The recycling process has an impact on mechanical and rheological properties. The main factors are the degradation of the thermoplastic matrix and the reduction in fiber length. The main effect is indeed due to matrix degradation in terms of molecular weight decrease, rather than shortening of the reinforcement fibers. The main reason is as follows. In the longitudinal direction, both E_1 and $\sigma_Y^{0^\circ}$ remained unchanged for recycled Onyx, but the material became more brittle, with lower deformation at break ($\varepsilon_{ul}^{0^\circ}$). Therefore, it is reasonable to assume that the main difference with respect to the virgin material is that the thermoplastic matrix has degraded as a result of the recycling process, while the fibers have not been affected in a significant way. The significantly lower values of both $\varepsilon_{ul}^{90^\circ}$ and γ_{ul} for recycled Onyx confirm the greater role of matrix degradation than that of reinforcement fibers. For fiber shortening to produce a very significant effect, fiber length should have been reduced below the critical length, and this would have had consequences on the longitudinal properties of stiffness and strength, which seem to remain unchanged.

Table 4.5:Stiffness, yield strength and ultimate strain results from tensile tests, values in parentheses represent standard deviation

Mechanical property	V	R
$E_1[\mathrm{GPa}]$	3.68 (0.06)	3.83 (0.06)
$E_2[\mathrm{GPa}]$	1.64 (0.15)	2.27 (0.03)
ν_{12}	0.40 (0.02)	0.33 (0.03)
$G_{12}[\mathrm{GPa}]$	0.60 (0.04)	0.74 (0.04)
$\sigma_Y^{0^\circ}[\mathrm{MPa}]$	43.70 (0.45)	42.72 (1.12)
$\sigma_Y^{90^\circ}[\mathrm{MPa}]$	27.56 (1.79)	32.21 (0.94)
$\tau_Y\ [\mathrm{MPa}]$	12.62 (0.48)	15.19 (0.76)
$\varepsilon_{ul}^{0^\circ}[mm/mm]$	0.14 (0.02)	0.09 (0.02)
$\varepsilon_{ul}^{90^\circ}[mm/mm]$	0.15 (0.02)	0.05 (0.01)
$\gamma_{ul}\ [mm/mm]$	0.29 (0.05)	0.16 (0.02)

This behaviour is well documented in scientific literature and has been reported in many papers [89], [90], [91], [93]. The most striking feature is that the recycled material in filament form is often weaker than virgin material [88], [90], due to the partial degradation of the recycled material. Nevertheless, the mechanical properties of the recycled material exceed those of the virgin material when it is printed. This phenomenon was first observed by Ding et al.[89], who attributed it to improved impregnation of the carbon fibres by the PA matrix. Lohr et al.[90] and Vidakis et al.[91] noticed the same behavior and justified it based on a plasticization-like effect, while Bandinelli et al.[93] ascribed it to better wettability and a reduction in voids. Interestingly, the last paper shows that this effect is more pronounced in tubular specimens (i.e. in the transverse direction) than in the longitudinal direction. This is exactly what was found in the present study. This suggests that this effect must be explained in terms of matrix mechanical behavior.

In fact, void content alone cannot explain the observed phenomenon. The main void percentage reduction when going from V to R (about 35%) occurs in the longitudinal direction, where fiber mechanical behavior is dominant. Therefore, the reason for the increase in transverse and shear properties from V to R must be sought elsewhere. Matrix crystallinity may be a suitable explanation because lower molecular weight generally induces higher crystallinity for kinetic reasons. However, this hypothesis is also not convincing since, in the present case,

the crystallinity percentage is low and similar for V and R (Table 4.3), even though more rapid crystallization kinetics were also observed here.

The most likely explanation is shown in Fig. 4.13, which illustrates the transverse cross sections of V (Fig. 4.13a) and R (Fig. 4.13b). Low molecular weight results in lower viscosity (see Fig. 4.4a and Fig. 4.4b), and with the same printing parameters, the R material is more fluid. Consequently, the deposited 3D-printed lines spread better on the previously deposited material. This is consistent with observations from stereomicroscope surface analysis (Fig. 4.9 and 4.10), which show that R is more compact and has larger contact surfaces. This can be seen in both the interlayer areas (i.e. between one layer and the next, the red areas in Fig. 4.13) and the intralayer areas (i.e. between one deposited line and the next, the green areas in Fig. 4.13).

Furthermore, when new molten material is extruded, it encounters the material that has already been deposited, in both the adjacent lines and on the previous layer. This material then undergoes a temperature increase, leading to partial remelting [110]. Molecular diffusion then occurs in this state, and once cooled, welding is achieved. The strength of both the interlayer and the intralayer adhesion are closely related to weld strength [111], [112], which in turn is closely related to molecular diffusion at the interface [113], [114], [115]. This is enhanced by the lower molecular weight of R, which favours self-diffusivity.

In fact, it is well known from the literature that the chain self-diffusion coefficient in an entangled polymer melt generally increases with the decrease of molecular weight. This is a fundamental result of reptation theory, which predicts that self-diffusion is inversely proportional to the square of the average molecular weight [116], [117]. Recent studies tackled this issue from an experimental [118], [119] and numerical point of view [120], [121], [122], and a dependence with slightly different exponent is normally found, yet it is well understood that polymer chains of low molecular weight self-diffuse faster. Moreover, self-diffusivity is also enhanced by the mainly amorphous nature of the matrix material, as crystallinity does not exceed 20%, thus making it more prone to the diffusion of smaller molecules.

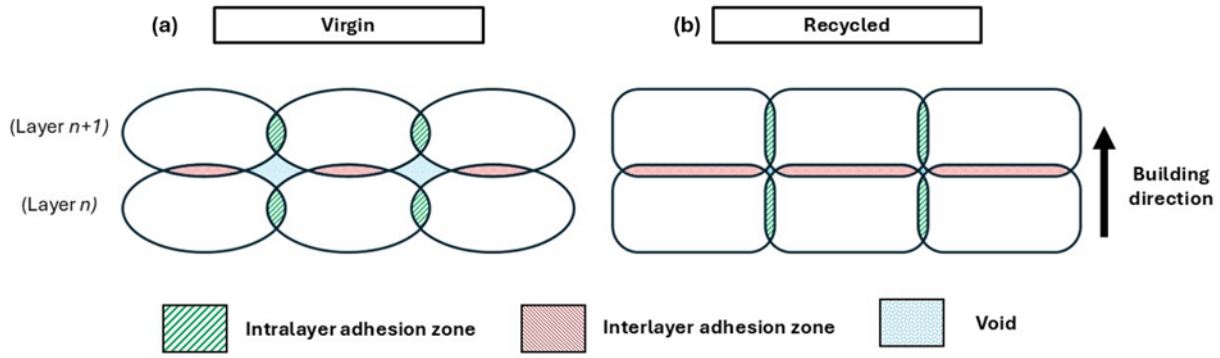

Figure 4.13: Adhesion zones and voids distribution in a) V and b) R FDM cross section

The behavior described so far is confirmed by the fracture surface obtained from the samples at 90° (Fig.4.14). In the case of V (Fig. 4.14a), a ductile fracture can be observed, and the successive layers are clearly visible. In contrast, R (Fig. 4.14b) exhibits a brittle fracture, with a more compact section and layering that is less distinct than in V.

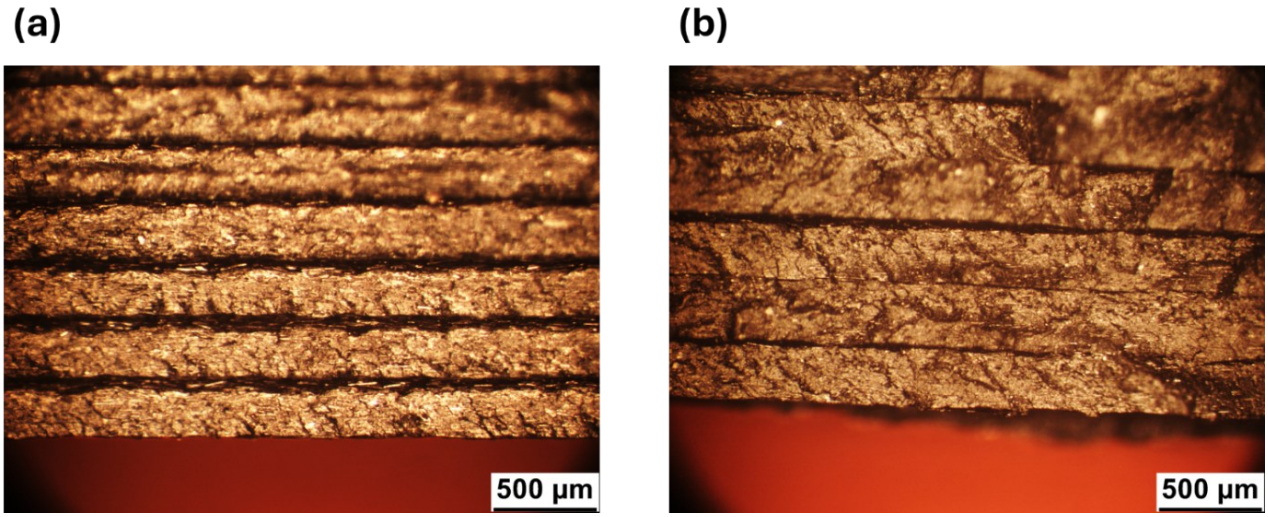

Figure 4.14: Fracture surface from 90° sample for a) V and b) R

Stiffness anisotropy

The results of the tensile tests revealed a narrowing of the gap between the longitudinal and transverse properties when moving from virgin to recycled materials. Therefore, the latter tends to behave more isotropically. The anisotropy of the in-plane stiffness properties for the tested materials can be analyzed and quantified as reported in Section 3.2.1. Once E_1, E_2, G_{12}, ν_{12} are known, the anisotropic behavior can be evaluated graphically and qualitatively from the generalized Mohr's circles (Fig. 4.15), and quantitatively from the ratios $\frac{U_2}{U_1}$, $\frac{U_3}{U_1}$ and its constituents(Tab. 4.6).

Looking at R, the distance between the centers increases while the radii decrease slightly with respect to V. Both factors are linked to an increase in the isotropy of the material: the greater separation of the circles means that the isotropic component (U_1) increases, while the decrease in the radii is linked to a decrease in the orthotropic components (U_2, U_3).

This behavior is also confirmed by the fact that both anisotropic ratios for the R material decrease compared to the V material. The ratio $\frac{U_3}{U_1}$ does not decrease much while the most marked decrease can be seen in $\frac{U_2}{U_1}$. Therefore, anisotropy is primarily affected by the difference between longitudinal and transverse properties rather than shear properties. Nevertheless, the lower degree of anisotropy of R with respect to V is due to the reduced difference between longitudinal and transverse properties.

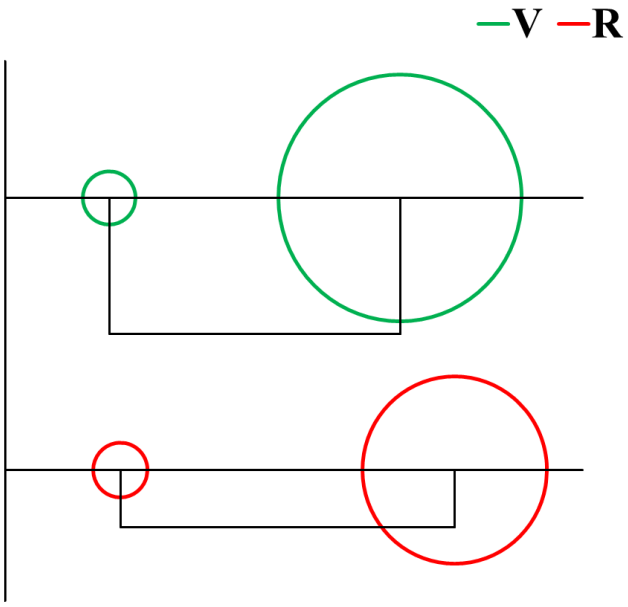

Figure 4.15: Comparison of generalized Mohr circles referred to V and R

Table 4.6: Orthotropic fractions for the analyzed materials

	Printed materials	
Ratio	V	R
$\frac{U_2}{U_1}$	0.42	0.28
$\frac{U_3}{U_1}$	0.10	0.08

4.4 Conclusions and future developments

The work reported in this chapter investigated the mechanical recycling of FDM 3D-printed short carbon fiber-reinforced polyamide, focusing on the feasibility of grinding the material and producing a filament suitable for further 3D printing. The topic is highly relevant due to its implications for eco-sustainability and circular economy. The virgin (V) and recycled (R) materials were compared in terms of their thermal, rheological, and tensile mechanical

properties. Rheological analysis clearly indicated that grinding and remelting the material led to a decrease in molecular weight, as evidenced by a significant reduction in complex viscosity.

Unexpectedly, the transverse strength and stiffness of R-printed parts did not reflect this reduction in molecular weight. This behavior cannot be attributed to an increase in material crystallinity or a reduction in void content. Additionally, fiber orientation is unlikely to play a major role, since longitudinal properties are nearly identical for V and R.

The most plausible explanation is related to an increase in the interlayer and intralayer contact areas and adhesion during printing. The lower molecular weight of R enhances polymer self-diffusivity, promoting improved interlayer and intralayer welding, which in turn positively affects the mechanical properties. This effect is more pronounced in transverse and shear directions than in the longitudinal one, as welds are primarily loaded in these orientations. Therefore, the material's behavior becomes more isotropic because its transverse and shear properties increase, while its longitudinal properties remain almost unchanged. These findings highlight an important consideration: in 3D printing, whether the feedstock is virgin or recycled, the molecular weight distribution of the polymer plays a critical role. In particular, the presence of an appropriate fraction of low-molecular-weight chains is essential because it enhances self-diffusion within the material. This, in turn, facilitates more effective intra- and inter-layer bonding between the newly deposited molten material and the previously deposited one. Consequently, this improves the strength of the welds generated and subsequently the structural integrity and mechanical performance of the printed part.

After completing the first reprocessing cycle, an attempt was made to carry out a second round of recycling and printing. Unfortunately, it was not possible to produce a filament within tolerance and with a quality suitable for FDM technology. It is expected that multiple reprocessing cycles would reduce the molecular weight further, resulting in a material with such a low viscosity that it cannot hold itself in the winding phase after extrusion.

There are many interesting future developments related to this work. For example, the transition to pellet-based 3D printing technology, which would eliminate the thermal step of filament extrusion and could make the material processable in multiple steps. Alternatively, if continuing with filament technology, countermeasures must be taken, such as blending with virgin material or incorporating suitable toughening agents.

This project was created with the aim of increasing sustainability by making use of technical, high-quality waste materials specifically developed for industrial applications. A further idea is to investigate other types of materials suitable for FDM. These materials could include different fibers and matrices and would still be appropriate for structural.

5. Mechanical characterization and anisotropy evaluation of 3D printed continuous basalt fiber composites

5.1 Introduction

To further improve the mechanical performance of additively manufactured components beyond the levels achievable with short fiber-reinforced thermoplastics, as described in Section 1.2.4, several techniques enable the 3D printing of continuous fibers as reinforcement. These systems represent a significant technological advancement because they combine the design flexibility inherent to additive manufacturing with the superior stiffness, strength, and fatigue resistance characteristic of continuous fiber composites. This unique synergy opens up new possibilities for lightweight structural applications, particularly in sectors such as aerospace and automotive, where high strength-to-weight ratios are essential.

The most widely studied and commercially available continuous reinforcement fibers are carbon, glass and Kevlar. Their properties and characteristics are discussed and compared in detail in Section 1.3.2 and related subsections. The environmental impact of such fibers is quite relevant due to their synthetic nature; therefore reinforcement fibers of natural origin are increasingly studied and also employed in various industrial applications, due to their attractive eco-sustainability [38].

Continuous basalt fibers (CBF) are an interesting type of natural fiber that is already commercially available in filament form, making them suitable for 3D printing technologies. Basalt is of mineral origin and is proposed as a more eco-friendly alternative to the more widely used synthetic fibers. Its properties have been included in Section 1.3.2.2, which deals with natural continuous fibers and their characteristics.

To the best of the author's knowledge, few studies in the literature address CBF-reinforced 3D-printed composites using commercially available printers developed specifically for this purpose. Specifically, the machine used for all works is an Anisoprint Composer, which uses the out-of-nozzle technique, as discussed in Section 1.2.4. Qu et al. [123] tested a multi-cavity structure realized with CBF and two different thermoplastic matrices were evaluated: PA12 and PLA. Kong et al. [124] combined the use of continuous carbon fiber (CCF) to create mixed structures reinforced with both carbon and basalt, using a thermoplastic PET matrix. In both articles the composites were tested in tension and bending but only in the longitudinal

direction, and a novel numerical model based on Peridynamics was proposed for the simulation of the failure mode. The multi-cavity structures studied consist of a central part made up of linear infill reinforced with continuous fiber, and an outer body made entirely of thermoplastic (TP) material, consisting of the top and bottom layers and the outer shells (Fig. 5.1a).

Malik et al. [125] investigated the tensile and flexural properties of a composite made with a PLA matrix reinforced with CBF with different fiber volume fractions (0%, 10%, 20%) and raster angles (0°, 90°, ±45°). Similar works were been carried out by the same authors with regard to impact resistance and interlaminar shear strength[126], and the hydrothermal aging effects on mechanical performance [127]. In both cases, to evaluate the different fiber volume fractions, the number and sequence of layers containing fiber reinforcement and those containing only TP were varied (Fig. 5.1b).

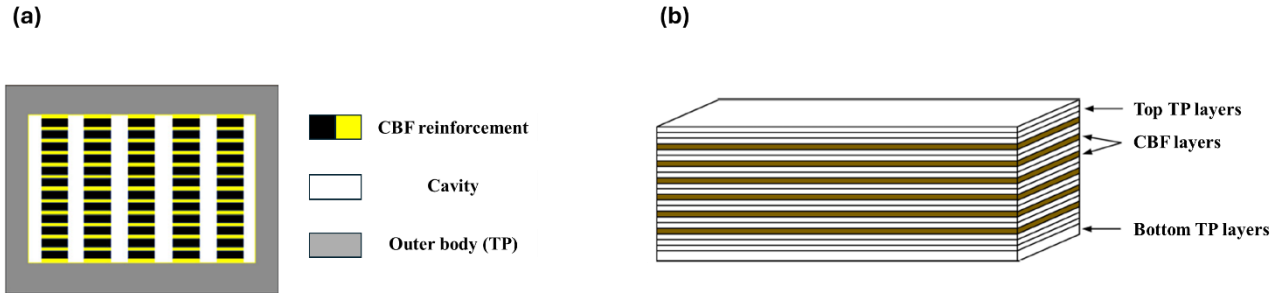

Figure 5.1: Representation of a) multi-cavity structure [123] and b) layered samples [124] reinforced with CBF

This chapter aims to characterize the in-plane stiffness and strength properties of a 3D-printed composite made from continuous basalt fiber-reinforced PA12, produced using a commercial out-of-nozzle printer. Its anisotropic behavior was then evaluated both qualitatively and quantitatively. The results are compared with those obtained from the characterization of the matrix alone: an unfilled PA12.

Compared to the work described in the previous chapter, a material with better mechanical performance is used thanks to the continuous fiber. It is also more eco-friendly in terms of both the matrix and the fiber. As described in Section 1.3.2.2, basalt fiber is clearly more sustainable than carbon fiber. Similarly, as reported in Section 2.2.3, PA12 is preferable to PA6.

Furthermore, unlike the literary works mentioned above [123], [124], [125], [126], [127], no particular structures or printing configurations are tested here. The focus is on the complete characterization of the in-plane properties for the continuous fiber-reinforced composite. This enables to better understand its performance and to better assess its actual applicability in industrial settings for structural components.

5.2 Materials and methods

5.2.1 Materials

The materials used in this paper are listed in Tab. 5.1 together with the information declared in the technical data sheet. Both the thermoplastic matrix and the continuous reinforcement fiber were purchased from Anisoprint Sarl (Luxembourg): the former filament is an unfilled PA12 and the latter is a continuous basalt fiber (CBF). The producer declares that such a fiber is coated by a thermoset (TS) resin.

Table 5.1: Materials description from technical data sheets

Material	Composition	Fiber mass fraction [%]	Diameter [mm]
Matrix	PA12	-	1.75
CBF	TS coated basalt fiber	65 ÷ 75	0.28

5.2.2 3D printer

All specimens were printed using a Composer A3 by Anisoprint: a 3D printer based on out-of-nozzle technique and with three inputs. The printhead is equipped with two different extruders (Fig. 5.2): the left one is a standard bowden device with a 0.4 mm nozzle and receives an ordinary thermoplastic filament TP_1 . This extruder works like a standard FDM machine with an input for solid TP filament and an output for extruded material. The right one is input with the continuous reinforcement fiber and another thermoplastic filament TP_1 that is molten within a melting chamber and co-extruded with the fiber through a 0.8 mm nozzle. The two input materials are joined together, resulting in a single output: the coextruded composite.

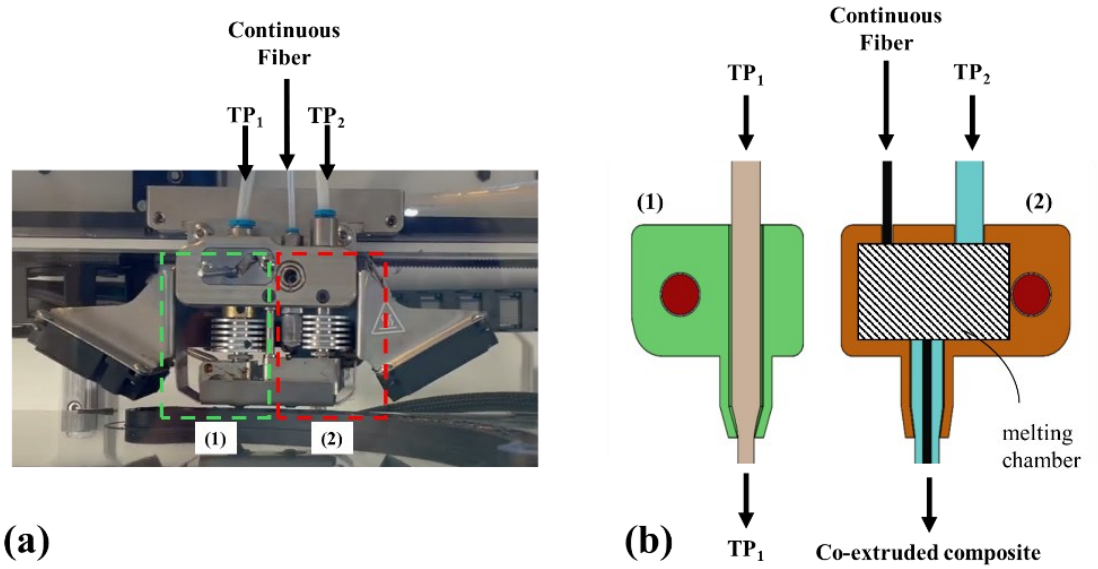

Figure 5.2: Printhead of the Anisoprint Composer A3: a) picture and b) schematic representation

Going into more detail about the transition of the fiber in the composite extruder, on the right, three distinct zones can be clearly identified (Fig. 5.3). In the cutting area, a circular blade, driven by a servomotor, cuts the fiber when the reinforcement deposition is complete. This is followed by a 30 mm addressing zone that leads to a 15 mm coextrusion chamber. From the inlet to the outlet of the co-extrusion head, the fiber is guided through channels with a diameter of 1 mm. This ensures that once the fiber has been cut, printing can automatically resume because the fiber is accurately guided toward the coextrusion chamber.

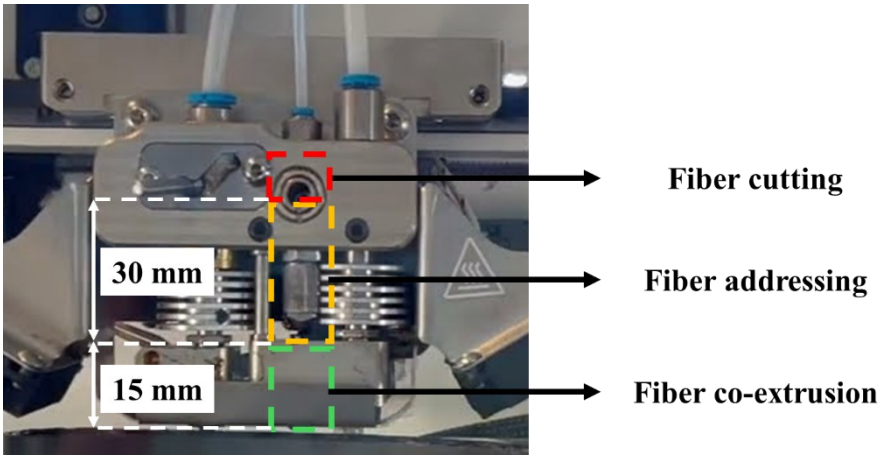

Figure 5.3: Focus on the zones of the composite extruder

The slicing software used is the open version of Aura, which allows the management of the various printing parameters in both extruders, such as printing speed, fiber-matrix ratio and fiber orientation during the co-extrusion process. Aura makes it possible to completely fill a

layer of fiber by depositing them with a specific raster angle to obtain a unidirectional lamina. Alternatively, a reinforced infill can be created, where the specific pattern (triangles, honeycomb…) consists of coextruded continuous fiber. In both cases, curved trajectories and changes of direction are critical due to the stiffness of the continuous fiber. To overcome this problem, the software adopts two different solutions simultaneously: different fiber feeding techniques (Fig. 5.4) and path discretization (Fig. 5.5).

In straight sections, active feeding is used, where both the continuous fiber and the TP matrix are fed into the chamber, by the action of both feeding motors (Fig. 5.4a). Passive feeding is used near curved sections, where the fiber feeding motor is switched off and the TP matrix motor is switched on (Fig. 5.4b). In doing so, the fiber is pulled by the movement of printhead and the extrusion of the matrix simultaneously.

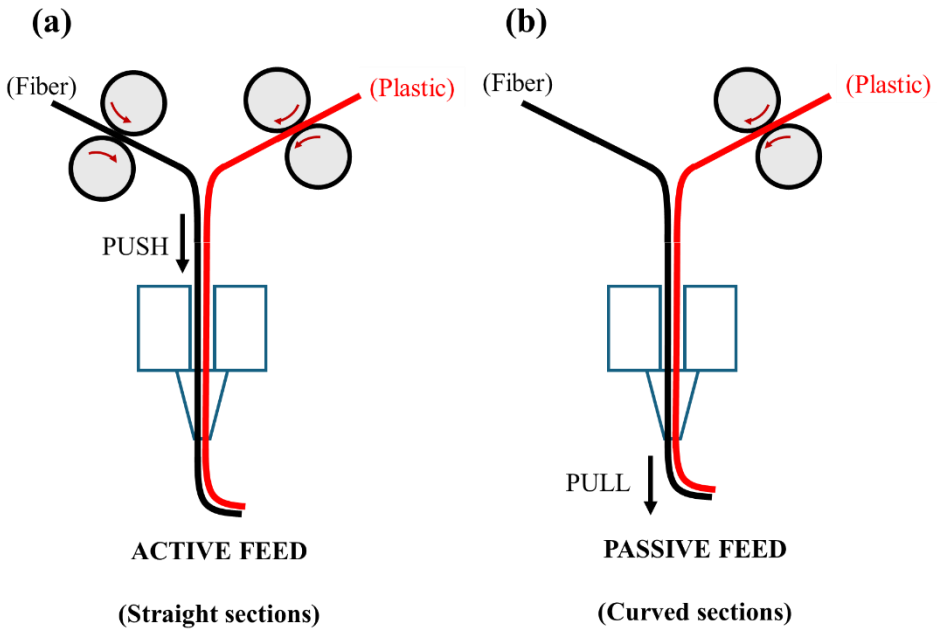

Figure 5.4: Different feeding strategy for a) straight and b) curved sections

Besides these different feeding techniques, to print the specific pattern of the fiber, Aura discretizes the original trajectory to ensure that the fiber follows it as closely as possible (Fig. 5.5). Moreover, the printing speed is slowed down considerably near curved sections, so that the fiber is brought into the required trajectory closely. The points at which a change in direction

occur, resulting in the discretization of the trajectory, can induce weak points, poor aesthetics, increased presence of voids and dimensional inaccuracy.

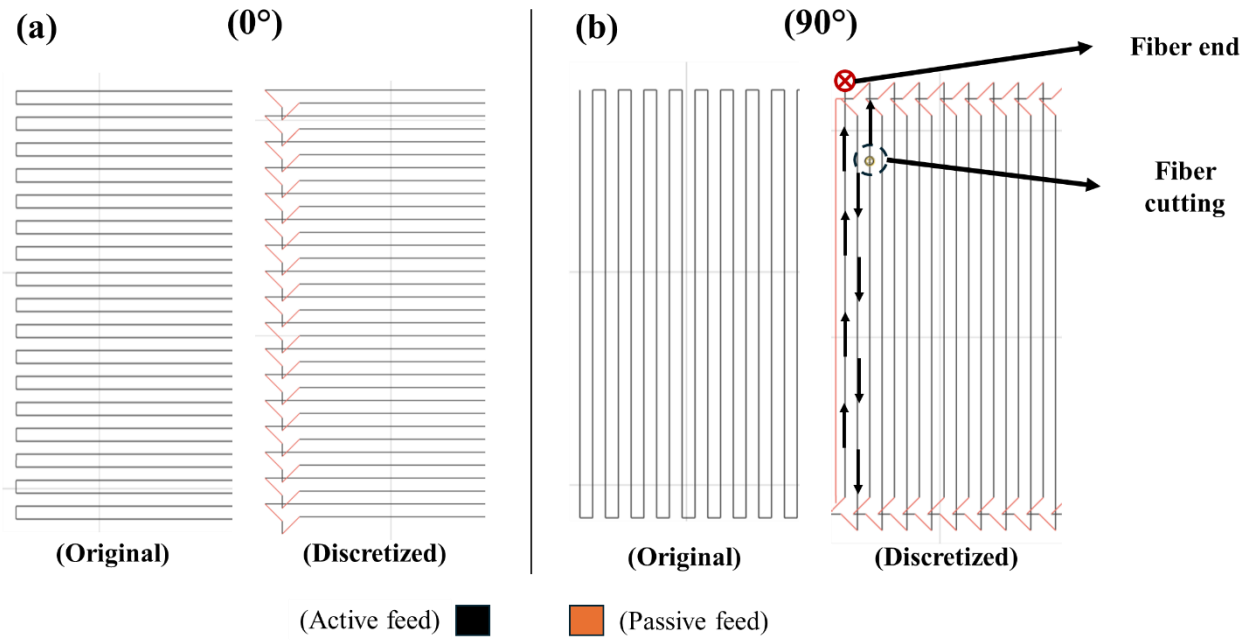

Figure 5.5: Original and discretized trajectories for a) 0° and b) 90° pattern

From the print preview of the discretized trajectory, it is also possible to evaluate how many times and where the fiber is cut within the same layer. The slicer optimizes deposition in order to cut as few times as possible, thus ensuring greater continuity in the deposition of the continuous reinforcement fiber. Once the cut has been made (yellow dot in Fig.5.5), the printer deposits the last 45 mm of fiber in passive feed mode. This final length is relative to the distance from the cutting area to the exit of the coextrusion chamber (Fig.5.3). If multiple cuts are required within the same layer due to the geometry of the part, the software will attempt to complete the fiber deposition as close to the outer edge as possible. This also helps to ensure as much continuity as possible of the fiber in the reinforced area of the sample.

5.2.3 Specimen preparation

The samples needed for testing the PA12 matrix alone were produced using the extruder on the left, so the printer worked like a standard FDM machine. CBF reinforced PA12 specimens were obtained by co-extrusion using the right extruder of the A3 Composer printer. The acronym CBF_{cc}, which stands for CBF co-extruded composite, is used in this paper to refer to this material. All specimens were printed using a single line skirt to purge and prepare the extruder

before printing, without external shells, top or bottom layers. The bed was heated at 65 °C and polyamide-based filament was dried at 80°C for 24 h and the spool was stored in a passive dry box (Polymaker, China) containing silica salts during printing. To achieve a complete characterization of the in-plane properties, the samples were printed in flat configuration and different raster angles were considered (0°, 90°, $[\pm 45°]_{2s}$). The main printing parameters are listed in Tab. 5.2 for each material.

Table 5.2: Printing parameters of samples for the two materials

Characteristic	PA12	CBF_{cc}
Layer height [mm]	0.2	0.3
Line width [mm]	0.4	0.6
Extrusion temperature [°C]	250	250
Printing speed [mm/s]	40	30

Notice that while the matrix is an unfilled PA12, CBF_{cc} is a composite reinforced with continuous fiber. This peculiarity is well described in Fig.5.6. Fig. 5.7 shows the fiber orientation for CBF_{cc}, for the three raster angle orientations. It is possible to observe fiber bending at the edges, especially for 90° and ±45°, related to the discretization of the trajectory.

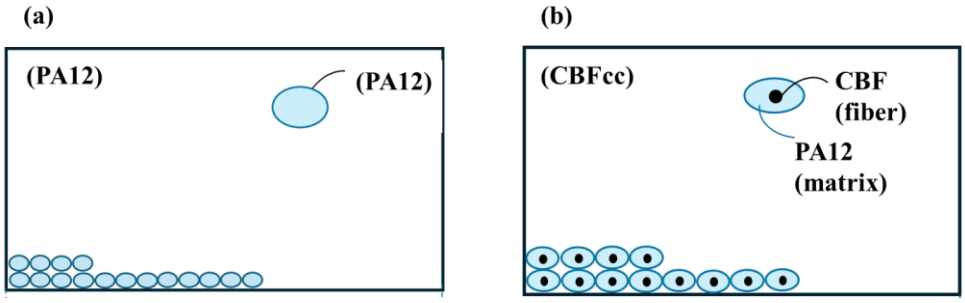

Figure 5.6: Representative section of specimens for a) PA12 and b) CBFcc

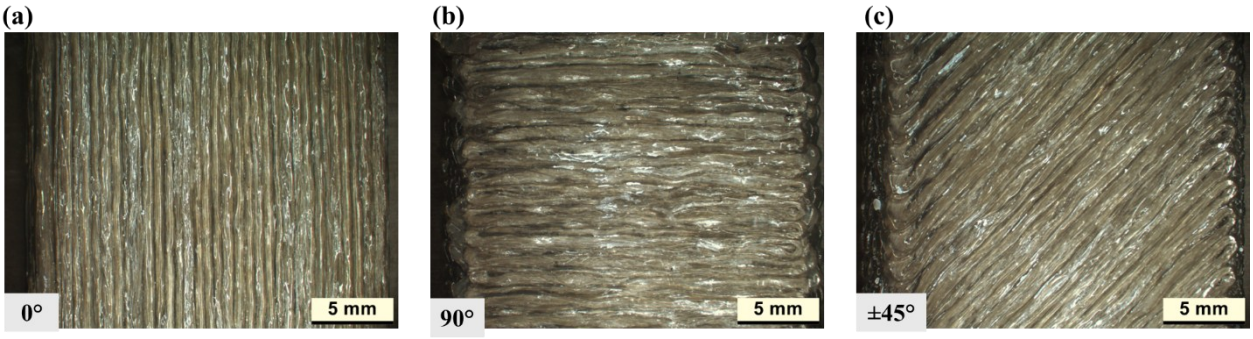

Figure 5.7: CBFcc fiber orientation at a) 0°, b) 90° and c) ±45°

5.2.4 Material characterization

Tensile characterization

As in the previous chapter, tensile tests were carried out for both materials in accordance with the procedures detailed in Section 3.2.2, in order to achieve complete characterization of the in-plane properties. ASTM D3039 standard [79] is used to measure longitudinal and transverse properties, by printing specimens at 0° and 90° raster angle. Shear properties are evaluated through ASTM D3518 standard [80] and 10° off-axis tensile test [81], [82]. The former is used to measure the shear modulus (G_{12}) directly, via the shear stress-strain response of the material. The latter is employed to evaluate only S_{LT} through Eq.9 (Section 3.2.1) by setting σ_x equals to $\sigma_Y^{10^\circ}$. This value is then compared with that obtained using $\sigma_Y^{45^\circ}$.

For both cases, the samples are rectangular in shape, 200 mm long, 20 mm wide and 2.4 mm thick. The tests were performed on three samples per raster angle (0°, 90°, 10°, ±45°), for a total of twelve samples per material. For all specimens, Digital Imaging Correlation (DIC) was used to measure both longitudinal and transverse strain, as an average value over the analyzed area.

Finally, after characterizing the materials, the anisotropy of the in-plane stiffness properties was evaluated for both virgin and recycled materials, as proposed in Section 3.2.1.

Voids measurements

Density was measured for the two starting filaments before printing $\rho_{CBF}^f, \rho_{PA12}^f$ and for the tensile rectangular specimens before testing $\rho_{CBFcc}^s, \rho_{PA12}^s$. Measurement techniques and the instrumentation used are reported in detail in Section 3.3. The density of the co-extruded composite ρ_{CBFcc}^f is estimated using the rule of mixtures (ROM):

$$\rho_{CBFcc}^f = \rho_{CBF}^f \phi_{CBF} + \rho_{PA12}^f \phi_{PA12} , \qquad (20)$$

where ϕ_{CBF} and ϕ_{PA12} are the volume fractions of the two materials, obtained by Aura during the print preview, respectively.

Voids percentage of the specimens was evaluated according to Eq.10, as reported in Section 3.3.

Rheological tests

Rheological characterization was performed in dynamic oscillation and strain-controlled mode, for the PA12 matrix. The specimens are in the shape of a disc, 25 mm in diameter and 2 mm thick. Prior to testing, a void content of less than 10% was verified so that the accuracy of the measurements was ensured.

Three types of rheological experiments were done: strain, frequency and time sweeps, all performed at 200 °C. Rheological analysis techniques and the instrumentation used are reported in detail in Section 3.5.

Thermal analysis

PA12 and CBF filament were analyzed through DSC and TGA analysis. The latter was performed to evaluate the fiber, or filler, mass fraction for both filaments. DSC was used to determine the crystalline fraction (χ_c) and characteristic temperatures, such as the glass transition temperature T_g and the melting temperature T_m. Equation 11 was used to calculate the crystalline fraction, setting ΔH_{m0} equal to 245 J/g [128].

The instrumentation and procedure for thermal analysis are detailed in Section 3.4.

5.3 Results and discussion

5.3.1 Thermal characterization results

The thermal stability of the filaments and their mass loss as a function of temperature are shown in the thermograms from non-isothermal TGA (Fig.5.8).

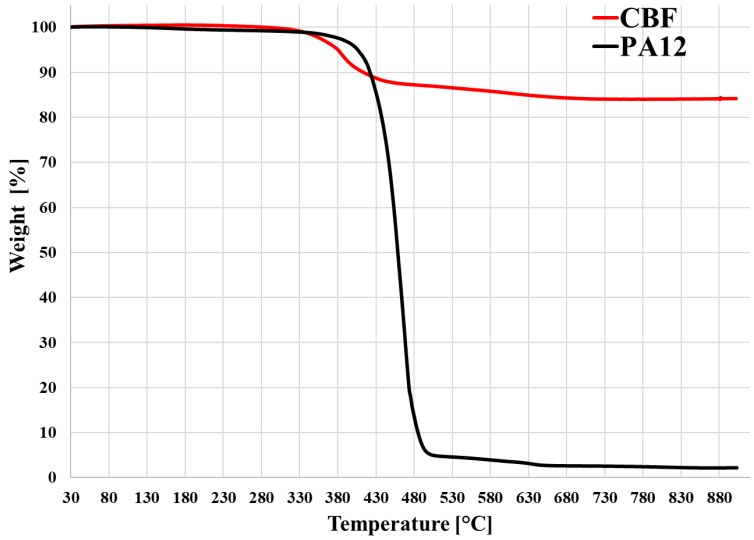

Figure 5.8: TGA derivative curves for PA12 and CBF

The results obtained for both PA12 and CBF filament agree with the material datasheet as reported by the producer (Tab 5.1). In particular, PA12 shows the onset of degradation at 435°C, with 2.2% residual mass at the end of the test, which may indicate a small presence of mineral fillers. CBF thermogram shows an onset of degradation around 358 °C and 84.2% residual mass at 900°C. At around 350 °C the curve shows a 12% drop, as described also in [129], which is referred to the degradation of the organic coating commonly used on structural basalt fibers. Also, notice that the curve is flat up to 280 °C, thus it is this temperature that must not be exceeded during co-extrusion to prevent fiber degradation.

Concerning DSC analyses, the thermograms are shown in Fig.5.9 for the two filaments.

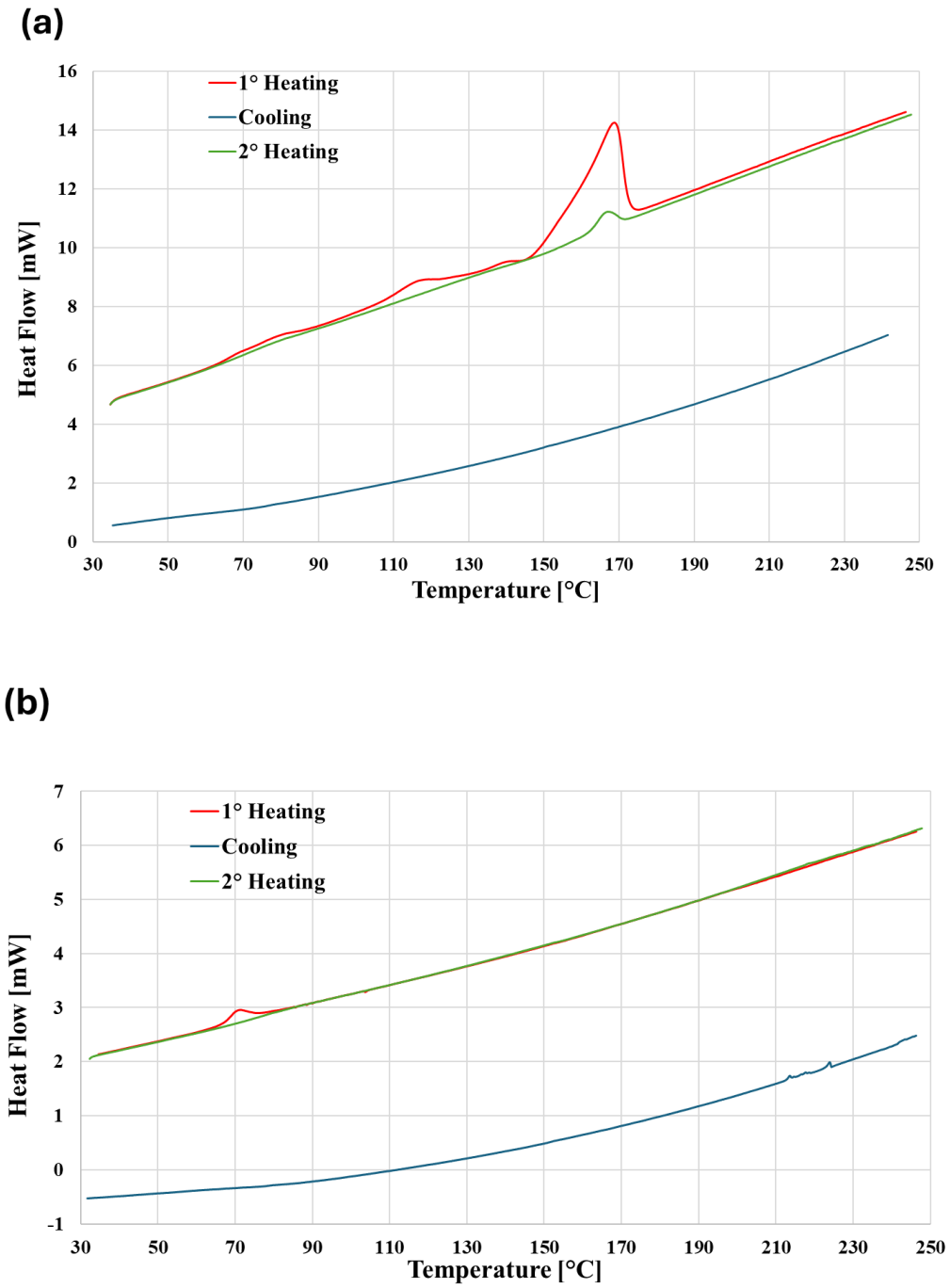

Figure 5.9: Thermograms of a) PA12 matrix and b) CBF filaments

Tab.5.3 summarizes characteristic temperatures and degree of crystallinity, which agree with those found in [123], [124].

Table 5.3: Characteristic temperatures and degree of crystallinity for the two filaments

	PA12			CBF		
	T_g [°C]	T_m [°C]	χ_c [%]	T_g [°C]	T_m [°C]	χ_c [%]
1° Heating	64.9	168.6	11.48	66.5	nd	nd
2° Heating	67.9	166.6	1	76.5	nd	nd

Glass transition temperature of PA12 agree with these for PA12. The melting peak is present only in the first heating, while it is barely visible in the second heating. This shows a rather large difference in crystallinity between first and second heating, which indicates that the crystallinity observed was mainly induced by the stretching part of the filament manufacturing process. On the other hand, crystallinity values are very low, which shows that the material is essentially amorphous. This behavior renders this material ideal for 3D printing, as printing amorphous materials limits warping and ensures good dimensional stability.

For the CBF filament, only the glass transition temperature of 76.5°C is observed, while the melting temperature cannot be determined both in the first and second heating, indicating that the resin used for the coating of the basalt fiber is amorphous.

5.3.2 Rheological results

The strain sweep tests ensured that a strain of 1% was sufficient for remaining within the LVR and this value was used for performing the other two rheological measurements. Fig. 5.10a shows the trend of complex viscosity η^* is given as a function of frequency ω. At low frequencies, part of the Newtonian plateau can be seen with zero shear viscosity (η_0) of around 5500 Pa·s.

The thermal stability of the materials was assessed using a time sweep test at a frequency of 1 rad/s over a total duration of 600 seconds. Figure 5.10b depicts the evolution of G^* over time. As the curve is flat, the material remains stable throughout the test period, which is longer than the time that the TP matrix remains in the coextrusion chamber.

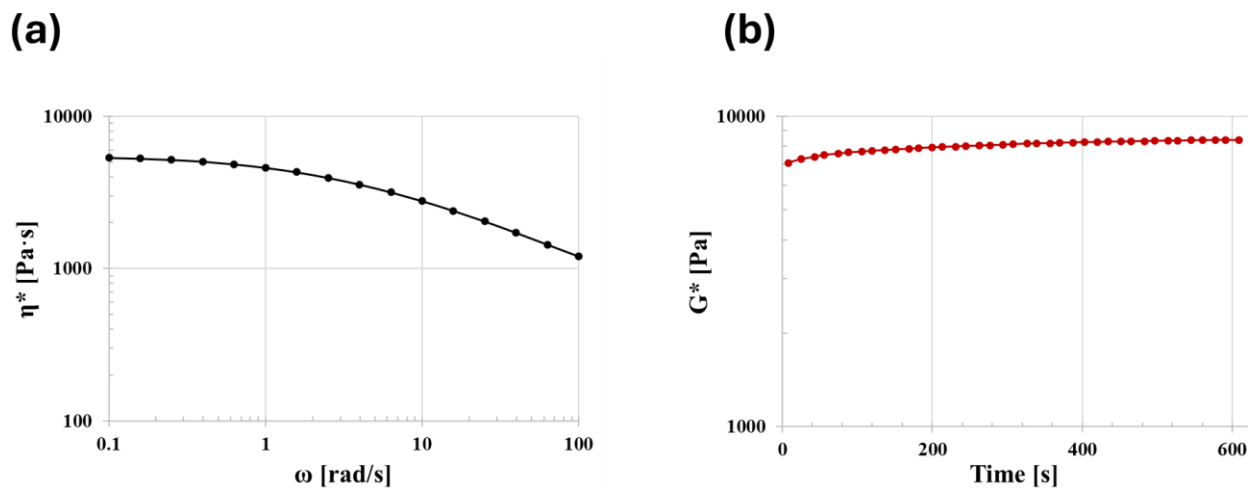

Figure 5.10: Trend of a) complex viscosity as a function of frequency and b) complex modulus as a function of time

5.3.3 Density and voids measurements

Initially, the densities of the two starting filaments were measured, both for the TP matrix (ρ^f_{PA12}) and for the continuous basalt reinforcement fiber (ρ^f_{CBF}). The density for the co-extruded composite material (ρ^f_{CBFcc}) was calculated following Eq.20 (Section 5.2.4), using the volumetric fractions ϕ_{PA12}= 0.66 and ϕ_{CBF}= 0.34. The four density values are shown in Tab.5.4. CBF density is higher than the TP matrix due to the presence of the basalt fiber, while CBF_{cc} density is intermediate due to the co-extrusion process.

Table 5.4: Densities for the two starting filaments, values in parentheses represent standard deviation, and that calculated for the co-extruded composite

Filament density [g/cm^3]		Co-extruded density [g/cm^3]
ρ^f_{PA12}	ρ^f_{CBF}	ρ^f_{CBFcc}
0.99 (0.002)	1.82 (0.07)	1.28

These data allow the calculation of void percentage according to Eq. 10 (Section 3.3), and the corresponding values are listed in Tab. 5.5. It is important to note that void percentage is heavily dependent on the raster angle of the specimens, therefore the results are presented also in terms of this parameter.

Void percentages are around 5% and, in some cases, even lower. For all samples there is a low standard deviation, and this indicates good print quality and process repeatability. For each material, the longitudinal configuration has lower voids percentage, and this is mainly due to the lower number of direction changes during printing, as described in Fig.5.7. To achieve the pattern at 90° and ±45°, more changes of direction are required, resulting in a slight increase in voids, and this is true especially for PA12. For CBF_{cc}, the highest percentage of voids is found in samples at ±45°, while at 90° is very low. This is due to the fact that to manufacture these specimens it was necessary to reduce the z-offset during printing, which resulted in greater compaction of the material and limited voids.

Table 5.5: %voids for all configurations, values in parentheses represent standard deviation

	% Voids			
Material	0°	90°	10°	±45°
CFCPA	3.5 (0.7)	5.2 (0.2)	4.9 (0.2)	5.6 (0.4)
CBF_{cc}	1.4 (0.2)	2.8 (0.4)	3.72 (0.8)	5.7 (0.8)

CBF filament is made from continuous basalt fiber and TS coating. The basalt volume fraction of the filament ϕ_{BAS} can be evaluated from the following equations:

$$\frac{1}{\rho_{CBF}^{f}} = \frac{\Psi_{BAS}}{\rho_{\mathrm{BAS}}} + \frac{1-\Psi_{BAS}}{\rho_{\mathrm{TS}}} \tag{21}$$

$$\rho_{CBF}^{f} = \rho_{BAS}\phi_{BAS} + \rho_{TS}(1-\phi_{BAS}) , \tag{22}$$

where Ψ_{BAS} is the basalt mass fraction equal to 0.842, evaluated from TGA analysis, ρ_{BAS} is the density of raw basalt that from literature equals 3 g/cm^3 [130] and ρ_{CBF}^{f} is the density of the basalt filament, which was calculated previously. The only unknowns are the density of the TS coating, ρ_{TS} , and ϕ_{BAS}, which result 0.59 g/cm^3 and 0.51, respectively. Taking this value into account, the effective volume fraction of basalt fiber of CBF_{cc} samples is finally 0.18, which corresponds to a mass fraction of 0.41.

5.3.4 Mechanical characterization

Representative stress-strain curves of the different configurations are provided in Fig. 5.11a for PA12 and in Fig. 5.11b for CBF_{cc}.

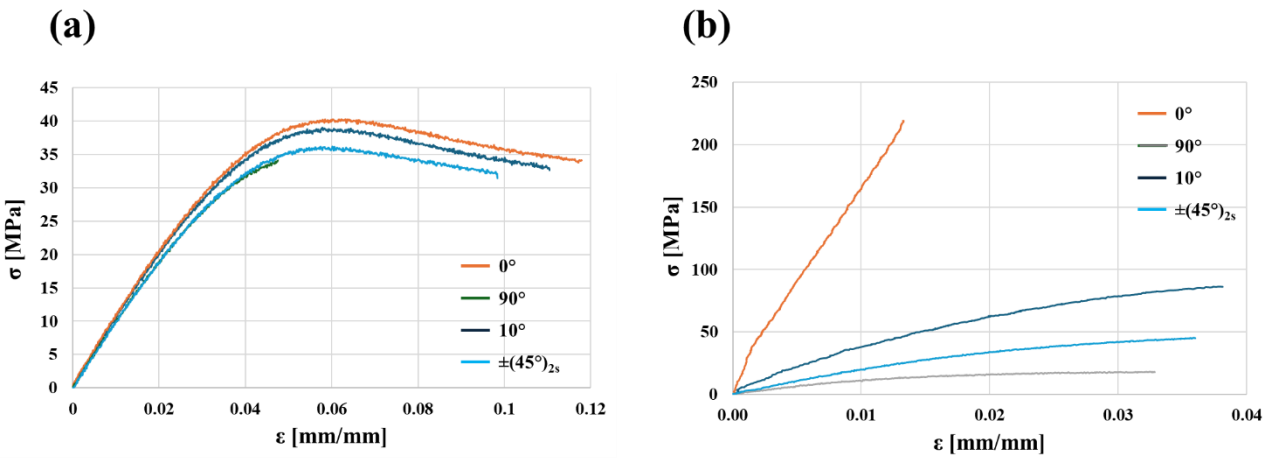

Figure 5.11: Stress-strain curves at different orientations for a) PA12 and b) CBFcc

Fig. 5.11a shows an elasto-plastic behavior, and the four curves overlap in the initial linear elastic region, regardless of the printing orientation, therefore PA12 stiffness behavior can be assumed isotropic. On the other hand, there is a slight difference in terms of yield stress, but this is not enough to conclude that the material is anisotropic in terms of strength, therefore it can be reasonably considered completely isotropic.

For CBF_{cc} the development of the curves is completely different (Fig. 5.11b). 0° curve has significantly higher stiffness and strength than other orientations. The behavior differs significantly from the longitudinal direction at 10°, and this difference is even more pronounced at 90° and ±45°. Therefore, this material exhibits markedly anisotropic behavior. Furthermore, the material is brittle in the longitudinal direction, but ductile in the other three directions.

Tab. 5.6 shows the four elastic constants required for stiffness characterization for the two materials. Comparing the matrix (PA12) and the co-extruded composite (CBF_{cc}), the latter has higher mechanical properties, especially E_1 which increases by more than an order of magnitude, while concerning E_2 and G_{12} there is only a slight increase. Indeed, in the 0° configuration the fibers are placed in the same direction as the applied load. Thus, fibers are the load bearing component of the composite. At 90° and ±45° orientations, fibers have a less favorable orientation, thus the behavior depends by a greater amount on the matrix. Poisson's ratio is about 0.45, for all materials.

Table 5.6: Elastic properties for all materials, values in parentheses represent standard deviation

Material	E_1 *[GPa]*	E_2 *[GPa]*	ν_{12}	G_{12} *[GPa]*
PA12	1.11 (0.05)	1.07 (0.03)	0.41 (0.02)	0.35 (0.05)
CBF_{cc}	17.96 (0.67)	1.43 (0.03)	0.48 (0.06)	0.49 (0.02)

From the tensile tests, the strength and ultimate strain values were also evaluated and are shown in Tab. 5.7. The strength behavior has the same trend as the stiffness.

It can be seen that the S_{LT} calculated using the two methods is of the same order of magnitude for both materials. In the case of CBF_{cc}, there is a slight difference and the higher value obtained from the ±45° test is subject to greater variability (3.37 MPa over 15.63 MPa). However, in the case of PA12, the values are practically the same.

The values for PA12 are about the same in the longitudinal and transverse direction. The shear strength values, calculated at both 10° and ±45°, are about half S_L and S_T, in agreement with the hypothesis of isotropy.

For CBF_{cc}, S_L is approximately 20 times larger than S_{LT} and S_T. The transverse strength for CBF_{cc} is lower than that of the matrix (PA12) and this is in agreement with the literature [76], since it's expected that for unidirectional composites fibers weaken the material in the transverse direction. This does not appear in the case of shear strength obtained with ASTM D3518 but notice that there is a considerably higher results dispersion for CBF_{cc}. All these results are a clear indication of a high degree of anisotropy of CBF_{cc} with respect to the isotropic matrix (PA12), also in the case of strength.

As can be seen, CBF_{cc} shows an approximately 30% decrease in S_T compared to the matrix alone (PA12). Considering the low porosity (Table 5.5), it is reasonable to assume that there is poor compatibility and interface between PA12 and the TS coating of the continuous basalt fiber. For all stiffness and strength characteristics, a very low standard deviation of less than 5% from the average reference value can be observed, which indicates good printing quality and process repeatability.

Table 5.7: Strength properties for all materials, values in parentheses represent standard deviation

Material	S_L *[MPa]*	S_T *[MPa]*	$S_{LT}^{45^\circ}$ *[MPa]*	$S_{LT}^{10^\circ}$ *[MPa]*
PA12	18.15 (1.14)	18.61 (1.88)	9.01 (0.46)	8.52 (0.35)
CBF_{cc}	222.27 (11.87)	12.32 (0.63)	15.63 (3.37)	9.34 (0.42)

Stiffness anisotropy

As described in Section 3.2.1 and in the previous chapter, once E_1, E_2, G_{12}, ν_{12} are known, the anisotropic behavior can be evaluated graphically and qualitatively. The unfilled PA12 matrix and continuous basalt fiber composite will be compared with virgin Onyx. The latter is a compromise in terms of mechanical performance between the two materials in this chapter, because it is polyamide-based but reinforced with short fibers.

Referring to the generalized Mohr's circles for PA12 (Fig.5.12a), the radii (U_2, U_3) are very small compared to the distance between the centers (U_1), meaning that the orthotropic components are much smaller than the isotropic one. The two circles tend to collapse at one point. This behavior is also confirmed quantitatively by both ratios, which are very close to zero, indicating that the material is substantially isotropic.

Looking at the other two materials (Fig.5.12a), both the distance between the centers and the radii increase with respect to PA12, denoting that the mechanical properties are higher. Moreover, the proportion of the orthotropic components with respect to the isotropic one increases from CFCPA to V-Onyx and even more to CBF_{cc} (Tab. 5.8). This can be easily seen by the size of the radii compared to the distance of the centers: for V-Onyx the circles are getting closer, while they even intersect for CBF_{cc}.

This trend indicates that the behavior is increasingly anisotropic, with a stronger degree in the case of CBF_{cc} than V-Onyx, since both ratios increase by 35%.

In addition, both anisotropic ratios increase in comparison with PA12, to a larger extent in the case of CBF_{cc}. For both the latter and V-Onyx, the major contribution is made by $\frac{U_2}{U_1}$, so anisotropy is mainly due to the difference between the longitudinal and transverse properties.

For completeness and in order to have a better understanding of the anisotropy estimate through generalized Mohr circles, two other materials taken from the literature were compared with CBF_{cc} (Fig.5.12b, Tab.5.8). The first one is a 3D printed composite reinforced with

unidirectional continuous carbon fiber (CCF) [131] and the second one is an epoxy-based composite reinforced with a [0°/90°] carbon fabric [132].

The circles of CCF are larger and more widely spaced than those of CBF_{cc}, because carbon fibers are much stiffer than basalt. On the other hand, looking at the anisotropy ratios of CCF and CBF_{cc}, the corresponding ones are basically identical and this shows that CCF is anisotropic in the same way of CBF_{cc}. The trend is the same as before when comparing V-Onyx with CBF_{cc}, and again the left circle is smaller than the right circle.

The generalized Mohr circles of the fabric are completely different from the CBF_{cc}, as the two circles are widely spaced, with respect to the size of the radii, and the left one is larger than right one. The type of anisotropy is completely different because reinforcing fibers are present in the longitudinal and transverse direction in equal amount. Since the ratio $\frac{U_3}{U_1}$ is approximately 10 times of $\frac{U_2}{U_1}$, anisotropy is mainly due to the shear properties.

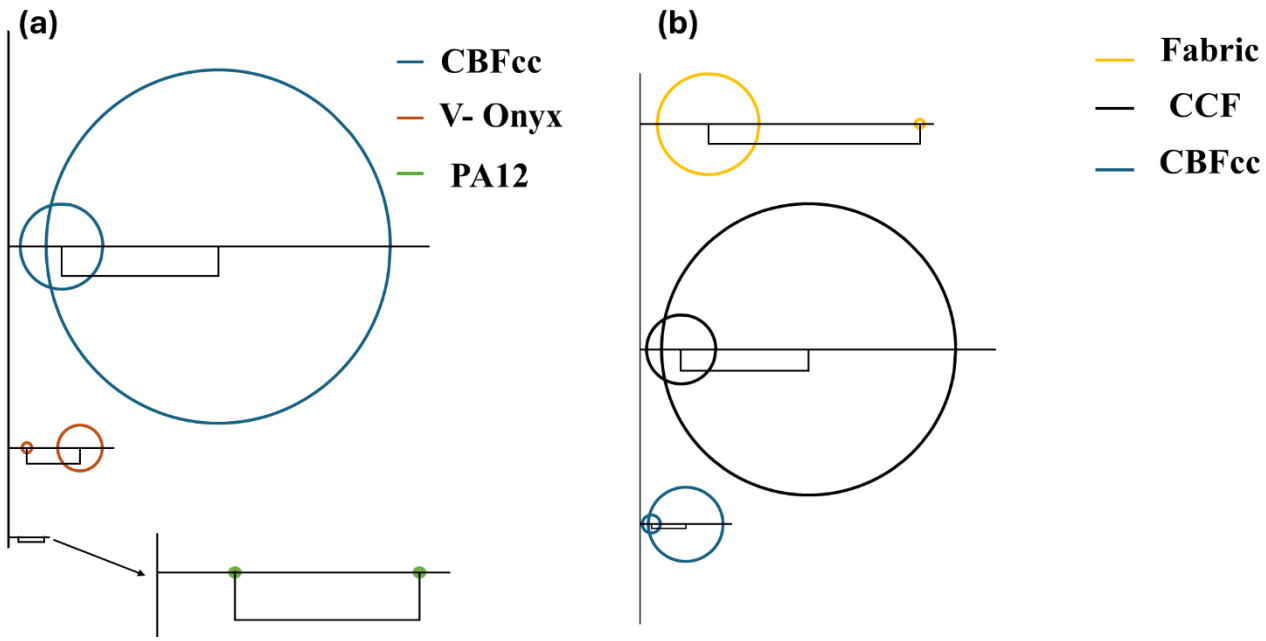

Figure 5.12: Comparison of generalized Mohr circles referred to CBFcc: a) with respect to PA12 and V-Onyx, b) with respect to CCF [131] and fabric [132]

Table 5.8: Orthotropic fractions for the five materials

	Printed materials			Literature references	
Ratio	PA12	V-Onyx	CBF_{cc}	CCF [131]	Fabric [132]
$\frac{U_2}{U_1}$	0.02	0.42	1.10	1.15	0.02
$\frac{U_3}{U_1}$	0.02	0.10	0.26	0.27	0.24

5.4 Conclusions and future developments

In this chapter, two different materials were 3D printed with FFF technology and tested in simple tension to obtain a complete characterization of the in-plane properties and an evaluation of their anisotropy.

A low percentage of voids was achieved for all materials, which was allowed by the good setting of the 3D printer, and with a final effective volume fraction of basalt fiber of only 18% for CBF_{cc}.

For the co-extruded composite (CBF_{cc}), the use of continuous basalt fiber increases longitudinal stiffness and strength by more than an order of magnitude compared to the matrix (PA12). On the other hand, the transverse and shear properties are very low for CBF_{cc} and comparable to PA12. CBF_{cc} has a marked anisotropy, while the matrix shows isotropic behavior.

The anisotropic behavior of these 3D printed composites was also evaluated using the method proposed in Section 3.2.1. Virgin Onyx was taken from the previous chapter for convenience as a comparison, since it is a polyamide-based composite but reinforced with short fibers. The increasing impact of the orthotropic component on the isotropic one can be observed moving from an unfilled material to a short-fiber reinforced one and then to a material with continuous fiber as reinforcement.

For CBF_{cc}, the longitudinal properties meet structural requirements, but the transverse and shear properties are not completely satisfactory. The optimization of the fiber deposition direction, as a function of the expected external loads, can be a possible strategy to make the most out of the directionality of the material properties. Another possibility to increase

transverse and shear properties can be to perform post-treatments [133], and this may also be useful in decreasing the voids percentage.

CBF_{cc} is a 3D-printed structural composite that is more eco-friendly than the one analyzed in the previous chapter, both in terms of matrix and fiber: basalt fiber is clearly more sustainable than carbon fiber, and PA12 is preferable to PA6. Thus, a development in the direction of more eco-friendly structural composites could involve using a more sustainable vegetable-based matrix and fiber that are both compostable.

6. Continuous vegetable fiber as reinforcement in 3D printing

6.1 Introduction

The application of natural materials to additive manufacturing (AM) opens a promising pathway toward more sustainable and circular production practices. In recent years, increasing attention has been devoted to the development of bio-based composites specifically tailored for AM processes and structural applications. The usage of such materials aims not only to maximize resource efficiency and minimize waste but also to substantially reduce the overall carbon footprint compared to conventional petroleum-based polymers. In this context, the combination of biobased matrices and continuous vegetable fibers enables the production of 3D-printed biocomposites. These systems effectively combine design flexibility, inherent to AM, with the environmental and mechanical advantages of bio-based continuous reinforcements, making them promising candidates for applications in fields ranging from consumer goods to automotive and construction sectors.

The aim of this chapter is to provide a comprehensive overview of the various types of vegetable fibers currently used or considered suitable for composite and additive manufacturing applications. Particular attention will be devoted to their chemical composition, microstructural characteristics, and physical–mechanical properties, such as tensile strength, modulus, and thermal stability. Equally important will be the discussion of the inherent drawbacks associated with these fibers, including variability in properties due to agricultural and processing conditions, and issues of compatibility with polymeric matrices. Building on this foundation, the chapter will then review the most relevant and up-to-date literature on 3D-printed continuous fiber biocomposites. The goal is to map the current state of the art in terms of materials, processing technologies and achievable performance.

6.2 Vegetable fibers

Fibers of vegetable origin are composed of natural polymers: the most important ones are cellulose, hemicellulose, pectin and lignin [134]. The weight percentages of the main constituents of the different types of fibers are given in Table 6.1.

Table 6.1: Chemical composition of vegetable fibers

Fiber	Constituents				
	Cellulose [wt%]	Hemicellulose [wt%]	Lignin [wt%]	Pectin [wt%]	Wax [wt%]
Flax	71	18.6 - 20.1	2.2	2.3	1.7
Hemp	70.2 – 74.4	17.9 – 22.4	3.7 – 5.7	0.9	0.8
Jute	61 – 71.5	13.6 – 20.4	12 - 13	0.2	0.5
Ramie	68.6 – 76.2	13.1 – 16.7	0.6 – 0.7	1.9	0.3

Cellulose, hemicellulose and lignin are the basic components, which determine the physical properties of the fibers. Cellulose is the stiffest and strongest organic constituent in vegetable fibers [135]. It is a common element and also the most abundant. It is important to note that cellulose gives a hydrophilic nature to vegetable fibers, giving them the tendency to absorb water and moisture. Hemicellulose is the second most abundant polymer in vegetable fibers, and its most important biological role is to help strengthen the cell wall in synergy with cellulose [136]. Lignin is an amorphous, three-dimensionally irregular and highly branched aromatic polymer. The functions of lignin in the vegetable cell wall are to provide structural support and to protect against chemical or biological attack [135]. In addition, the lignin content increases significantly over the growth period [137]. Lignin has lower properties than cellulose and together with pectin, it is the main component of the cell wall. Understanding these aspects is essential to understand why vegetable fibers can have different properties.

In addition to the characteristics of the individual constituents, an understanding of their distribution within the fiber structure is also important for a better comprehension of the mechanical behavior of vegetable fibers (Fig.6.1). All vegetable fibers exhibit a hierarchical and complex organization that includes a central lumen. Starting from the outermost layer and

moving inwards, the primary wall is formed, followed by the secondary walls (S1, S2 and S3 layers). These layers determine the overall fiber structure. The fiber is not considered fully formed until the central lumen is closed. The secondary walls are mainly composed of helically arranged cellulose microfibrils bound together by a hemicellulose matrix, and the structure is made rigid by the presence of lignin and pectin [138]. The amorphous parts of the wall are mainly made of pectin and hemicellulose [139].

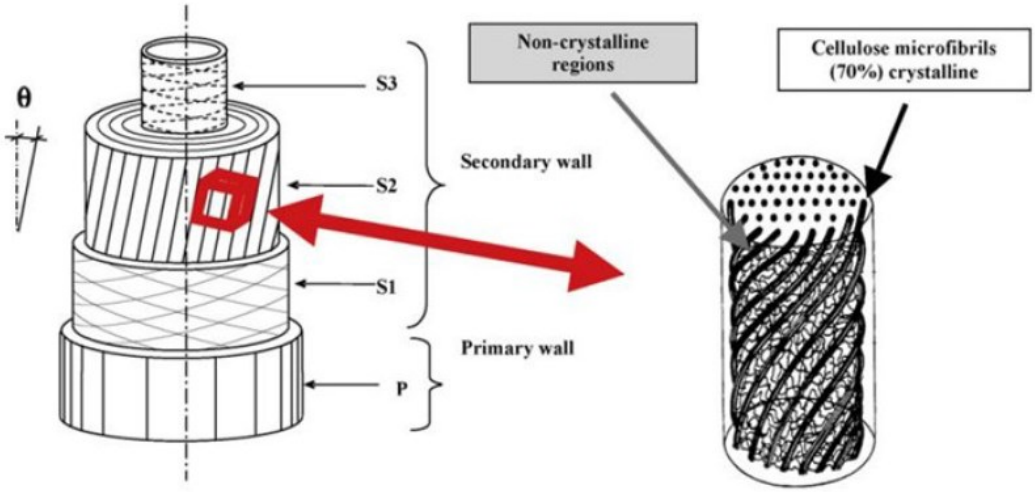

Figure 6.1: The structure of a fiber cell

The microfibril angle (θ or MFA) is the angle that microfibrils make with respect to the fibre axis, and plays a critical role in determining the mechanical properties of vegetable fibers. Higher tensile stiffness and strength are achieved with small angles of inclination of the microfibrils, as the microfibrils are more aligned with the fiber axis. Conversely, a larger MFA results in increased extensibility and reduced stiffness, as the load is distributed at an angle, allowing for greater deformation under stress [138]. Moreover, smaller diameters and a high surface area/volume ratio of the fibers increase the mechanical performance.

6.2 3D printed biocomposites: state of the art in literature

3D printing of biocomposites can be achieved using various techniques, and the most widely studied fibers in the scientific literature are jute, ramie, flax and hemp [140], [141], [142], [143].

Continuous natural fiber–reinforced biocomposites fabricated through additive manufacturing present notable advantages in terms of sustainability, performance, and design flexibility. The

use of renewable, biodegradable fibers contributes to reducing environmental impact, while maintaining a favorable strength-to-weight ratio. The combination of 3D printing technology and biopolymers enables the creation of complex, customized geometries with high mechanical performance thanks to continuous reinforcement. Furthermore, the lower processing temperatures of biopolymers help to preserve fiber properties and reduce energy consumption. These characteristics make continuous natural fiber biocomposites a promising and sustainable alternative to conventional synthetic materials [142]. Despite their potential, vegetable fiber-reinforced biocomposites in additive manufacturing still face several challenges that hinder large-scale adoption, as also noted in Section 1.3.2.2. The intrinsic variability of natural fibers is linked to a great variety of external factors such as cultivation, harvesting, and extraction, and this often results in largely heterogeneous properties and reduced reproducibility of printed parts. Their hydrophilic nature is the cause of their moisture sensitivity, affecting both processing and long-term performance. Critical issues also arise in fiber impregnation and interfacial bonding. In fact, insufficient wetting limits stress transfer and also the different chemical nature of vegetable fibers, which are hydrophilic, and common polymers, which are mainly hydrophobic, determines a generally weak interface. Finally, the relatively low thermal stability of many vegetable fibers restricts the choice of printable matrices, as degradation may occur at temperatures above 200 °C [144], [145].

This section will summarize the current state of the art in the literature, focusing on the materials involved, the tests performed, the printers and the techniques used. As almost all authors carry out thermal, morphological and fracture surface analyses, this study will only report and compare the mechanical tests performed in the various articles. The different 3D printing methods are detailed in Section 1.2.4. For convenience, In-Situ Impregnation process, PrePreg Filament technique and Out-Of-Nozzle method will be indicated with the acronyms ISI, PPF and OON respectively. In addition, the fiber volume fraction (FVF) in the final composite, the TEX value and the yarn diameter (Φ) will be reported for all analyzed biocomposites, where indicated. It is important to note that the TEX value is a direct measurement of the fineness of textile fibers. It is defined as the weight in grams of 1,000 meters of fiber or yarn; therefore, as the TEX increases, so does the diameter of the filament.

As detailed in Section 1.2.4, it is important to note that the term 'PrePreg' is used incorrectly in scientific literature related to the 3D printing of biocomposites. The filament enters in the 3D

printer as a fully consolidated solid composite filament, while in the field of classic composites, the term 'PrePreg' has a different definition. It strictly defines a semi-finished product consisting of reinforcement fibers impregnated with a polymeric matrix, typically a partially cured thermoset resin. By definition, this material requires a subsequent consolidation cycle involving heat and pressure (e.g., autoclave curing) to achieve full polymerization and final structural properties.

6.2.1 Flax fibers as continuous reinforcement

Flax is the most widely used natural fiber in 3D printed biocomposite, due to its excellent balance of mechanical performance, industrial availability and environmental sustainability. Its high cellulose content provides a good elastic modulus (typically between 27 and 85 GPa) and tensile strength values ranging from several hundreds to over 1000 MPa, making it superior to many other vegetable fibers. Thanks to its relatively low density (~1.5 g/cm^3), flax exhibits a high specific strength and stiffness, which is especially advantageous in sectors where lightweight is particularly convenient, such as automotive, marine, and sporting goods. In addition, flax cultivation is well established, particularly in Europe, ensuring a stable and competitive supply chain [135], [146], [147]. Table 6.2 summarizes the main properties of 3D printed biocomposites with continuous flax yarns found in the literature.

Most of the works reported in Table 6.2 employed PLA as a thermoplastic matrix, except for Terekhina et al. [148] and Wang et al. [149], which uses PA6 and PE respectively. In addition, Fruleux et al. [150] explores the usage of PolyButylene Succinate (PBS), PolyButylene Adipate Terephthalate (PBAT) and PolyButylene Succinate Adipate (PBSA).

Table 6.2: 3D printed biocomposites with continuous flax fiber in literature, the value in parentheses is the raster angle

Printing Technique [1]	Yarn [2]	FVF [%]	Mechanical characterization [3]	Reference
PPF	68 TEX, Φ = 0.5 mm	32.6	T (0°, 90°, ±45°)	[150]
		30.4	T (0°, 90°)	[151]
		26.4	T (0°)	[152]
		26.4	T (0°, 90°, ±45°)	[153]
		30.4	/	[154]
		32.6	/	[155]
	TEX N.D., Φ = 0.40 mm	16.0	T, B, C	[156]
	68 TEX, Φ = 0.5 mm	From 10 to 30	T, B	[157]
	TEX N.D., Φ N.D.	N.D.	B (0°)	[149]
PPF, ISI	67 TEX, Φ = 0.3 mm	55.1 (ISI), 44.1 (PPF)	T (0°), B (0°)	[158]
	500 TEX, Φ = 0.77 mm	13.5	T (0°)	[159]
ISI	67 TEX, Φ = 0.30 mm	25.3	T (0°), B (0°), EA (0°)	[160]
	TEX N.D., Φ = 0.5 mm	24.4	T (0°), B (0°)	[161]
	26 TEX, Φ = 0.16 mm	15.0	T (0°, 90°, ±45°)	[148]
	100 TEX, Φ = 0.28 mm	2.5	B (0°)	[162]
	67 TEX, Φ = 0.30 mm	38.0	/	[163]
	TEX N.D., Φ N.D.	From 18.15 to 36.35	T (0°)	[164]
OON	105 TEX, Φ = 0.35 mm	21.0	T (0°, 90°, ±45°)	[165]

[1] ISI: In-Situ Impregnation, PPF: PrePreg Filament, OON: Out-Of-Nozzle. [2] Φ diameter, N.D.: not declared. [3] T: Tensile, C: Compression, B: Bending, EA: Energy Absorption

3D Printing techniques employed

All studies based on ISI and PPF techniques were developed using modified commercial 3-axis cartesian or self-built printers. Only two published works incorporated 5-axis printers, which introduced two degrees of rotation to the plate, enabling curved samples [157] or inclined tubular structures[156] to be created.

ISI and PPF techniques are the most exploited, while Wu et al. [165] was the sole study to use flax fiber with the OON technique, utilizing the Anisoprint Composer A4 printer. This printer is based on co-extrusion and provides a constant FVF in the reinforcement areas. The other two techniques (ISI and PPF) enable the volumetric fraction of materials to be managed. In the PPF method, the volumetric fiber fraction is controlled during the pre-print filament preparation phase by adjusting the co-extrusion ratio of fiber to matrix [25], [37], [53]. Conversely, for the ISI technique, the main factor affecting the FVF is the nozzle diameter, which can be varied to change the amount of matrix extruded for a given fiber diameter. Other important parameters to consider with this technique are layer height and line width [52].

Tensile properties

The mechanical tests that are carried out are mainly tensile tests with the fibers deposited at 0°, i.e., parallel to the direction of load application, while only a few jobs print and study other printing directions (90°, 45°) [148], [150], [151], [153], [165].

The FVF depends on the printing technique used, and having a higher FVF leads to higher mechanical performance, thanks to the increased presence of reinforcing fibers. This can be seen by analyzing the mechanical properties at 0° in relation to the respective FVFs of various works in the literature (Fig.6.2): both Young's modulus E^{0° (Fig.6.2a) and maximum stress at break $\sigma_{max}^{0^\circ}$ (Fig.6.2b) decrease as FVF decreases.

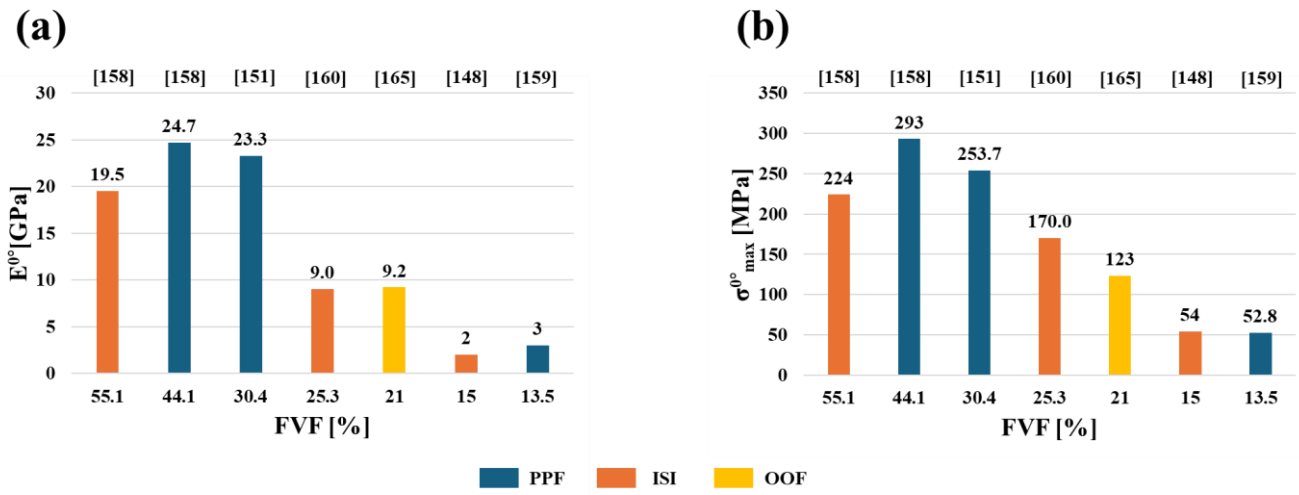

Figure 6.2: Comparison based on FVF for a) Young's modulus and b) maximum stress at break of samples at 0° tested in the literature for flax reinforcement

When the fiber volume fraction in a composite becomes too high, mechanical properties can actually decrease, as can be seen from Long et al. [158] with ISI technique. The reasons are multiple: first, excessive fiber content hampers matrix impregnation, giving rise to voids, pores, and poor wetting. Second, load transfer from matrix to fiber becomes less efficient, especially when the interface bonding is weak, or fibers are misaligned. Third, fiber-fiber interactions (agglomeration, entanglement, waviness) increase defects and reduce uniform stress distribution. Lastly, there are stress concentrators in zones with poor matrix presence, which reduce tensile properties. Thus, there is an optimal fiber volume fraction, beyond which adding more fibers does not help and often hurts mechanical performance [166], [167]. Conversely, lower tensile properties are associated with a smaller FVF. Terekhina et al. [148] used a PA6 as matrix with very low mechanical properties (E=0.7 GPa, σ_{max}=34 MPa) and a very thin flax fiber with below-average performance (E=24 GPa, σ_{max}=377 MPa). Therefore, the values shown in Figure 6.2 are due to the combination of the low mechanical properties of the base materials with the volumetric fraction of reinforcement at 15%.Instead, Dos Santos et al. [159] produced the biocomposite on a large scale. They did this by printing with a nozzle diameter of approximately 3 mm, combining the PPF and ISI techniques, thereby achieving a low FVF.

Other types of characterization and testing

Fruleux et al. [155] investigated the geometric limitations related to 3D printing with continuous flax fiber, such as the minimum diameter required for tubular structures and the optimal radius for corners. Several studies have focused on specific aspects of 4D printing. Time is considered the fourth dimension because, unlike 3D printing, which produces static objects, 4D printing produces objects that can dynamically change shape and/or properties over time when exposed to external stimuli such as heat, humidity, light, magnetic fields and pH changes. With regard to that, Fruleux et al.[150] and de Kergariou et al.[154] characterized the hydro-expansion properties that underlie 4D printing. Le Duigou et al. [152], Wang et al. [149] and Long et al. [163] explored the effect of the printing parameters on the mechanical performance of the 3D printed biocomposite. The most interesting results are that a reduction in the layer height leads to lower porosity and higher strength, and a low printing speed is recommended to promote adhesion between lines and thus overall mechanical performance.

6.2.2 Ramie fibers as continuous reinforcement

The second most widely employed and studied fiber is ramie, also known as chinese nettle. This type of fiber is gaining attention among natural fibers due to its notable mechanical properties, relatively low density, and environmental benefits. With a high cellulose and very low lignin content, ramie exhibits excellent tensile strength (≈220–938 MPa) and Young's modulus (≈44–128 GPa). Its density (~1.5 g/cm^3) results in a favorable specific strength and stiffness, making it suitable for lightweight and strong applications. Today, China is the world's leading producer of ramie, followed by Japan and other far eastern countries. This crop has a low environmental impact and a rapid growth cycle, which has contributed to its rapid market expansion. To date, the main challenge is the process of extracting ramie fiber, which is energy and chemical-intensive, affecting the overall sustainability of the fiber [168], [169]. The main works focusing on ramie fiber are described in Table 6.3.

All works carried out on ramie fibers was performed using the ISI technique and PLA, except for Cai et al. [170], which used PP.

Compared to flax fiber, much more work has focused on analyzing the effect of printing parameters on the mechanical performance of 3D-printed biocomposites [171], [172], [170],

[173], [174]. The trend is the same as that observed with previous fibers. It has also been found that excessively high processing temperatures can degrade the fibers, thereby reducing their mechanical performance. Greater attention was paid to the compression and energy absorption properties of ramie fibers by comparing fully filled samples and optimized structures[175], [176], [177] . Despite this, tensile tests remain the most widely used characterization method [179], [171], [174], [180], [178] .

Table 6.3: 3D printed biocomposites with continuous ramie fiber in literature, the value in parentheses is the raster angle

Printing Technique [1]	Yarn [2]	FVF [%]	Mechanical characterization [3]	Reference
ISI	42 TEX, Φ = 0.40 mm	20.1	T (0°, ±45°)	[179]
	310 TEX, Φ = 1.00 mm	14.6	T (0°)	[171]
	28 TEX, Φ = 0.35 mm	N.D.	T (0°)	[174]
			T	[180]
	42 TEX, Φ = 0.40 mm	N.D.	T, C, EA	[178]
	330 TEX, Φ = 0.74 mm	17.2	B (0°)	[162]
	28 TEX, Φ = 0.35 mm	From 24.3 to 39.1	C, EA	[177]
	42 TEX, Φ = 0.40 mm	20.1	C, EA	[176]
	28 TEX, Φ = 0.35 mm	24.3	EA	[175]
	28 TEX, Φ = 0.35 mm	24.3	/	[175]
	310 TEX, Φ = 1.00 mm	14.5	/	[173]
	28 TEX, Φ = 0.35 mm	N.D.	/	[170]
	42 TEX, Φ = 0.40 mm	N.D.	/	[172]

[1] ISI: In-Situ Impregnation, PPF: PrePreg Filament, OON: Out-Of-Nozzle. [2] Φ diameter, N.D.: not declared. [3] T: Tensile, C: Compression, B: Bending, EA: Energy Absorption

6.2.3 Other fibers of different nature as continuous reinforcement

Other vegetable fibers explored in the literature are juta, sisal and hemp. These are less common in 3D printed composites than flax and ramie for a combination of reasons related to mechanical properties, processability, availability, and chemical-physical characteristics. These fibers have a much higher lignin content, making them incompatible with most polymer

matrices and results in the composite being very stiff and brittle. This can lead to problems during spinning and weaving. They are also heterogeneous and coarse due to less standardized cultivation and harvesting conditions. In contrast, flax and ramie have more established supply chains and more uniform fibers. These fibers are less competitive for engineering composites, so they remain attractive only for more economical or non-structural applications (bags, carpets, geotextiles, padding). Table 6.4 provides the main details of the work on 3D printed biocomposites made with less common continuous vegetable fibers. Regardless of the type of fiber used, PLA has always been used as the matrix. ISI and PPF techniques are the most exploited, while Ginoux et al. [181] was the only study to use OON technique, in particular with the Anisoprint Composer A4 printer. The effect of printing parameters on mechanical properties [40], [54], [56], and on print quality and geometric aspects [42], [57] has also been extensively studied.

Table 6.4: 3D printed biocomposites with less common continuous vegetable fiber in literature, the value in parentheses is the raster angle

Fiber type	Printing Technique [1]	Yarn [2]	FVF [%]	Mechanical characterization [3]	Reference
Jute	ISI	250 TEX, Φ = N.D.	6.1	T (0°)	[185]
				/	[186]
		330 TEX, Φ = 0.52 mm	17.2	B (0°)	[162]
				T (0°)	[171]
				/	[173]
Sisal	ISI	1800 TEX, Φ = 1.39 mm	41.2	B (0°)	[162]
				T (0°)	[171]
				/	[173]
Hemp	PPF	(TEX, Φ) N.D.	N.D.	T (0°)	[187]
	OOF	316 TEX, Φ N.D.	33.3 (Pure) 26.4 (Com.)	T (0°)	[181]
Cotton	ISI	TEX N.D., Φ=0.16 mm	From 5.0 to 8.9	T (0°), B (0°)	[184]
	PPF	TEX N.D., Φ=0.6, 0.8, 1.0 mm	From 10.2 to 35.3	B (0°), EA (0°)	[188]

Pineapple leaf	ISI	TEX N.D., Φ=0.1 mm	25.0	T (45°)	[182]
Banana	ISI	TEX N.D., Φ=0.19 mm	N.D.	/	[183]

[1] ISI: In-Situ Impregnation, PPF: PrePreg Filament, OON: Out-Of-Nozzle. [2] Φ diameter, N.D.: not declared. [3] T: Tensile, C: Compression, B: Bending, EA: Energy Absorption

Tensile properties

Tensile tests are the most prevalent [171], [173], [181], [182], [184], [185], [187]. Similarly to what was previously done for flax fibers, Figure 6.3 reports the mechanical properties at 0° (E^{0°, $\sigma_{max}^{0^\circ}$) in relation to the respective FVFs of various works in the literature for all the other vegetable fibers used.

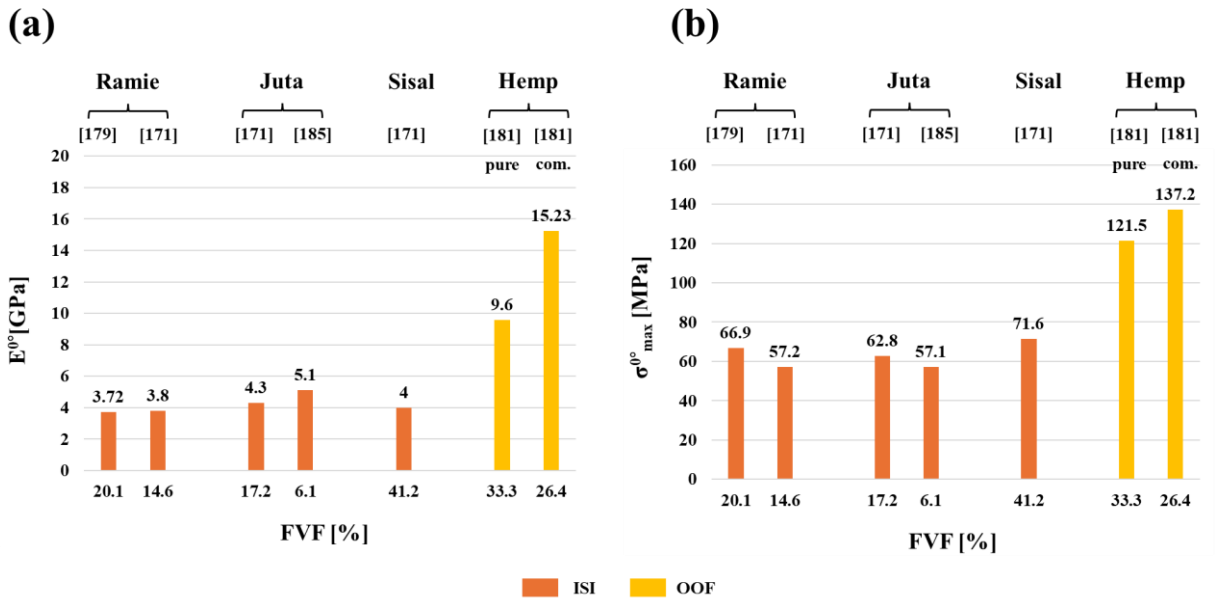

Figure 6.3: Comparison based on FVF for a) Young's modulus and b) maximum stress at break of samples at 0° tested in the literature for all fibers other than flax

As with flax fibers, the same trend in mechanical properties can be observed for ramie fibers as FVF decreases [171], [179]. This is particularly evident in terms of strength. For stiffness, however, there is a small difference that can be explained by the intrinsic variability of the fiber and the method used by the different authors to evaluate Young's modulus. Dos Santos et al. [171] produced a biocomposite reinforced with jute fiber that has an FVF of 17.2%, whereas the FVF of that produced by Matsuzaki et al. [185] is only 6.1%. Although the latter has a

reinforcement percentage of about one third compared to the former, it has greater stiffness and slightly lower strength. The authors explain these low mechanical properties based on the combination of large-scale 3D printing and the size of the fibers used, which have a diameter of 0.52mm. The impregnation of the fiber by the matrix has a significant impact on load transfer capacity and fiber-matrix adhesion, which affects the composite performances. A very interesting result was obtained by Ginoux et al. [181] in tensile tests on biocomposites reinforced with hemp fiber. The as-purchased hemp yarn was compared with a hybrid yarn prepared by commingling with PLA, before printing. The hybrid yarn-based biocomposite exhibited a higher impregnation rate accompanied by a reduced void content, more aligned fibers, and a more homogeneous distribution of the different constituents, resulting in significantly higher mechanical properties. Superior mechanical performance was obtained while having lower fiber fraction with the use of hybrid yarns, raising awareness about the importance of improving the impregnation of the vegetable fibers as well as the FVF.

6.2.4 Key common features among the works analyzed

Regardless of the type of continuous fiber used to create the 3D-printed biocomposite, certain key features can be observed in all of the analyzed works.

3D Printing techniques employed

ISI and PPF are the most widely used 3D printing techniques for biocomposites. Both techniques allow higher volumetric fractions to be achieved, but the printing process is more complex to manage, because in both cases commercial printers need to be modified and G-Code programmed [157], [179], [184], [188]. These systems are ideal for testing samples with simple shapes that are fully filled with reinforcing fiber in each layer. However, they are not suitable for producing components with complex shapes, for which path programming is crucial, nor for reinforcing only certain layers if specific mechanical properties are required. For these reasons if 3D printed biocomposites must be used for structural applications in as many sectors as possible, they must be implemented in the simplest, most standard and automated way that is possible. Only Ginoux et al.[34] and Wu et al.[53] worked with OON printers. Specifically, they used the Anisoprint machine, which has already been developed and marketed for the 3D printing of continuous fiber-reinforced composites. It is important to note that both authors state that they modified the composite coextrusion system to adapt it to

natural fiber yarn. As detailed in Section 5.2.2, Anisoprint implements two different fiber feeding techniques to ensure continuous fiber deposition. Active feeding pushes both the continuous fiber and the TP matrix into the coextrusion chamber, through the action of both feeding motors. On the other hand, with passive feeding the fiber motor is switched off and the TP matrix motor is switched on. In doing so, the fiber is pulled by the movement of printhead and the extrusion of the matrix simultaneously. In both works, the fiber is always printed in passive mode only. Therefore, the process is comparable to ISI printing, and the technology that has already been developed and is available is not being fully exploited.

Tensile characterization

In order to use 3D-printed biocomposites for structural applications, it is essential to understand how they perform mechanically. From a design and application point of view, the first step is to characterize their in-plane mechanical properties, as detailed in Section 3.2. Since continuous fiber reinforced composites tend to be anisotropic, for a complete characterization, it can be assumed that 4 independent constants are required for stiffness and 3 for strength. These are associated with longitudinal, transverse, and shear properties: the first two are obtained from samples printed at 0° and 90° respectively, through ASTM D3039 [79], while the shear properties are evaluated from samples at 10° or with the $[\pm 45°]_{ns}$ stacking sequence, via 10° off-axis method and ASTM D3518 respectively [80], [81], [82]. Regardless of the type of reinforcing fiber or printing technique used, all papers performed tensile tests 0°. Only a few also printed at 90° [148], [150], [151], [153], [165], while a few more also printed at 45° [148], [150], [151], [153], [165], [179], [182]. For the latter orientation, in all tests the samples do not comply with the shear characterization, as each layer is printed at 45° and the sequence indicated by the standard is not followed. De Kergariou et al. [153] was the only study that carried out a complete characterization of the in-plane mechanical properties, through standards mentioned previously. The paper describes the influence provided by humidity on the mechanical and failure properties of 3D printed composites made by continuous flax fibers reinforcing a PLA matrix. The samples were specially conditioned prior to testing to achieve specific moisture content levels. The longitudinal and transverse elastic moduli of the composites, together with their transverse and shear strengths show an almost exponential decay with the increase of the moisture content. However, the longitudinal strength remains constant over the range of relative humidity considered. This work was carried out using the PPF method and the samples were made with a customized Prusa i3 MK3S printer.

Pre-printing fiber treatment

Regardless of the type of reinforcing fiber, the work of Ginoux et al. [181] was one of the few to focus on the pre-print fiber preparation method. Quereilhac et al. [164] have developed similar work, comparing the properties of flax fiber as is with those of a hybrid yarn commingled with PLA. The trend is the same as that found by Ginoux et al. [181]. Intra-yarn porosity decreases and mechanical properties increase thanks to commingling. Other studies have proposed a different pre-printing approach, focusing on chemical treatments of the fiber. Long et al. [160] used silane coupling agents to treat the surface of flax yarns, improving their wettability and interfacial performance. It was found that the mechanical properties of the biocomposites were greatly improved after the treatments which induced very low void contents of less than 1.1%, due to the improved wettability and the interfacial bonding between the flax yarns and resin matrix. Instead, Song et al. [188] based the work on alkali treatment of cotton fiber. Also in this case, the mechanical performance improved after the treatment. All other works reported in this literature review use natural reinforcement fibers as they are, regardless of the printing technique.

6.3 Conclusions and future developments

Among continuous natural fibers, flax and ramie are currently the most widely ones employed as reinforcement in the 3D printing of biocomposites. Their predominance is largely attributable to the existence of a well-established industrial supply chain, which ensures availability, processing know-how and relatively consistent quality. In addition, these fibers exhibit superior intrinsic characteristics compared with other vegetable reinforcements, lower variability in cross-section and fineness, and a more regular surface morphology that facilitates impregnation and bonding with thermoplastic matrices during the additive manufacturing process. These factors collectively make flax and ramie particularly suitable for the production of continuous-fiber reinforced structures via 3D printing, where both reproducibility and mechanical performance are critical.

From this analysis of the state of the art of 3D-printed biocomposites reinforced with continuous vegetable fiber, it is clear that there are still some aspects to be explored. To the best of the author's knowledge, only one paper provides a complete characterization of the in-plane mechanical properties of the composite [153], through PPF method. To use these biocomposites for structural and industrial applications, they must be manufactured using

processes and technologies that make them easy to produce, in the most standard and automated way that is possible. Only two works use OON technology, through printers already developed and marketed for 3D printing of continuous fiber composites [165], [181]. However, both papers claim to have modified the printing part of the composite and do not complete a full characterization of the mechanical performance. Finally, there are few studies that focus on the preparation of the fiber prior to printing [181], [160], [188]. These individual aspects, or combinations of them, offer ample scope for future development.

7. Continuous vegetable fiber preparation phase: workflow and fiber analysis

7.1 Introduction

As described and analyzed up to now, the in-situ impregnation technique and the prepreg method have been applied mainly within academic and research settings, whereas the out-of-nozzle approach has already achieved broad commercialization. This latter process has been developed and marketed for several years by the industry leader Markforged, which pioneered the first commercial CFRTPC solution. Alternatively, Anisoprint has implemented a co-extrusion method, positioning it as a complementary option to the Markforged system. As described in Chapter 4, the Markforged printer is designed for industrial applications and ready-to-use components. Consequently, the range of materials is limited, as are the process parameters that can be modified. These restrictions imposed by the manufacturer, coupled with the inherent variability of vegetable fibers, severely limit the use of this printer with this type of reinforcement. Therefore, a more flexible technological solution is required to use vegetable fiber as continuous reinforcement with a commercial printer. Instead, as discussed in Section 5.2.2, the Anisoprint printer offers greater flexibility in terms of process parameter modifications and can accomodate different materials for both the matrix and fiber reinforcement. It therefore represents a viable industrial solution for producing 3D-printed biocomposites.

For Anisoprint machines, the fiber moves through a series of predetermined zones and channels before printing begins, ensuring the printing process is automatized. The channels leading from the spool to the coextrusion head have a diameter of 1 mm, while coextrusion occurs through a 0.8 mm nozzle (Section 5.2.2). Since a sufficient amount of matrix must be extruded while ensuring that the nozzle does not get clogged, a maximum acceptable diameter of 0.5 mm is reasonable. The fiber must also move through its specific feeding system, to fully take advantage of the available technology. Therefore, the reinforcing fibers used must meet the dimensional and physical requirements necessary for handling and 3D printing.

In order to meet these last two requirements, the vegetable fiber must be as consistent as possible in terms of yarn diameter and shape. One solution to these issues is to create a coated

filament with a final diameter that is suitable for passing through all the channels and for automated use by the printer without clogging.

Reinforcing filament can be made by coating the vegetable fiber with a thermoset or thermoplastic matrix. Using the latter, however, presents several key difficulties. First, achieving strong fiber–matrix adhesion is challenging because many thermoplastics have limited chemical affinity with vegetable fibers. This can result in weak interfaces and reduced load transfer. Furthermore, incomplete impregnation or gas entrapment during manufacturing can generate micro-voids within the filament, which act as stress concentrators and degrade mechanical performance of the printed part. Finally, the combination of high viscosity and fiber irregularity complicates the achievement the uniformity of final prepreg diameter , especially since small dimensions and tight tolerances are required [189], [190], [191].

A thermoset matrix is preferable for the last two reasons, especially because it helps guarantee adequate dimensional tolerances. The crosslinking reaction during curing further stabilizes the filament shape, minimizing shrinkage or deformation. On the other hand, the use of thermoset resins comes with an environmental trade-off: unlike thermoplastics, they are often only partially derived from vegetable origin and in any case they cannot be remelted. This limits the eco-sustainability of the final material [192], [193].

The choice between thermoset and thermoplastic matrices represents a compromise between process reliability and mechanical performance versus recyclability and ecological considerations. For this project, a thermoset resin was chosen in an attempt to standardize the shape of the fiber as much as possible and meet the printer's dimensional requirements, despite a slight reduction in sustainability.

There are two main techniques for producing coated filaments with thermosetting resins, distinguished primarily by the mechanism used to initiate resin curing. In the first one, the resin is hardened through the application of heat during or immediately after coating, triggering thermal curing. This method presents a significant limitation when continuous vegetable fibers are used, as prolonged exposure to elevated temperatures can lead to fiber degradation, reduction in tensile properties, and loss of structural integrity. The second approach relies on curing induced by exposure to ultraviolet (UV) light. This technique allows the resin to polymerize at much lower temperatures, thereby minimizing thermal stress on the fibers and preserving their mechanical performance.

Recent studies exploring the production of coated filaments for 3D printing of thermoset composites have investigated both thermal and UV curing methods, each presenting distinct advantages and limitations. Rahman et al. [194] dealt with continuous carbon fiber-reinforced composites using UV-curable thermoset resins, demonstrating that UV-induced curing allows efficient polymerization at low temperatures, preserving fiber integrity and enhancing mechanical performance. A follow-up study by Rahman et al. [195] compared dual-cured composites (employing both thermal and UV curing), showing that careful optimization of these conditions can improve mechanical properties while maintaining process flexibility. Mantelli et al. [196] focused on UV-assisted 3D printing using thermally and mechanically recycled carbon fibers, combining environmental benefits with acceptable structural performance, though emphasizing challenges in achieving uniform impregnation. Finally, Yang et al. [197]presented a rapid in-situ thermal curing approach, enabling high-speed processing of engineering thermoset composites, but also highlighting the risk of fiber degradation due to elevated temperatures.

Overall, these studies illustrate a trade-off between curing method, processing temperature, and material integrity: UV-based techniques favor fiber preservation and lower processing temperatures, while thermal curing allows rapid production but requires careful control to avoid fiber degradation. The choice of resin and fiber type, as well as the curing strategy, thus directly influence the quality, reproducibility, and performance of 3D-printed thermoset composites. Consequently, both methods require careful optimization of processing parameters (e.g. exposure time, resin viscosity, and fiber alignment) to balance curing efficiency with the preservation of fiber integrity and overall filament quality.

To the best of the author's knowledge, the literature on coated filaments is limited to continuous carbon fiber with thermoset resins. There are currently no studies exploring the use of vegetable or natural fibers.

This chapter details the development of two-stage curing process for the production of coated filament made by continuous vegetable fibers and thermoset resin. The aim is to obtain consistent dimensions that are suitable for use with a commercial printer that has been specifically developed for continuous fiber-reinforced composites. The resulting filament will be analyzed using morphological and statistical analysis. Flax fiber was chosen as the vegetable reinforcing fiber for this project. The selection is based on the fiber higher properties,

its lower variability in dimension, and its more regular surface morphology compared with other vegetable reinforcements, as detailed in Chapter 6.

7.2 Materials and methods

7.2.1 Materials

Fibers

In this study, three different resins and two types of flax fibers were considered. The fibers were provided by Linificio e Canapificio Nazionale Srl (Bergamo, Italy) and their difference was related to the pretreatment operated by the manufacturer to remove impurities to enhance resin impregnation and to standardize the morphology regarding diameter and surface cleanliness[198], [199], [200]. As stated by the supplier, one fiber type was only boiled in caustic soda and calcium carbonate, while the other one was also bleached in hydrogen peroxide after the previous treatment. The initial boiling phase acts as chemical wash, removing as much as possible non-cellulosic substances naturally present in the fiber, such as pectin, lignin, waxes, fats and oils. Cleaning hydrophobic and low-polarity substances allows the fiber to open up and expose cellulose and hemicellulose, which are naturally hydrophilic and polar due to their hydroxyl groups ($-OH$). Subsequently, the hydrogen peroxide bleaches the fiber by oxidizing the lignin, pectin and residual waxes, thereby cleaning impurities more thoroughly. This makes the fiber more uniform and absorbent by increasing the exposure of cellulose and, consequently, the polar groups($-OH$).

Both fibers were selected based on a comparable linear density (TEX), to ensure equivalent fineness for comparison purposes and to meet the dimensional requirements described previously. For the purposes of this study, BO refers to flax fiber that has only been boiled, while BL refers to flax fiber that has been subsequently bleached.

The characteristics of the fibers from the manufacturer datasheets are shown in Table 7.1, and all data (yarn strength, TEX values, thick and thin places, neps, and the coefficient of variation of mass CVm) refer to average yearly production values. Thick and thin place values are related to localized bulges and thinner points due to poor spinning regularity. Neps are small clumps or nodules of fibers formed during harvesting or processing. Finally, CVm quantifies the variation in linear density along the yarn axis, providing a comprehensive measure of mass unevenness over the tested length. In practical terms, a high CVm reflects significant variations

in the yarn cross-section, appearing as sudden accumulations of fibers (slubs) followed by thinner segments. The uniformity and regularity of the yarn is directly related to the values of these four parameters; lower values indicate a more uniform and regular yarn. These parameters show that boiled fibers appear to be slightly more irregular than bleached fibers.

Table 7.1: Flax fiber properties from technical datasheets

	Fiber type	
Property	BO	BL
TEX	18	20
Average strength [MPa]	260	280
Average stiffness [GPa]	17	19
Thick place (+50%)/km	1307	1270
Thin place (-50%)/km	2252	1870
Neps (+200%)/km	4068	4051
CVm [%]	29	28

Resins

For the coating, a UV-curing thermoset resin was selected. The chemical composition of a UV-curable resin typically includes a photoinitiator and a monomer or oligomer. Exposure to the UV source causes the photoinitiator to decompose, initiating the polymerization reaction. After that, a crosslinker binds the polymer chains together, giving them hardness and strength. As a result, the monomer or oligomer reacts with reactive species, forming long polymer chains. The longer the chains become, the more viscous and solid the material becomes. The presence of pigments or additives reduces the depth of cure and consequently increases the time required to complete the process.

The main parameters that influence UV curing are wavelength, radiation intensity, exposure time, thickness, distance and temperature[201], [202]. The typical wavelength range is between 365 and 405 nm. If the UV light is not in the correct band, polymerization will be incomplete or slow. Insufficient UV radiation intensity causes under-polymerization and fragility, while an excessive dosage causes over-polymerization, resulting in yellowing and distortion. Exposure time must be calibrated according to the intensity and type of resin. Too

little time results in soft parts due to possible incomplete curing, while too much time causes brittleness and distortion. Thicker layers require longer times because UV light penetration is reduced. The distance between UV source and the resin is linked to the time to complete the process. Higher temperatures accelerate the reaction but can introduce internal stress.

Three different UV-curing thermoset resins were considered in this work. They were all developed for use with SLA technology and thuscure in the wavelength range between 365 and 405 nm.

The first resin, namely 'UV Plant-Based', was purchased from Anycubic (Shenzhen, Guangdong, China) and was chosen because 45% of its weight is derived from soybean oil. The other two resins were both purchased from Formlabs (Somerville, Massachusetts, USA) under the trade names 'Fast Model' and 'Rigid 10K'. They were selected as the fastest and most rigid commercially available products, respectively. They will be referred to as Fast and Rigid.

Table 7.2 shows the main characteristics of the resins, as taken from the technical datasheet. The heat deflection temperature (HDT), which indicates thermal resistance, i.e. the temperature limit at which the mechanical properties are guaranteed, is also reported. Resin type "Rigid" is reinforced with glass powder, which results in the best performance concerning both mechanical and thermal properties, and the highest density. On the other hand, "Plant" is the lightest but has the lowest thermo-mechanical performance. "Fast" is intermediate and was considered because the manufacturer claims it cures faster than the others, so it could be useful for maintaining dimensional tolerances.

Table 7.2: UV-resins properties from technical datasheets

	Resin type		
Property	Plant	Fast	Rigid
Density [g/cm^3]	1.10 - 1.25	1.12	1.63
Young's Modulus [GPa]	0.45	2.67	10
Tensile strength [MPa]	36	62	53
HDT @ 0.45 MPa [°C]	60	76	218

Table 7.3 lists the main components of the resins investigated in this study, as obtained from the Material Safety Data Sheet (MSDS). All resins used in 3D printing with SLA technology are mainly based on acrylates and methacrylates. The differences are in the chemical composition of the starting base, the type of initiator, and the crosslinker.

“Fast” has a more classic and “rapid” formulation for UV, characterized by a high percentage of methacrylic monomer with low viscosity, which guarantees fast polymerization and greater surface hardness. In this resin, phosphine oxide is used as the photoinitiator and urethane dimethacrylate as the crosslinker.

“Rigid” also uses this type of crosslinker, but at a higher percentage (≈ 25 wt%). Isobornyl methacrylate, a very low molecular weight monomer, was used to ensure the high glass powder content.

”Plant” resin is a more bio-based solution, incorporating epoxidized esters derived from soybeans. This acts as a plasticizer, improving flexibility and decreasing overall mechanical performance, as shown in the properties listed in Table 7.2. Furthermore, “Plant” resin is an acrylate rather than a methacrylate, which is stronger than the former. To counteract this to some extent, a multifunctional diacrylate is used as a cross-linker, making the resin stiffer and more brittle. By contrast, the urethane dimethacrylate used in the other two resins produces a tougher, more elastic result.

Table 7.3: Main components and relative wt% present in the three resins considered

Substance role	Plant	Fast	Rigid
Chemical base	Acrylates (30%) + epoxidized esters derived from soybeans (45%)	Methacrylates (≈ 85%)	Isobornyl methacrylate + glass powder (65 %)
Photoiniziator	Hydroxyketone (10%)	Phosphine oxide (<1%)	N.D.

Crosslinker	Multifunctional diacrylate (15%)	Urethane dimethacrylate (≈ 15 %)	Urethane dimethacrylate (≈ 25 %)

To achieve effective coating between the flax fiber and the resin, it is important that they are chemically compatible. Acrylate resins are highly reactive due to their abundance of vinyl double bonds. On the other hand, flax fiber is primarily polar because of cellulose, which is rich in $-OH$ groups. These hydroxyl groups can form hydrogen bonds with the acrylates, but stable covalent bonds are not created unless specific functional groups are introduced. As mentioned previously, the growth in polarity and availability of $-OH$ groups is linked to the boiling and bleaching processes. This increase in hydroxyl groups promotes a greater number of interactions with the acrylates, improving both hydrogen bonding and the wettability of the fiber. The increase in hydrophilicity, while beneficial for adhesion, presents an additional challenge: a greater sensitivity to water adsorption. This can lead to a risk of degradation and a loss of adhesion in humid environments. Furthermore, without a compatibilization treatment (such as silanization, acetylation, or grafting with methacrylates), adhesion remains predominantly physical rather than chemical (non-covalent).

7.2.2 Two-stage curing process

This section will provide a detailed description of the system developed for coating flax fiber with thermoset resin. As these resins were developed and marketed specifically for SLA technology, the typical workflow of this additive manufacturing process inspired the creation of the coated filament. Using SLA technology, the initial UV curing is only partial, leaving the part in a 'green state' because the resin has not fully cross-linked yet. Next, the component is washed in isopropyl alcohol (IPA) to remove any uncured resin. This step is essential to prevent residual resin from curing randomly afterwards, which can result in lumps forming, loss of detail or dimensional changes. Finally, a post-curing phase is carried out using a UV and/or thermal source to encourage the complete cross-linking of the resin. The workflow is therefore divided into two parts: an initial stage that includes UV treatment and washing, and a secondary stage of post-curing and dimensional control. In both stages, homemade devices were developed, consisting of both commercial and non-commercial parts. The latter were all 3D printed, fully filled, using a Sovol SV06 printer and PLA, with an extrusion temperature at 210 °C and with 0.4mm nozzle. Printer and material are both supplied by Sovol (Shenzhen, China).

First-stage

The first stage of the coated filament production process was carried out using a custom-built device, consisting of four main parts (Fig.7.1). The overall dimensions have been designed to allow sufficient room to monitor each phase. The system is fixed on a base consisting of a laminated wooden board. The initial fiber spool is held in place by a central cylinder fixed to the board. This ensures that the spool can freely rotate while preventing it from slipping off. At the beginning, the fiber unwinds and is guided to the next zone by two 3D printed guides screwed directly onto the wooden basement (zone 1 in Fig.7.1). Next, the fiber passes into a second zone consisting of a tray containing the thermoset resin (zone 2 in Fig.7.1). It then proceeds to the UV curing zone (zone 3 in Fig.7.1) before being collected on a final spool. The winding is powered by a three-phase asynchronous motor, which is mounted on a commercial metal frame made (zone 4 in Fig.7.1).

The individual areas will be described in more detail below, both in terms of their function and constituent parts. It is important to note that the configuration for each area represents the final and optimized design.

In the current process, two separate impregnation steps are made in the resin tray, one immediately following the other, to make the shape of the fiber as uniform as possible. After the first step, the spool containing the fiber is removed from the motor and repositioned at the beginning of the first zone. The fiber then retraces the entire path and is wound onto a new spool.

Preliminary analyses have indicated that there is no significant increase in fiber diameter between the first and second impregnation steps. Therefore, for the remainder of this study, the measured diameters of the coated filament will refer to the final pass.

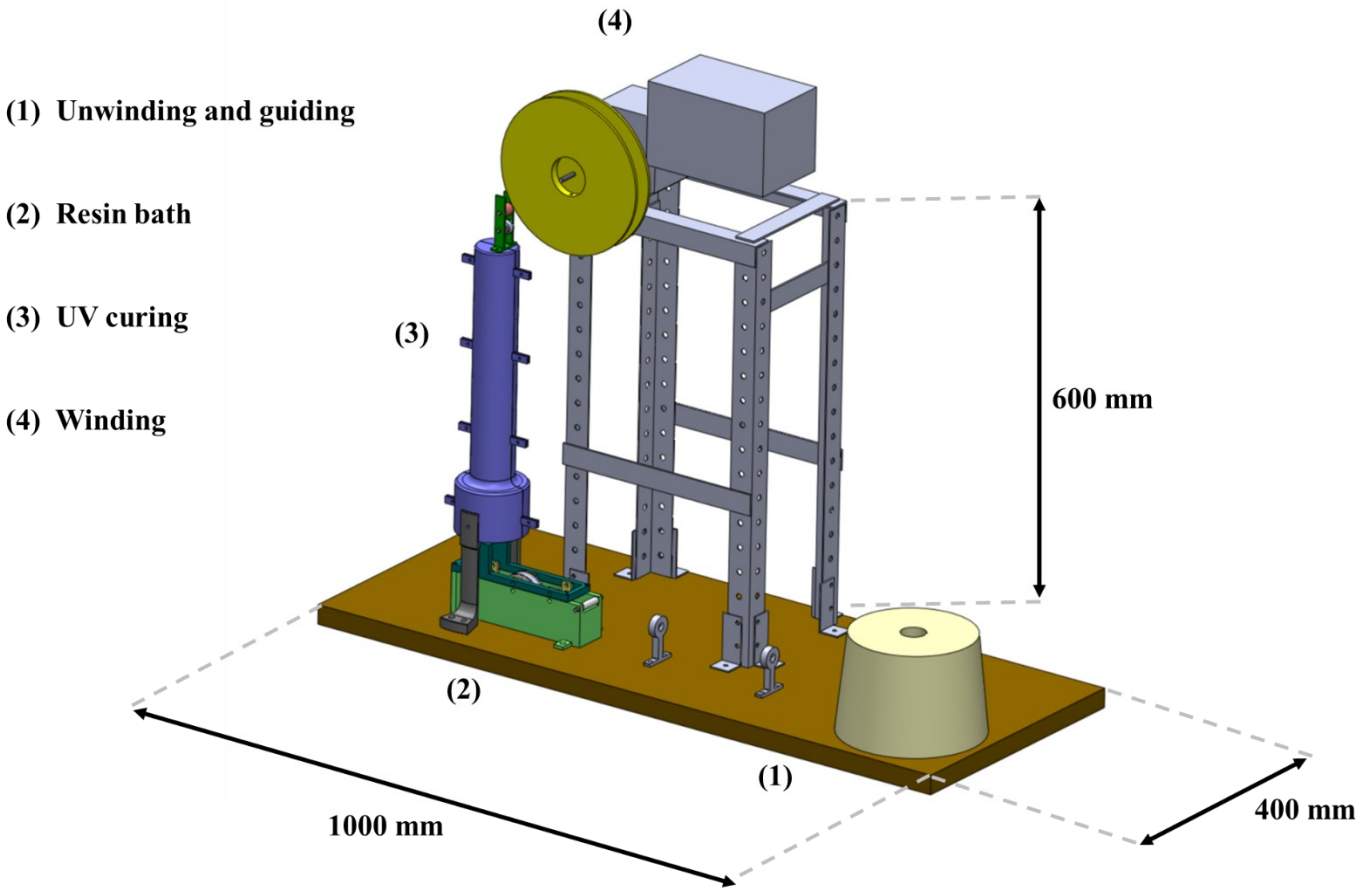

Figure 7.1: The four main areas of the device developed for the first stage

Resin bath

The structure of the resin bath tray consists of a base and a top cover (Fig.7.2a). Figure 7.2b shows a top view detailing all components and their positions. The tray base is screwed directly to the wooden platform. The top cover has been attached to the base using four screws at the corners. The base utilizes hot-plugged inserts, to provide secure, functional connection points for the components.

At the inlet tray, a nylon cylindrical guide is positioned to facilitate the entry of the fiber and prevent it from rubbing. Inside the tray there are three nylon wheels (Masidef, Varese, Italy) to guide the fiber towards the exit: two with a diameter of 40 mm and one with a diameter of 60 mm. All wheels have a central recess on their outer surface to ensure that the fiber remains centered. At the tray outlet there is a fabric roller with a diameter of 17 mm (Tecnomat, Milan, Italy), which can be moved and adjusted thanks to a buttonhole in the tray's closure part. Both the fabric roller and the cylinder at the entrance have a central through hole, which allows for

the use of a small M5 threaded bar for closure and connection to the upper part. The first one is completely locked in place once the correct position has been found, while the second one is left free to rotate, thus facilitating the sliding of the fiber. The internal wheels are held in place by supports, enabling free rotation. To ensure correct positioning, these supports are connected with M5 screws to both the tray base and the upper cover.

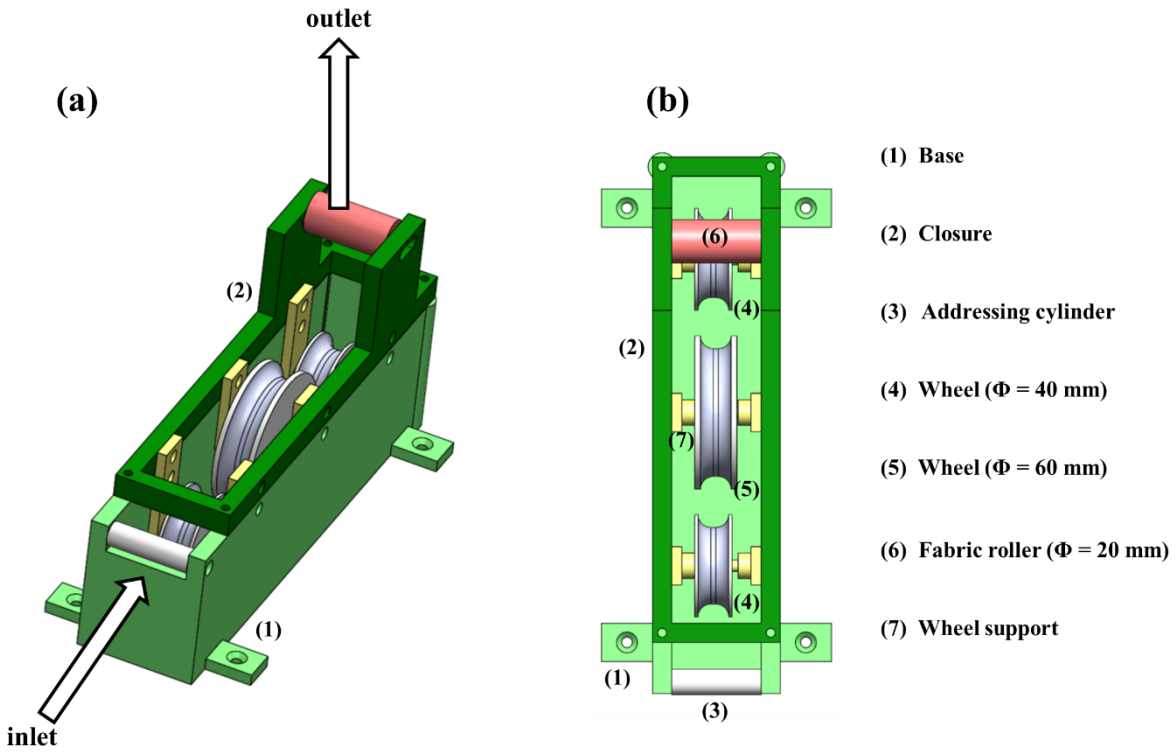

Figure 7.2: Resin tray in a) axonometric and b) from above view

Figure 7.3 shows in more detail the path that the fiber follows inside the tray, presented through a cross-sectional view. This configuration for the wheels has been optimized to maximize the efficiency of the winding motor, keeping the fiber taut and centered in the tray. Considering that the resin fills the tray to almost half its depth, the fiber is fully immersed while in contact with the two smaller wheels and exits the resin bath when passing over the large central wheel.

Once the fiber exits the resin tank, it is directed towards the fabric roller. This roller is deliberately held in place to ensure that the fiber rubs against it, allowing it to come into full contact with the fabric. This has a dual effect of removing excess resin and homogenizing the fiber as much as possible. Due to the fiber irregularities, localized knots or thickening may be

present. As they pass through the resin, they become wet and may swell due to the additional resin deposits. The forced contact with the fabric roller subsequently spreads and reduces their size, resulting in voluntary homogenization of the fiber.

This fiber regularization is clearly visible in Figure 7.4, which shows two consecutive frames extracted from a video during preliminary optimization tests. It can be seen that the irregularities in the fiber have become enlarged due to resin deposits (Fig.7.4a). These irregularities are then homogenized by friction against the roller (Fig.7.4b). The buttonhole at the tray top part is used to adjust the position of the roller, and therefore to control the pressure applied to the fiber.

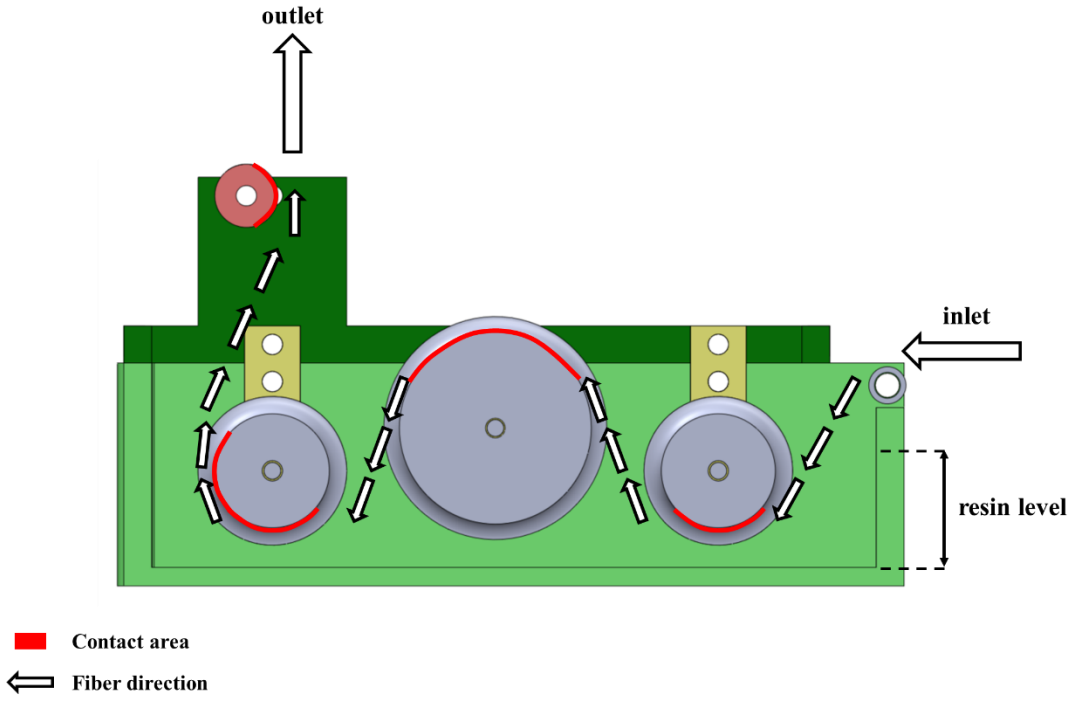

Figure 7.3: Section view of the resin tray

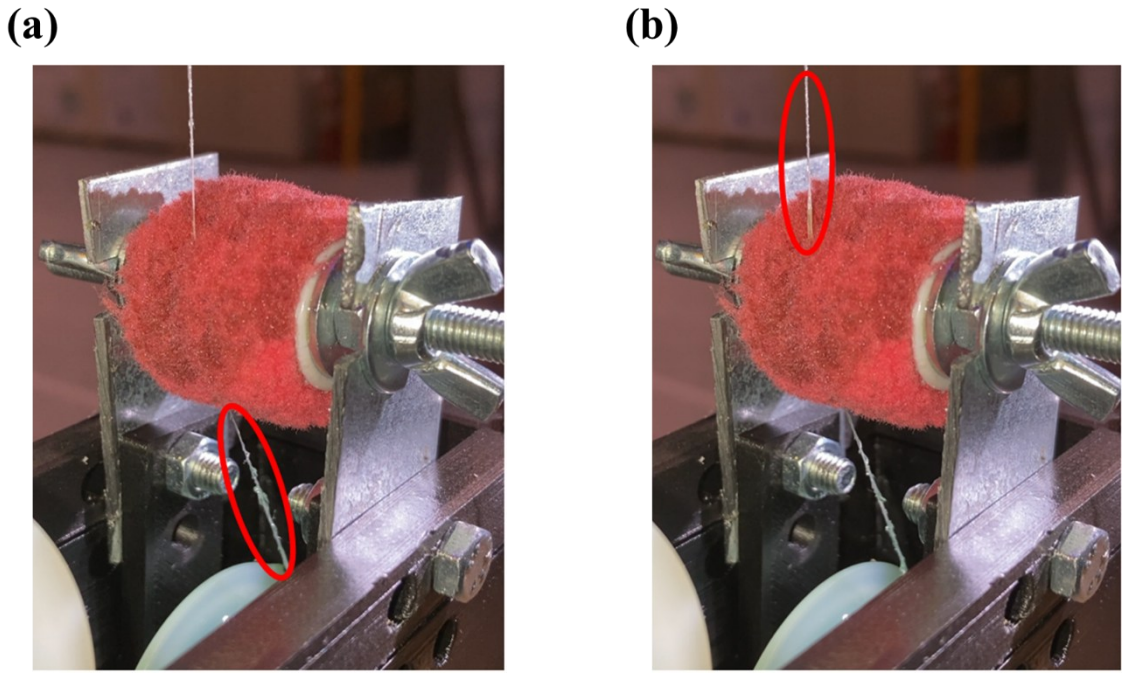

Figure 7.4: Consecutive frames showing a) the enlargement of irregularities and b) their subsequent homogenization

UV curing and cleaning

The UV curing phase was performed using a 5-meter-long LED strip with a wavelength of 395-405 nm (Eleganted, China). This strip was wound in a spiral pattern inside the tube, covering a length of 300 mm around the inner surface of the tube, which has a diameter of 50 mm. The interior of the tube has been designed to provide housing for the LED strip, which can be inserted and positioned in a spiral pattern inside the tube. The internal tube diameter and effective UV light length have been optimized to provide the best curing conditions and allow for the installation of LEDs. The design maximizes the UV light exposure time and minimizes the distance between the curing source and the thermoset. To ensure that the UV light is confined inside the tube and does not hit the resin in the tray below, an intermediate cap has been inserted. This cap is connected to the tube by interference and has a small central hole that allows the resin-coated fiber to pass through. The tube is connected to two L-shaped supports, which are in turn screwed directly onto the wooden base (Fig. 7.5a). Figure 7.5b shows a cross-section of the tube, highlighting the main parts.

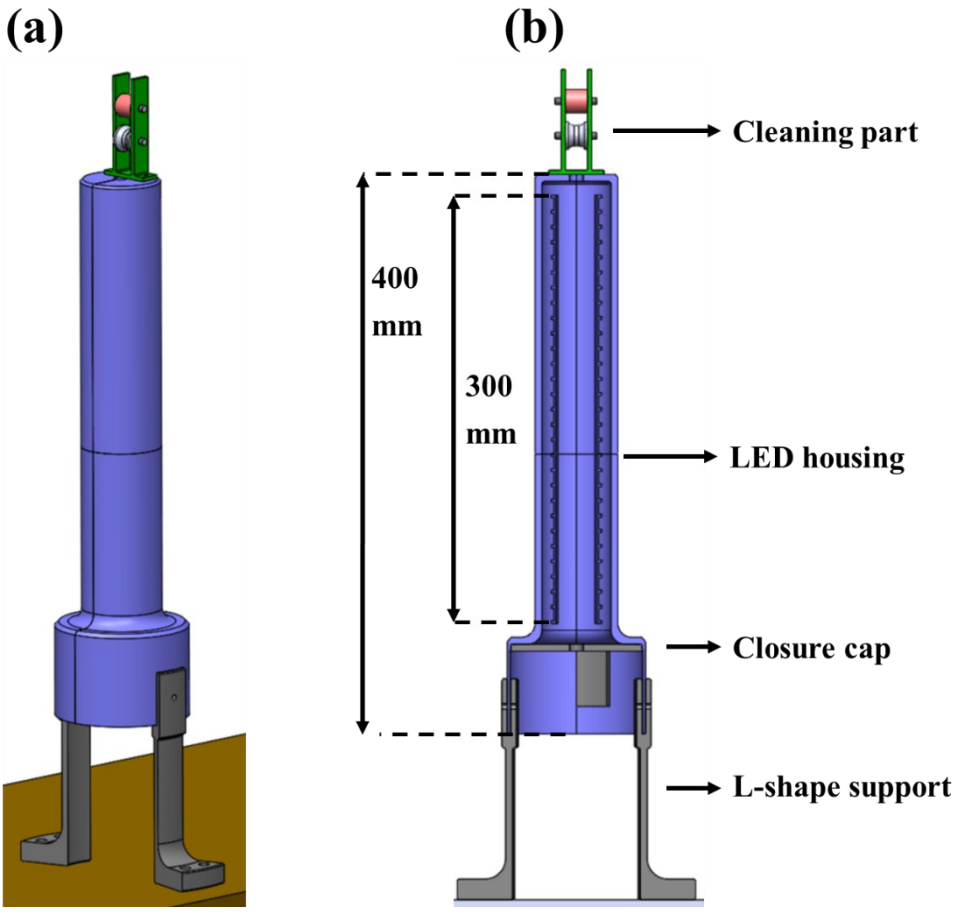

Figure7. 5: UV curing tube in a) axonometric and b) sectional view

Since the maximum size of the printer plate is 250 mm, the tube was divided into 4 parts for printing. After the sections were assembled, the UV LED was inserted to create the spiral. Once this phase was complete, the two halves of the tube were closed and connected to each other (Fig.7.6).

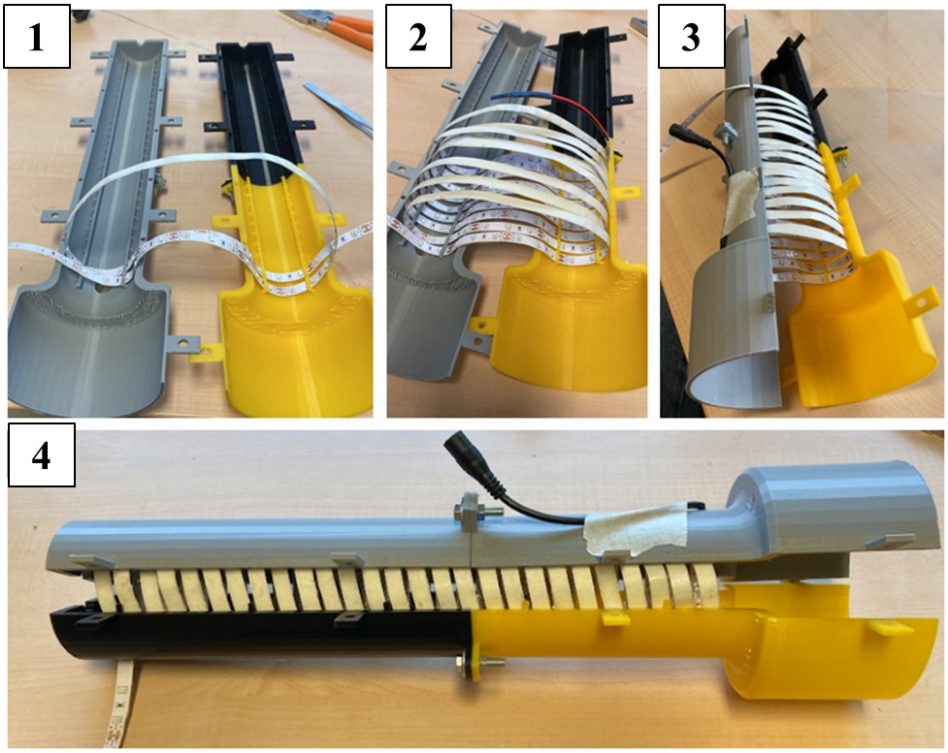

Figure 7.6: Sequential stages of LED insertion

Following the UV treatment phase, the cleaning section was located at the outlet of the tube (Fig.7.7). As mentioned before, the fiber is passed through the resin twice. During the first pass, a nylon wheel (Masidef, Varese, Italy) with a diameter of 10 mm was used. This wheel was held in place by a small M5 threaded bar and is free to rotate, and serving to guide and direct the fiber towards the winding area. During the second pass, a fabric roller was also inserted. This roller was similar to the one used at the outlet of the tray. With a diameter of 17 mm, the fiber only came into contact with it, avoiding contact with the nylon wheel. The fabric roller was soaked in IPACOL isopropyl alcohol (P.C.M, Ferrara, Italy) to remove uncured resin residues. The wheel and the roller support were 3D printed in the same way as the other parts of the tube.

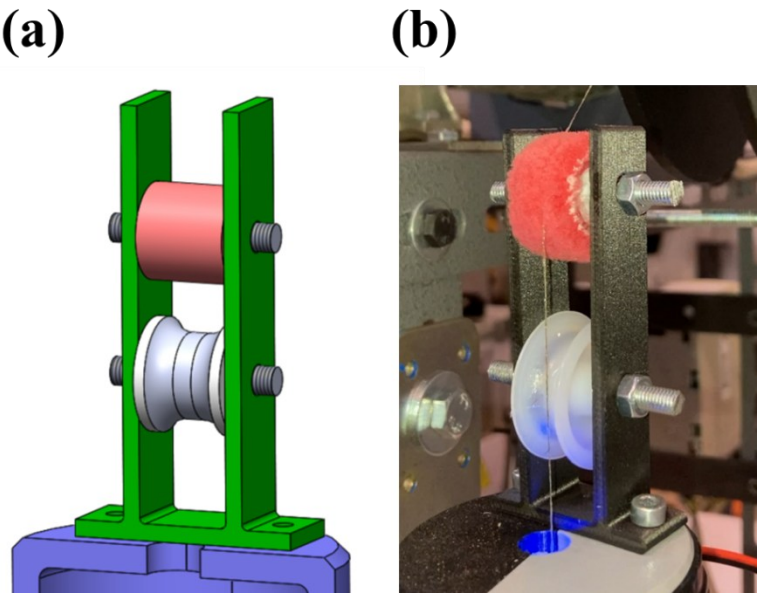

Figure 7.7: Resin cleaning in a) CAD representation and b) photos of the parts produced

Winding

The fiber is wound onto a 170 mm diameter spool, which was 3D printed like the previous parts in other areas. A three-phase asynchronous motor combined with a VF/W series gear motor was used for the movement, with speed controlled through an inverter (SYN10S22005AF model). All three components were supplied by Bonfiglioli (Bologna, Italy). The spool was attached to the shaft at the output of the gear motor, and a spacer was used to ensure the correct positioning of the spool relative to the tube outlet (Fig.7.8).

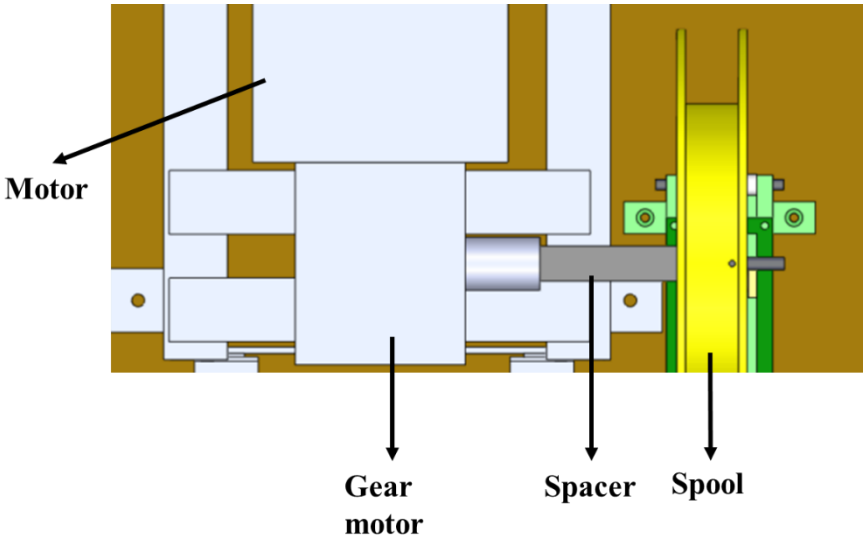

Figure 7.8: Winding configuration

According to the manufacturer's data, the output speed of the gear motor is 70 rpm at a reference frequency of 50 Hz. Setting the inverter to the minimum achievable frequency of 1 Hz reduces this speed to 1.4 RPM (or 0.15 rad/s). Since the winding is carried out on a spool with a diameter of 170 mm, a linear fiber movement speed of 1.2 cm/s is obtained. Consequently, with a UV section of 310 mm, the curing time is approximately 25 s.

Second-stage: post-processing and dimensional control

The post-processing phase is carried out thermally, using a vertical forced-ventilation oven (Mazzali System, Reggio Emilia, Italy), which has a 900 mm long heating zone and is equipped with two holes at the top and bottom, allowing the fiber to pass from the upper zone to the lower zone (Fig.7.9a).

The spool containing the fiber is placed on an unwinding structure above the oven (Fig.7.9b). Below the oven, there is a fiber collection and winding system after post-processing (Fig.7.9c). The latter system consists of a 170mm diameter spool driven by a NEMA 17 stepper motor, which in turn is controlled by an Anet3D v1.5 control board (Anet Technology Co., Shenzhen, Guangdong, China) (Fig.7.9d). Both the spool and the support structure for the motor and control board were 3D printed. The oven was set to 85 °C and the board programmed to ensure that the fiber remained at that temperature for 5 minutes.

As mentioned in Section 5.2.2, the coated filament must pass through 1 mm-diameter channels from the spool to the coextrusion head and then through a 0.8 mm nozzle during printing. Given the tight tolerances, a two-step dimensional check was carried out before using the fiber. This control is necessary because vegetable fiber is inherently irregular, regardless of all these methods to homogenize it. Therefore, localized swelling can occur due to the initial shape of the fiber or unwanted resin deposits related to the process.

To address this issue, a dimensional control station was developed. During the first step, the uncontrolled fiber is passed through a 1 mm diameter teflon tube and then wounded onto a new spool containing only the controlled fiber. The second step is done in the same way, but the fiber is passed through a 3D printing nozzle with a diameter of 0.6 mm. The nozzle and quick couplings, which secure the Teflon tube in place, are screwed directly onto two supports. Both the latter and the reel holders are 3D printed and screwed directly onto a wooden base

(Fig.7.10a). Irregularities that do not comply with the size limit (Fig. 7.10b, Fig. 7.10c) are carefully trimmed or reduced manually using sandpaper until they pass the dimensional check.

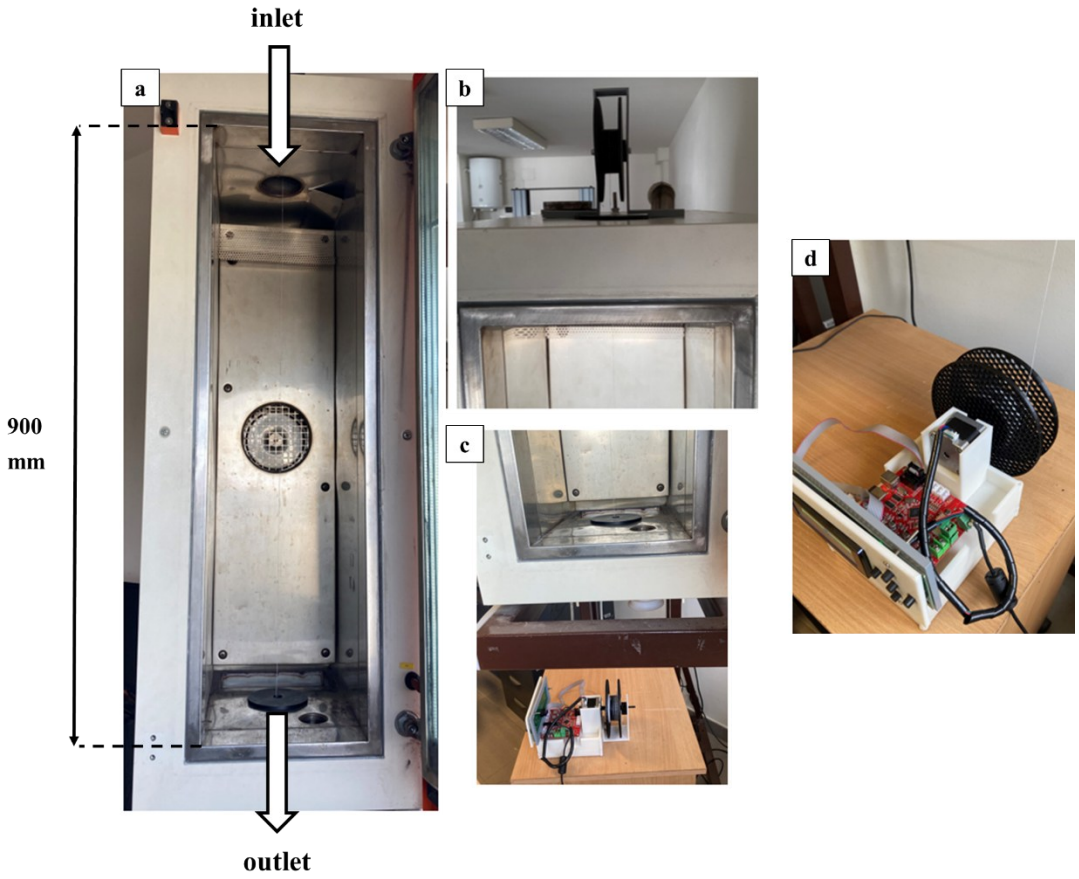

Figure 7.9: Details of post-processing phase for a) the oven, b) the upper unwinding and c) the lower winding structure, and d) the winding control system

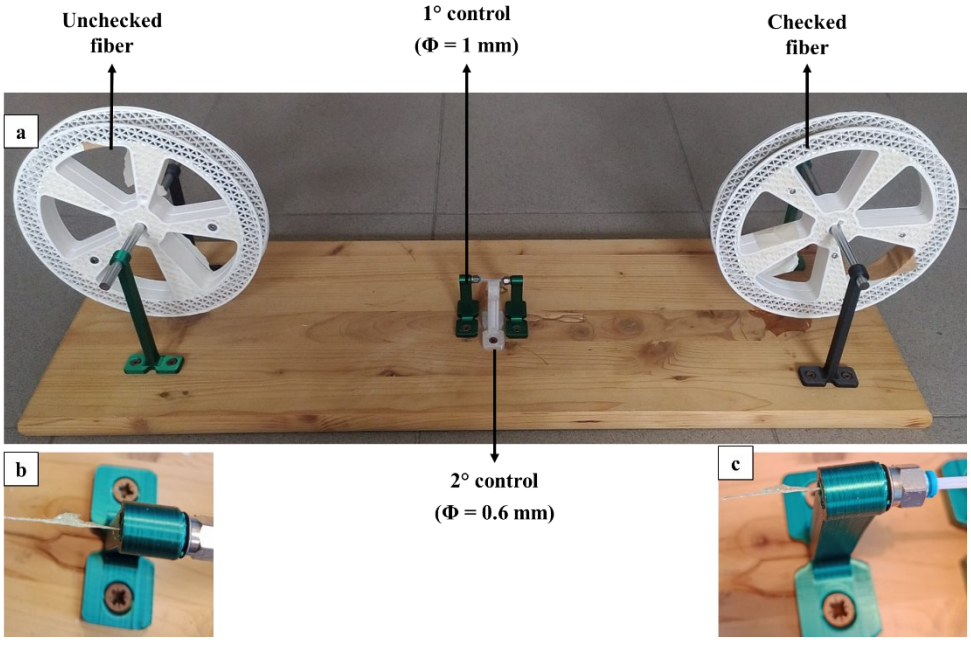

Figure 7.10: Dimensional control system: a) overview and b), c) non-compliant fiber points

7.2.3 Morphological analysis

Morphological analysis was performed on both raw flax yarns and coated filaments using a stereomicroscope. The average diameter was calculated from a total of 270 measurements: nine readings were acquired at random locations along the length of thirty distinct 100-mm segments. The diameters of the two initial flax fibers ($D_{fib}^{BO}, D_{fib}^{BL}$) and the two coated filaments (D_F^{BO}, D_F^{BL}) were calculated in this way. Furthermore, it was possible to see the cross section of the coated filament produced through an optical microscope. Section 3.7.5 outlines the equipment specifications and preparation procedure.

7.2.4 Density and fiber volume fraction evaluation

The average diameter of each of the thirty segments is obtained using the nine associated measurements. Next, each segment examined was weighed, using the equipment described in Section 3.7.2. The density of each segment can be obtained by associating its mass with its relative average diameter. Consequently, the density of the flax fibers ($\rho_{fib}^{BO}, \rho_{fib}^{BL}$) and the coated filaments (ρ_F^{BO}, ρ_F^{BL}) is evaluated by taking the average of the densities of the 30 segments that have just been achieved. In the same way, the average mass of the starting flax fibers($M_{fib}^{BO}, M_{fib}^{BL}$) and coated filaments ($M_F^{BO}, M_F^{BL}$) can be obtained. These values are used to calculate the fiber mass fraction (Ψ^{BO}, Ψ^{BL}). Finally, fiber volume fractions (ϕ^{BO}, ϕ^{BL}) are obtained using the following equations:

$$\frac{1}{\rho_F^x} = \frac{\Psi^x}{\rho_{fib}^x} + \frac{1-\Psi^x}{\rho_{TS}^x} \tag{22}$$

$$\rho_F^x = \rho_{fib}^x \phi^x + \rho_{TS}^x (1-\phi^x)\,, \tag{23}$$

where the superscript x represents the type of fiber considered (BO or BL) and the only unknowns are the density of the thermoset resin ρ_{TS}^x and ϕ^x.

7.2.5 Statistical analysis

Statistical analysis was applied to evaluate the increase in diameter of the coated filament compared to the starting fiber. To do this, it is essential to assess the normality of the data. The

main parametric statistical methods assume that the underlying data are normally distributed. Deviations from this assumption may compromise the test reliability and potentially lead to biased estimates or incorrect statistical inferences. For these reasons, it is important to check for the normality distribution of the dataset beforehand [203].

Data distribution

The Lilliefors test, which is based on Kolmogorov-Smirnov test ,is used to determine the goodness of fit between a sample distribution and a reference probability distribution, such as the normal distribution [204], [205], [206]. Both tests assume that the parameters (e.g. mean, standard deviation) of the theoretical distribution are known. However, Lilliefors test is specifically used if the parameters of the theoretical distribution are estimated from the data sample and not fixed a priori. To take this into account, the method used to compare the sample and reference distributions is made more restrictive.

The Lilliefors method tests the null hypothesis (H_0) that a sample $x_1, \dots, x_n$ is normally distributed. To do this, the statistical variable $D(n, \alpha)$ is defined and tabulated according to Lilliefors et al. [206], where n is the sample size and α is the significance level (typically 0.05). To determine whether to reject the null hypothesis, reference is made to the maximum absolute difference between the observed sample values and the expected values from a normal distribution. If this difference does not exceed the critical value $D(n, \alpha)$, the null hypothesis cannot be rejected. This outcome allows to assume that the sample data is normally distributed.

In the present study the Lilliefors test was selected to assess the normality of the coated filament and fiber sample datasets, given the medium sample sizes and the experimental origin of the data.

Data comparison

When both data sets are normally distributed, the T-test is used to check for significant differences between the means [207]. The t-test is based on Student's t-statistics, which relates the difference between sample means to the variability of the data and the sample size. In other words, it assesses how much of the observed difference between means can be attributed to random chance compared to the expected variability under the null hypothesis. The null hypothesis (H_0) of the T-test is that there is no difference between the means considered (or that the mean of a sample is equal to the reference value). If the *p*-value

associated with the test is lower than the pre-set significance level (usually 0.05), the null hypothesis is rejected, and it is concluded that the observed difference is statistically significant.

If one of the two or both data sets are not normally distributed, the T-test cannot be used. In this case, the Mann–Whitney U test, also known as the Wilcoxon rank-sum test and described by Kvam et al. [208], is used. This non – parametric test can be useful to compare two independent groups to determine if they come from the same distribution or if there is a statistically significant difference between them. In this test, null hypothesis H_0 indicates that the distributions of the two samples are identical. As seen before when the *p*-value is lower than 0.05 there is evidence against the H_0, so statistically there is a significant difference.

7.2.6 Thermal and rheological analysis

TGA analysis was performed on both BO and BL raw fibers and coated filaments, and the instrumentation and full procedure for thermal analysis are detailed in Section 3.7.3.

Rheological characterization was performed in steady shear mode, for the three thermoset resins. Analysis details and the instrumentation used are reported in Section 3.7.4.
The selection of the correct resin is based on rheological analysis. The chosen resin used must allow the fiber shape to be homogenized as much as possible and must not create further dimensional problems.

This requirement relates to a widely studied and described physical phenomenon known as “beading” or the dripping effect, linked to the creation of fluid droplets on a surface [209], [210]. The tendency of a resin to form droplets results from the combined effects of surface tension and viscosity, which together govern its wettability on the substrate and its propensity towards coalescence or separation. High liquid viscosity hinders flow and spreading, causing the resin to remain localized on the surface, favoring droplet formation. At the same time, surface tension acts to minimize the free surface area of the liquid. When this tension is high relative to the adhesion energy between the resin and the substrate, the liquid retracts into droplets rather than spreading. Droplet formation is further promoted when the internal cohesive forces of the liquid exceeds the adhesive forces at the interface. Overall, increasing viscosity enhances the

tendency of the resin to preserve a droplet-like shape because of its internal resistance to flow combined with the prevailing effect of surface tension.

Beyond this general behavior, the specific characteristics of natural fibers must also be considered: their intrinsically low wettability amplifies the role of surface tension, promoting droplet formation, while surface irregularities may locally retain the liquid yet still hinder uniform spreading. In addition, the presence of functional groups (e.g., $-OH$ groups in cellulose) can influence the interaction with the resin depending on polarity.

7.3 Results and discussions

7.3.1 Rheological results

The results of the rheological analyses (Fig.7.11) are consistent with the characteristics of the resins shown in Table 7.2: “Rigid” is the most viscous, “Fast” has a viscosity that is half that of the previous one and “Plant” is the most fluid. All resins showed a Newtonian behavior, at least within the shear rate range that was considered, thus viscosity is almost constant and the average values are 1.57, 0.64 and 0.16 Pa·s, respectively.

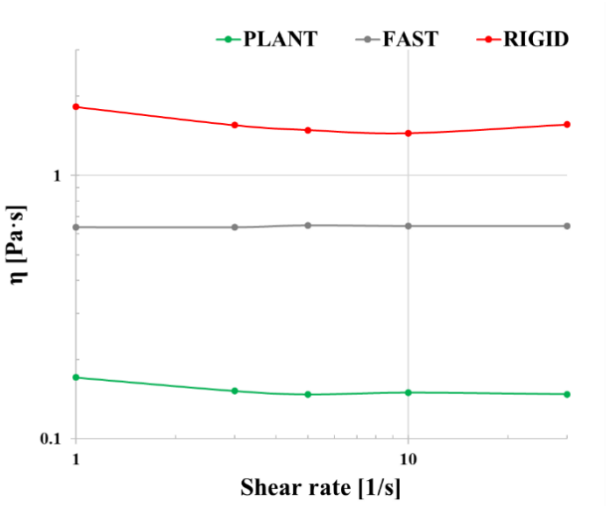

Figure 7.11: Results for the viscosity evaluation of the three different resins analysis

All coated fibers, obtained with the three resins and both fiber types, were evaluated under the stereomicroscope described in Section 3.7.5. This preliminary analysis allowed for the qualitative observation of the “the dripping effect”. This was done under the same process conditions as described in Section 7.2.2. These preliminary results follow the trend described above: “Rigid” and “Fast” tend to exhibit dripping , while “Plant” provides a uniform deposition (Fig.7.12). “Plant” resin is the best solution for homogenizing the fiber under the same manufacturing conditions. Hence, this resin will be selected and all coated filaments will therefore be made with it.

Figure 7.12: Preliminary analysis on dripping effect made with a) “Plant”, b) “Fast” and c) “Rigid” resin

7.3.2 Fiber morphology and diameter evaluation

The morphology of both fibers as they are and of the coated filaments was investigated. The materials were evaluated using a stereomicroscope and measurements were taken to calculate the diameter. Four representative images are shown for each type of flax: two for the starting fiber and two for the coated filaments. These are shown in Figures 7.13 and 7.14 for boiled and bleached flax, respectively. Regarding the initial fibers, the BL fiber has a much more regular shape than BO fiber. This is a direct consequence of the chemical refining process reported in Section 7.2.1. This initial homogeneity significantly influences the coated filaments: the BO coated filaments are very irregular, whereas those made with the BL fiber filaments are more uniform.

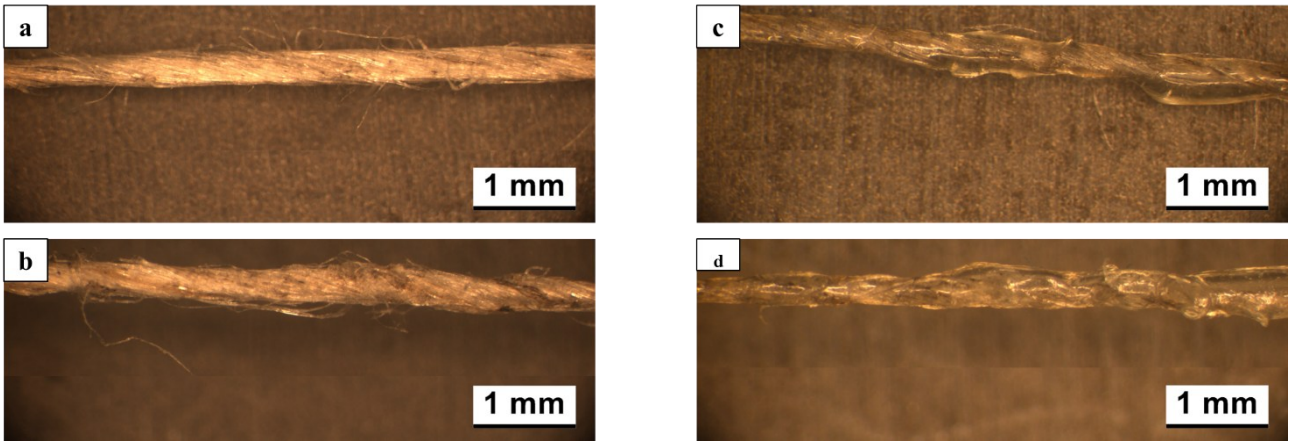

Figure 7.13: Representative acquisition from stereomicroscope for the boiled flax fiber a),b) as is and c),d) in the coated filament form

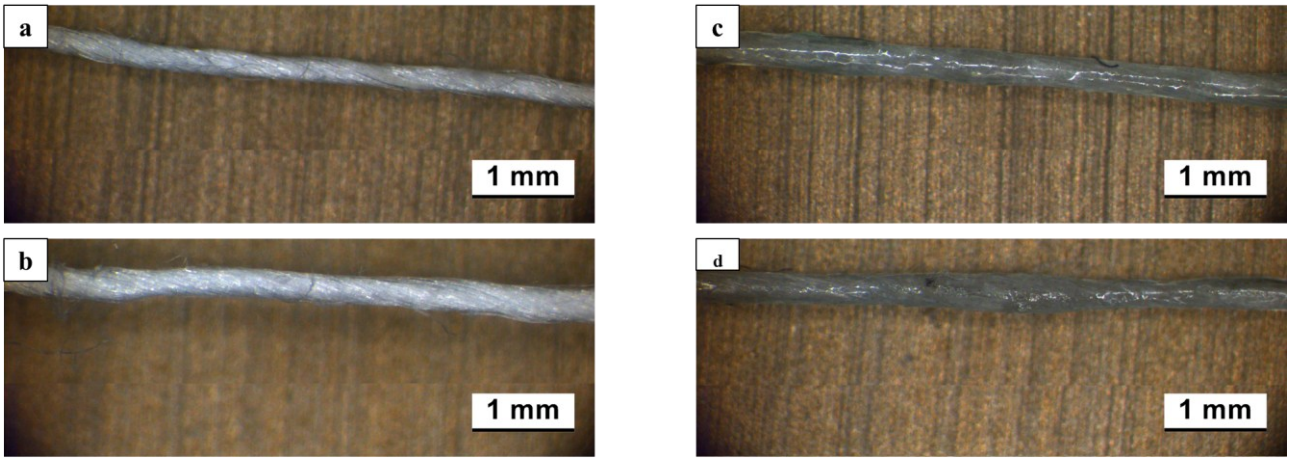

Figure 7.14: Representative acquisition from stereomicroscope for the bleached flax fiber a),b) as is and c),d) in the coated form

The cross-section of the coated filaments was analyzed using the optical microscope, and Figure 7.15 shows a representative image for each of the two flax fibers. The interface that separates the resin used to coat the fiber from the embedding resin (the resin employed to incorporate and prepare the filaments before the optical analysis) is clearly visible. Coated filaments made with BO fiber have an uneven distribution of fibrils, while BL fiber has a more compact distribution. This is in agreement with the trend seen previously, whereby the initial irregularities in the neat fiber are also reflected in the final coated filament.

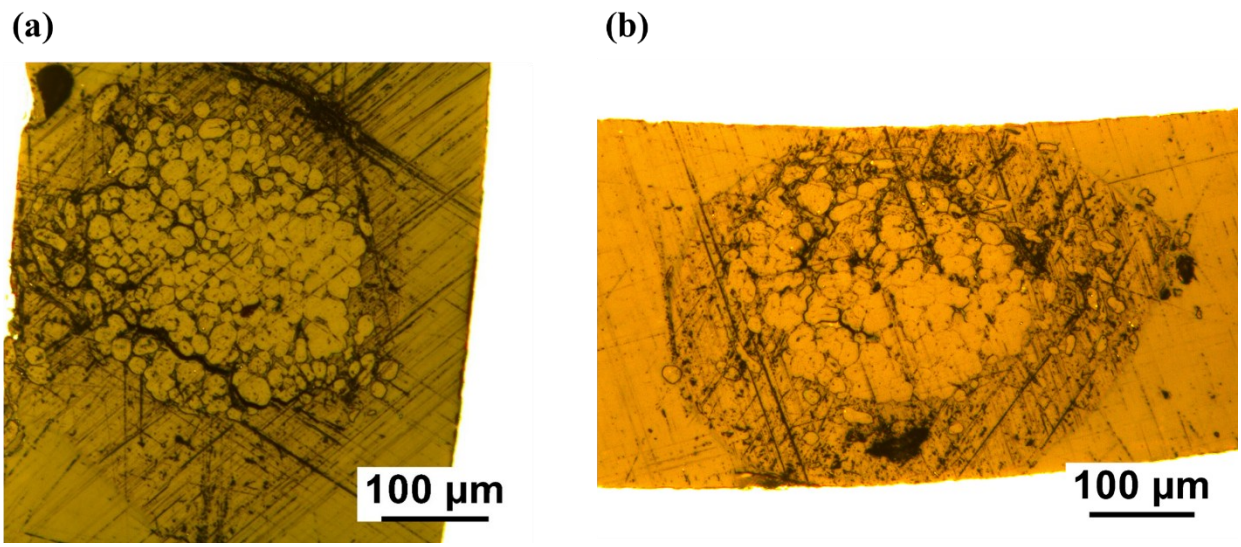

Figure 7.15: Representative cross-section from optical microscope for the coated filament obtained from a) boiled and b) bleached flax fiber

The average diameter of the fibers ($D_{fib}^{BO}, D_{fib}^{BL}$) and coated filaments ($D_F^{BO}, D_F^{BL}$) were evaluated through 270 acquisitions using the stereomicroscope. The masses $M_{fib}^{BO}, M_{fib}^{BL}$, M_F^{BO} and M_F^{BL} were calculated as the average of the thirty segments analyzed for each material. From these measurements, the density of the starting fibers ($\rho_{fib}^{BO}, \rho_{fib}^{BL}$) and coated filaments ($\rho_F^{BO}, \rho_F^{BL}$) was calculated. For the latter, it was also possible to calculate the fiber mass fraction (Ψ^{BO}, Ψ^{BL}). Finally, Equations 22 and 23 can be used to calculate the density of the thermoset ($\rho_{TS}^{BO}, \rho_{TS}^{BL}$)and the fiber volume fraction (Φ^{BO}, Φ^{BL}) present in coated filaments. Table 7.4 shows all of the values mentioned above.

Table7. 4: Diameters, densities, volumes and mass fractions of the fibers obtained from materials analysis. The values in parentheses represent the standard deviation of the averaged quantities.

	BO	BL
M_{fib}^{x} [mg]	5.35 (0.67)	4.89 (0.63)
M_F^{x} [mg]	11.97 (1.82)	9.73 (1.23)
D_{fib}^{x} [mm]	0.27 (0.04)	0.25 (0.03)
D_F^{x} [mm]	0.40 (0.06)	0.34 (0.05)

ρ_{fib}^{x} [g/cm³]	0.93 (0.15)	0.98 (0.13)
ρ_{F}^{x} [g/cm³]	0.97 (0.13)	1.10 (0.14)
Ψ^{x} [%]	45	51
ρ_{TS}^{x} [g/cm³]	1.01	1.25
Φ^{x} [%]	47	56
superscript x represents the type of fiber considered (BO or BL)		

The density of both initial fibers is much lower than that typically found for flax, which is around 1.5 g/cm³ [134]. This is because the flax fibers are in yarn form. This means there may be internal porosity due to the spinning and weaving processes. Despite this, BL flax has a higher density than BO flax, which is consistent with the results and effects of the chemical bleaching treatment it has undergone.

After the coating process, both mass and diameter have increased. The BO fiber diameter increases by 46%, and its mass by 124%. The same trend can also be seen for BL fiber, where the diameter has increased by 35% and the mass by 100%. These changes indicate that both increases are due to greater resin deposition on the outer surface.

Coated filaments with BO fiber has a lower fiber mass fraction (45%) compared to the BL fiber (51%). Moreover, the density of the filaments rises by only 4.5% for BO and by 12% for BL in relation to the initial fiber. The calculation of the fiber volume fraction is consistent with previous observations, and once again, BL fiber has a higher fiber volume fraction (56%) than BO fiber.

In summary, coated filaments made with BO flax have a greater increase in mass and diameter than those with BL flax, which is related to a higher resin deposition. It is reasonable to assume that the lower effect on the increase in density, and consequently the lower fiber volume fraction value, is due to the definition of average diameter (Fig.7.16). Diameter measurements were taken at 270 individual points, which are used to represent the overall trend. Therefore, since these specific values are averaged during the calculation, D_{F}^{x} is a representative value for the entire filament.

The bleached fiber is very regular and uniform, so the average diameter (dashed lines) fits the real filament almost perfectly. On the other hand, D_F^{BL} does not fit very well because the boiled fiber has more frequent diameter variations and irregularities. Consequently, the calculation includes empty areas, i.e., those between the white dotted line and the actual edge of the black coated filament. While these areas are geometrically part of the average diameter, they have no mass and therefore do not affect the density calculation. This discrepancy is also confirmed by the ρ_{TS}^{x} values obtained, which are equal to 1.01 and 1.25 g/cm^3 for BO and BL coated filament, respectively. $\rho_{TS}^{BL}$is more representative of the "Plant" resin density reported in Table 7.2. This is not the case for ρ_{TS}^{BO} which is 1.01 g/cm^3. This unusual value, which differs greatly from that reported by the manufacturer, is due to the definition of average diameter, because the value obtained for this density also takes into account empty areas.

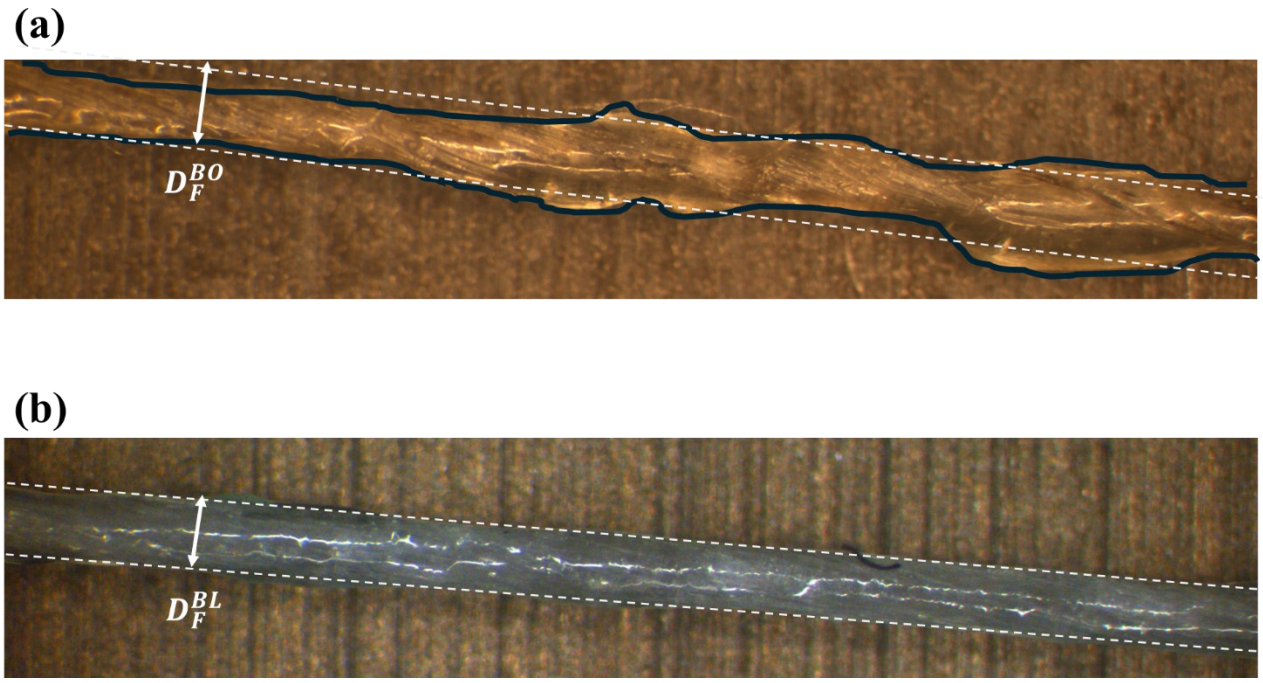

Figure 7.16: Average diameter representation for coated filament made with a) BO and b) BL flax fiber

Taking the previous discussion into account, the average diameter of bleached filament is more representative because it is more uniform. A reasonable representation of the coated filament cross-section is shown in Figure 7.17. The one made with BO fiber has a larger diameter than the one made with BL fiber, and the starting fibers also follow the same size trend. Following

the results, a thicker circular resin crown is visible around the BO flax, which correlates with its lower fiber volume fraction.

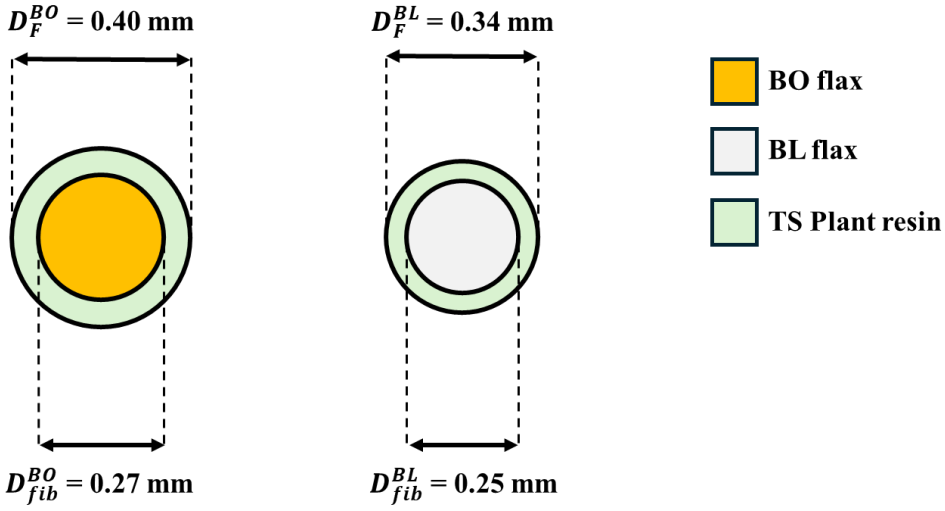

Figure 7.17: Reasonable schematic representation of the coated filament section

The boxplot graphical analysis (Fig.7.18) also supported the previous results and considerations regarding the filament diameter. The average value and the median for coated filaments have increased compared to the relative starting fibers. This effect is more pronounced in boiled flax and is presumably due to greater intrinsic irregularities in the original fiber structure.

Although box plots are useful for gaining an initial visual understanding of differences and variability, they are insufficient for determining whether an increase in diameter due to resin deposition is statistically significant. To do this, a specific statistical test is required.

Four sets of data relating to diameters are being analyzed, two for the starting flax fiber and two for the resulting coated filaments. First, the normality of the data sets was assessed with Lilliefors test, and the following statistical variable was used for all four materials: $D(270) = 0.054, \alpha < 0.05$. For all the data sets analyzed, the maximum absolute difference between the actual values and the expected value from a normal distribution is greater than 0.054. Hence, we can assume that the sample data are not normally distributed. For this reason, the nonparametric Mann-Whitney U test must be used to compare the data sets between the starting fiber and its corresponding coated version. For both BO and BL linen, the *p*-value is much lower than 0.5, meaning that the increase in diameter in the coated filament is statistically significant in both cases.

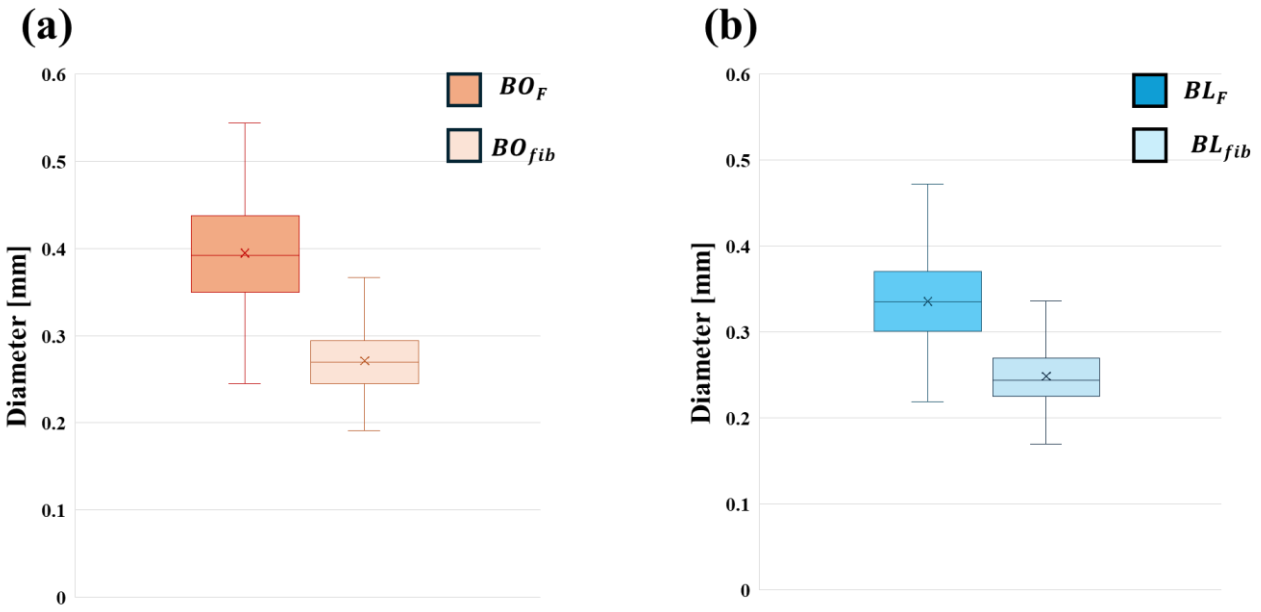

Figure 7.18: Graphical representation of the values relating to the diameters of the starting fiber and the coated filament for a) bleached flax and b) boiled flax

7.3.3 Thermal results

Thermogravimetric analysis (TGA) was performed to evaluate the thermal stability of the reinforcement materials and to assess the protective effect of the thermoset coating. Figure 7.19 compares the thermograms of the raw flax fibers (BO_{fib}, BL_{fib}) with their respective coated filaments (BO_F, BL_F). Beyond the moisture release phase, all samples exhibit a region of thermal stability up to approximately 300 °C, where the main decomposition step occurs. The onset of thermal degradation marks the decomposition of the main structural components. While the raw fibers display a sharp degradation step typical of lignocellulosic materials, the coated filaments exhibit a combined degradation profile of the fiber and the thermoset matrix. The presence of the resin coating modifies the degradation kinetics, smoothing the mass loss curve

Flax fiber consists of several components that have different thermal stabilities: cellulose mainly degrades between 300 and 380 °C, hemicellulose between 200 and 300 °C, lignin, meanwhile, has a very wide degradation range (200 - 500 °C) and yields a high amount of carbon residue. The boiling treatment removes waxes and pectins while preserving more lignin and amorphous components. This results in less chemical degradation of the cellulose

chain. Conversely, the bleaching process is more aggressive, resulting in a substantial decrease in lignin, hemicellulose and pectins. There is also a risk of oxidation and cleavage of cellulose chains. Comparing the mass residues of the two starting flax fibers, a wt% of 30% is observed for BO_{fib} and 20% for BL_{fib}. This is due to the different fiber treatment processes. Boiling preserves the most thermally stable components to a greater extent, so it is correct to observe a greater residue at the end of TGA.

Both filaments (BO_F, BL_F) are coated with a polyester-based thermoset UV resin, named Plant (Tab. 7.3). In general, once fully cured, this type of resin begins to degrade at around 250 °C. This is followed by major degradation up to 350 °C, with a more rapid loss of mass, and above 400 °C it is basically completely volatilized. Therefore, in coated filaments, the resin is the thermally weakest component of the system. TS resin does not contribute to the residue, and it reduces the char percentage of the fiber. The residue in TGA is dominated by fibers, rather than the resin.

Analyzing the boiled fiber (Fig. 7.13a), the residue goes from 30% for BO_{fib} to 20% for BO_F. On the other hand, the residue for bleached fiber (Fig. 7.13b) drops from 20% for BL_{fib} to 15% for BL_F. In the first case, there is a sharp decline in the residual, while in the other, the decrease is less pronounced. This behavior is related to the amount of TS resin deposited in the coating, which has a strong influence on these results. In accordance with what we have seen previously (Fig.7.17, Fig. 7.18), boiled fiber has a higher TS resin deposition in the coating than bleached fiber. While TS contributes to the initial reference weight, it does not contribute to the final residue. The TGA analysis provides an output showing the percentage of mass lost, calculated in relation to the initial starting mass. Therefore, if there is a high amount of TS resin present, this will increase the initial weight but reduce the final residue.

Furthermore, the morphology of the coated fibers must be taken into account: boiled fiber has a more uneven and irregular structure, while bleached fiber is more homogeneous (Fig.7.16). Hence, when it comes to boiled fiber in particular, it is necessary to take into account the intrinsic variability of the coated filament in terms of diameter, and therefore the mass of TS present.

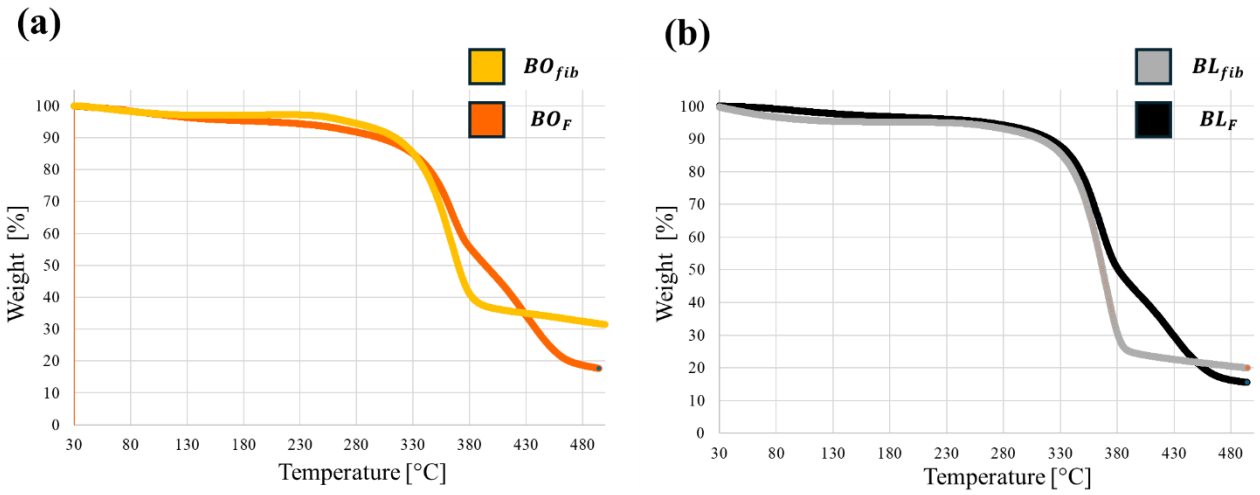

Figure 7.19: TGA thermograms of the raw flax fiber and the coated filament for a) boiled and b) bleached configuration

7.4 Conclusions and future developments

The work reported in this chapter successfully demonstrated the technical feasibility of developing continuous flax filaments coated with thermoset resin compatible with the OON technique.

Flax fiber was selected as the vegetable reinforcement fiber due to its superior intrinsic characteristics and more regular surface morphology compared to other vegetable reinforcements. Two different types of flax fiber, subjected to different chemical treatments, were considered: one was only boiled and the other was also bleached. This allowed to assess whether and how the initial condition of the fibers affects the final result of the coated filament. Similarly, three different UV-curing thermosetting resins, each developed for specific purposes, were evaluated.

In this chapter, a two-stage process was developed to obtain coated filament. The first stage utilized a customized device to partially cure the coated filament. The fiber was passed through a tray containing liquid resin and then through a UV curing zone before being collected on a reel.

This process was repeated twice to ensure adequate resin deposition and maximize structural homogenization. After the second pass, the coated filament is cleaned using a roller soaked in isopropyl alcohol to remove any excess uncured resin.

The second stage involved thermal post-curing process at 85°C for 5 minutes, to complete the resin cure. The coated filament is then checked for dimensional accuracy: first using a 1 mm hole, representative of the passage and movement channels of the fiber in the printer, and then 0.6 mm, to ensure that the fiber exits the nozzle. Non-compliant parts were carefully brought into tolerance manually.

Both rheological results and preliminary dripping tests demonstrated that “Plant” resin is the best solution. It ensures uniform resin distribution, structure, and final filament shape, thanks to the absence of droplet formation. The results of thermal analyses show that filaments coated with this thermoset resin are stable up to 300 °C.

Optical analyses were used to evaluate the diameter and shape of both coated filaments obtained and the starting fibers. The initial fiber morphologies are consistent with their treatments: the boiled starting fiber is much more irregular, while the bleached fiber is more uniform. The boiled coated filament showed a greater increase in mass and diameter, at the expense of lower volume fraction and mass. This is due to the significant irregularity of the fiber at the outset, which is reflected and amplified in the formation of the coated filament. The bleached one has a more regular and uniform structure and shape. For this reason, the average diameter assessment is also more realistic with the latter.

The analyses revealed clear morphological differences between the two types of fiber, which were also reflected in the produced coated filaments. In both cases, dimensional control required manual intervention, which was more frequent for boiled fibers. Nevertheless, the dimensions of both coated filaments are adequate with the requirements of commercial OON printers, confirming their potential as reinforcing fibers in 3D printing.

8. 3D printing of biocomposites reinforced with continuous flax fiber: mechanical characterization and comparison

8.1 Introduction

The state-of-the-art analysis carried out in Chapter 6 showed that OON technique is preferable for the standard production of biocomposites. This is due to its ability to limit the influencing parameters and its reliance on already developed technologies. These features make it suitable for industrial and ready-to-use parts. Following this reasoning, among the vegetable fibers analyzed, flax is the one with the most mature and developed production chain, combined with high mechanical performance.

Taking into account the dimensional restrictions imposed by commercial OON machines, it is reasonable to estimate that the maximum acceptable diameter for the reinforcement filament is 0.5 mm. To use continuous vegetable fibers in the most standardized way possible, it is necessary to homogenize their shape. One way to achieve this is to create coated filaments, starting from the raw fiber.

Chapter 7 discusses the possibility of manufacturing them using thermoplastic or thermosetting matrices. The choice between the two matrices represents a compromise between process reliability, achievable final tolerances and mechanical performance on one hand, and recyclability and ecological considerations on the other one. A thermoset resin solution was chosen, primarily due to dimensional issues, with UV curing preferred over thermal curing to prevent fiber degradation during the process. As a result, two coated filaments were developed, utilizing two types of flax fibers: one boiled and one bleached. Both meet the initial dimensional requirements, but their shape and structure are quite different from each other.

To the best of the author's knowledge, the only work that uses continuous flax fiber as reinforcement with the OON technique is that by Wu et al. [165]. Specifically, they used the Anisoprint printer, and the authors state that they modified the composite co-extrusion system to adapt it to natural fiber yarn. Therefore, the process is comparable to ISI printing, meaning that the already developed technology and available is not being fully exploited. Furthermore, the biocomposite was only mechanically tested with tensile tests only in the longitudinal and transverse directions.

The aim of this chapter is to 3D print both coated filaments realized in the previous chapter and perform a complete characterization of their in-plane mechanical properties, extending the analysis beyond the longitudinal and transverse directions. By comparing the mechanical results, it will be possible to assess whether there are significant differences between coated filaments made with boiled or bleached fiber. The mechanical tests are supported by fracture surface investigations using SEM micrography and optical analysis. This approach will allow for the evaluation of the best solution for potential industrial use, considering both mechanical performance and the structure and regularity of the reinforcement used.

8.2 Materials and methods

8.2.1 Materials

PLA (Raise3D, Stafford, TX, USA) was employed as the thermoplastic matrix for the fabrication of the 3D-printed biocomposite. The reinforcement phase consisted of the two flax fibers previously produced and thoroughly characterized in the previous chapter. The main properties of the materials are summarized in Table 8.1, which includes the technical datasheet information for the matrix and the characteristics of the flax fibers. For clarity, in the following sections the acronyms BO_F and BL_F will be used to indicate the boiled and bleached flax coated filaments, respectively, as described earlier.

Table 8.1: Materials description from technical data sheets, values in parentheses represent the standard deviation

Material	Composition	Fiber volume fraction [%]	Diameter [mm]
PLA	PLA	-	1.75
BO_F	TS coated - boiled flax fiber	47	0.40 (0.06)
BL_F	TS coated - bleached flax fiber	56	0.34 (0.05)

8.2.2 3D printer and specimen prepraration

All specimens were printed using the Composer A3 printer by Anisoprint, and its related slicing software, which are widely described in Chapter 5. As with previous uses, the left extruder is equipped with a 0.4 mm nozzle and the right one for the composite with a 0.8 mm nozzle.

Samples for testing the neat PLA matrix alone were produced using the left extruder, while continuous fiber-reinforced biocomposite specimens were obtained by co-extrusion using the right extruder. In this paper, the acronyms BO_C and BL_C are used to refer to the latter materials: BO_C stands for BO_F co-extruded composite, while BL_C for the corresponding with BL_F. This peculiarity is well described in Fig.8.1.

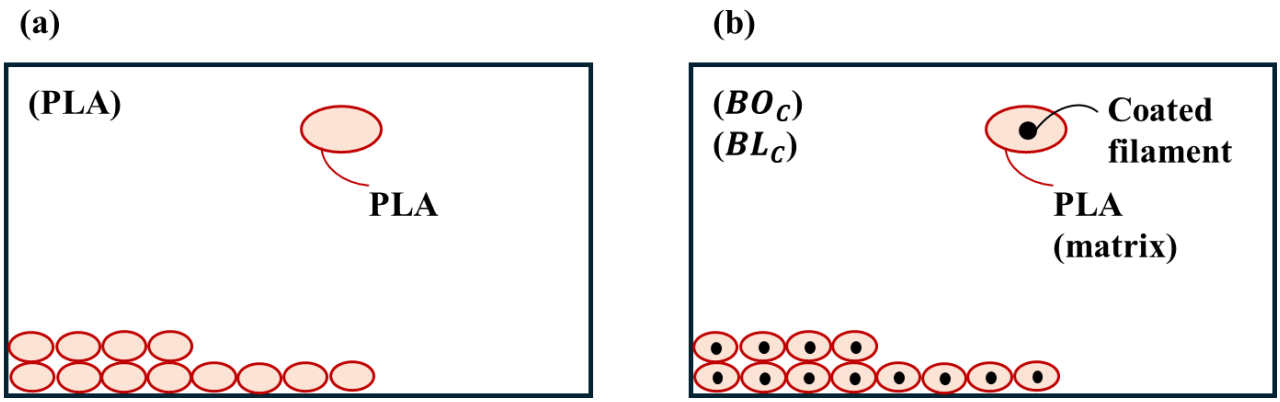

Figure 8.1: Representative section of specimens for a) PLA and b) co-extruded composites

For all three materials (PLA, BO_C e BL_C), the samples were printed without external shells and top or bottom layers. Before printing, the PLA filament was dried at 60°C for 24 h and the spool was stored in a passive dry box (Polymaker, China) containing silica salts during printing. The bed was heated at 60 °C. To achieve a complete characterization of the in-plane properties, samples with different raster angles were considered (0°, 90°, 10°). The main printing parameters for each material are listed in Tab. 8.2.

Table 8.2: Printing parameters of samples for the two materials

Characteristic	PLA	BO_C, BL_C
Layer height [mm]	0.2	0.5
Line width [mm]	0.4	0.7
Extrusion temperature [°C]	215	215

Printing speed [mm/s]	40	30

The samples were rectangular, measuring 110 mm in length, 15 mm in width and 2 mm in thickness. To obtain samples with raster angles of 10° and 90°, larger plates were initially printed at a 0° orientation (Fig. 8.2b, Fig. 8.2c) and subsequently laser-cut to the required dimensions. By contrast, the 0° specimens were printed individually and directly in their final size (Fig. 8.2a). The thick contour indicates the effective sample obtained directly for longitudinal orientation or via the laser cutting, for 10° and 90°.

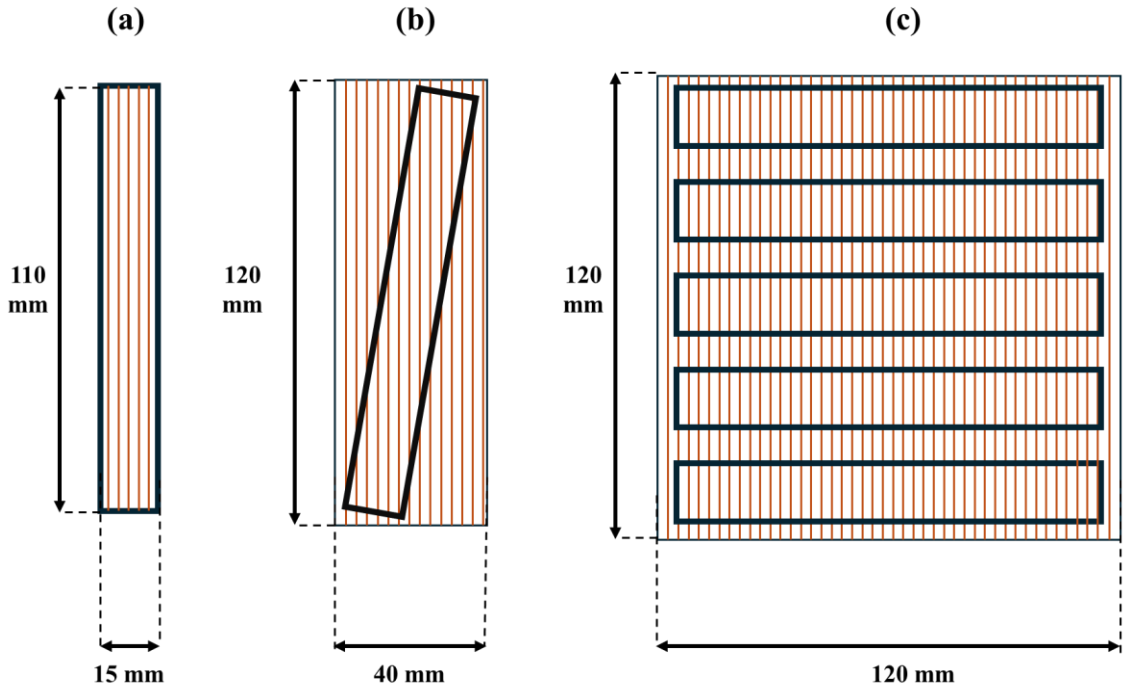

Figure 8.2: Dimensions for producing samples directly at a) 0° and using larger plates for b) 10° and c) 90° orientation.

8.2.3 Material characterization

Tensile characterization

Tensile tests were carried out for both materials in accordance with the procedures detailed in Section 3.2.2, in order to achieve complete characterization of the in-plane properties. ASTM D3039 [79] was used to measure longitudinal and transverse properties from specimens printed at 0° and 90° raster angle, respectively. Shear properties were evaluated through 10° off-axis tensile test [81], [82]. Considering $\vartheta = \frac{\pi}{18}$, the shear modulus (G_{12}) is obtained from

Eq.5 (Section 3.2.1)by setting E_x equals to E_{10°, while S_{LT} is calculated through Eq.9 (Section 3.2.1)by setting σ_x equals to $\sigma_Y^{10^\circ}$.

The tests were performed on three samples per raster angle (0°, 90°, 10°), for a total of nine samples per material. The instruments and details of the test conditions are given in Section 3.7.1. Finally, after characterizing the materials, the anisotropy of the in-plane stiffness properties was evaluated for all three materials, as proposed in Section 3.2.1.

Voids measurements

The density of the PLA filament (ρ_{PLA}) was measured before printing. The densities of the two continuous reinforcements (ρ_F^X) refer to those obtained in the previous chapter for the two coated filaments. The letter X represents the type of fiber considered, BO and BL for the boiled and bleached fibers, respectively. The nominal density of the co-extruded composite $(\rho_{Xc})^{nom}$ was estimated using the rule of mixtures (ROM):

$$(\rho_{Xc})^{nom} = \rho_F^X \phi_F^X + \rho_{PLA}\phi_{PLA}\,, \tag{24}$$

where ϕ_{PLA} and ϕ_F^X are the volume fractions of the materials, respectively, as obtained by Aura during the print preview. After printing the co-extruded composite samples, their effective density $(\rho_{Xc})^{eff}$ was calculated using the instrumentation and procedure described in Section 3.7.2. Once both densities were known, voids percentage of the specimens was evaluated according to Eq.10 in Section 3.3. The techniques and the instrumentation used are reported in detail in Section 3.3.

Considering the Eq.24 for calculating $(\rho_{Xc})^{nom}$, the volume fraction of coated reinforcing filament (ϕ_F^X) varies depending on whether boiled (X=BO) or bleached (X=BL) fiber is used. Since the biocomposite is produced using co-extrusion and the sample sizes are all the same, regardless of the raster angle, printing a completely full one requires 9.5 meters of coated filament and 1.6 cm^3 of PLA. As described in Section 7.3.2 (Table 7.4, Fig.7.18) the diameter of coated filaments depends on the type of fiber. Consequently, the total volume of reinforcement filament used also changes proportionally, and subsequently also ϕ_F^X. This behavior can be clearly seen in Figure 8.3. As discussed and evaluated in detail in the previous chapter, it is worth to notice that reinforcing filament consists of a fiber coated with a thermoset resin. Taking this into account it is possible to calculate the effective volumetric fraction of continuous flax fiber ϕ^xwithin the 3D printed biocomposite.

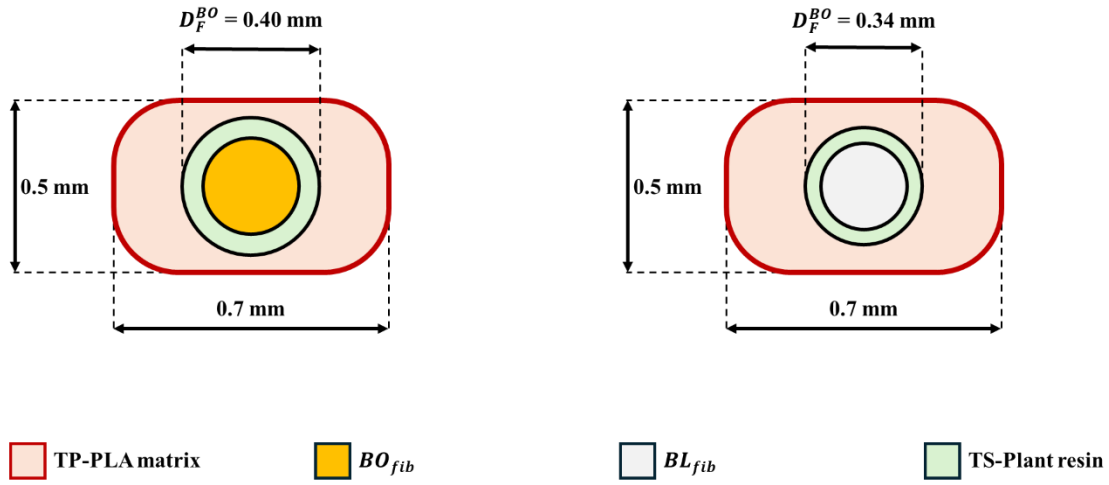

Figure 8.3: Schematic representation of the different fiber volume fractions in the co-extruded biocomposite

Optical analysis

Morphological observations of the longitudinal and transverse cross-sections of untested tensile specimens were analyzed to evaluate the printing quality and fracture surface. The samples were analyzed using a stereomicroscope, and SEM micrographs were collected only for the fracture surface of the samples at 0°. Section 3.7.5 outlines the equipment specifications and preparation procedure.

Rheological tests

Rheological characterization of the PLA matrix was performed in dynamic oscillation and strain-controlled mode. The specimens were in the shape of a disc of 25 mm in diameter and 2 mm thick. Prior to testing, a void content of less than 10% was verified to ensure the accuracy of the measurements.

Three types of rheological experiments were performed: strain, frequency and time sweeps, all performed at 185 °C. The rheological analysis techniques and the instrumentation used are reported in detail in Section 3.7.4.

Thermal analysis

PLA matrix filament was analyzed through DSC analysis to determine the crystalline fraction (χ_c) and characteristic temperatures, such as the glass transition temperature T_g and the

melting temperature T_m. Equation 11 was used to calculate the crystalline fraction, setting ΔH_{m0} equal to 93.6 J/g [211]. The instrumentation and procedure for thermal analysis are detailed in Section 3.7.3.

8.3 Results and discussion

8.3.1 Thermal and rheological

DSC thermal analysis revealed that the crystallinity of PLA was 27%, meaning that the material can be considered slightly crystalline, and a melting peak was found around 150 °C.

Regarding the rheological analysis, the strain sweep tests ensured that a strain of 1% was within the LVR and this value was used for performing the other two rheological measurements. Fig. 8.4a shows the trend of complex viscosity η^* as a function of frequency ω. At low frequencies, a portion of the Newtonian plateau can be seen, with zero shear viscosity η_0 of around 1800 Pa·s.

The thermal stability of the materials was assessed using a time sweep test at a frequency of 1 rad/s over a total duration of 600 seconds. Figure 8.4b depicts the evolution of G^* over time. As the curve is flat, the material remains stable throughout the test period, which is longer than the time that the TP matrix remains in the coextrusion chamber.

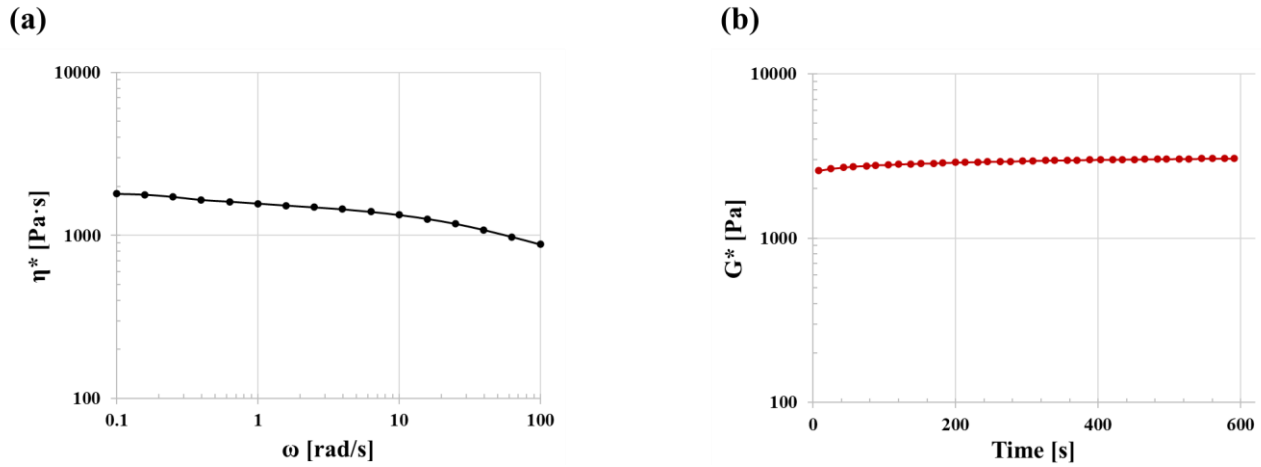

Figure 8.4: Trend of a) complex viscosity as a function of frequency and b) complex modulus as a function of time

8.3.2 Density and voids measurements

The PLA matrix was found to have a density of 1.25 (±0.01) g/cm^3. Referring to the results obtained in the previous chapter, the densities of the two coated filaments were found to be equal to 0.97 (±0.13) and 1.10 (±0.14) g/cm^3 for BO_F and BL_F, respectively. From the print preview provided by Aura, it is possible to calculate the nominal density $(\rho_{Xc})^{nom}$ of the co-extruded composite, following Eq.24 (Section 8.2.3). As mentioned above, considering the different diameters of the coated filaments, it is possible to obtain ϕ_{PLA} and ϕ_F^X, for the related co-extruded biocomposite. Subsequently, it is also possible to achieve the effective volumetric fraction of continuous flax fiber (ϕ^x) within the 3D printed biocomposite. The fiber volume fraction and density values are shown in Tab.8.3.

The volume fraction of reinforcement is greater in the case of biocomposite reinforced with BO coated filament. On the other hand, since the latter has a lower fiber volume fraction (47% towards 56%), the coextrusion process results in the same effective fiber fraction value.

Table 8.3: Densities and volume fractions for the components of the 3D printed co-extruded composites

	BO	BL
$(\rho_{Xc})^{nom}$ [g/cm^3]	1.14	1.20
ϕ_{PLA} [%]	58	66
ϕ_F^x [%]	42	34
ϕ^x [%]	20	19
superscript X represents the type of fiber considered (BO or BL)		

Effective density of the printed co-extruded composite $(\rho_{Xc})^{eff}$ allows the calculation of void percentage, and the corresponding values are listed in Tab.8. 4. It is important to note that void percentage is heavily dependent on the raster angle of the specimens, therefore the results are presented also in terms of this parameter. Similarly, voids were also evaluated for samples printed with the TP matrix alone. Void percentages are around 5% for PLA matrix samples and 10% for both 3D printed biocomposites. For the matrix, the longitudinal configuration has lower voids percentage, and this is mainly due to the lower number of direction changes during printing, as described also in Chapter 5. Conversely, for both biocomposites, the samples at 90° and 10° exhibit lower porosity than the longitudinal direction. This relates to the process of

creating samples using laser cutting, whereby the outer parts of the plate are removed, leaving only the central part (Fig.8.2).

Table 8.4: %voids for all configurations, values in parentheses represent standard deviation

	% Voids		
Material	0°	90°	10°
PLA	5.6 (0.4)	6.6 (0.7)	6.2 (0.5)
BO_C	11.9 (1.0)	9.8 (1.2)	11.3 (1.3)
BL_C	11.7 (1.4)	10.6 (1.2)	9.7 (0.9)

8.3.3 Mechanical characterization

Representative stress-strain curves of the different configurations are provided in Fig.8.5a for PLA and in Fig. 8.5b for the biocomposites.

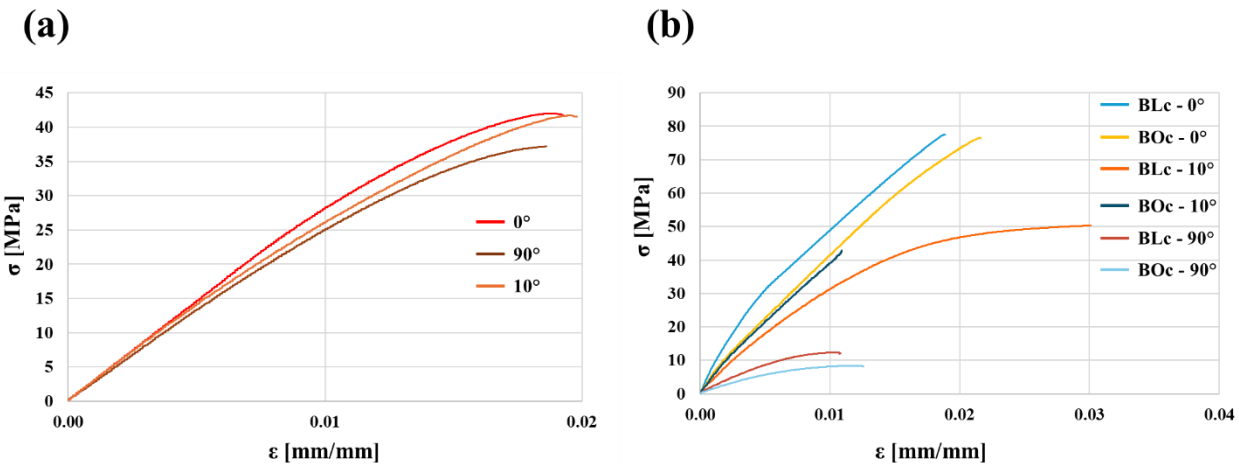

Figure 8.5: Stress-strain curves at different orientations for a) PLA and b) BOc and BLc

The neat PLA shows a slight elasto-plastic behavior, and the three curves overlap in the initial linear elastic region, regardless of the printing orientation, therefore PLA stiffness behavior can be assumed as isotropic (Fig. 8.5a). On the other hand, there is a slight difference in terms of yield stress, but this is not enough to conclude that the material is anisotropic in terms of strength, therefore it can be reasonably considered completely isotropic.

The development of the curves for the two biocomposites is completely different (Fig. 8.5b). The 0° curve for BL_C has significantly higher stiffness and strength than other orientations. The

behavior differs significantly from the 10° direction, and this difference is even more pronounced at 90°. In addition, the 0° curve for BL_C has a double slope, with the first section steeper than the second, and therefore stiffer. This well-known and widely studied behavior in continuous fiber-reinforced composites indicates that the fibers initially carry the load effectively, providing high stiffness in the elastic regime [212], [213]. However, beyond a certain strain, interfacial debonding, matrix yielding, and micro-crack formation reduce the efficiency of stress transfer from the matrix to the fibers. As a result, the apparent stiffness decreases, producing a second slope with lower inclination. This behavior is commonly reported in the literature for natural fiber composites and reflects the intrinsic limitations of fiber–matrix compatibility and matrix ductility [214].

For the composite made with BO coated filament, the 0° and 10° curves have a similar slope in the initial region, while the 90° curve is completely different. Also in this case, the longitudinal direction is stiffer and stronger than the other two directions. The 10° curve exhibits brittle failure, and it is highly plausible that the observed mechanism is related to cleavage, which can occur both within the matrix and along the fiber–matrix interface [215]. In samples oriented at 10°, the applied load decomposes into a component transverse to the fiber direction, which must be carried primarily by the matrix and the interface. When these induced stresses exceed the strength of either constituent, a brittle and relatively sharp fracture occurs. This failure can manifest as intra-matrix cleavage, with cracks propagating through the matrix, or as interfacial cleavage, due to limited fiber–matrix adhesion, often evidenced by clean fracture surfaces. This behavior is particularly pronounced in unidirectional biocomposites, where fiber–matrix adhesion is generally more critical [216].

The 0° curve for BO_C has a slightly lower slope than that for BL_C, although their ultimate strength is comparable. In the transverse direction, BL_C is stiffer and stronger, but it has a slightly lower strain at break. At 10 °C, the curves diverge significantly, with the BO_C becoming stiffer and more brittle. However, in both cases, there is a significant anisotropy in the mechanical characteristics.

Tab. 8.5 shows the four elastic constants required for stiffness characterization for the three materials. When comparing the PLA matrix and the two co-extruded composites, it can be seen that the latter two have doubled E_1. This is because, in the 0° configuration, the fibers are placed in the same direction as the applied load. Therefore, they are the load-bearing

component of the composite. For both BL_C and BL_C, E_2 has fallen significantly compared to the value of the matrix. At 90° orientation, fibers have a less favorable orientation, thus the behavior depends by a greater amount on the matrix properties and on the fiber–matrix interface quality. This behavior is not consistent with what is reported in the literature for transverse properties [75], [76] and with was similarly seen in the chapter 5.3.4.
PLA matrix has a transverse stiffness of 2.68 GPa, while both BO_{CC} and BL_{CC} have E_2 which is about half of that for the matrix alone, relatively 1.35 GPa and 1.95 GPa. It is reasonable to assume that this is due to the ineffective interface between the TS resin coating the flax and the coextruded PLA. In this condition, the continuous fibers do not improve the mechanical properties, but they act as if they were cavities, which obviously weaken the matrix. In fact, if the fiber volume fraction of continuous filament (ϕ_F^x, Tab.8.3) is added to the intrinsic voids due to 3D printing process (Tab. 8.4), the overall porosity is approximately 50%. This is perfectly in line with the drastic decrease in the transverse stiffness of the composite compared to the matrix alone.

Although both the PLA and the filament coating are ester-based, it is not possible to achieve a good interface because the resin is already fully cured prior to contact with the PLA matrix. Complete curing results in a highly crosslinked network characterized by the absence of chain mobility and by the consumption of reactive functional groups. As a consequence, no covalent bonding or molecular interdiffusion can occur at the TS-PLA interface. Interactions are therefore limited to weak physical forces, such as van der Waals and dipole–dipole interactions, which are insufficient to ensure effective load transfer across the interface.

The interfacial adhesion is further reduced by the semicrystalline nature of the PLA matrix. At a crystallinity degree of approximately 30%, a significant fraction of PLA chains is confined within crystalline lamellae, leading to reduced segmental mobility and lower availability of functional groups at the surface. This results in decreased surface energy and limited chain rearrangement at the interface, promoting stress concentration and interfacial debonding. Consequently, the combination of a fully cured thermoset and semicrystalline PLA represents an intrinsically unfavorable condition for interfacial adhesion.

G_{12} for BL_C is equal to that obtained for the neat PLA, while the value obtained for BO_C is double that of the other two. Poisson's ratio is about 0.40, for all materials.

Table 8.5: Stiffness properties for all materials, values in parentheses represent standard deviation

Material	E_1 *[GPa]*	E_2 *[GPa]*	ν_{12}	G_{12} *[GPa]*
PLA	2.94 (0.14)	2.68 (0.02)	0.42 (0.02)	0.65 (0.08)
BO_C	5.32 (0.32)	1.35 (0.19)	0.38 (0.04)	1.08 (0.28)
BL_C	5.75 (0.67)	1.95 (0.12)	0.36 (0.03)	0.66 (0.08)

From the tensile tests, the strength and ultimate strain values were also evaluated and are shown in Tab. 8.6.

The values for neat PLA are about the same in the longitudinal and transverse direction. The shear strength values, calculated at 10°, are about half S_L and S_T, in agreement with the hypothesis of isotropy.

Both BO_C and BL_C have S_L that is approximately 6 times larger than S_{LT} and S_T. In both cases, the transverse strength is lower than that of the neat PLA matrix and this is in agreement with the literature [75], [76], since it's expected that for unidirectional composites, fibers weaken the material in the transverse direction. The strength properties also demonstrate significant anisotropy, as the stiffness characteristics do.

Table 8.6: Ultimate strain and strength properties for all materials, values in parentheses represent standard deviation

	0°		*90°*		*10°*	
Material	S_L *[MPa]*	ε_{ul} *[mm/mm]*	S_T *[MPa]*	ε_{ul} *[mm/mm]*	S_{LT} *[MPa]*	ε_{ul} *[mm/mm]*
PLA	40.44 (2.43)	0.019 (0.001)	37.49 (0.31)	0.020 (0.003)	19.51 (0.68)	0.018 (0.002)
BO_C	74.78 (4.07)	0.022 (0.002)	8.39 (1.06)	0.014 (0.002)	8.18 (1.40)	0.015 (0.003)
BL_C	74.15 (2.15)	0.021 (0.002)	10.90 (1.37)	0.009 (0.003)	12.98 (1.13)	0.028 (0.002)

The results obtained from the tensile tests for BO_C and BL_C can be compared with those obtained by Wu et al. [165] , the only study, to the best of the author's knowledge, to have 3D printed continuous flax fiber using an OON technique. In both this work and the literature reference [1], the final fiber volume fraction in the 3D-printed biocomposite is practically the same and around 20%. To enable a better comparison, Table 8.7 summarizes the main parameters and their mechanical values. The raw fibers in the work by Wu have a slightly larger diameter and are five times higher in TEX than those used in this work. These differences are due to the yarn manufacturing process, as the linear density obtained depends on how the yarn is twisted. Furthermore, the mechanical properties of its flax fibers are approximately twice those of the fibers used in this chapter. Looking at the matrix employed, PLA was adopted in both cases, and in this work, a slightly stiffer matrix with lower strength was used.

Comparing the longitudinal mechanical properties, it can be seen that E_1 and S_L , obtained for BO_C and BL_C, are approximately half those reported by Wu. This is reasonable, given that we are comparing biocomposites with the same reinforcement volume fraction, but the mechanical properties of the starting fiber are twice as high in the case of Wu.

The contribution of the matrix is what matters most in the transversal properties of the biocomposite . E_2 found by Wu is the same as that for neat PLA, while that for BO_C and BL_C is half that of the reference for the matrix. Furthermore, the presence of TS in this study results in a significantly lower volume fraction of PLA (58% and 66% for BO_C and BL_C, respectively) compared to the 80% observed in Wu's study. In both cases, S_T is about six times lower than S_L. These values mainly depend on the strength of PLA matrix. In the case of Wu et al., neat PLA has a strength which is about 10 MPa higher than that used in this work. This trend is also evident in the transverse strength values obtained for the final biocomposites, because there is a difference of about 10 MPa between BO_C and $BL_C$and Wu's results. This study also provides a complete characterization of shear properties, which has not been addressed in the reference literature cited to date. G_{12} is approximately twice as much for BO_C as for BL_C, as can also be seen qualitatively from the curves in Fig.8.5. On the other hand, BL_C exhibits more ductile shear behavior than BO_C: it has an ultimate deformation that is twice as high and S_{LT} greater than 60%.

Table 8.7: Comparison between the properties obtained in this work and those found in the literature, values in parentheses represent standard deviation

	Property	Wu et al. [165]	BO_C	BL_C
Flax Yarn	TEX	105	18	20
	D *[mm]*	0.35	0.27 (0.04)	0.25 (0.03)
	E *[GPa]*	34.8 (2.5)	17	19
	S *[MPa]*	492 (30)	260	280
PLA matrix	E *[GPa]*	2.4 (0.1)	2.94 (0.14)	
	S *[MPa]*	48 (3)	40.44 (2.43)	
3D printed biocomposite	ϕ *[%]*	21	20	19
	E_1 *[GPa]*	9.2 (0.6)	5.32 (0.32)	5.75 (0.67)
	E_2 *[GPa]*	2.4 (0.4)	1.35 (0.19)	1.95 (0.12)
	S_L *[MPa]*	123 (5)	74.78 (4.07)	74.15 (2.15)
	S_T *[MPa]*	20 (2)	8.39 (1.06)	10.90 (1.37)

From the stiffness data obtained from tensile tests at 0°, it is possible to estimate the contribution of the flax fibers alone. Since the biocomposite is produced by co-extrusion, the following rule of mixtures (ROM) applies:

$$(E_1)_{Xc} = E_F^X \phi_F^X + E_{PLA}(1 - \phi_F^X)\,, \tag{25}$$

where E_{PLA}, $(E_1)_{Xc}$and the volume fraction of the coated filament (ϕ_F^X)are known and listed in Table 8.6 and Table 8.3, respectively. At the same time, it should be remembered that both BO- and BL-coated filament also consists of a TS resin component and a fiber component. Therefore, the following ROM also applies:

$$E_F^X = E_{fib}^X \phi^{\mathrm{x}} + E_{TS}(1 - \phi^{\mathrm{x}})\,, \tag{26}$$

where the fiber volume fraction of the two different coated filament (ϕ^{x}) is reported in Table 8.3, and the stiffness of the "Plant" resin (E_{TS}) is 0.45 GPa, as declared in the datasheet (Tab 7.2). Substituting Eq.26 into Eq.25, the following is obtained:

$$(E_1)_{Xc} = (E_{fib}^X \phi^{\mathrm{x}} + E_{TS}(1 - \phi^{\mathrm{x}}))\phi_F^X + E_{PLA}(1 - \phi_F^X)\,, \tag{27}$$

where the only unknown is the stiffness of the fiber (E_{fib}^{X}). Notice that the letter X represents the type of fiber considered, BO and BL for the boiled and bleached fibers, respectively.

E_{fib}^{BO} results 18.8 GPa, while E_{fib}^{BL} results 20.2 GPa. These values are in agreement with those reported by the manufacturer in the technical data sheet (Tab 8.6) and are equal to 17 GPa and 19 GPa for boiled and bleached fiber, respectively. The estimated stiffness contribution of the fiber, based on the biocomposite tensile results, is consistent with the values indicated in the supplier's datasheet. This indicates that the coated filament preparation process and the subsequent 3D printing did not compromise the integrity of the fiber, without damaging its performance.

Stiffness anisotropy

As described in Section 3.2.1 and in the previous Chapters 4 and 5, once the elastic constants E_1, E_2, G_{12}, ν_{12} are known, the anisotropic behavior can be evaluated graphically and qualitatively. The PLA matrix and the two biocomposites will be compared with CBFc. The latter is a 3D-printed composite that is slightly less sustainable than BO_C and BL_C, as it is realized coextruding PA12 and continuous basalt fiber, and it is fully characterized in Chapter 5.

The generalized Mohr's circles for the four materials are reported in Figure 8.6. Referring to PLA matrix, the radii (U_2, U_3) are very small compared to the distance between the centers (U_1), meaning that the orthotropic components are much smaller than the isotropic one. The two circles tend to collapse into a single point. This behavior is also quantitatively confirmed by both anisotropic ratios, which are very close to zero, indicating that the material is substantially isotropic.

For both BO_C and BL_C, the distance between the centers and the radii increase with respect to the neat PLA, denoting higher mechanical properties. Moreover, the proportion of the orthotropic components with respect to the isotropic one increases from neat PLA to BO_C and BL_C (Tab. 8.8).

This is visible when comparing the size of the radii to the distance of the centers: for BO_C, the circles are closer than BL_C. This closeness indicates an increase in anisotropy. The lower separation of the circles means that the isotropic component (U_1) decreases, while the decrease in the radii is linked to a decrease in the orthotropic components (U_2, U_3). This trend

indicates that the behavior is increasingly anisotropic, with a stronger degree of anisotropy observed in BO_C than in BL_C.

This is also confirmed by the fact that both anisotropic ratios for the BO_C and BL_C increase compared to neat PLA matrix. The ratio $\frac{U_2}{U_1}$ is practically the same for the two biocomposites, and in both cases $\frac{U_2}{U_1}$ is significantly greater than $\frac{U_3}{U_1}$. This means that anisotropy is primarily affected by the difference between longitudinal and transverse properties, rather than from shear properties. Nevertheless, looking at the details, we can see that the ratio $\frac{U_3}{U_1}$ is approximately double for BL_C compared to BO_C. This implies that for BL_C there is a higher orthotropic component linked to shear properties.

Comparing these results with those of CBF_{cc}, it is clear that its mechanical properties are superior and it exhibits much greater anisotropy compared to the two biocomposites printed with flax fiber. Its generalized Mohr's circles are wider and even intersect, and furthermore its anisotropic ratios are also significantly higher.

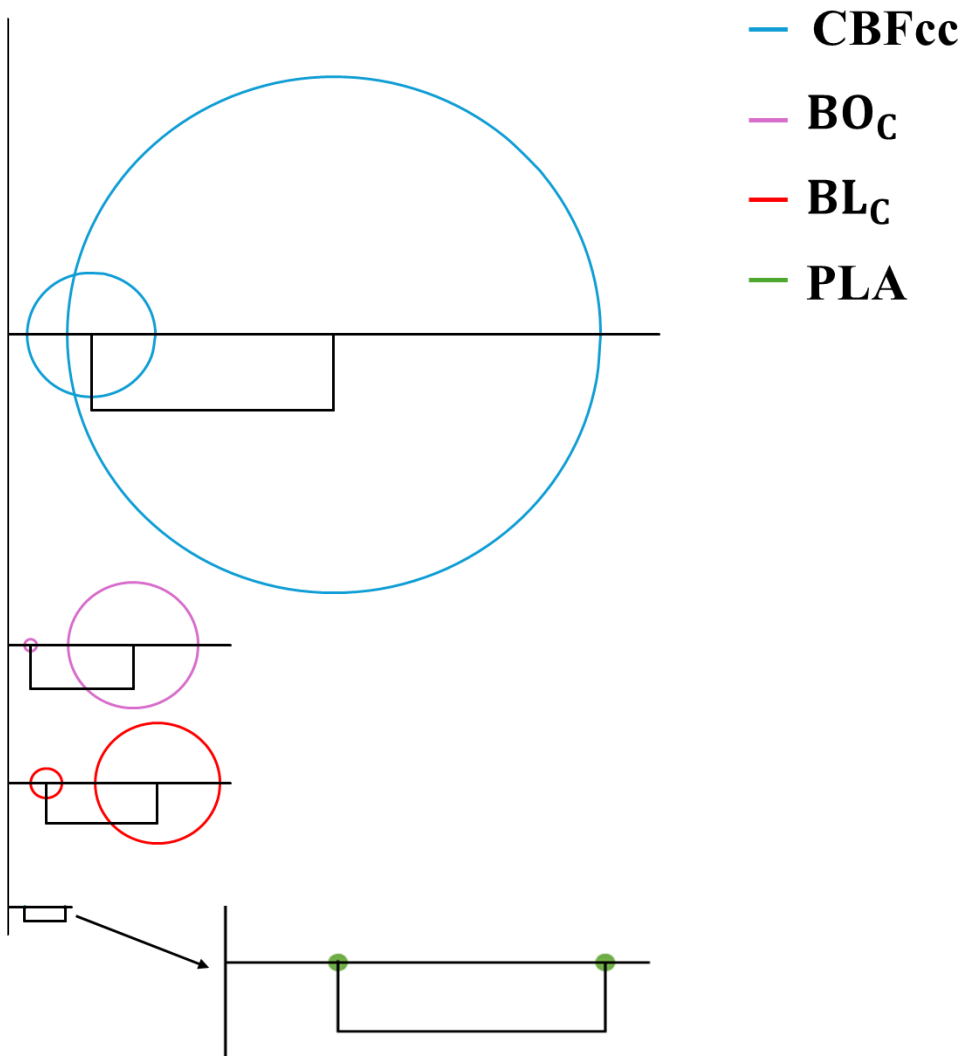

Figure 8.6: Comparison of generalized Mohr circles referred to BOc and BLc with respect to PLA matrix and CBFcc

Table 8.8: Orthotropic fractions for the four materials

Ratio	PLA	BO_C	BL_C	CBF_{cc}
$\frac{U_2}{U_1}$	0.03	0.63	0.56	1.10
$\frac{U_3}{U_1}$	0.03	0.06	0.14	0.26

8.3.4 Morphological observations

Untested specimens – cross sections

The polished transversal cross sections observed from 0° samples are shown in Fig. 8.7 for the BL_C (Fig. 8.7a) and BO_C (Fig. 8.7b). In both cases, the presence of TS material used as a coating around the fiber can be seen, even after printing. This is in accordance with what is seen in Chapter 7. The results of the TGA analysis of both coated filaments (Fig. 7.12, Section 7.3.1) showed that both are thermally stable at the printing temperature of 215 °C. For both biocomposites, the deposition speed is 30 mm/s (Tab.8.2), and considering that the printer's co-extrusion chamber is 15 mm long (Fig. 5.3, Section 5.2.2), the passage time of the reinforcement filament inside it is 0.5 s. This brief period during which the filament passes through a temperature that does not degrade, it is consistent with the presence of the coating even after printing.

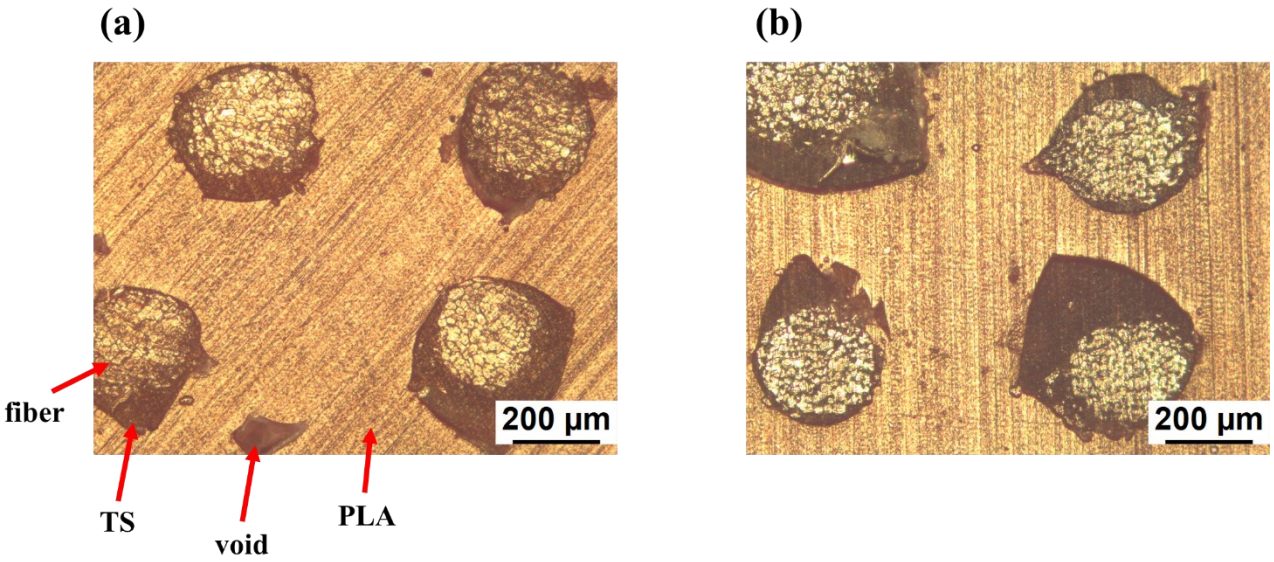

Figure 8.7: Representative transversal cross sections for untested specimens of a) BLc and b) BOc

Fracture surface – optical analysis

Figure 8.8 and Figure 8.9 show the fracture surface obtained from BO_C (Fig. 8.7a) and BL_C samples, respectively. In both cases, the reinforcement fibers have a shiny coating after fracture. This is consistent with what was observed in the cross-section of the untested samples. This effect appears to be slightly more pronounced in the case of BO_C than for BL_C.

This observation should be related to the thicker resin deposit on boiled fiber compared to bleached fiber, as seen in Chapter 7.

In the longitudinal direction, collapse of the matrix can be observed in both biocomposites. In the case of BL_C (Fig. 8.9a), the broken fibers are clearly visible, whereas for BO_C (Fig. 8.8a) this is less evident. This may be due to the different thickness of TS coating, which allows the integrity of the fibers to be maintained better in the case of BO_C. This can also be seen by comparing the strength of the fiber from the datasheet with those calculated from mechanical tests at 0° (Eq.26, Section 8.3.3). The strength calculated for the bleached fiber is practically the same as that reported in the datasheet. However, the strength obtained for the boiled fiber is 30 MPa lower than that declared by the manufacturer.

The fracture surface analyses at 90° and 10° are consistent with the behavior observed from the stress-strain curves in Fig. 8.5. In the transverse direction, greater whitening of the matrix is observed in the case of BO_C (Fig. 8.8b), indicating that it underwent greater plastic deformation before failure compared to BL_C (Fig. 8.9b). At 10°, a clear and marked fracture can be observed for BO_C (Fig. 8.8c), while for BL_C (Fig. 8.9c) is more limited and contained. The former is consistent with the cleavage mechanism, as hypothesized in Section 8.3.3.

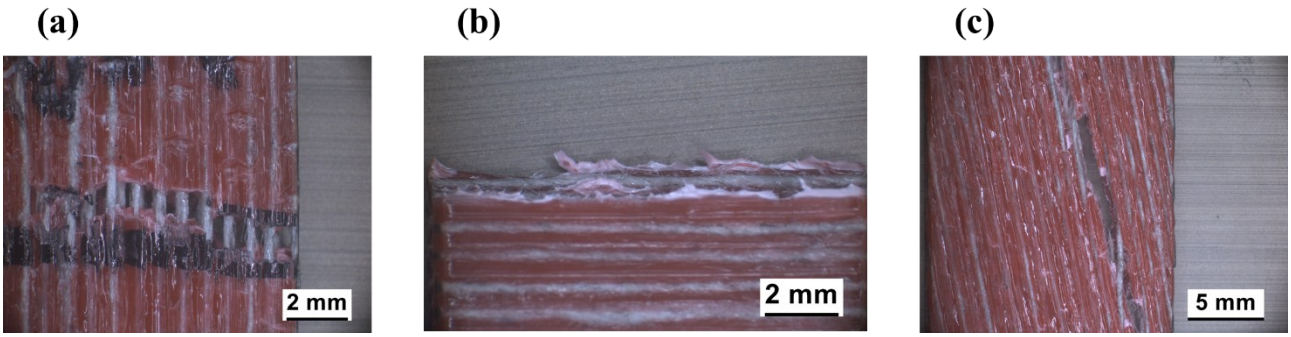

Figure 8.8: Representative fracture surface for BOc at a) 0°, b) 90° and c) 10° orientation, obtained with stereomicroscope

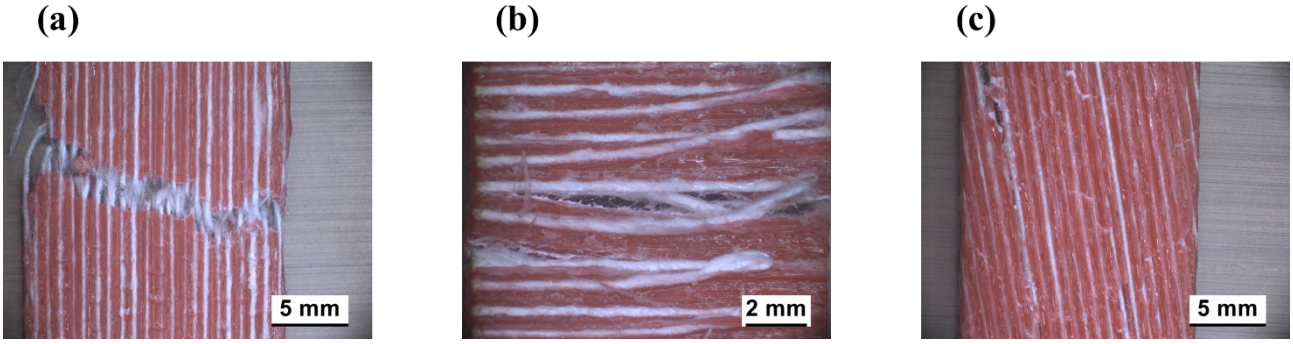

Figure 8.9: Representative fracture surface for BLc at a) 0°, b) 90° and c) 10° orientation, obtained with stereomicroscope

Fracture surface – SEM

To further investigate the fracture characteristics, SEM micrographs were taken of the sample fracture surfaces at 0° (Fig.8.10, Fig.8.11). In addition, spectra were also acquired at different points to analyze the chemical composition of the materials.

Three different spectra were acquired for BO_C (Fig. 8.10a) and the relative composition is shown in Table 8.5. Based on the wt% of the components present, it is reasonable to conclude that the spectra acquired at points 1 and 2 are significantly different from the spectrum at point 3. Therefore, the first two points can be associated with the PLA matrix, while the last with the presence of thermoset resin around the fiber. This evidence is even clearer in Figure 8.10b, where a portion of TS material can be seen between the matrix and the flax fiber.

The BL_C sample also follows this trend. The spectra acquired in Figure 8.11a, with corresponding data in in Table 8.6, shows a material surrounding the fiber whose composition is reasonably similar to the TS resin identified in point 3 for BO_C (Fig. 8.10a). This confirms that

a residual TS layer remains around the fiber which is further confirmed by the material analysis shown in Figure 8.11b.

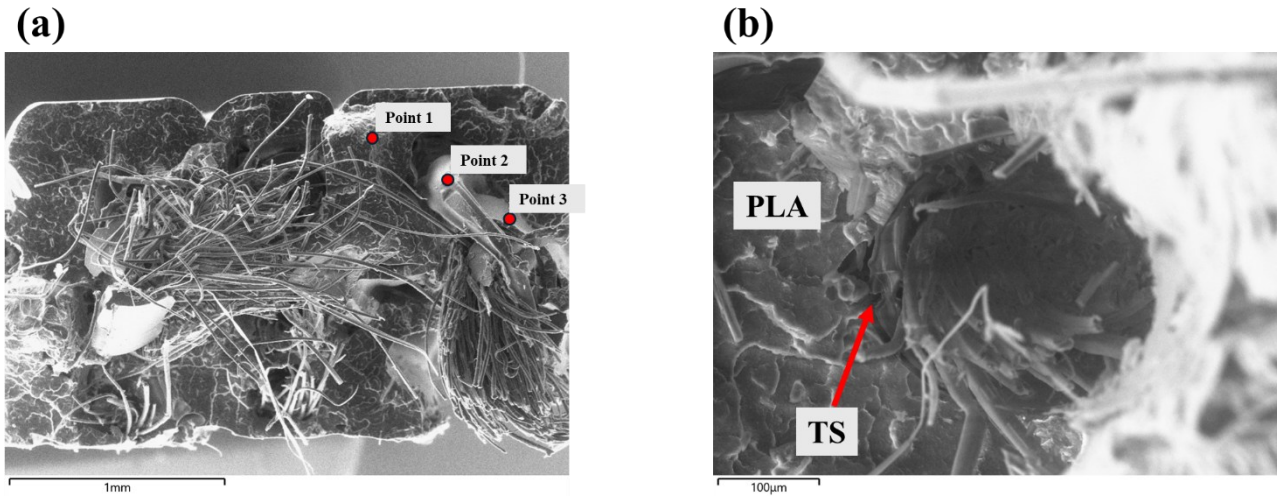

Figure 8.10: SEM microscopy for BOc: a) the first analysis site with the points where the spectra were analyzed and b) the second analysis site in which the various components are highlighted

Table 8.9: Components present and relative %wt, obtained from the spectra analyzed at the points highlighted in Figure 10a

	Component (wt%)								
Point	C	O	Na	Al	Si	S	Cl	K	Ca
1	67.6	31.33	0.19	0.14	0.28	0.07	0.22	0.07	0.09
2	69.17	30.53	/	/	0.23	/	0.07	/	/
3	57.44	41.44	0.19	0.15	0.15	0.05	0.16	0.11	0.3

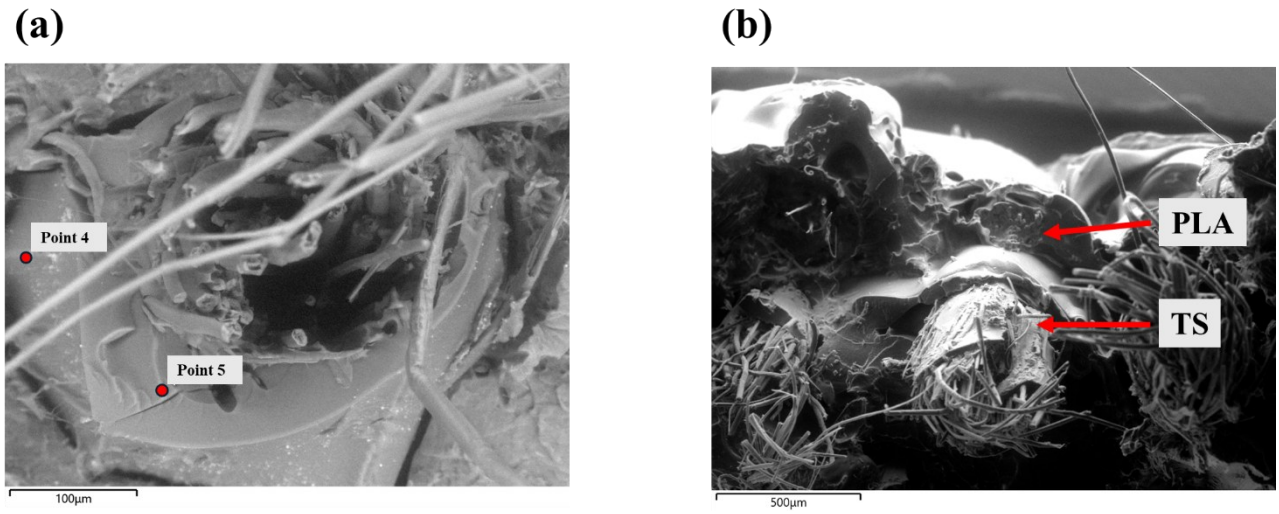

Figure 8.11: SEM microscopy for BLc: a) the first analysis site with the points where the spectra were analyzed and b) the second analysis site in which the various components are highlighted

Table 8.10: Components present and relative %wt, obtained from the spectra analyzed at the points highlighted in Figure 11a

	Component (wt%)						
Point	C	O	Na	Al	Si	P	Cl
4	56.01	42.53	0.08	1.12	0.12	0.07	0.07
5	56.25	42.05		1.34	0.14	0.13	0.09

Stereomicroscopy and SEM analyses of the fracture surfaces provide direct evidence of the weak interfacial adhesion between the reinforcement filament and the PLA matrix. In all samples investigated with stereomicroscopy (Fig.8.8, Fig.8.9), the surface of the reinforcement filament appears clean and smooth after fracture, with no detectable traces of PLA adhering to the filament surface. This observation is characteristic of an interfacial (adhesive) failure and confirms the negligible load transfer across the interface. SEM observations further corroborate this behavior, showing a complete absence of matrix remnants on the reinforcement surface, consistent with interfacial debonding occurring prior to filament failure. These morphological features are fully consistent with the absence of chemical bonding and with the limited physical interactions at the cured thermoset - PLA interface.

8.4 Conclusions and future developments

In this chapter, two biocomposites reinforced with continuous flax fiber were printed with FFF technology and tested in simple tension to obtain a complete characterization of the in-plane properties and an evaluation of their anisotropy. The results were compared with those obtained for the neat matrix and literature data for similar studies [165].

The produced biocomposites exhibited a void percentage around 10%, with final effective fiber volume fractions of 20% and 19% for BO_C and BL_C, respectively.

The incorporation of continuous flax fiber in both co-extruded composites increases the longitudinal stiffness and strength, which approximately doubled the values measured for the neat PLA matrix. The shear properties of the composite made with bleached fiber were found to be comparable to those of the neat matrix. Conversely, using boiled fiber significantly increases the shear modulus, but this improvement is followed by a brittle, catastrophic failure due to cleavage mechanism. However, the transverse properties are very low for both BO_C and BL_C. The results obtained for both materials are consistent with those obtained by Wu et al. [165] at the same fiber volume fraction (around 20%), who achieved similar results using a reinforcement fiber with higher mechanical performance.

Both BO_C and BL_C have a marked anisotropy, while the neat matrix shows isotropic behavior. The anisotropic behavior of these 3D printed composites was also evaluated using the method proposed in Section 3.2.1. For comparison purpose, CBF_{cc} was included, since it is a continuous fiber reinforced composite but it is realized with basalt fibers. The increasing impact of the orthotropic component on the isotropic one was observed when moving from BL_C to BO_C and was more pronounced with continuous basalt fiber as reinforcement.

The analysis of the fracture surfaces, both under a stereomicroscope and SEM, revealed the presence of TS resin around the fiber even after 3D printing. It is reasonable that this allows the integrity of the fibers to be maintained. This can also be seen by comparing the stiffness of the fiber from the datasheet with those calculated from mechanical tests at 0°. The estimated stiffness contribution of the fiber is consistent with the values indicated in the supplier's datasheet. This indicates that the coated filament preparation process and the subsequent 3D printing did not affect the integrity of the fiber, without damaging its performance.

Overall, bleached fiber has a performance and structure more suitable for structural applications. Boiled fiber has good longitudinal properties, but its shear and transverse properties are not entirely satisfactory. This can be reasonably attributed to the irregularity of the fiber and the resulting negative implications for stress transfer.

The use of TS resin as a coating was shown to provide excellent results in 3D-printed biocomposites. Specifically, it homogenized the fiber shape, especially with the bleached one, and successfully preserved its mechanical performance. Undoubtedly, an important future development will be finding a more sustainable TS resin, with the aim of achieving a 100% biobased composite. Furthermore, optimizing the interfaces between the fibre-TS and between the TS and the thermoplastic matrix is important for improving the transverse properties.

Conclusions and future developments

The work presented in this thesis has explored how additive manufacturing can serve as a versatile platform for combining high mechanical performance with environmental sustainability using fiber-reinforced materials. The thesis addresses these issues progressively from recycled short-fiber composites, to mineral-based continuous fibers, and finally to almost fully bio-derived continuous-fiber biocomposites.

The first stage of the research focused on PA6 reinforced with short carbon fibers, comparing the virgin material with its mechanically recycled version. Thermal and rheological analyses confirmed that the recycling process induces degradation, as expected. Yet, once printed, the recycled material exhibited better transverse and shear properties than the virgin one. This seemingly counterintuitive result highlighted how, in additive manufacturing, material performance cannot be evaluated independently from the printing process. Degradation during the recycling process reduces the viscosity of the recycled PA6. This increases the molecular diffusion between the newly deposited material and the material already present, resulting in stronger inter- and intra-layer adhesion. Morphological analyses supported this interpretation, revealing more compact and flattened filament cross-sections. Overall, these findings suggest that one-time recycling fiber-reinforced polyamides is not only feasible but may even produce materials more suitable for printing than their virgin counterparts, thereby contributing to circular-economy strategies within the field of additive manufacturing.

The second part of the work examined continuous basalt fiber–reinforced composites produced via co-extrusion 3D printing with a PA12 matrix, rather than the PA6 matrix used previously. The aim was to assess whether a mineral-based natural fiber could provide a sustainable alternative to more conventional synthetic fibers, while maintaining good mechanical performance to ensure structural applications. The usage of continuous reinforcement fibers instead of short fibers showed extremely large increases in stiffness and strength along the fiber direction, whereas the transverse and shear properties remained similar to those of the neat matrix. This pronounced anisotropy, which was further confirmed through a generalized Mohr circle analysis, is typical of unidirectionally reinforced materials. It reflects the fact that the continuous fiber carries most of the load when properly aligned. The mechanical performance is significantly superior to that of short fibers and is satisfactory for ready-to-use applications, even though the fibers are mineral rather than synthetic.

The third research direction involved a shift toward fully bio-derived materials with the study of continuous vegetable fibers and their applicability to 3D printing processes. The literature review highlighted that flax and ramie currently represent the most promising natural fibers for additive manufacturing, due to their industrial availability, relatively consistent morphology and superior mechanical properties compared with other vegetable fibers. However, the state of the art still shows several shortcomings: printing setups are often non-standard, many systems rely on custom modifications rather than commercial AM equipment, and complete in-plane mechanical characterization is rarely performed. In addition, the intrinsic variability of natural fibers and their sensitivity to moisture pose further challenges that remain only partially resolved.

To overcome some of these limitations, a complete workflow for the preparation of continuous vegetable fibers has been developed, based on a thermosetting coating that can be polymerized with UV rays. Two versions of flax were chosen as the continuous reinforcing fiber, corresponding to two different fiber treatments carried out by the supplier: boiling (BO) and bleaching (BL). The aim was to produce a continuous filament with stable geometry and suitable dimensions for co-extrusion using commercially available printing methods, based on the principles previously applied to basalt fibers. For both flax fibers, morphological, rheological and thermal analyses confirmed that the method complies with the required dimensional specifications of the reinforcement filament. In addition, this UV coating solution

preserved the intrinsic mechanical properties of the fibers: the values of stiffness and strength inferred from tensile tests were consistent with the manufacturer's datasheet, demonstrating that neither coating nor printing damaged the reinforcement.

In the final stage of the research, the previously coated filaments were used to fabricate 3D-printed biocomposites made from a PLA matrix reinforced with continuous flax fibers. The results revealed a strongly directional mechanical behavior, analogous to that observed in the basalt-reinforced composite. The PLA matrix behaved instead almost isotropically, as expected. The mechanical integrity of the flax fibers was preserved, and the behavior of the printed biocomposites confirmed the feasibility of producing 3D-printed, fully bio-derived structures with reliable and predictable structural performance, particularly in the direction of reinforcement.

Taken together, these results illustrate that additive manufacturing can indeed serve as a platform for integrating sustainable materials without fully compromising performance. Recycled polyamides can be reused successfully at least once after recycling, with performance suitable for 3D printing. Continuous basalt fibers offer a balanced compromise between mechanical properties and environmental impact. Vegetable fibers, when properly prepared, enable the fabrication of entirely bio-based composites compatible with commercial printing processes and suitable for low- and medium-load applications.

Looking ahead, numerous research directions remain open: understanding the effects of multiple recycling loops on mechanical behavior of short-fiber reinforced materials, limiting the variability of natural fibers through treatments or hybrid yarns, optimizing fiber-matrix compatibility using more sustainable approaches and expanding mechanical characterization campaigns to include out-of-plane properties, fatigue behavior and fracture mechanics. In parallel, combining natural fibers with fully bio-based or recyclable matrices represents a particularly promising frontier, potentially enabling the creation of 3D-printed composites that are not only high-performing but also deeply aligned with circular-life-cycle principles.

In conclusion, this thesis shows that the integration of new materials, advanced additive manufacturing processes and sustainability-oriented design can pave the way for a new generation of fiber-reinforced composites, where technological innovation and environmental responsibility can progress together rather than in opposition.

List of acronyms and symbols

BL_{fib}	[-]	Bleached flax fiber
BL_F	[-]	Coated filament realized with bleached flax fiber
BL_C	[-]	Co-extruded composite realized with BL_F
BO_{fib}	[-]	Boiled flax fiber
BO_F	[-]	Coated filament realized with boiled flax fiber
BO_C	[-]	Co-extruded composite realized with BO_F
CBF	[-]	Filament made by continuous basalt fiber, coated with thermoset resin
CBF_{cc}	[-]	CBF co-extruded composite
CVm	[-]	Coefficient of variation of mass
$D(n, \alpha)$	[-]	Lilliefors statistical variable: n is the sample size and α is the significance level (= 0.05)
D_{fib}^X	[-]	Diameter of the initial raw flax fiber, x is the type of fiber (BO or BL)
D_F^X	[-]	Diameter of the coated filament, x is the type of fiber (BO or BL)
E_{fib}^X	[GPa]	Young's modulus of the initial raw flax fiber, x is the type of fiber (BO or BL)
E_1	[GPa]	Young's modulus in longitudinal direction
E_2	[GPa]	Young's modulus in transverse direction
E_{10}	[GPa]	Young's modulus at 10°
G_{12}	[GPa]	Shear modulus
G'	[Pa]	Storage modulus
G''	[Pa]	Loss modulus
G^*	[Pa]	Complex modulus
ISI	[-]	In-Situ Impregnation process
M_{fib}^X	[g]	Mass of the initial raw flax fiber, x is the type of fiber (BO or BL)
M_F^X	[g]	Mass of the coated filament, x is the type of fiber (BO or BL)
OON	[-]	Prepreg Filament technique
PPF	[-]	Out-Of-Nozzle method

S_L	[MPa]	Longitudinal strength
$(S_L)_{PLA}$	[MPa]	Longitudinal strength for PLA matrix
$(S_L)_{Xc}$	[MPa]	Longitudinal strength of the co-extruded biocomposite, x is the type of fiber (BO or BL)
S_F^X	[MPa]	Strength of the coated filament, x is the type of fiber (BO or BL)
S_{fib}^X	[MPa]	Strength of the initial raw flax fiber, x is the type of fiber (BO or BL)
S_T	[MPa]	Transverse strength
S_{TS}	[MPa]	Strength of the thermoset resin used as coating material
S_{LT}	[MPa]	Shear strength
$S_{LT}^{45°}$	[MPa]	Shear strength obtained from 45° samples
$S_{LT}^{10°}$	[MPa]	Shear strength obtained from 10° samples
T_m	[°C]	Melting temperature
T_g	[°C]	Glass transition temperature
U_1, U_4	[GPa]	Isotropic contributions – Tsai and Pagano anisotropy evaluation
U_2, U_3	[GPa]	Orthotropic contributions – Tsai and Pagano anisotropy evaluation
$\frac{U_2}{U_1}$	[-]	Weight of the longitudinal-transverse orthotropic component (U_2) with respect to the isotropic one
$\frac{U_3}{U_1}$	[-]	Weight of the shear orthotropic component (U_3) with respect to the isotropic one
$\%v$	[%]	Voids percentage
wt%	[%]	Weight percentage of the component

γ_{12}	[mm/mm]	Shear strain
γ_{ul}	[mm/mm]	Ultimate shear strain
ε	[mm/mm]	Strain
$\varepsilon_{ul}^{0°}$	[mm/mm]	Ultimate strain at 0° (longitudinal)
$\varepsilon_{ul}^{90°}$	[mm/mm]	Ultimate strain at 90° (transverse)
$\varepsilon_{ul}^{10°}$	[mm/mm]	Ultimate strain at 10°
η^*	[Pa·s]	Complex viscosity
ν_{12}	[-]	Poisson's ratio

ρ_{fib}^{X}	[g/cm^3]	Density of the initial raw flax fiber, x is type of fiber (BO or BL)
ρ_{F}^{X}	[g/cm^3]	Density of the coated filament, x is the type of fiber (BO or BL)
ρ_{TS}^{X}	[g/cm^3]	Density of thermoset resin in the coated filament realized with the specific type of fiber x (BO or BL)
ρ_{X}^{f}	[g/cm^3]	Filament density before printing, x is the considered material
ρ_{X}^{s}	[g/cm^3]	3D printed sample density before testing, x is the considered material
ρ_{Xc}	[g/cm^3]	Density of the co-extruded biocomposite, x is the type of fiber (BO or BL)
σ	[MPa]	Stress
$\sigma_{Y}^{0^\circ}$	[MPa]	Yield strength at 0° (longitudinal)
$\sigma_{Y}^{10^\circ}$	[MPa]	Yield strength at 10°
$\sigma_{Y}^{45^\circ}$	[MPa]	Yield strength at 45°
$\sigma_{Y}^{90^\circ}$	[MPa]	Yield strength at 90° (transverse)
τ	[MPa]	Shear stress
τ_{Y}	[MPa]	Yield shear strength
ϕ_{F}^{X}	[%]	Coated filament volume fraction in the co-extruded biocomposite, x is the type of fiber (BO or BL)
ϕ_{X}	[%]	Material volume fraction, x is the considered material
χ_{c}	[%]	Crystalline fraction
Ψ_{X}	[%]	Material mass fraction, x is the considered material

References

[1] T. A. Yeshiwas, A. B. Tiruneh, e M. A. Sisay, «A review article on the assessment of additive manufacturing», *J. Mater. Sci. Mater. Eng.*, vol. 20, fasc. 1, p. 85, lug. 2025, doi: 10.1186/s40712-025-00306-8.

[2] L. Zhou, J. Miller, J. Vezza, M. Mayster, M. Raffay, Q. Justice, Z. Al Tamimi, G. Hansotte, L. D. Sunkara, e J. Bernat, «Additive Manufacturing: A Comprehensive Review», *Sensors*, vol. 24, fasc. 9, p. 2668, apr. 2024, doi: 10.3390/s24092668.

[3] T. Kerr e S. Barrett, *Arduino IV: DIY Robots: 3D Printing, Instrumentation, and Control*. Cham: Springer International Publishing, 2022. doi: 10.1007/978-3-031-11209-6.

[4] G. Gao, F. Xu, J. Xu, G. Tang, e Z. Liu, «A Survey of the Influence of Process Parameters on Mechanical Properties of Fused Deposition Modeling Parts», *Micromachines*, vol. 13, fasc. 4, p. 553, mar. 2022, doi: 10.3390/mi13040553.

[5] D. Syrlybayev, B. Zharylkassyn, A. Seisekulova, M. Akhmetov, A. Perveen, e D. Talamona, «Optimisation of Strength Properties of FDM Printed Parts—A Critical Review», *Polymers*, vol. 13, fasc. 10, p. 1587, mag. 2021, doi: 10.3390/polym13101587.

[6] L. Malagutti, V. Mazzanti, e F. Mollica, «Tensile properties of FDM 3D-printed wood flour filled polymers and mathematical modeling through classical lamination theory», *Rapid Prototyp. J.*, vol. 28, fasc. 9, pp. 1834–1842, ott. 2022, doi: 10.1108/RPJ-11-2021-0298.

[7] C. Tóth, K. Molnár, e Á. D. Virág, «Short fiber reinforcement in material extrusion 3D printing: A meta-analysis review with insights into sustainable alternatives», *Polym. Compos.*, p. pc.29850, apr. 2025, doi: 10.1002/pc.29850.

[8] A. Nasirov, A. Gupta, S. Hasanov, e I. Fidan, «Three-scale asymptotic homogenization of short fiber reinforced additively manufactured polymer composites», *Compos. Part B Eng.*, vol. 202, p. 108269, dic. 2020, doi: 10.1016/j.compositesb.2020.108269.

[9] S. Yu, Y. H. Hwang, K. T. Lee, S. O. Kim, J. Y. Hwang, e S. H. Hong, «Outstanding Strengthening and Toughening Behavior of 3D-Printed Fiber-Reinforced Composites Designed by Biomimetic Interfacial Heterogeneity», *Adv. Sci.*, vol. 9, fasc. 3, p. 2103561, gen. 2022, doi: 10.1002/advs.202103561.

[10] S. Lu, B. Zhang, J. Niu, C. Yang, Y. Cao, e C. Sun, «Effect of fiber content on mechanical properties of carbon fiber-reinforced polyether-ether-ketone composites prepared using screw extrusion-based online mixing 3D printing», *Addit. Manuf.*, vol. 80, p. 103976, gen. 2024, doi: 10.1016/j.addma.2024.103976.

[11] S. Yu, Y. H. Hwang, J. Y. Hwang, e S. H. Hong, «Analytical study on the 3D-printed structure and mechanical properties of basalt fiber-reinforced PLA composites using X-ray microscopy», *Compos. Sci. Technol.*, vol. 175, pp. 18–27, mag. 2019, doi: 10.1016/j.compscitech.2019.03.005.

[12] L. Sang, S. Han, Z. Li, X. Yang, e W. Hou, «Development of short basalt fiber reinforced polylactide composites and their feasible evaluation for 3D printing applications», *Compos. Part B Eng.*, vol. 164, pp. 629–639, mag. 2019, doi: 10.1016/j.compositesb.2019.01.085.

[13] H. L. Tekinalp, V. Kunc, G. M. Velez-Garcia, C. Duty, L. J. Love, A. K. Naskar, C. A. Blue, e S. Ozcan, «Highly oriented carbon fiber–polymer composites via additive manufacturing», *Compos. Sci. Technol.*, vol. 105, pp. 144–150, dic. 2014, doi: 10.1016/j.compscitech.2014.10.009.

[14] N. Giani, L. Mazzocchetti, T. Benelli, F. Picchioni, e L. Giorgini, «Towards sustainability in 3D printing of thermoplastic composites: Evaluation of recycled carbon fibers as

reinforcing agent for FDM filament production and 3D printing», *Compos. Part Appl. Sci. Manuf.*, vol. 159, p. 107002, ago. 2022, doi: 10.1016/j.compositesa.2022.107002.
[15] Y. Abderrafai, A. Rhoul, R. Chegdani, S. Gmouh, e A. Belhachmi, «Additive manufacturing of short carbon fiber-reinforced polyamide composites by fused filament fabrication: Formulation, manufacturing and characterization», *Mater. Des.*, vol. 214, p. 110358, feb. 2022, doi: 10.1016/j.matdes.2021.110358.
[16] P. Wang, B. Zou, S. Ding, C. Huang, Z. Shi, Y. Ma, e P. Yao*et al.*, «Preparation of short CF/GF reinforced PEEK composite filaments and their comprehensive properties evaluation for FDM-3D printing», *Compos. Part B Eng.*, vol. 198, p. 108175, ott. 2020, doi: 10.1016/j.compositesb.2020.108175.
[17] C. Tóth, N. L. Lukács, e N. K. Kovács, «The role of the fiber–matrix interface in the tensile properties of short fiber–reinforced 3D -printed polylactic acid composites», *Polym. Compos.*, vol. 45, fasc. 15, pp. 13589–13602, ott. 2024, doi: 10.1002/pc.28720.
[18] Y.-T. Fu, J. Li, Y.-Q. Li, S.-Y. Fu, e F.-L. Guo, «Full-process multi-scale morphological and mechanical analyses of 3D printed short carbon fiber reinforced polyetheretherketone composites», *Compos. Sci. Technol.*, vol. 236, p. 109999, mag. 2023, doi: 10.1016/j.compscitech.2023.109999.
[19] P. Cheng, Y. Peng, S. Li, Y. Rao, A. Le Duigou, K. Wang, and S. Ahzi, «3D printed continuous fiber reinforced composite lightweight structures: A review and outlook», *Compos. Part B Eng.*, vol. 250, p. 110450, feb. 2023, doi: 10.1016/j.compositesb.2022.110450.
[20] P. Cheng, Y. Peng, K. Wang, A. Le Duigou, e S. Ahzi, «3D printing continuous natural fiber reinforced polymer composites: A review», *Polym. Adv. Technol.*, vol. 35, fasc. 1, p. e6242, gen. 2024, doi: 10.1002/pat.6242.
[21] H. Zheng, S. Zhu, L. Chen, L. Wang, H. Zhang, P. Wang, K. Sun, H. Wang, and C. Liu, «3D Printing Continuous Fiber Reinforced Polymers: A Review of Material Selection, Process, and Mechanics-Function Integration for Targeted Applications», *Polymers*, vol. 17, fasc. 12, p. 1601, giu. 2025, doi: 10.3390/polym17121601.
[22] S. Yu, H. Bale, S. Park, J. Y. Hwang, e S. H. Hong, «Anisotropic microstructure dependent mechanical behavior of 3D-printed basalt fiber-reinforced thermoplastic composites», *Compos. Part B Eng.*, vol. 224, p. 109184, nov. 2021, doi: 10.1016/j.compositesb.2021.109184.
[23] P. Consul, K.-U. Beuerlein, G. Luzha, e K. Drechsler, «Effect of Extrusion Parameters on Short Fiber Alignment in Fused Filament Fabrication», *Polymers*, vol. 13, fasc. 15, p. 2443, lug. 2021, doi: 10.3390/polym13152443.
[24] J. Yan, E. Demirci, A. Ganesan, e A. Gleadall, «Extrusion width critically affects fibre orientation in short fibre reinforced material extrusion additive manufacturing», *Addit. Manuf.*, vol. 49, p. 102496, gen. 2022, doi: 10.1016/j.addma.2021.102496.
[25] E. Shulga, R. Karamov, I. S. Sergeichev, S. D. Konev, L. I. Shurygina, I. S. Akhatov, S. D. Shandakov, and A. G. Nasibulin , «Fused Filament Fabricated Polypropylene Composite Reinforced by Aligned Glass Fibers», *Materials*, vol. 13, fasc. 16, p. 3442, ago. 2020, doi: 10.3390/ma13163442.
[26] A. Yadav, P. Rohru, A. Babbar, R. Kumar, N. Ranjan, J. S. Chohan, and M. Gupta , «Fused filament fabrication: A state-of-the-art review of the technology, materials, properties and defects», *Int. J. Interact. Des. Manuf. IJIDeM*, vol. 17, fasc. 6, pp. 2867–2889, dic. 2023, doi: 10.1007/s12008-022-01026-5.
[27] B. Shaqour, M. Abuabiah, S. Abdel-Fattah, A. Juaidi, R. Abdallah, W. Abuzaina, M. Qarout, and B. Verleije , «Gaining a better understanding of the extrusion process in fused filament

fabrication 3D printing: a review», *Int. J. Adv. Manuf. Technol.*, vol. 114, fasc. 5–6, pp. 1279–1291, mag. 2021, doi: 10.1007/s00170-021-06918-6.
[28] S. Sommacal, A. Matschinski, J. Holmes, K. Drechsler, e P. Compston, «Detailed void characterisation by X-ray computed tomography of material extrusion 3D printed carbon fibre/PEEK», *Compos. Struct.*, vol. 308, p. 116635, mar. 2023, doi: 10.1016/j.compstruct.2022.116635.
[29] D. Yang, H. Zhang, J. Wu, e E. D. McCarthy, «Fibre flow and void formation in 3D printing of short-fibre reinforced thermoplastic composites: An experimental benchmark exercise», *Addit. Manuf.*, vol. 37, p. 101686, gen. 2021, doi: 10.1016/j.addma.2020.101686.
[30] Y.-T. Fu, J. Li, F.-L. Guo, Y.-Q. Li, e S.-Y. Fu, «Micro-structure and tensile property analyses of 3D printed short carbon fiber reinforced PEEK composites», *Compos. Commun.*, vol. 41, p. 101655, ago. 2023, doi: 10.1016/j.coco.2023.101655.
[31] S. Prajapati, J. K. Sharma, S. Kumar, S. Pandey, e M. K. Pandey, «A review on comparison of physical and mechanical properties of PLA, ABS, TPU, and PETG manufactured engineering components by using fused deposition modelling», *Mater. Today Proc.*, p. S2214785324003146, mag. 2024, doi: 10.1016/j.matpr.2024.05.018.
[32] B. Mallikarjuna, P. Bhargav, S. Hiremath, K. G. Jayachristiyan, e N. Jayanth, «A review on the melt extrusion-based fused deposition modeling (FDM): background, materials, process parameters and military applications», *Int. J. Interact. Des. Manuf. IJIDeM*, vol. 19, fasc. 2, pp. 651–665, feb. 2025, doi: 10.1007/s12008-023-01354-0.
[33] D. Acierno e A. Patti, «Fused Deposition Modelling (FDM) of Thermoplastic-Based Filaments: Process and Rheological Properties—An Overview», *Materials*, vol. 16, fasc. 24, p. 7664, dic. 2023, doi: 10.3390/ma16247664.
[34] K. I. Ismail, T. C. Yap, e R. Ahmed, «3D-Printed Fiber-Reinforced Polymer Composites by Fused Deposition Modelling (FDM): Fiber Length and Fiber Implementation Techniques», *Polymers*, vol. 14, fasc. 21, p. 4659, nov. 2022, doi: 10.3390/polym14214659.
[35] J. Li, Y. Durandet, X. Huang, G. Sun, e D. Ruan, «Additively manufactured fiber-reinforced composites: A review of mechanical behavior and opportunities», *J. Mater. Sci. Technol.*, vol. 119, pp. 219–244, ago. 2022, doi: 10.1016/j.jmst.2021.11.063.
[36] K. Badogu, R. Kumar, e R. Kumar, «3D Printing of Glass Fiber-Reinforced Polymeric Composites: A Review», *J. Inst. Eng. India Ser. C*, vol. 103, fasc. 5, pp. 1285–1301, ott. 2022, doi: 10.1007/s40032-022-00873-1.
[37] M. N. Ahmad, M. R. Ishak, M. Mohammad Taha, F. Mustapha, e Z. Leman, «A Review of Natural Fiber-Based Filaments for 3D Printing: Filament Fabrication and Characterization», *Materials*, vol. 16, fasc. 11, p. 4052, mag. 2023, doi: 10.3390/ma16114052.
[38] V. Mazzanti, L. Malagutti, e F. Mollica, «FDM 3D Printing of Polymers Containing Natural Fillers: A Review of their Mechanical Properties», *Polymers*, vol. 11, fasc. 7, p. 1094, giu. 2019, doi: 10.3390/polym11071094.
[39] J. Gonzalez-Gutierrez, S. Cano, S. Schuschnigg, C. Kukla, J. Sapkota, e C. Holzer, «Additive Manufacturing of Metallic and Ceramic Components by the Material Extrusion of Highly-Filled Polymers: A Review and Future Perspectives», *Materials*, vol. 11, fasc. 5, p. 840, mag. 2018, doi: 10.3390/ma11050840.
[40] J. Jacob, D. Pejak Simunec, A. E. Z. Kandjani, A. Trinchi, e A. Sola, «A Review of Fused Filament Fabrication of Metal Parts (Metal FFF): Current Developments and Future Challenges», *Technologies*, vol. 12, fasc. 12, p. 267, dic. 2024, doi: 10.3390/technologies12120267.

[41] Z. Liu, L. Zhang, Z. Li, C. Wang, Z. Wu, S. Wu, H. Wu, P. Geng, S. Chen, G. Liu, L. Yang, Z. Xia, C. Yan, e Y. Shi , «Continuous basalt fibers into fireproof and thermal insulation architectures using an additive manufacturing manipulator», *Mater. Des.*, vol. 235, p. 112434, nov. 2023, doi: 10.1016/j.matdes.2023.112434.
[42] Z. Dong, J. Ji, Z. Liu, C. Wu, G. Wu, H. Zhu, e P. Zhang, «I-shaped ECC/UHPC composite beams reinforced with steel bars and BFRP sheets», *Sustain. Struct.*, vol. 3, fasc. 1, 2023, doi: 10.54113/j.sust.2023.000022.
[43] H. Liu, Y. Yu, Y. Liu, M. Zhang, L. Li, L. Ma, Y. Sun, e W. Wang , «A Review on Basalt Fiber Composites and Their Applications in Clean Energy Sector and Power Grids», *Polymers*, vol. 14, fasc. 12, p. 2376, giu. 2022, doi: 10.3390/polym14122376.
[44] P. Russo, G. Simeoli, L. Vitiello, e G. Filippone, «Bio-Polyamide 11 Hybrid Composites Reinforced with Basalt/Flax Interwoven Fibers: A Tough Green Composite for Semi-Structural Applications», *Fibers*, vol. 7, fasc. 5, p. 41, mag. 2019, doi: 10.3390/fib7050041.
[45] H. J. Aida, R. Nadlene, M. T. Mastura, L. Yusriah, D. Sivakumar, e R. A. Ilyas, «Natural fibre filament for Fused Deposition Modelling (FDM): a review», *Int. J. Sustain. Eng.*, vol. 14, fasc. 6, pp. 1988–2008, nov. 2021, doi: 10.1080/19397038.2021.1962426.
[46] M. H. M. Nasir, M. M. Taha, N. Razali, R. A. Ilyas, V. F. Knight, e M. N. F. Norrrahim, «Effect of Chemical Treatment of Sugar Palm Fibre on Rheological and Thermal Properties of the PLA Composites Filament for FDM 3D Printing», *Materials*, vol. 15, fasc. 22, p. 8082, nov. 2022, doi: 10.3390/ma15228082.
[47] N. R. Rajendran Royan, J. S. Leong, W. N. Chan, J. R. Tan, e Z. S. B. Shamsuddin, «Current State and Challenges of Natural Fibre-Reinforced Polymer Composites as Feeder in FDM-Based 3D Printing», *Polymers*, vol. 13, fasc. 14, p. 2289, lug. 2021, doi: 10.3390/polym13142289.
[48] D. Rigotti, L. Fambri, e A. Pegoretti, «Bio-composites for Fused Filament Fabrication. Effects of Maleic Anhydride Grafting on Poly(Lactic Acid) and Microcellulose», 3 settembre 2021, *In Review*. doi: 10.21203/rs.3.rs-839482/v1.
[49] M. A. S. Siddiqui, M. S. Rabbi, R. U. Ahmed, e Md. M. Billah, «Biodegradable natural polymers and fibers for 3D printing: A holistic perspective on processing, characterization, and advanced applications», *Clean. Mater.*, vol. 14, p. 100275, dic. 2024, doi: 10.1016/j.clema.2024.100275.
[50] J. A. Brydson, *Plastics materials*, 7th ed. Oxford Boston: Butterworth-Heinemann, 1999.
[51] J. E. Mark, A c. di, *Physical properties of polymers handbook*, 2nd ed. New York: Springer, 2006.
[52] G. G. Odian, *Principles of polymerization*, 4th ed. Hoboken, N.J: Wiley-Interscience, 2004.
[53] A. Ravve, *Principles of Polymer Chemistry*. New York, NY: Springer New York, 2012. doi: 10.1007/978-1-4614-2212-9.
[54] J.E. Mark, «Polymer Data Handbook-version 3», 1999
[55] M. Choi, J. Byun, D. Kang, K. Jeong, J. Lee, S. M. Kim, e J. Han, «Environmental analysis of nylon 6,6 production from gamma-valerolactone derived from kenaf», *Ind. Crops Prod.*, vol. 204, p. 117365, nov. 2023, doi: 10.1016/j.indcrop.2023.117365.
[56] M. I. Khan, M. T. Islam, L. Wang, e R. Padhye, «Comparative energy demand and carbon footprint analysis of textile waste management systems in Australia», *Environ. Sci. Pollut. Res.*, vol. 32, fasc. 13, pp. 8529–8546, mar. 2025, doi: 10.1007/s11356-025-36200-1.
[57] M. Y. Kondo *et al.*, «Recent advances in the use of Polyamide-based materials for the automotive industry», *Polímeros*, vol. 32, fasc. 2, p. e2022023, 2022, doi: 10.1590/0104-1428.20220042.

[58] J. Dubois, «Arkema's Integrated Plant-Based Factories», in *Chemicals and Fuels from Bio-Based Building Blocks*, 1ª ed., F. Cavani, S. Albonetti, F. Basile, e A. Gandini, A c. di, Wiley, 2016, pp. 535–548. doi: 10.1002/9783527698202.ch20.
[59] Z. Guo, J. Wu, e J. Wang, «Chemical degradation and recycling of polyethylene terephthalate (PET): a review», *RSC Sustain.*, vol. 3, fasc. 5, pp. 2111–2133, 2025, doi: 10.1039/D4SU00658E.
[60] E. Bezeraj, S. Debrie, F. J. Arraez Hernandez, P. Reyes Isaacura, P. Van Steenberge, D. D. D'hooge, e M. Edeleva, «State-of-the-art of industrial PET mechanical recycling: technologies, impact of contamination and guidelines for decision-making», *RSC Sustain.*, vol. 3, fasc. 5, pp. 1996–2047, 2025, doi: 10.1039/D4SU00571F.
[61] M. N. Siddiqui, H. H. Redhwi, A. A. Al-Arfaj, e D. S. Achilias, «Chemical Recycling of PET in the Presence of the Bio-Based Polymers, PLA, PHB and PEF: A Review», *Sustainability*, vol. 13, fasc. 19, p. 10528, set. 2021, doi: 10.3390/su131910528.
[62] L. Avérous, Polylactic Acid: Synthesis, Properties and Applications», Monomers, Polymers and Composites from Renewable Resources, Chapter 21, 2008
[63] S. Farah, D. G. Anderson, e R. Langer, «Physical and mechanical properties of PLA, and their functions in widespread applications — A comprehensive review», *Adv. Drug Deliv. Rev.*, vol. 107, pp. 367–392, dic. 2016, doi: 10.1016/j.addr.2016.06.012.
[64] R. M. Rasal, A. V. Janorkar, e D. E. Hirt, «Poly(lactic acid) modifications», *Prog. Polym. Sci.*, vol. 35, fasc. 3, pp. 338–356, mar. 2010, doi: 10.1016/j.progpolymsci.2009.12.003.
[65] H. Tsuji, «Poly(lactide) Stereocomplexes: Formation, Structure, Properties, Degradation, and Applications», *Macromol. Biosci.*, vol. 5, fasc. 7, pp. 569–597, lug. 2005, doi: 10.1002/mabi.200500062.
[66] R. E. Drumright, P. R. Gruber, e D. E. Henton, «Polylactic Acid Technology», *Adv. Mater.*, vol. 12, fasc. 23, pp. 1841–1846, dic. 2000, doi: 10.1002/1521-4095(200012)
[67] M. Barletta, C. Aversa, M. Ayyoob, A. Gisario, K. Hamad, M. Mehrpouya, e H. Vahabi, «Poly(butylene succinate) (PBS): Materials, processing, and industrial applications», *Prog. Polym. Sci.*, vol. 132, p. 101579, set. 2022, doi: 10.1016/j.progpolymsci.2022.101579.
[68] J. Han, J. Shi, Z. Xie, J. Xu, e B. Guo, «Synthesis, Properties of Biodegradable Poly(Butylene Succinate-co-Butylene 2-Methylsuccinate) and Application for Sustainable Release», *Materials*, vol. 12, fasc. 9, p. 1507, mag. 2019, doi: 10.3390/ma12091507.
[69] V. Rajgond, A. Mohite, N. More, e A. More, «Biodegradable polyester-polybutylene succinate (PBS): a review», *Polym. Bull.*, vol. 81, fasc. 7, pp. 5703–5752, mag. 2024, doi: 10.1007/s00289-023-04998-w.
[70] J. Xu e B. Guo, «Poly(butylene succinate) and its copolymers: Research, development and industrialization», *Biotechnol. J.*, vol. 5, fasc. 11, pp. 1149–1163, nov. 2010, doi: 10.1002/biot.201000136.
[71] L. Ranakoti, B. Gangil, S. K. Mishra, T. Singh, S. Sharma, R. A. Ilyas, e S. El-Khatib , «Critical Review on Polylactic Acid: Properties, Structure, Processing, Biocomposites, and Nanocomposites», *Materials*, vol. 15, fasc. 12, p. 4312, giu. 2022, doi: 10.3390/ma15124312.
[72] M. Zanelli, G. Ronconi, N. Pritoni, A. D'Iorio, M. Bertoldo, V. Mazzanti, e F. Mollica , «3D Printing of Continuous Basalt Fiber-Reinforced Composites: Characterization of the In-Plane Mechanical Properties and Anisotropy Evaluation», *Polymers*, vol. 16, fasc. 23, p. 3377, nov. 2024, doi: 10.3390/polym16233377.
[73] M. Somireddy, C. V. Singh, e A. Czekanski, «Analysis of the Material Behavior of 3D Printed Laminates Via FFF», *Exp. Mech.*, vol. 59, fasc. 6, pp. 871–881, lug. 2019, doi: 10.1007/s11340-019-00511-5.

[74] M. Somireddy e A. Czekanski, «Anisotropic material behavior of 3D printed composite structures – Material extrusion additive manufacturing», *Mater. Des.*, vol. 195, p. 108953, ott. 2020, doi: 10.1016/j.matdes.2020.108953.
[75] Gibson, R. Principles of composite materials mechanics. 2016, Chapter 2, CRC Press USA
[76] Agarwal, B.D.; Broutman, L.J.; Chandrashekhara, K. Analysis and Performance of Fiber Composites. 2017, 4th ed., Chapter 5, Wiley
[77] S. W. Tsai, N.J. Pagano, «Invariant properties of composite materials», Technical report AFML-TR-67-349, 1968
[78] S.W. Tsai, «Introduction to composite materials». 1980, Chapter 2, Technomic
[79] ASTM D3039; Standard Test Method for Tensile Properties of Polymer Matrix Composite Materials. ASTM International: West Conshohocken, PA, USA, 2014.
[80] ASTM D3518; Standard Test Method for In-Plane Shear Response of Polymer Matrix Composite Materials by Tensile Test of a ±45◦ Laminate. ASTM International: West Conshohocken, PA, USA, 2018
[81] C. C. Chamis e J. H. Sinclair, «Ten-deg off-axis test for shear properties in fiber composites: It is demonstrated that the 10-deg off-axis tensile test is an accurate and convenient test method for the intralaminar-shear characterization of unidirectional fiber composites», *Exp. Mech.*, vol. 17, fasc. 9, pp. 339–346, set. 1977, doi: 10.1007/BF02326320.
[82] S. Lee e M. Munro, «Evaluation of in-plane shear test methods for advanced composite materials by the decision analysis technique», *Composites*, vol. 17, fasc. 1, pp. 13–22, gen. 1986, doi: 10.1016/0010-4361(86)90729-9.
[83] H. Ho, M. Y. Tsai, J. Morton, e G. L. Farley, «A comparison of three popular test methods for determining the shear modulus of composite materials», *Compos. Eng.*, vol. 3, fasc. 1, pp. 69–81, gen. 1993, doi: 10.1016/0961-9526(93)90032-F.
[84] G. Odegard e M. Kumosa, «Determination of shear strength of unidirectional composite materials with the Iosipescu and 10 o -axis shear tests».
[85] Yeow. H. F. Brinson, «A comparison of simple shear characterizatk)n methods for composite laminates».
[86] M. Ateeq, M. Shafique, A. Azam, e M. Rafiq, «A review of 3D printing of the recycled carbon fiber reinforced polymer composites: Processing, potential, and perspectives», *J. Mater. Res. Technol.*, vol. 26, pp. 2291–2309, set. 2023, doi: 10.1016/j.jmrt.2023.07.171.
[87] K. I. Ismail, T. C. Yap, e R. Ahmed, «3D-Printed Fiber-Reinforced Polymer Composites by Fused Deposition Modelling (FDM): Fiber Length and Fiber Implementation Techniques», *Polymers*, vol. 14, fasc. 21, p. 4659, nov. 2022, doi: 10.3390/polym14214659.
[88] M. Mergulhão, S. Magalhães, e J. M. Costa, «Recycling Potential of Onyx Composite for Additive Manufacturing», *UPorto J. Eng.*, vol. 9, fasc. 3, pp. 91–101, apr. 2023, doi: 10.24840/2183-6493_009-003_001845.
[89] S. Ding, B. Zou, P. Wang, C. Huang, J. Liu, e L. Li, «Geometric modeling and recycling of 3D printed fiber reinforced thermoplastic composite plain weft knitted structures», *Compos. Part Appl. Sci. Manuf.*, vol. 149, p. 106528, ott. 2021, doi: 10.1016/j.compositesa.2021.106528.
[90] C. Lohr, A. Trauth, J. Schukraft, S. Leher, e K. A. Weidenmann, «Investigation on the recycling potential of additively manufactured carbon fiber reinforced PA 6.6», *Compos. Struct.*, vol. 352, p. 118683, gen. 2025, doi: 10.1016/j.compstruct.2024.118683.
[91] N. Vidakis *et al.*, «Sustainable Additive Manufacturing: Mechanical Response of Polyamide 12 over Multiple Recycling Processes», *Materials*, vol. 14, fasc. 2, p. 466, gen. 2021, doi: 10.3390/ma14020466.

[92] M. Kohutiar *et al.*, «Comprehensive Review: Technological Approaches, Properties, and Applications of Pure and Reinforced Polyamide 6 (PA6) and Polyamide 12 (PA12) Composite Materials», *Polymers*, vol. 17, fasc. 4, p. 442, feb. 2025, doi: 10.3390/polym17040442.
[93] F. Bandinelli, E. Tito, E. Parisi, L. Peroni, e M. Scapin, «Recycling a carbon fiber-reinforced polyamide through 3D printing: A mechanical and physicochemical analysis», *Compos. Part B Eng.*, vol. 294, p. 112147, apr. 2025, doi: 10.1016/j.compositesb.2025.112147.
[94] Markforged. Datasheet (v 5.1). https://markforged.com/landing/material-data-sheet/. [Accessed 5 January 2025].
[95] C. Millot, L.-A. Fillot, O. Lame, P. Sotta, e R. Seguela, «Assessment of polyamide-6 crystallinity by DSC: Temperature dependence of the melting enthalpy», *J. Therm. Anal. Calorim.*, vol. 122, fasc. 1, pp. 307–314, ott. 2015, doi: 10.1007/s10973-015-4670-5.
[96] I. Papa, A. T. Silvestri, M. R. Ricciardi, V. Lopresto, e A. Squillace, «Effect of Fibre Orientation on Novel Continuous 3D-Printed Fibre-Reinforced Composites», *Polymers*, vol. 13, fasc. 15, p. 2524, lug. 2021, doi: 10.3390/polym13152524.
[97] V. Mishra, S. Negi, e S. Kar, «FDM-based additive manufacturing of recycled thermoplastics and associated composites», *J. Mater. Cycles Waste Manag.*, vol. 25, fasc. 2, pp. 758–784, mar. 2023, doi: 10.1007/s10163-022-01588-2.
[98] V. Shanmugam, O. Das, R. E. Neisiany, K. Babu, S. Singh, M. S. Hedenqvist, F. Berto, e S. Ramakrishna, «Polymer Recycling in Additive Manufacturing: an Opportunity for the Circular Economy», *Mater. Circ. Econ.*, vol. 2, fasc. 1, p. 11, dic. 2020, doi: 10.1007/s42824-020-00012-0.
[99] D. Kobayashi, Y.-T. Hsieh, e A. Takahara, «Interphase structure of carbon fiber reinforced polyamide 6 revealed by microbeam X-ray diffraction with synchrotron radiation», *Polymer*, vol. 89, pp. 154–158, apr. 2016, doi: 10.1016/j.polymer.2016.02.057.
[100] P. P. X. Yap, Z. Yen, T. Salim, H. C. A. Lim, C. K. Chung, e Y. M. Lam, «The impact of mechanical recycling on the degradation of polyamide», *Polym. Degrad. Stab.*, vol. 225, p. 110773, lug. 2024, doi: 10.1016/j.polymdegradstab.2024.110773.
[101] M. E. B. Dos Santos, G. F. D. M. Morgado, L. F. D. P. Santos, E. H. Backes, J. Marini, L. S. Montagna, F. R. Passador, «Mechanical Recycling Process: An Alternative for CF/PA6 Composite Waste from the Automotive Industry», *ACS Sustain. Resour. Manag.*, vol. 1, fasc. 11, pp. 2394–2403, nov. 2024, doi: 10.1021/acssusresmgt.4c00245.
[102] J. E. Crespo, F. Parres, M. A. Peydró, e R. Navarro, «Study of rheological, thermal, and mechanical behavior of reprocessed polyamide 6», *Polym. Eng. Sci.*, vol. 53, fasc. 4, pp. 679–688, apr. 2013, doi: 10.1002/pen.23307.
[103] K. H. Lee, S. J. Lim, e W. N. Kim, «Rheological and thermal properties of polyamide 6 and polyamide 6/glass fiber composite with repeated extrusion», *Macromol. Res.*, vol. 22, fasc. 6, pp. 624–631, giu. 2014, doi: 10.1007/s13233-014-2086-x.
[104] P. P. X. Yap, Z. Yen, T. Salim, H. C. A. Lim, C. K. Chung, e Y. M. Lam, «The impact of mechanical recycling on the degradation of polyamide», *Polym. Degrad. Stab.*, vol. 225, p. 110773, lug. 2024, doi: 10.1016/j.polymdegradstab.2024.110773.
[105] S. V. Levchik, E. D. Weil, e M. Lewin, «Thermal decomposition of aliphatic nylons», *Polym. Int.*, vol. 48, fasc. 7, pp. 532–557, lug. 1999, doi: 10.1002/(SICI)1097-0126(199907)48:7%3C532::AID-PI214%3E3.0.CO;2-R.
[106] A. Bonardi, R. Cilloni, V. Paganuzzi, e N. Grizzuti, «Effects of Degree of Recycling on the Rheology and Processability of Thermoplastic Polymers», *J. Polym. Eng.*, vol. 23, fasc. 2, mar. 2003, doi: 10.1515/POLYENG.2003.23.2.79.

[107] W. Dong e P. Gijsman, «Influence of temperature on the thermo-oxidative degradation of polyamide 6 films», *Polym. Degrad. Stab.*, vol. 95, fasc. 6, pp. 1054–1062, giu. 2010, doi: 10.1016/j.polymdegradstab.2010.02.030.
[108] K. Chen, Y. Wang, L. Zhou, J. Dai, W. Chen, e W. Lu, «Characteristics and competitive mechanisms of polycondensation and cyclization induced by end-groups in polyamide 6 melt», *J. Polym. Sci.*, vol. 62, fasc. 22, pp. 5019–5029, nov. 2024, doi: 10.1002/pol.20240463.
[109] Karstens, T.; Rosbach, V. «Thermo-oxidative degradation of polyamide 6 and 66. Kinetics of the formation and inhibition of UV/VIS-active chromophores». Makromol. Chem. 190, 3033-3053 (1989)
[110] J. E. Seppala, S. H. Han, K. E. Hillgartner, e C. S. Davis, «Weld formation during material extrusion additive manufacturing»,Soft Matter., Vol.13, pp. 6761-6769, 2017. https://doi.org/10.1039/C7SM00950J.
[111] C. McIlroy e P. D. Olmsted, «Disentanglement effects on welding behaviour of polymer melts during the fused-filament-fabrication method for additive manufacturing», Polymer., Vol. 123 , pp. 376-391, 2017 http://dx.doi.org/10.1016/j.polymer.2017.06.051.
[112] S. Qi, X. Gao, Y. Su, X. Dong, D. Cavallo, e D. Wang, «Correlation between welding behavior and mechanical anisotropy of long chain polyamide 12 manufactured with fused filament fabrication», Polymer., vol. 213, p.123318, 2021, https://doi.org/10.1016/j.polymer.2020.123318.
[113] S. Liparoti, D. Sofia, A. Romano, F. Marra, e R. Pantani, «Fused Filament Deposition of PLA: The Role of Interlayer Adhesion in the Mechanical Performances», Polymers., vol.13, p. 399. https://doi.org/10.3390/polym13030399.
[114] A. Lepoivre, N. Boyard, A. Levy, e V. Sobotka, «Heat Transfer and Adhesion Study for the FFF Additive Manufacturing Process», Proc. Manufac., vol.47, pp. 948-955, 2020, https://doi.org/10.1016/j.promfg.2020.04.291.
[115] V. Speranza, S. Liparoti, V. Volpe, G. Titomanlio, e R. Pantani, «Modelling of morphology development towards spherulites and shish–kebabs: Application to isothermal flow-induced crystallization experiments on isotactic polypropylene», Polymer., vol.196, p.122459, 2020, https://doi.org/10.1016/j.polymer.2020.122459
[116] P. G. De Gennes, «Reptation of a Polymer Chain in the Presence of Fixed Obstacles», *J. Chem. Phys.*, vol. 55, fasc. 2, pp. 572–579, lug. 1971, doi: 10.1063/1.1675789.
[117] M.Doi, S.F. Edwards, «The theory of Polymer Dynamics». Clarendon Press, Oxford, 1988
[118] T. P. Lodge, «Reconciliation of the Molecular Weight Dependence of Diffusion and Viscosity in Entangled Polymers», *Rev.Lett.*, vol. 83, fasc. 16, 1999.
[119] H. Tao, T. P. Lodge, e E. D. Von Meerwall, «Diffusivity and Viscosity of Concentrated Hydrogenated Polybutadiene Solutions», *Macromolecules*, vol. 33, fasc. 5, pp. 1747–1758, mar. 2000, doi: 10.1021/ma991983r.
[120] K. Hagita e H. Takano, «Self-Diffusion of a Polymer Chain in a Melt», *J. Phys. Soc. Jpn.*, vol. 72, fasc. 8, pp. 1824–1827, ago. 2003, doi: 10.1143/JPSJ.72.1824.
[121] P. Lan, Q. Zhao, G. Lv, G. S. Sheridan, D. G. Cahill, e C. M. Evans, «Molecular-Weight Dependence of Center-of-Mass Chain Diffusion in Polymerized Ionic Liquid Melts», *Macromolecules*, vol. 56, fasc. 9, pp. 3383–3392, mag. 2023, doi: 10.1021/acs.macromol.2c02388.
[122] S. Shanbhag e Z. Wang, «Molecular Simulation of Tracer Diffusion and Self-Diffusion in Entangled Polymers», *Macromolecules*, vol. 53, fasc. 12, pp. 4649–4658, giu. 2020, doi: 10.1021/acs.macromol.0c00680.

[123] P. Qu, H. Kong, X. Li, Y. Lei, A. Guo, S. Wang, H. Wang, Y. Hu, Y. Wan, J. Takahashi, «Additive manufacturing of hybrid continuous carbon/basalt fiber reinforced composites based on bi-matrix co-extrusion», *J. Mater. Res. Technol.*, vol. 30, pp. 8683–8704, mag. 2024, doi: 10.1016/j.jmrt.2024.05.241.

[124] H. Kong, P. Qu, X. Li, D. Kong, A. Guo, S. Wang, Y. Wan, J. Takahashi,, «An investigation into mechanical properties of a 3D printed two-matrix continuous fiber composites with multi-cavity structure», *J. Mater. Res. Technol.*, vol. 26, pp. 4365–4386, set. 2023, doi: 10.1016/j.jmrt.2023.08.132.

[125] M. Malik, D. Ruan, e P. Saxena, «Effect of Raster Orientation and Fiber Volume Fraction on 3D-Printed Continuous Basalt Fiber-Reinforced Polylactic Acid Composites», *J. Mater. Eng. Perform.*, mar. 2025, doi: 10.1007/s11665-025-11076-x.

[126] M. Malik e P. Saxena, «3D-Printed Continuous Basalt Fiber-Reinforced Polylactic Acid Composites: Effect of Printing Parameters on Impact and Interlaminar Shear Strength», *J. Mater. Eng. Perform.*, feb. 2025, doi: 10.1007/s11665-025-10767-9.

[127] M. Malik e P. Saxena, «A comparative assessment of hydrothermal aging effects on performance and failure modes of additively manufactured continuous basalt fiber-reinforced thermoplastic composites», *Compos. Part Appl. Sci. Manuf.*, vol. 199, p. 109195, dic. 2025, doi: 10.1016/j.compositesa.2025.109195.

[128] Blaine, R.L. Thermal Applications Note Polymer Heats of Fusion; TA Instruments: New Castle, DE, USA; Volume TN048

[129] L. C. Hao e W. D. Yu, «Evaluation of thermal protective performance of basalt fiber nonwoven fabrics», *J. Therm. Anal. Calorim.*, vol. 100, fasc. 2, pp. 551–555, mag. 2010, doi: 10.1007/s10973-009-0179-0.

[130] J. G. Moore, «Density of basalt core from Hilo drill hole, Hawaii», *J. Volcanol. Geotherm. Res.*, vol. 112, fasc. 1–4, pp. 221–230, dic. 2001, doi: 10.1016/S0377-0273(01)00242-6.

[131] M. Iragi, C. Pascual-González, A. Esnaola, C. S. Lopes, e L. Aretxabaleta, «Ply and interlaminar behaviours of 3D printed continuous carbon fibre-reinforced thermoplastic laminates; effects of processing conditions and microstructure», *Addit. Manuf.*, vol. 30, p. 100884, dic. 2019, doi: 10.1016/j.addma.2019.100884.

[132] F. Dau, M.-L. Dano, B. Vérone, J. Girardot, Z. Aboura, e J.-M. Morvan, «In-plane and out-of-plane characterization of a 3D angle interlock textile composite», *Compos. Part Appl. Sci. Manuf.*, vol. 149, p. 106581, ott. 2021, doi: 10.1016/j.compositesa.2021.106581.

[133] L. Malagutti, G. Ronconi, M. Zanelli, F. Mollica, e V. Mazzanti, «A Post-Processing Method for Improving the Mechanical Properties of Fused-Filament-Fabricated 3D-Printed Parts», *Processes*, vol. 10, fasc. 11, p. 2399, nov. 2022, doi: 10.3390/pr10112399.

[134] D. Ray, A c. di, *Biocomposites for high-performance applications: current barriers and future needs towards industrial development*. in Woodhead Publishing series in composites science and engineering. Duxford, United Kingdom: Woodhead Publishing, an imprint of Elsevier, 2017.

[135] L. Yan, N. Chouw, e K. Jayaraman, «Flax fibre and its composites – A review», *Compos. Part B Eng.*, vol. 56, pp. 296–317, gen. 2014, doi: 10.1016/j.compositesb.2013.08.014.

[136] H. V. Scheller e P. Ulvskov, «Hemicelluloses», *Annu. Rev. Plant Biol.*, vol. 61, fasc. 1, pp. 263–289, giu. 2010, doi: 10.1146/annurev-arplant-042809-112315.

[137] M. Liu, D. Fernando, G. Daniel, B. Madsen, A.S. Meyer, M.T. Ale, A. Thygesen, «Effect of harvest time and field retting duration on the chemical composition, morphology and mechanical properties of hemp fibers», *Ind. Crops Prod.*, vol. 69, pp. 29–39, lug. 2015, doi: 10.1016/j.indcrop.2015.02.010.

[138] A. Bourmaud, C. Morvan, A. Bouali, V. Placet, P. Perré, e C. Baley, «Relationships between micro-fibrillar angle, mechanical properties and biochemical composition of flax fibers», *Ind. Crops Prod.*, vol. 44, pp. 343–351, gen. 2013, doi: 10.1016/j.indcrop.2012.11.031.

[139] K. Charlet, S. Eve, J. P. Jernot, M. Gomina, e J. Breard, «Tensile deformation of a flax fiber», *Procedia Eng.*, vol. 1, fasc. 1, pp. 233–236, lug. 2009, doi: 10.1016/j.proeng.2009.06.055.

[140] B. Devarajan, R. LakshmiNarasimhan, B. Venkateswaran, S. Mavinkere Rangappa, e S. Siengchin, «Additive manufacturing of jute fiber reinforced polymer composites: A concise review of material forms and methods», *Polym. Compos.*, vol. 43, fasc. 10, pp. 6735–6748, ott. 2022, doi: 10.1002/pc.26789.

[141] N. V. Dos Santos, A. Giubilini, P. Minetola, L. Iuliano, M. D. Banea, e D. C. T. Cardoso, «Towards sustainable additive manufacturing of continuous natural yarn-reinforced thermoplastic biocomposites: a review», *Cellulose*, vol. 32, fasc. 10, pp. 5763–5793, lug. 2025, doi: 10.1007/s10570-025-06594-9.

[142] A. Le Duigou, D. Correa, M. Ueda, R. Matsuzaki, e M. Castro, «A review of 3D and 4D printing of natural fibre biocomposites», *Mater. Des.*, vol. 194, p. 108911, set. 2020, doi: 10.1016/j.matdes.2020.108911.

[143] S. Pervaiz, T. A. Qureshi, G. Kashwani, e S. Kannan, «3D Printing of Fiber-Reinforced Plastic Composites Using Fused Deposition Modeling: A Status Review», *Materials*, vol. 14, fasc. 16, p. 4520, ago. 2021, doi: 10.3390/ma14164520.

[144] M. Li, Y. Pu, V.M. Thomas, C.G. Yoo, S. Ozcan, Y. Deng, K. Nelson, A.J. Ragauskas, «Recent advancements of plant-based natural fiber–reinforced composites and their applications», *Compos. Part B Eng.*, vol. 200, p. 108254, nov. 2020, doi: 10.1016/j.compositesb.2020.108254.

[145] J. Ribeiro, M. Rodriguez-Martin, J. Barreiro, A. Fernandez-Abia, R. Garcia-Martin, J. Rocha, S. Martinez-Pellitero, «New trends of additive manufacturing using materials based-on natural fibers and minerals : A systematic review», *Heliyon*, vol. 11, fasc. 2, p. e41993, gen. 2025, doi: 10.1016/j.heliyon.2025.e41993.

[146] S. Islam, M. B. Hasan, F. Karim, M. Kodric, M. R. Islam, M.M. Khatun, K. Z. M. Abdul Motaleb, «Thermoset and thermoplastic polymer composites reinforced with flax fiber: Properties and application—A review», *SPE Polym.*, vol. 6, fasc. 1, p. e10172, gen. 2025, doi: 10.1002/pls2.10172.

[147] M. Z. Rahman, «Mechanical and damping performances of flax fibre composites – A review», *Compos. Part C Open Access*, vol. 4, p. 100081, mar. 2021, doi: 10.1016/j.jcomc.2020.100081.

[148] S. Terekhina, S. Egorov, T. Tarasova, I. Skornyakov, L. Guillaumat, e M. L. Hattali, «In-nozzle impregnation of continuous textile flax fiber/polyamide 6 composite during FFF process», *Compos. Part Appl. Sci. Manuf.*, vol. 153, p. 106725, feb. 2022, doi: 10.1016/j.compositesa.2021.106725.

[149] M. Wang, X. Song, Z. Yang, C. Luo, S. Chi, e H. Jiang, «Flexural properties of 3D printed continuous flax fiber reinforced polyethylene composites», *PeerJ Mater. Sci.*, vol. 7, p. e34, apr. 2025, doi: 10.7717/peerj-matsci.34.

[150] T. Fruleux, M. Castro, P. Sauleau, R. Matsuzaki, e A. Le Duigou, «Matrix stiffness: A key parameter to control hydro-elasticity and morphing of 3D printed biocomposite», *Compos. Part Appl. Sci. Manuf.*, vol. 156, p. 106882, mag. 2022, doi: 10.1016/j.compositesa.2022.106882.

[151] A. Le Duigou, A. Barbé, E. Guillou, e M. Castro, «3D printing of continuous flax fibre reinforced biocomposites for structural applications», *Mater. Des.*, vol. 180, p. 107884, ott. 2019, doi: 10.1016/j.matdes.2019.107884.

[152] A. Le Duigou, G. Chabaud, R. Matsuzaki, e M. Castro, «Tailoring the mechanical properties of 3D-printed continuous flax/PLA biocomposites by controlling the slicing parameters», *Compos. Part B Eng.*, vol. 203, p. 108474, dic. 2020, doi: 10.1016/j.compositesb.2020.108474.

[153] C. De Kergariou, H. Saidani-Scott, A. Perriman, F. Scarpa, e A. Le Duigou, «The influence of the humidity on the mechanical properties of 3D printed continuous flax fibre reinforced poly(lactic acid) composites», *Compos. Part Appl. Sci. Manuf.*, vol. 155, p. 106805, apr. 2022, doi: 10.1016/j.compositesa.2022.106805.

[154] C. De Kergariou, B. C. Kim, A. Perriman, A. Le Duigou, S. Guessasma, e F. Scarpa, «Design of 3D and 4D printed continuous fibre composites via an evolutionary algorithm and voxel-based Finite Elements: Application to natural fibre hygromorphs», *Addit. Manuf.*, vol. 59, p. 103144, nov. 2022, doi: 10.1016/j.addma.2022.103144.

[155] T. Fruleux, M. Castro, D. Correa, K. Wang, R. Matsuzaki, e A. L. Duigou, «Geometric limitations of 3D printed continuous flax-fiber reinforced biocomposites cellular lattice structures», *Compos. Part C Open Access*, vol. 9, p. 100313, ott. 2022, doi: 10.1016/j.jcomc.2022.100313.

[156] H. Zhang, X. Lei, Q. Hu, S. Wu, M. Aburaia, J. Gonzalez-Gutierrez, H. Lammer, «Hybrid Printing Method of Polymer and Continuous Fiber-Reinforced Thermoplastic Composites (CFRTPCs) for Pipes through Double-Nozzle Five-Axis Printer», *Polymers*, vol. 14, fasc. 4, p. 819, feb. 2022, doi: 10.3390/polym14040819.

[157] H. Zhang, D. Liu, T. Huang, Q. Hu, e H. Lammer, «Three-Dimensional Printing of Continuous Flax Fiber-Reinforced Thermoplastic Composites by Five-Axis Machine», *Materials*, vol. 13, fasc. 7, p. 1678, apr. 2020, doi: 10.3390/ma13071678.

[158] Y. Long, Z. Zhang, K. Fu, Z. Yang, e Y. Li, «Design and fabrication of high-performance 3D printed continuous flax fibre/PLA composites», *J. Manuf. Process.*, vol. 99, pp. 351–361, ago. 2023, doi: 10.1016/j.jmapro.2023.05.044.

[159] N. V. Dos Santos, A. Giubilini, D. C. T. Cardoso, e P. Minetola, «Exploring printing methods for continuous natural fiber-reinforced thermoplastic biocomposites: A comparative study», *Sustain. Mater. Technol.*, vol. 43, p. e01253, apr. 2025, doi: 10.1016/j.susmat.2025.e01253.

[160] Y. Long, Z. Zhang, K. Fu, e Y. Li, «Efficient plant fibre yarn pre-treatment for 3D printed continuous flax fibre/poly(lactic) acid composites», *Compos. Part B Eng.*, vol. 227, p. 109389, dic. 2021, doi: 10.1016/j.compositesb.2021.109389.

[161] S. Kuschmitz, A. Schirp, J. Busse, H. Watschke, C. Schirp, e T. Vietor, «Development and Processing of Continuous Flax and Carbon Fiber-Reinforced Thermoplastic Composites by a Modified Material Extrusion Process», *Materials*, vol. 14, fasc. 9, p. 2332, apr. 2021, doi: 10.3390/ma14092332.

[162] N. V. dos Santos, D. K. K. Cavalcanti, J. S. S. Neto, M. D. Banea, e D. C. T. Cardoso, « Mechanical properties and adhesion of Fused Filament Fabrication (FFF) printed biocomponents with continuous vegetable fiber reinforcement», Conference Paper, lug. 2023, doi: 10.5281/ZENODO.8113853.

[163] Y. Long, Z. Zhang, C. Yan, Z. Huang, K. Fu, e Y. Li, «Multi-objective optimization for improving printing efficiency and mechanical properties of 3D-printed continuous plant fibre composites», *Compos. Commun.*, vol. 35, p. 101283, nov. 2022, doi: 10.1016/j.coco.2022.101283.

[164] D. Quereilhac, T. Caillault, S. Terekhina, M. Bar, G. Morel, M. Fazzini, M. Abida, E. De Luycker, P. Ouagne, «Development of a custom commingled flax/PLA wrapped yarn for additive manufacturing of long-fibre biocomposites», *Mater. Des.*, vol. 258, p. 114628, ott. 2025, doi: 10.1016/j.matdes.2025.114628.

[165] X. Wu, G. Ginoux, J. Paux, e S. Allaoui, «Damage and fracture studies of continuous flax fiber-reinforced composites 3D printed by in-nozzle impregnation additive manufacturing», *Int. J. Damage Mech.*, vol. 34, fasc. 4, pp. 640–661, apr. 2025, doi: 10.1177/10567895241279845.

[166] J. I. P. Singh, S. Singh, e V. Dhawan, «Influence of fiber volume fraction and curing temperature on mechanical properties of jute/PLA green composites», *Polym. Polym. Compos.*, vol. 28, fasc. 4, pp. 273–284, mag. 2020, doi: 10.1177/0967391119872875.

[167] B. Madsen, A. Thygesen, e H. Lilholt, «Plant fibre composites – porosity and volumetric interaction», *Compos. Sci. Technol.*, vol. 67, fasc. 7–8, pp. 1584–1600, giu. 2007, doi: 10.1016/j.compscitech.2006.07.009.

[168] M. H. Shakir e A. K. Singh, «Ramie fiber and its composites: A review», *Polym. Compos.*, vol. 46, fasc. 8, pp. 6813–6841, giu. 2025, doi: 10.1002/pc.29417.

[169] C. Mudi e A. Shaw, «Investigations on the Mechanical Performance and Durability of Ramie Fibers Under Various Environmental Conditions», *J. Nat. Fibers*, vol. 22, fasc. 1, p. 2433043, dic. 2025, doi: 10.1080/15440478.2024.2433043.

[170] R. Cai, W. Wen, K. Wang, Y. Peng, S. Ahzi, e F. Chinesta, «Tailoring interfacial properties of 3D-printed continuous natural fiber reinforced polypropylene composites through parameter optimization using machine learning methods», *Mater. Today Commun.*, vol. 32, p. 103985, ago. 2022, doi: 10.1016/j.mtcomm.2022.103985.

[171] N. V. Santos e D. C. T. Cardoso, «3D printing of vegetable yarn-reinforced polymer components», *J. Clean. Prod.*, vol. 415, p. 137870, ago. 2023, doi: 10.1016/j.jclepro.2023.137870.

[172] R. Cai, H. Lin, P. Cheng, Z. Zhang, K. Whang, Y. Peng, Y. Wu, S. Ahzi, «Investigation on dynamic strength of 3D -printed continuous ramie fiber reinforced biocomposites at various strain rates using machine learning methods», *Polym. Compos.*, vol. 43, fasc. 8, pp. 5235–5249, ago. 2022, doi: 10.1002/pc.26816.

[173] N. V. Dos Santos, D. K. K. Cavalcanti, J. S. S. Neto, H. F. M. De Queiroz, M. D. Banea, e D. C. T. Cardoso, «Analysis of voids, interfacial and thermal properties of additively manufactured continuous natural fiber-reinforced biocomposites», *Prog. Addit. Manuf.*, vol. 10, fasc. 8, pp. 5401–5422, ago. 2025, doi: 10.1007/s40964-024-00913-5.

[174] P. Cheng, K. Wang, X. Chen, J. Wang, Y. Peng, S. Ahzi, C. Chen, «Interfacial and mechanical properties of continuous ramie fiber reinforced biocomposites fabricated by in-situ impregnated 3D printing», *Ind. Crops Prod.*, vol. 170, p. 113760, ott. 2021, doi: 10.1016/j.indcrop.2021.113760.

[175] P. Cheng, Y. Peng, K. Wang, A. Le Duigou, S. Yao, e C. Chen, «Quasi-static penetration property of 3D printed woven-like ramie fiber reinforced biocomposites», *Compos. Struct.*, vol. 303, p. 116313, gen. 2023, doi: 10.1016/j.compstruct.2022.116313.

[176] K. Wang, H. Lin, A. Le Duigou, R. Cai, Y. Huang, P. Cheng, H. Zhang, Y. Peng, «Geometric Accuracy and Energy Absorption Characteristics of 3D Printed Continuous Ramie Fiber Reinforced Thin-Walled Composite Structures», *Chin. J. Mech. Eng.*, vol. 36, fasc. 1, p. 150, dic. 2023, doi: 10.1186/s10033-023-00982-7.

[177] P. Cheng, K. Wang, X. Chen, A. Le Duigou, Y. Peng, e W. Wen, «Compressive property and shape memory effect of 3D printed continuous ramie fiber reinforced biocomposite

corrugated structures», *Smart Mater. Struct.*, vol. 31, fasc. 12, p. 124003, dic. 2022, doi: 10.1088/1361-665X/ac95e4.
[178] P. Cheng, K. Wang, Y. Peng, S. Ahzi, F. Xu, e Z. Huang, «A novel 3D printed continuous ramie fiber reinforced variable stiffness biocomposite honeycomb structure», *Vacuum*, vol. 215, p. 112301, set. 2023, doi: 10.1016/j.vacuum.2023.112301.
[179] K. Wang, Y. Huang, P. Cheng, Y. Xiong, A. Le Duigou, Y. Peng, Y. Rao, S. Ahzi, «Novel application of dual-nozzle 3D printer for enhanced in-situ impregnation 3D printing of dry continuous fiber reinforced composites», *Compos. Part Appl. Sci. Manuf.*, vol. 183, p. 108231, ago. 2024, doi: 10.1016/j.compositesa.2024.108231.
[180] P. Cheng, K. Wang, A. Le Duigou, J. Liu, Z. Liu, Y. Peng, S. Ahzi, «A novel dual-nozzle 3D printing method for continuous fiber reinforced composite cellular structures», *Compos. Commun.*, vol. 37, p. 101448, gen. 2023, doi: 10.1016/j.coco.2022.101448.
[181] G. Ginoux, X. Wu, C. Laqraa, D. Soulat, J. Paux, M. Ferreira, A.R. Labanieh, S. Allaoui, «Continuous additive manufacturing of hemp yarn-reinforced biocomposites with improved impregnation method», *Compos. Sci. Technol.*, vol. 251, p. 110561, mag. 2024, doi: 10.1016/j.compscitech.2024.110561.
[182] J. Suteja, H. Firmanto, A. Soesanti, e C. Christian, «Properties investigation of 3D printed continuous pineapple leaf fiber-reinforced PLA composite», *J. Thermoplast. Compos. Mater.*, vol. 35, fasc. 11, pp. 2052–2061, nov. 2022, doi: 10.1177/0892705720945371.
[183] O. Rivero-Romero, I. Barrera-Fajardo, e J. Unfried-Silgado, «Effects of printing parameters on fiber eccentricity and porosity level in a thermoplastic matrix composite reinforced with continuous banana fiber fabricated by FFF with in situ impregnation», *Int. J. Adv. Manuf. Technol.*, vol. 125, fasc. 3–4, pp. 1893–1901, mar. 2023, doi: 10.1007/s00170-022-10799-8.
[184] V. Mishra, C. K. Ror, S. Negi, e V. Mahesh, «On mechanical characterization and damage analysis of additively manufactured continuous fiber/poly-lactic acid bio-composite using in-nozzle technique», *Polym. Compos.*, vol. 45, fasc. 6, pp. 5017–5027, apr. 2024, doi: 10.1002/pc.28106.
[185] R. Matsuzaki, M. Ueda, M. Namiki, T.K. Jeong, H. Asahara, K. Horiguchi, T. Nakamura, A. Todoroki, Y. Hirano, «Three-dimensional printing of continuous-fiber composites by in-nozzle impregnation», *Sci. Rep.*, vol. 6, fasc. 1, p. 23058, mar. 2016, doi: 10.1038/srep23058.
[186] N. V. Dos Santos, D. K. K. Cavalcanti, H. F. M. De Queiroz, J. S. S. Neto, M. D. Banea, e D. C. T. Cardoso, «Mono and bi-material adhesive joints with additively manufactured continuous natural fiber-reinforced biocomposite adherends», *Polym. Compos.*, vol. 46, fasc. 12, pp. 11121–11136, ago. 2025, doi: 10.1002/pc.29674.
[187] Y. Yaguchi, K. Takeuchi, T. Waragai, T. Tateno, «Durability Evaluation of an Additive Manufactured Biodegradable Composite with Continuous Natural Fiber in Various Conditions Reproducing Usage Environment», *Int. J. Autom. Technol.*, vol. 14, fasc. 6, pp. 959–965, nov. 2020, doi: 10.20965/ijat.2020.p0959.
[188] X. Song, Y. Ye, S. Huang, X. Han, Z. Huang, W. Guan, Z. Yang, M. Wang, «3D printing of continuous cotton thread reinforced poly (lactic acid)», *Sci. Rep.*, vol. 14, fasc. 1, p. 30858, dic. 2024, doi: 10.1038/s41598-024-81699-y.
[189] A. N. Dickson, H. M. Abourayana, e D. P. Dowling, «3D Printing of Fibre-Reinforced Thermoplastic Composites Using Fused Filament Fabrication—A Review», *Polymers*, vol. 12, fasc. 10, p. 2188, set. 2020, doi: 10.3390/polym12102188.
[190] J. Zhang, Q. Wu, C. F. De Hoop, S. Chen, e I. Negulescu, «Fused deposition modeling 3D printing of continuous natural and regeneration fibers reinforced polymer composites and

its mechanical properties under extreme environmental conditions—A critical review», *BioResources*, vol. 20, fasc. 2, mar. 2025, doi: 10.15376/biores.20.2.Zhang.

[191] W. Zhu, Q. Zhi, D. Li, L. Fu, Z. Zhang, e C. Jiang, «Process-induced property loss of prepreg filaments with continuous fiber content of 65 vol% suitable for direct 3D printing», *J. Manuf. Process.*, vol. 131, pp. 1928–1941, dic. 2024, doi: 10.1016/j.jmapro.2024.10.008.

[192] O. G. Kravchenko, S. G. Kravchenko, e R. B. Pipes, «Chemical and thermal shrinkage in thermosetting prepreg», *Compos. Part Appl. Sci. Manuf.*, vol. 80, pp. 72–81, gen. 2016, doi: 10.1016/j.compositesa.2015.10.001.

[193] J. Liu, S. Wang, Y. Peng, J. Zhu, W. Zhao, e X. Liu, «Advances in sustainable thermosetting resins: From renewable feedstock to high performance and recyclability», *Prog. Polym. Sci.*, vol. 113, p. 101353, feb. 2021, doi: 10.1016/j.progpolymsci.2020.101353.

[194] M. A. Rahman, M. Z. Islam, L. Gibbon, C. A. Ulven, e J. J. La Scala, «3D printing of continuous carbon fiber reinforced thermoset composites using UV curable resin», *Polym. Compos.*, vol. 42, fasc. 11, pp. 5859–5868, nov. 2021, doi: 10.1002/pc.26266.

[195] M. A. Rahman, E. Hall, L. Gibbon, M. Z. Islam, C. A. Ulven, e J. J. La Scala, «A Mechanical Performance Study of Dual Cured Thermoset Resin Systems 3D-Printed with Continuous Carbon Fiber Reinforcement», *Polymers*, vol. 15, fasc. 6, p. 1384, mar. 2023, doi: 10.3390/polym15061384.

[196] A. Mantelli, A. Romani, R. Suriano, M. Diani, M. Colledani, E. Sarlin, S. Turri, M. Levi, «UV-Assisted 3D Printing of Polymer Composites from Thermally and Mechanically Recycled Carbon Fibers», *Polymers*, vol. 13, fasc. 5, p. 726, feb. 2021, doi: 10.3390/polym13050726.

[197] Z. Yang, W. Zhu, J. Shi, Z. Yang, F. Chen, e X. Han, «Rapid in-situ thermal curing 3D printing of engineering thermosetting resins», *Virtual Phys. Prototyp.*, vol. 20, fasc. 1, p. e2553180, dic. 2025, doi: 10.1080/17452759.2025.2553180.

[198] B. Lazić, S. Janjić, V. Ivanović, M. Kostić, e N. Bostjan, «EFFECT OF HYDROGEN-PEROXIDE TREATMENT ON THE PHYSICO-MECHANICAL PROPERTIES OF FLAX FIBERS», *J. Chem. Technol. Environ.*, vol. 4, fasc. 1, pp. 14–19, dic. 2023, doi: 10.59919/JCTE04202301E219.

[199] A. Amiri, C. Ulven, e S. Huo, «Effect of Chemical Treatment of Flax Fiber and Resin Manipulation on Service Life of Their Composites Using Time-Temperature Superposition», *Polymers*, vol. 7, fasc. 10, pp. 1965–1978, ott. 2015, doi: 10.3390/polym7101493.

[200] Y. Y. Then, N. A. Ibrahim, N. Zainuddin, B. W. Chieng, H. Ariffin, e W. M. Z. Wan Yunus, «Influence of Alkaline-Peroxide Treatment of Fiber on the Mechanical Properties of Oil Palm Mesocarp Fiber/Poly(butylene succinate) Biocomposite», *BioResources*, vol. 10, fasc. 1, pp. 1730–1746, gen. 2015, doi: 10.15376/biores.10.1.1730-1746.

[201] Tanoue, Matsumura, e Atsuta, «Curing depth of a composite veneering material polymerized with seven different laboratory photo-curing units», *J. Oral Rehabil.*, vol. 25, fasc. 3, pp. 199–203, mar. 1998, doi: 10.1046/j.1365-2842.1998.00224.x.

[202] P.L. Fan, R.M. Schumacher, K. Azzolin, R. Geary, F.C. Eichmiller, «Curing-light intensity and depth of cure of resin-based composites tested according to international standards», JADA, vol.133, 2022

[203] M. R. Spiegel, J. J. Schiller, e R. A. Srinivasan, «*Schaum's outlines: probability and statistics*», 3rd ed. New York: McGraw Hill Professional, 2011.

[204] N. Smirnov, « On the empirical determination of a distribution law », Wahrscheinlichkeitsrechung, pp 316-335, 1931

[205] N. Smirnov, «On the estimation of the discrepancy between empirical curves of distribution for two independent samples», Bulletin Mathematique de l'Universitè de Moscou, vol.2, 1939
[206] H. W. Lilliefors, «On the Kolmogorov-Smirnov Test for Normality with Mean and Variance Unknown», Journal of the American Statistical Association, vol. 62, pp.399-402, 1967
[207] Spiegel M. R., Probabilità e statistica, McGraw-Hill, USA, 1994
[208] P. H. Kvam e B. Vidakovic, *Nonparametric statistics with applications to science and engineering*. Hoboken, N.J: Wiley-Interscience, 2007. doi: 10.1002/9780470168707.
[209] D. Li e A. W. Neumann, «Surface heterogeneity and contact angle hysteresis», *Colloid Polym. Sci.*, vol. 270, fasc. 5, pp. 498–504, mag. 1992, doi: 10.1007/BF00665995.
[210] «Advances in Contact Angle, Wettability and Adhesion, Volume Two».
[211] Fernandez-Tena *et al.*, «Mechanical, barrier, and photodegradation properties of biodegradable PLA-based blend films», *RSC Sustainability*, vol. 3, pp. 4622–4631, 2025, doi: 10.1039/d5su00454c.
[212] C. Baley, «Analysis of the flax fibres tensile behaviour and analysis of the tensile stiffness increase», *Compos. Part Appl. Sci. Manuf.*, vol. 33, fasc. 7, pp. 939–948, lug. 2002, doi: 10.1016/S1359-835X(02)00040-4.
[213] A. Bledzki, «Composites reinforced with cellulose based fibres», *Prog. Polym. Sci.*, vol. 24, fasc. 2, pp. 221–274, mag. 1999, doi: 10.1016/S0079-6700(98)00018-5.
[214] Pickering, K. L., Efendy, M. A., & Le, T. M. (2016). A review of recent developments in natural fibre composites and their mechanical performance. Composites Part A: Applied Science and Manufacturing, vol. 83, pp. 98–112, apr. 2016, doi: 10.1016/j.compositesa.2015.08.038
[215] M. R. Piggott, «Load bearing fibre composites: second version », 2016
[216] G. Ronconi, A. Behrens, R. Hirschberg, M. Zanelli, N. Graupner, J. Mussig, P. Russo, F. Mollica, V. Mazzanti , «Mechanical characterisation and interfacial analysis of continuous flax fibre reinforced unidirectional green composites using filament winding», *Compos. Part Appl. Sci. Manuf.*, vol. 194, p. 108940, lug. 2025, doi: 10.1016/j.compositesa.2025.108940.